metals

Special Issue Reprint

Recent Advances in Cast Irons

Edited by
Annalisa Fortini and Chiara Soffritti

mdpi.com/journal/metals

MDPI

Recent Advances in Cast Irons

Recent Advances in Cast Irons

Editors

Annalisa Fortini
Chiara Soffritti

MDPI

Basel • Beijing • Wuhan • Barcelona • Belgrade • Novi Sad • Cluj • Manchester

Editors

Annalisa Fortini
Department of Engineering,
University of Ferrara,
Ferrara, Italy

Chiara Soffritti
Department of Engineering,
University of Ferrara,
Ferrara, Italy

Editorial Office
MDPI
St. Alban-Anlage 66
4052 Basel, Switzerland

This is a reprint of articles from the Special Issue published online in the open access journal *Metals* (ISSN 2075-4701) (available at: https://www.mdpi.com/journal/metals/special_issues/advances_cast_irons).

For citation purposes, cite each article independently as indicated on the article page online and as indicated below:

Lastname, A.A.; Lastname, B.B. Article Title. *Journal Name* **Year**, *Volume Number*, Page Range.

ISBN 978-3-0365-8716-5 (Hbk)
ISBN 978-3-0365-8717-2 (PDF)
doi.org/10.3390/books978-3-0365-8717-2

Contents

metals

MDPI

Editorial

Recent Advances in Cast Irons

Annalisa Fortini * and Chiara Soffritti *

Department of Engineering, University of Ferrara, Via Saragat 1/E, 44122 Ferrara, Italy
* Correspondence: frtnls@unife.it (A.F.); chiara.soffritti@unife.it (C.S.)

1. Introduction

Cast irons are widely used in industry due to their excellent castability, allowing for the production of near-net shape components with complex geometries without the need for additional forging or machining processes. They also are a cost-effective material with good machinability, corrosion resistance, and vibration damping properties, as well as relatively high wear resistance, thanks to graphite's self-effect. However, achieving the optimal combination of microstructure and mechanical properties requires optimizing the process parameters, solidification conditions, and heat treatment for a specific chemical composition. Hence, continuous research efforts in cast iron are crucial for the improvement of in-service performance.

In this frame, this Special Issue includes original research papers and a review that cover the most recent research and development aimed at improving the chemical, physical and metallurgical characteristics of cast irons that, in turn, affect their mechanical, tribological and corrosion performance.

2. Contributions

The book collects manuscripts from cutting-edge academic researchers and consists of one review paper regarding the research progress in improving the corrosion wear resistance of a novel hypereutectic high-chromium cast iron (HCCI) [1] and eight experimental research papers focused on methods for enhancing the corrosion, mechanical and microstructural features of cast irons in general, i.e., nodular, gray, vermicular, austempered ductile iron (ADI) and HCCI [2–9].

The review by Gong et al. [1] provides a detailed analysis of the development and research progress in improving the corrosion wear resistance of a novel hypereutectic HCCI, obtained by increasing its chromium and carbon contents. HCCIs are frequently used in abrasive environments where wear and corrosion can be present. The study analyzes various methods for improving the corrosion wear resistance of HCCI, such as primary carbide refinement, heat treatment, deep cooling treatment, and alloying elements addition. Given that the corrosion resistance of HCCIs is closely related to the microstructure of the matrix and number, size, shape, and distribution of carbides, primary carbide refinement, heat treatment, deep cooling treatment and alloying are addressed in detail. The review suggests research directions to expand the application of HCCI and research directions and contents to enhance the corrosion wear resistance of these materials by modification, alloying and heat treatment methods.

Concerning nodular cast irons, relevant contributions have been proposed [2,3,5]. The paper by Vicente et al. [2] concerns the applicability of the Hollomon–Jaffe parameter, usually used to establish an equivalence between time and temperature in a tempering treatment, to predict the hardness of nodular cast iron after quenching and tempering treatments. The obtained results reveal the efficacy of the parameter in studying the tempering process and in estimating the final hardness of the alloy from this and from its initial hardness. In addition, focusing on ductile cast iron, Stan et al. [3] propose a study on the analysis of the cooling curve to detect the solidification pattern of non-Si

Citation: Fortini, A.; Soffritti, C. Recent Advances in Cast Irons. *Metals* **2023**, *13*, 980. https://doi.org/10.3390/met13050980

Received: 8 May 2023
Accepted: 10 May 2023
Published: 19 May 2023

alloyed (<3.0% Si), low (3.0–3.5% Si), and medium Si alloyed (4.5–5.5% Si) cast irons also considering inoculation simultaneous effects. From the events on the cooling curve (i.e., the lowest and the highest eutectic temperatures and the temperature at the end of solidification), and on its first derivative (i.e., the maximum recalescence rate, the lowest level at the end of solidification and different graphitizing factors), the authors found that silicon is an important influencing factor, but the base and minor elements also affect the equilibrium eutectic temperatures. In addition, the highest positive effect of inoculation was detected in non-Si alloyed cast irons, while low Si alloyed cast irons are more sensitive to high solidification undercooling, compared to medium Si ductile cast irons, at a lower undercooling level, and also at lower inoculation contribution. The paper by [5] deals with static tensile and strain-controlled fatigue tests on specimens taken from real off-highway axles made by an EN-GJS-450-10 nodular cast iron. More in detail, specimens with either machined or as-cast surfaces were fatigue tested under strain-control loading to determine the high-cycle downgrading factor due to the cast skin effect. The formers were fatigue tested under different strain ratios to analyze the influence of the mean strain. The experimental findings revealed that the stress ratio is different from the nominal strain ratio and that the tested material exhibits a hardening behavior, as suggested by the comparison of the cyclic stress–strain curve with the monotonic static curve highlighted. Lastly, the analysis of the fracture surfaces showed that machined specimens exhibit crack initiation from the surface, while as-cast specimens fail in most cases from the as-cast surface or from sub-surface defects, such as silicon oxides.

Within ductile irons, recent findings on ADI material have been reported by Cruz Ramírez et al. [7] and Angella et al. [6]. The paper by Cruz Ramírez et al. [7] deals with the metallurgical and mechanical performances of camshafts made of high-strength ADIs. Two austempered ductile irons were produced from ductile irons, low alloyed with vanadium and austempered at 265 °C and 305 °C, and tested through both block-on-ring wear tester and electric spin rig testers to check and ensure the durability of the camshaft under engineering specification parameters. The authors found that austempering at 265 °C leads to the formation of a fine ausferrite microstructure that aids in obtaining the highest wear resistance in the block-on ring wear test. No wear or pitting evidence was detected on the camshaft lobes and roller surfaces after the test protocol during the electric spin ring test at low and high conditions for the ADI alloyed with 0.2 wt. % V heat treated at 265 °C. A further contribution concerning the mechanical behavior of ADI has been proposed by Angella et al. [6] that investigated the ausferrite stability with three different nominal contents of nickel through tensile testing. The results on the effects of the solidification rates (thickness sections) of the original ductile iron on the resulting ADIs' microstructure and tensile mechanical properties are reported. Castings with different wall thicknesses and with different nickel contents were austenitized at the same temperature and time, and then austempered at three different temperatures and time conditions. Hence, the combined effects of section thickness, chemical composition and austempering conditions on the tensile mechanical properties of ausferrite were investigated and related to the ausferrite stability. As a result, while the nickel content and section thickness affect the graphite morphology, they do not significantly impact the ausferrite stability and tensile behavior when the section thickness was below 25 mm. However, the study finds that the tensile plastic behavior is consistently affected by specimen geometry, indicating the importance of considering specimen geometry in the analysis and comparison of tensile properties of ADIs.

The contributions of Obregon et al. [4] and Tonolini et al. [8] contain recent findings on gray cast irons (GCIs). Within the development of new lightweight materials, Obregon et al. [4] report the development of novel lightweight cast irons, with different amounts of Al (from 0 wt. % to 15 wt. %), to investigate the correlation of the amount of Al and its effect on the microstructure. The obtained results show that for the investigated EN-GJL-HB195 grade cast iron, the perlite content decreases with the increment of wt. % of Al, while the opposite occurs with the ferrite content, since the addition of Al promotes

the stabilization of ferrite. In the case of graphite, a slight increment occurs with 2 wt. % of Al, but a great decrease occurs until 15 wt. % of Al. In the work of Tonolini et al. [8], the wear resistance of GCI samples, taken from brake discs industrially produced with different percentages of niobium, was evaluated. Indeed, brake discs play a crucial role in the operation of vehicles, and GCIs with a pearlitic matrix and type-A graphite are the most widely used material in their manufacturing. However, due to the environmental impact of disc wear during braking, alternative materials and/or compositions to the standard ones are being investigated. Against this backdrop, the study investigates the effect of varying the niobium content (0–0.7 wt. %) on the microstructure and wear behavior through pin-on-disc (PoD) wear tests, with low-metallic-friction material discs serving as the counterparts. It was found that the wear strength of the alloy is enhanced by the addition of niobium, in comparison to the base alloy, which promoted an increase in the hardness and the formation of hard NbC particles that acted as a load-bearing phase. It was found that adding relatively low amounts of niobium (i.e., 0.3 wt. %) leads to the highest wear resistance, whereas any further increase does not significantly alter the properties and resulted in the coarsening of NbC particles. Hence, it is recommended that the composition of cast iron should not exceed 0.3 wt. % niobium to improve wear resistance and keep alloying costs low.

Finally, the contribution by Liu et al. [9] examines the surface evolution of vermicular cast iron in a high-frequency cyclic plasma and facial cooling airflow to gain insights into the behavior and mechanism of such material under unique thermal shock environments with different cooling conditions. The authors reported that the mass and linear loss show an inverted V-shaped relationship with the flux of the cooling airflow, while the change in roughness decreases continuously. Additionally, as the cooling airflow increases, the eroded region decreases, iron oxides lessen, and surface temperature fluctuation weakens. Finally, through thermodynamic calculations and thermal analysis, it was demonstrated that oxidation and mechanical erosion have contrary tendencies with the rising flux in the facial cooling airflow. The study showed that the transformation of the dominant factor from oxidation to peeling off by thermal stress and scouring leads to the evolution of mass and thickness.

3. Conclusions and Outlook

The Special Issue delves into the latest research and development endeavors aimed at enhancing the metallurgical mechanical, tribological, and corrosion performance of cast irons. The review and the papers cover various topics and demonstrate overall that cast irons are still highly relevant and can be studied in detail to enhance their performance, also taking into account their environmental impact.

Acknowledgments: As Guest Editors, we would like to especially thank the Managing Editor, for his valuable support in the publication processes. We are grateful to all the contributing authors and reviewers; without their excellent work, it would not have been possible to accomplish this Special Issue.

Conflicts of Interest: The authors declare no conflict of interest.

References

1. Gong, L.; Fu, H.; Zhi, X. Corrosion Wear of Hypereutectic High Chromium Cast Iron: A Review. *Metals* **2023**, *13*, 308. [CrossRef]
2. Salas Vicente, F.; Carcel Carrasco, J.; Fernández Antoni, R.; Ferrero Taberner, J.C.; Pascual Guillamón, M. Hardness Prediction in Quenched and Tempered Nodular Cast Iron Using the Hollomon-Jaffe Parameter. *Metals* **2021**, *11*, 297. [CrossRef]
3. Stan, I.; Anca, D.; Stan, S.; Riposan, I. Solidification Pattern of Si-Alloyed, Inoculated Ductile Cast Irons, Evaluated by Thermal Analysis. *Metals* **2021**, *11*, 846. [CrossRef]
4. Obregon, A.; Sanchez, J.M.; Eguizabal, D.; Garcia, J.C.; Arruebarrena, G.; Hurtado, I.; Quintana, I.; Rodriguez, P. Microstructural Evolution as a Function of Increasing Aluminum Content in Novel Lightweight Cast Irons. *Metals* **2021**, *11*, 1646. [CrossRef]
5. Scacco, F.; Campagnolo, A.; Franceschi, M.; Meneghetti, G. Strain-Controlled Fatigue Behavior of a Nodular Cast Iron in Real Off-Highway Axles: Effects of Casting Skin and Strain Ratio. *Metals* **2022**, *12*, 426. [CrossRef]

6. Angella, G.; Donnini, R.; Ripamonti, D.; Bonollo, F.; Cygan, B.; Gorny, M. On Ausferrite Produced in Thin Sections: Stability Assessment through Round and Flat Tensile Specimen Testing. *Metals* **2023**, *13*, 105. [CrossRef]
7. Cruz Ramírez, A.; Colin García, E.; Téllez Ramírez, J.; Magaña Hernández, A. Performance Evaluation of Austempered Ductile Iron Camshaft Low Alloyed with Vanadium on an Electric Spin Rig Test. *Metals* **2023**, *13*, 198. [CrossRef]
8. Tonolini, P.; Montesano, L.; Pola, A.; Bontempi, G.; Gelfi, M. Wear Behavior of Nb Alloyed Gray Cast Iron for Automotive Brake Disc Application. *Metals* **2023**, *13*, 365. [CrossRef]
9. Liu, L.; Zhao, K.; Zhang, H.; Tang, C.; Han, Q.; Chen, J.; Tao, D.; Yang, Z. Surface Evolution of Vermicular Cast Iron in High Frequent Cyclic Plasma and Different Facial Cooling Airflows. *Metals* **2023**, *13*, 577. [CrossRef]

metals

MDPI

Review

Corrosion Wear of Hypereutectic High Chromium Cast Iron: A Review

Liqiang Gong [1], Hanguang Fu [1,*] and Xiaohui Zhi [2]

[1] Key Laboratory of Advanced Functional Materials, Department of Materials Science and Engineering, Ministry of Education, Beijing University of Technology, Beijing 100124, China
[2] School of Mechanical Engineering, Shijiazhuang Tiedao University, Shijiazhuang 050043, China
* Correspondence: hgfu@bjut.edu.cn

Abstract: Hypereutectic High Chromium Cast Iron (HHCCI) is a new type of corrosion-wear-resistant material developed from ordinary high chromium cast iron by increasing the chromium and carbon content and is often used in abrasive environments where wear and corrosion interact. The corrosion wear resistance of the HHCCI is related to the number, size, shape and distribution of carbides and the microstructure of the matrix. This paper reviews the research progress in improving the corrosion wear resistance of HHCCI from various aspects such as primary carbide refinement, heat treatment, deep cooling treatment and alloying, etc. Among the methods of refining primary carbides are modification, semi-solid treatment and current pulse treatment. In addition, we also analyze the potential of Cr, V, Nb, Mo, Mn, W, Ni, Cu, Si, N and other alloying elements to improve the corrosion wear resistance of HHCCI. The mechanism for improving the corrosion wear resistance of HHCCI is also explored in depth and research contents worthy of attention are proposed to further improve the corrosion wear resistance of HHCCI. In the future, the author believes that modification + alloying + heat treatment is the most potential application method to improve the corrosion wear resistance of HHCCI. The corrosion wear resistance of HHCCI can be further improved by refining the primary carbide (such as adding rare earth, Ti and other modified elements) + heat treatment (with cryogenic treatment) to improve the strength + alloying (such as adding low-cost, high-potential alloy elements such as N and Si) to improve the corrosion wear resistance of the matrix.

Keywords: hypereutectic high chromium cast iron; corrosion wear resistance; carbide; alloying; heat treatment

Citation: Gong, L.; Fu, H.; Zhi, X. Corrosion Wear of Hypereutectic High Chromium Cast Iron: A Review. *Metals* **2023**, *13*, 308. https://doi.org/10.3390/met13020308

Academic Editors: Annalisa Fortini and Chiara Soffritti

Received: 27 December 2022
Revised: 24 January 2023
Accepted: 31 January 2023
Published: 2 February 2023

1. Introduction

High chromium cast iron is the third generation of corrosion-wear-resistant materials developed after ordinary white cast iron and nickel-hard cast iron [1]. Due to its own microstructural characteristics, high chromium cast iron has higher toughness, high temperature strength, heat resistance and wear resistance than ordinary cast iron. Ordinary high chromium cast iron has excellent wear resistance under dry wear conditions. As the service environment of the workpiece becomes more complex, it is often subjected to wear accompanied by the presence of corrosion, which accelerates the failure and degradation of high chromium cast iron.

According to the microstructure characterization of high chromium cast iron, it is mainly divided into hypoeutectic high chromium cast iron, eutectic high chromium cast iron and hypereutectic high chromium cast iron. The structure of hypoeutectic high chromium cast iron is mainly composed of primary austenite (γ) and eutectic structure ($\gamma + M_7C_3$), and the matrix can be transformed into martensite or bainite during subsequent cooling or heat treatment. The amount of carbides in hypoeutectic high chromium cast iron is small and the corrosion wear resistance is poor [2]. The hypereutectic high chromium cast iron (HHCCI) is mainly composed of primary M_7C_3 carbide and eutectic structure ($\gamma + M_7C_3$) [3]. Its higher chromium content not only promotes the generation of passivation films on the

surface of the material to improve corrosion resistance, but also promotes the formation of hard phase incipient hexagonal carbides [4], making the corrosion wear resistance of HHCCI much higher than that of hypoeutectic high chromium cast iron, with very excellent corrosion wear resistance potential. In order to improve the performance of HHCCI in the working environment and minimize maintenance costs, it is urgent to develop HHCCI with better corrosion wear resistance and longer service life. Up to now, many scientists have conducted in-depth research on improving the corrosion wear resistance of HHCCI, but there are no review papers on improving the corrosion wear resistance of HHCCI. In order to expand the application of HHCCI, it is hoped that this review paper will provide valuable research directions and contents for researchers to study the corrosion wear resistance of HHCCI. This paper reviews the research progress in improving the corrosion wear resistance of HHCCI from various aspects such as primary carbide refining, heat treatment, cryogenic treatment and alloying, and also proposes several studies that are worthy of attention to enhance the corrosion wear resistance of HHCCI.

2. Effect of Carbide on Corrosion Wear Resistance of HHCCI

2.1. Effect of Carbide Content on Corrosion Wear Resistance of HHCCI

Many studies have shown that the carbide content significantly affects the wear and corrosion resistance of HHCCI [5]. HHCCI with higher carbon content will increase the amount of primary carbides and reduce the amount of eutectic structure when solidifying. Chung et al. [5] prepared high carbon (6 wt.%) HHCCI and compared the corrosion wear resistance of hypoeutectic high-chromium cast iron and hypereutectic high-chromium cast iron. The research results show that for hypoeutectic high chromium cast iron, when the slurry flow rate increases from 2.5 m/s to 5 m/s, the corrosion wear rate gradually increases. For HHCCI, the wear rate decreases and then increases as the slurry flow rate rises, and the corrosion and wear resistance is better than that of hypoeutectic high chromium cast iron. This is because the higher carbide content gives HHCCI a higher hardness and better corrosion wear resistance. In the analysis of the HHCCI wear and corrosion mechanism, it was found that corrosion plays a major role in erosion at low rates of erosion, while wear occupies the major part of erosion at high rates of erosion. Chang et al. [6] investigated the effect of carbon content on the corrosion wear resistance of HHCCI from another aspect and found that as the carbon content of HHCCI increased from 3.5 wt.% to 4.85 wt.%, the corrosion resistance increased by almost 20 times. Because the increase in carbon content causes the primary carbide content to rise from 33.81 vol.% to 86.14 vol.%, the overall corrosion potential rises, reducing the selective corrosion of the austenite matrix in the corrosion solution and improving its corrosion resistance.

In order to gain a more comprehensive understanding of the effect of carbide content and type on the corrosion resistance of HHCCI, Tang et al. [7] studied the corrosion wear resistance of 45 wt.% Cr cast iron with the change of carbon content, and the microstructure was observed using SEM, as shown in Figure 1. When the carbon content is less than 2 wt.%, the carbide is mainly in the hypoeutectic state. When the carbon content is greater than 3 wt.%, the coarse primary carbides and fine eutectic carbides precipitate from the structure at the same time, and with the increase of carbon content, the size of coarse carbides will further coarsen. In the corrosion wear experiment, the volume loss of 45 wt.%Cr–1 wt.%C high chromium cast iron is 3–4 times that of 45 wt.%Cr–4 wt.%C high chromium cast iron. This shows that the corrosion wear resistance of 45Cr series high chromium cast iron increases with an appropriate increase of carbon content, which improves the resistance of the material to the synergistic effect of corrosion wear. When the carbon content is 4 wt.%, its eutectic carbide accounts for 37% of the total carbide, has the highest content of eutectic carbide in the test, and shows the most excellent corrosion wear resistance. The study found that its carbide is composed of M_7C_3 and $M_{23}C_6$. A core–shell structure with an outer shell of $M_{23}C_6$ and an inner core of M_7C_3 appears in the primary carbide. The appearance of this structure may be beneficial to the improvement of the material's corrosion wear resistance, but no relevant explanation is given in the literature test this hypothesis. As the

carbon content further increases (5–6 wt.%), the carbides are mainly M_7C_3 with a hexagonal close-packed structure. The volume fraction of carbides is too high, and there is not enough tough matrix support around them, which leads to the reduction of its corrosion wear resistance. Therefore, with an appropriate increase of carbide content, the corrosion wear resistance of HHCCI can be improved, but high carbon content will affect the corrosion wear resistance of HHCCI.

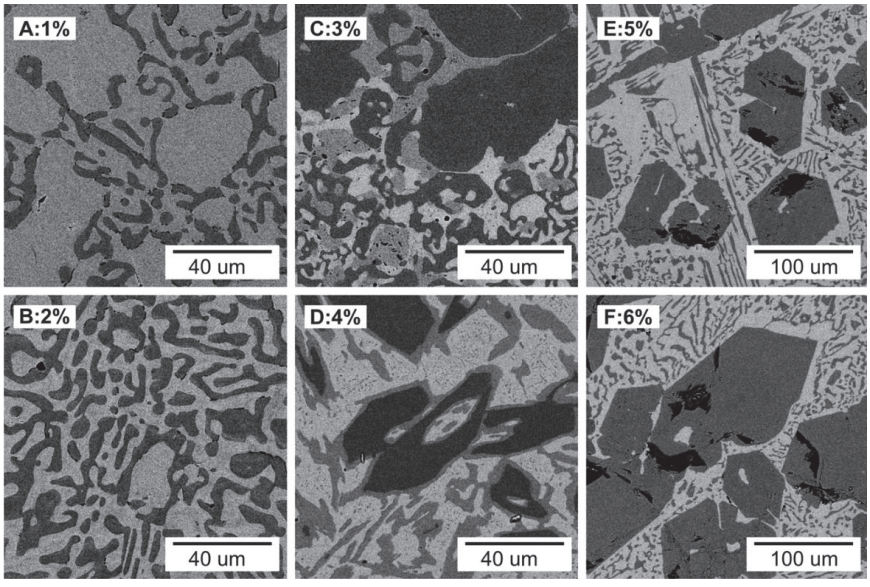

Figure 1. Back-scattered electron images of 45-series of HHCCIs (**A**–**F**: with varied nominal carbon of 1, 2, 3, 4, 5 and 6 wt.%, respectively) [7].

2.2. The Effect of Carbide Orientation on Corrosion Wear Resistance of HHCCI

In addition to the content of carbide, the orientation of carbides also affects the corrosion wear resistance of HHCCI. After directional solidification of HHCCI, the carbides in its structure are long rods parallel to each other and perpendicular to the chilled surface [8,9]. It has been shown [10,11] that when the carbides in HHCCI are oriented and arranged perpendicular to the wear surface, its corrosion wear resistance is significantly improved. J.J. Coronado's research results [12] also show that primary carbide has different wear resistance on different crystal planes, and the primary carbides in the transversal direction show higher wear resistance than longitudinal carbides.

In order to further study the effect of carbide orientation on the corrosion wear resistance of HHCCI, Ye et al. [13] carried out research on the effect of carbide orientation on the structure and corrosion wear resistance of HHCCI. In the corrosion wear test under strong alkali environment, the carbide in the directionally solidified structure exists in a directional arrangement. When the wear surface is perpendicular to the carbide and the average distance between the carbides is 16 to 17 μm, the weight loss rate of 182 $g/(h{\cdot}m^2)$ is less than 232 $g/(h{\cdot}m^2)$ of the ordinary sand casting sample. The corrosion wear resistance is better than that of the ordinary casting sample with intermittent carbide distribution. According to the observation of the structure, the oriented carbides are more fully wrapped by the matrix, which increases the fracture resistance and anti-falling properties of carbides in the corrosion wear test. The stability of carbides can be increased even after the phase boundary corrosion of the matrix occurs in the corrosion wear test. Among them, the hardness of carbides is also an important factor affecting the corrosion wear resistance of HHCCI. Comparing different sections of oriented carbides, it can be seen that the aver-

age micro-hardness (1828 HV) of the of carbides cross section is higher than the average micro-hardness (1415 HV) of the longitudinal section, which makes them show excellent wear resistance.

2.3. Effect of Carbide Refinement on Corrosion Wear Resistance of HHCCI

Many studies have shown that carbide refinement is one of the most effective means to improve the corrosion wear resistance of HHCCI [14]. The methods of refining primary carbides contain modification, semi-solid treatment and current pulse treatment.

2.3.1. Effect of Modification on Carbide Refinement and Corrosion Wear Resistance

The refinement of primary carbides is mainly related to the nucleation rate and growth rate. By providing a larger degree of undercooling to provide the corresponding solidification driving force, the nucleation of carbides can be promoted. As the degree of undercooling increases, higher cooling rate will increase the nucleation rate of primary carbides, resulting in a finer carbide [15–17]. It is a more feasible method to refine carbides by adding modifier to form heterogeneous nucleation sites and providing greater undercooling for nucleation particles. Yilmaz et al. [18] used TiBAl as a modifier to add HHCCI, and found that the primary carbides were significantly refined, where the size of secondary carbide formed in the matrix was less than 1 μm. The results indicated that the impact toughness (13.5 J/cm^2) of HHCCI added with 2.0 wt.% TiBAl was significantly higher than that of conventional HHCCI (11.9 J/cm^2). The higher hardness and excellent toughness improved the corrosion wear resistance potential of HHCCI. On this basis, Zhi et al. [19] calculated from the thermodynamic and kinetic formula combined with the Fe-C-Cr ternary phase diagram. They found that the solubility of Ti in the cast iron solution was 0.03% before the precipitation temperature point 1610 K of primary carbide. This indicates that when the Ti concentration is greater than 0.03%, TiC will be precipitated before the primary carbides are formed. The lattice mismatch between TiC (110) and M_7C_3 carbide (010) is 10%, which can be used as a heterogeneous nucleation site to refine the primary carbide, and the Ti element will also be enriched around the carbide.

By adding an appropriate amount of metamorphic elements such as TiBAl, Nb and Ti to HHCCI to form heterogeneous nucleation sites of carbides to refine carbides, it can be studied the adsorption of metamorphic elements on the carbide preferential growth surface, and adding appropriate Cr/C ratio adjustment is an important direction for future research on the refinement of HHCCI carbides and the improvement of corrosion wear resistance. The existing problem is that a large number of nucleating agents in the modificator are not formed in situ, and the external addition of the modificator is still a challenge to be solved. It is a more effective solution to mix the nano-scale modifier powder with the micron-scale alloy powder by mechanical ball milling. Under the high-speed operation of the ball mill, the modifier will be evenly distributed in the alloy, thereby improving the nucleation and refinement efficiency of the modifier [20].

The authors believe that in addition to using modification alone, suspension casting can also be used to refine the microstructure of HHCCI. Suspension casting refers to the addition of certain powder or liquid metal during the casting process, so that the temperature and composition of the metal solution fluctuate near the solidification front. With the increase of suspending agent, the nucleation rate of the alloy increases, which will hinder the growth of primary carbides, reduce the size of primary carbides in HHCCI and promote their uniform distribution. Therefore, the authors believe that using modification or suspension casting can effectively improve the cooling rate of HHCCI. This can predict the refinement structure and investigate the refinement mechanism by combining the lattice matching principle with first principle simulation calculation to give HHCCI excellent corrosion resistance potential.

2.3.2. Effect of Semi-Solid Treatment on Carbide Refinement and Corrosion Wear Resistance of HHCCI

In addition to using modification to refine carbides, semi-solid methods can also be used to refine carbides in HHCCI. Semi-solid treatment refers to the application of external force to stir the alloy during the solidification process, so that the solid–liquid mixed slurry with a certain solid phase component is uniformly suspended in the liquid alloy. The processing method of this solid–liquid mixed alloy slurry is called semi-solid treatment. For alloys with high melting point, methods such as inclined tilted plate cooling, semi-solid remelting, spray molding, ultrasonic treatment, electromagnetic stirring and other methods are often used to refine the grains. At present, the inclined plate cooling method is often used to refine the carbides of HHCCI. By increasing the radius and inclination angle of the groove, a larger area of semi-solid HHCCI will be chilled during the flow process, increasing the supercooling degree of HHCCI. Then, it increases the carbide nucleation rate and refines the primary carbides. Li Runjuan [21] prepared HHCCI by using the inclined plate cooling method of semi-solid slurry treatment. The results show that the size of primary carbide of HHCCI after semi-solid treatment is 109 μm dropped to 20 μm. When the semi-solid slurry of HHCCI flows through the sample plate, its primary carbide will continue to nucleate under the chilling effect of the cooling plate. With the flow of the solid slurry, the primary carbide will be broken and refined during the friction, collision, and shear process with the cooling plate. Which reduce the size of the primary carbide of HHCCI, thus increasing the corrosion wear potential of the HHCCI.

Compared with ordinary forming methods, the advantages of semi-solid forming are: the viscosity of semi-solid alloys is higher than that of liquid metals, the flow stress is lower than that of solid metals, and complex parts can be formed more quickly. It can also reduce the gas inclusion in the mold to reduce oxidation. Semi-solid forming has a wide range of applications and is a process that can be automated. However, semi-solid processing also has certain disadvantages and its production process and flow are complex, which increases the cost of raw material processing to a certain extent.

2.3.3. Effect of Pulse Current Treatment on Carbide Refinement and Corrosion Wear Resistance of HHCCI

Pulse current treatment is an excellent method to refine carbides in HHCCI, which has the advantages of environmental protection and low cost. There are several hypotheses about the mechanism of pulse current on the melt in the solidification process: 1. Joule heating effect: the conductivity of the solid alloy at the front of the solid–liquid interface is higher than that of the molten alloy. A certain amount of Joule heat will be generated inside the alloy to reduce the undercooling between the solid and liquid phases. It promotes the uniform solidification of the molten alloy liquid, and makes the distribution of crystalline structure more uniform. Thus, it can promote the refinement of carbide in HHCCI. 2. The electric field force caused by the pulse current will drive the directional migration of metal ions in the melt, so that the distribution of molten metal ions with different charges at the solid–liquid interface will change, thereby changing the structure of the solidified metal and achieving the purpose of refining the carbides in the HHCCI. Geng et al. [22] thinks that the growth of carbide in HHCCI is related to the content of Cr. Figure 2 is a schematic diagram of the growth of primary carbides during solidification. Under the action of pulse current, Fe ions and Cr ions with different energies will diffuse to different degrees. Along with the continuous diffusion of the Cr content of the carbide, it reduces the growth probability of the carbide and refines the size of the carbide.

Another hypothesis is that under the action of the external pulse current, a magnetic field with a corresponding frequency change will appear in the molten alloy, and a varying instantaneous pressure will be generated inside it. The dendrites growing at the solid–liquid front will break and fragment under the impact of the varying pressure, causing the carbide in HHCCI tend to spheroidize and grow in grains. Some studies [23] explained the refinement effect of pulsed current on the alloy in terms of the liquid structure theory of

the alloy melt. Which suggested that under the effect of pulse current, the aggregation of atomic groups in molten alloy liquid will be greater than the probability of dispersion. The atomic groups will become potential nucleation sites in further cooling, which will increase the occurrence probability of equiaxed crystals, thus producing refining effect.

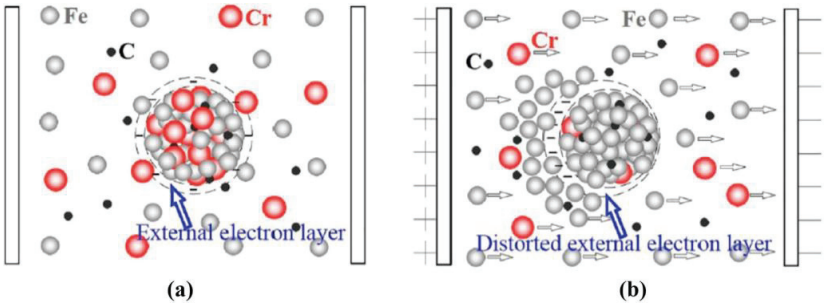

Figure 2. Schematic diagram of the growth of carbides during solidification. (**a**) Without ECP; (**b**) with ECP [22].

Bai Dan [24] applied a pulse current during the solidification process of HHCCI, which reduced the defects such as cracks and holes on the primary carbide. This is because the electromigration of the pulse current to the molten metal improves the diffusion ability of C atoms. It promotes the diffusion of C atoms into the tetrahedral gap of the hexagonal lattice of primary carbides, which increased the solid solution strength and density of carbides, thus reducing the cracks, holes and other defects of primary carbides. Under the magnetic contraction of the pulse current, the pressure of the molten metal is increased to achieve electric subcooling, which increases the nucleation rate of the primary carbide in the molten metal, so that the average equivalent diameter of the primary carbide is reduced from 150 μm down to 65 μm. The microhardness increased from 1398–1420 (HV) to 1485–1501 (HV), which improved the comprehensive mechanical properties of HHCCI.

In addition to the pulse current treatment can be used in the solidification process of HHCCI, the research shows that [25] auxiliary pulse current is added during the heat treatment of HHCCI, which can reduce the temperature at which HHCCI undergoes solid-state phase transition and increase the degree of phase transition. On this basis, Kang Mingyuan [26] studied the effect of pulse current on the corrosion resistance of HHCCI, and compared the electrochemical performance of HHCCI with or without pulse current treatment. The corrosion potential increased from (−511 mV) to (−475 mV), and the corrosion current density decreased from (7.38×10^{-7} A/cm^2) to (5.10×10^{-7} A/cm^2), thus improving the corrosion wear resistance potential of HHCCI.

At present, a lot of research work has been done to improve the corrosion wear resistance of HHCCI from the aspect of primary carbides, but only limited success has been achieved. Because the coarse carbides will cause brittle fracture during the wear process, it will aggravate the wear of the workpiece. while more carbon content will also make the carbides not have enough ductile matrix support, resulting in reduces corrosion wear resistance. Therefore, the authors of this paper believe that under the premise of controlling the appropriate chromium and carbon content, it is more feasible to generate carbides with an appropriate volume fraction, make them oriented and combine metamorphic treatment, semi-solid treatment and pulse current treatment to refine primary carbides. The research method can effectively enhance the strength and toughness of carbides in HHCCI and improve the corrosion wear resistance of HHCCI. For the application conditions of HHCCI, the carbide and the matrix need to have sufficient interfacial bonding strength to ensure that the carbide has sufficient wear time during the corrosion wear process. The interfacial bonding strength generally depends on the atomic bonding strength between the matrix and the carbide and the microstructure at the interface, and the interfacial force at the

atomic level is difficult to explain. In order to further study the corrosion wear resistance of HHCCI, the first-principle calculation method combined with high-resolution transmission analysis is an important direction to guide and improve the performance of HHCCI in the future.

3. Effect of Heat Treatment Corrosion Wear Resistance of HHCCI

The matrix is one of the main factors affecting the hardness and corrosion wear resistance of HHCCI. Studies found that [27] found that compared with carbides, the softer matrix is worn away in the process of corrosion and wear, so that the exposed isolated carbides are more likely to peel off with break. In view of the brittleness of HHCCI, high temperature austenitizing plus air cooling is a method to improve the corrosion wear resistance of HHCCI. Heat treatment promotes the transformation of the matrix from a large amount of austenite to martensite, which improves the ability of the matrix to support carbides and at the same time promotes the precipitation of secondary carbides. Adjusting the heat treatment method can make it uniformly distributed in the matrix, optimize the microstructure of HHCCI and enhance the corrosion wear resistance [28–30]. The matrix solid-state transformation temperature of HHCCI will change significantly with the degree of saturation of solute atoms (such as Cr, W) in austenite, and the precipitation of supersaturated elements in austenite will increase the martensite transformation temperature [31].

During heat treatment of HHCCI, Cr and C in the matrix will precipitate secondary carbides. When the cooling process after heat treatment, most of the austenite matrix transforms into martensite and retained austenite, and continues to precipitate secondary carbides [32,33]. In order to promote the transformation of more austenite into martensite during heat treatment and improve the corrosion wear resistance potential of HHCCI, the cooling rate of HHCCI casting should be greater than the critical cooling rate of pearlite transformation and bainite transformation. In the austenite structure of HHCCI, as the carbon content increases, its diffusion coefficient increases, thereby shortening the incubation period of pearlite, and the critical cooling rate also increases [30]. Researchers found that the quenching temperature significantly affects the microstructure evolution of HHCCI. Zhi et al. [30] studied the effect of different heat treatment temperatures on the properties of HHCCI. The results showed that as the heat treatment temperature increased from 850 °C to 1050 °C, the secondary carbides precipitated in the matrix changed from M_3C carbides to M_7C_3 carbides with higher hardness. The hardness first increased and then decreased, and reached the highest at 1000 °C. The maximum macro-hardness was 64.6HRC. The maximum micro-hardness of the matrix is 850 HV, the toughness can reach 6.1–6.9 J/cm^2, and 1000 °C is set as the optimum heat treatment temperature of HHCCI. In order to improve the corrosion wear resistance potential of HHCCI, since the optimal heat treatment temperature of HHCCI depends on the specific composition, after a large number of literature research and investigation, the approximate quenching temperature range is about 1000 °C, and the best holding time is 1–3 h. Transforming the HHCCI matrix into martensite through heat treatment and the precipitation of uniform secondary carbides is one of the effective means to improve the corrosion wear resistance of HHCCI. However, the influence of tempering temperature, times and holding time on the corrosion wear resistance of HHCCI and the related problems of mechanism need to be further studied and discussed.

It is not only quenching that affects the corrosion wear resistance of HHCCI, but also tempering can affect the corrosion wear resistance of HHCCI. Riki Hendra Purba et al. [34] compared the corrosion wear resistance of multi-element alloyed HHCCI in the as-cast state, quenched state and quenched + tempered state. The results showed that the corrosion wear rate of quenched state 18Cr-HHCCI was the smallest $(0.55 \pm 0.004) \times 10^{-3}$ cm^3/kg, showing the most excellent corrosion wear resistance. The SEM of the cross-section of the sample after corrosion wear is shown in Figure 3. Unlike the cast-state sample, which appears on the surface of the statue deformation area and more cracks. The quenched-state

sample has almost no deformation on the surface, only a small number of micro-cracks. The tempered treatment promotes the precipitation of carbides, thereby reducing the hardness of the matrix. The relatively soft matrix is easier to be removed during the corrosion wear process, so the selection of an appropriate tempering temperature should also be further considered. On this basis, A. T et al. [35] showed that when the tempering temperature of HHCCI is 473 to 503 K (200–230 °C), the toughness and wear resistance of HHCCI increase, and further increase of the tempering temperature will reduce the toughness.

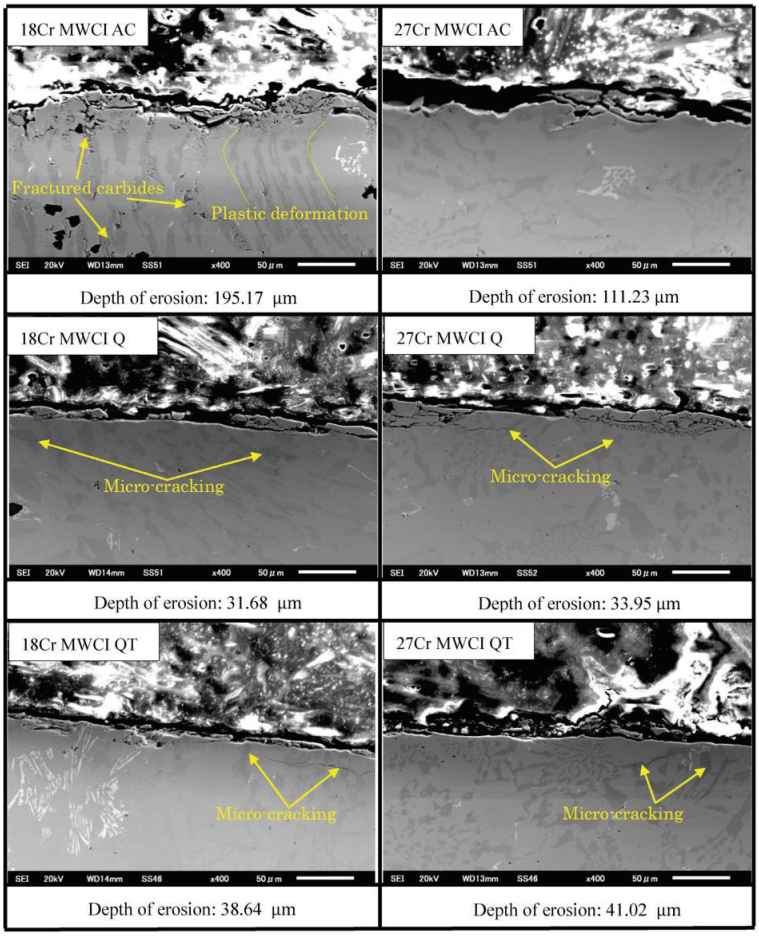

Figure 3. Cross-sectional observation of samples [34].

Therefore, the authors believe that, for HHCCI, it is necessary to promote the transformation of the matrix structure and the precipitation of secondary carbides through quenching treatment. This should be coupled with appropriate tempering temperature and holding time, because appropriate tempering temperature and holding time can increase the toughness of HHCCI and improve the corrosion wear resistance potential of HHCCI, while too high tempering temperature may reduce the toughness, which is not conducive to the optimization of the corrosion wear resistance of HHCCI.

4. Effect of Cryogenic Treatment on Corrosion Wear Resistance of HHCCI

In addition to using traditional heat treatment to improve the corrosion wear resistance of HHCCI, the authors believe that adding DCT after heat treatment can significantly improve the corrosion wear resistance of HHCCI. DCT refers to cooling the heat-treated sample to about −196 °C for several hours, and then slowly returning the sample temperature to room temperature. Slowly returning to room temperature can reduce the temperature gradient inside the sample, minimizing the residual stress. It also promotes the transformation of austenite into martensite, and promotes the precipitation and uniform distribution of fine secondary carbides, thereby increasing the corrosion wear resistance potential of HHCCI. Cryogenic treatment is a supplementary process to conventional heat treatment. It has long been used to improve the hardness, toughness, wear resistance, corrosion resistance and corrosion wear resistance of materials and reduce the residual stress of workpieces [36–38]. Studies have shown [39] that performing DCT before tempering at 230 °C can reduce the size of martensitic laths in the workpiece and promote the precipitation of secondary carbides, which can significantly improve the corrosion wear resistance potential of the material.

Liu et al. [40] found that DCT promoted the refinement and homogenization of the cast iron matrix, effectively reduced the content of retained austenite after destabilization treatment, promoted its transformation into martensite. The authors believe that DCT of HHCCI will significantly reduce retained austenite, but DCT cannot completely transform austenite into martensite. Studies have shown [41] that when the content of retained austenite in the cast iron matrix is about 20%, the wear resistance is the most excellent. Because the retained austenite in the matrix can passivate the crack tip and inhibit the crack propagation, the austenite content in the HHCCI should not be too low. In addition, the holding time of DCT will also affect the performance of the workpiece. Studies have shown [42] that the alloy has the best hardness, compressive strength and wear resistance after being held for 6 h by DCT, because there are more lamellar martensite and fine carbide in the alloy. With the extension of the DCT holding time to 12 h, the M_3C carbide gradually dissolves and the hardness and compressive strength decrease. The above research results show that DCT with an appropriate holding time can transform more retained austenite into martensite, promote the uniform precipitation of secondary carbides. Then, it will improve the hardness and corrosion wear resistance of HHCCI. In the future, the corrosion wear resistance potential of HHCCI can be considered from the aspect of secondary carbides, because the secondary carbides generated in HHCCI usually precipitate from the matrix in the form of coherent, semi coherent, twin, etc., playing a role in precipitation strengthening. There are two orientation relationships between $M_{23}C_6$ carbides and the matrix: cubic–cubic and non-cubic–cubic [43]. Although the toughness of $M_{23}C_6$ is 25% higher than that of M_7C_3, the formation of excessive secondary carbides, such as intergranular $M_{23}C_6$ carbides, will increase the brittleness of HHCCI. The authors believe that adopting heat treatment to allow an appropriate amount of secondary carbide precipitation can promote the transformation of the matrix and the homogenization of carbides, and improve the corrosion wear resistance potential of HHCCI. There is a hypothesis about the possible mechanism of cryogenic treatment on the corrosion wear resistance of HHCCI: researchers [44] believe that cryogenic treatment improves the wear resistance by affecting the quenched martensite structure and promoting the precipitation of fine carbides in martensite. It was pointed out that during the cooling process of cryogenic treatment, the carbon atoms in the martensitic lattice will interact with the dislocations and gather to form Coriolis air masses of carbon atoms. During the heating process, when the temperature is higher than 200 K, carbon atoms diffuse along locally connected linear air masses, gather at lattice defects and precipitate carbides. There are also studies [45] that show that cryogenic treatment can not only promote the formation and homogenization of carbides, but also increase the content of martensite and improve the corrosion wear resistance of HHCCI. He et al. [45] compared the structure morphology of HHCCI deep corrosion with and without cryogenic treatment, and the results are shown in Figure 4. The existence of secondary carbides

can be seen in the SEM of the structure without cryogenic treatment, while the secondary carbide can hardly be seen in the SEM of the structure after cryogenic treatment. This is because, in the electrolyte, secondary carbides and martensite form the primary battery to undergo electrochemical corrosion, and the low-potential martensite will be corroded as the anode, thus causing HHCCI without cryogenic treatment to be able to observe secondary carbides in the SEM diagram after deep corrosion. The cryogenic treatment martensite will precipitate fine carbides to reduce the corrosion potential difference between secondary carbides, resulting in uniform corrosion of secondary carbides and martensite, thereby the outline of secondary carbides cannot be seen, which also verifies that cryogenic treatment can improve the corrosion wear resistance of HHCCI. Therefore, the authors believe that, in addition to using normal heat treatment to optimize the performance of HHCCI, adding DCT after heat treatment is expected to further improve the corrosion wear resistance potential of HHCCI and increase the service life of HHCCI.

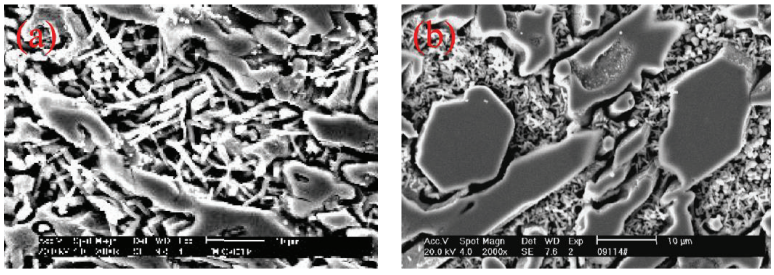

Figure 4. Scanning electron microscope images of samples: (**a**) Free cryogenic treatment SEM; (**b**) Cryogenic treatment SEM [45].

The method of quenching + air cooling or quenching + DCT can transform a large amount of austenite into martensite, and promote the precipitation of secondary carbides, thereby producing a dispersion strengthening effect on the matrix. The authors believe that the quenching temperature should be controlled at 1000–1050 °C. If the quenching temperature continues to rise to 1100 °C, secondary carbides will grow and partially re-dissolve, and the retained austenite content will be greatly increased. To avoid the use of high carbon (30–40 wt.%) and low chromium (1.5–2.4 wt.%) components to prepare HHCCI, the matrix is mainly ferrite and cannot be further heat treated. For workpieces used in corrosion-wear-resistant environments, the hardness is much lower than that of austenite and martensite matrix, and no work hardening will occur during the corrosion wear process. The current problem is that although the tempering treatment at 200–300 °C can increase the toughness of HHCCI, the impact of tempering temperature, times and holding time on the corrosion wear resistance of HHCCI and the mechanism need to be further studied and discussed. Therefore, transforming the HHCCI matrix into martensite by heat treatment + DCT and precipitation of uniform secondary carbides is one of the effective means to improve the corrosion wear resistance of HHCCI.

5. Effect of Alloying on Corrosion Wear Resistance of HHCCI

The carbide has a higher electrode potential than the HHCCI matrix. The corrosion potential difference between carbide and matrix will cause the corrosion of the matrix and lead to the failure of the workpiece. Reducing the potential difference between the matrix and carbide by adding alloy elements is one of the most effective methods to improve the corrosion resistance of HHCCI. The microstructure, mechanical properties, corrosion resistance and corrosion wear resistance of HHCCI can also be improved using alloying methods. Commonly used alloying elements are Cr, W, Mo, Mn, Nb, Cu, Si, Ni, etc. [46,47].

5.1. Effect of Strong Carbide Forming Elements on Corrosion Wear Resistance of HHCCI

Cr element exists in carbide and matrix at the same time. When HHCCI is eroded, Cr will form a passivation film of Cr_2O_3 on its surface, which can inhibit corrosion and reduce the synergistic effect of corrosion and wear. In a stable Fe-C system, an increase in the Cr content decreases the equilibrium temperature (Te) of the eutectic transformation. With the increase of Cr content, more Cr will be solid-dissolved into the matrix, which will increase the hardness of the matrix and increase the electrode potential of the matrix. The addition of Cr, a strong carbide-forming element, is also conducive to the formation of carbides and increases the corrosion wear resistance of HHCCI. The corrosion resistance of HHCCI is closely related to the Cr content. Studies have found [48] that if the Cr/C ratio is too high, the corrosion resistance of cast iron will be reduced. When the Cr/C ratio is around 9.65, the workpiece shows the most excellent corrosion wear resistance. A. Wiengmoon et al. [49] compared the corrosion behavior of HHCCI with chromium content of 20 wt.%, 27 wt.% and 36 wt.%. The electrochemical results are shown in Figure 5. As the Cr content increases from 20 wt% to 36 wt%, the corrosion potential of the as-cast alloy increased from −590 mV to −510 mV, and the results show that the corrosion resistance of HHCCI increases with the increase of Cr content.

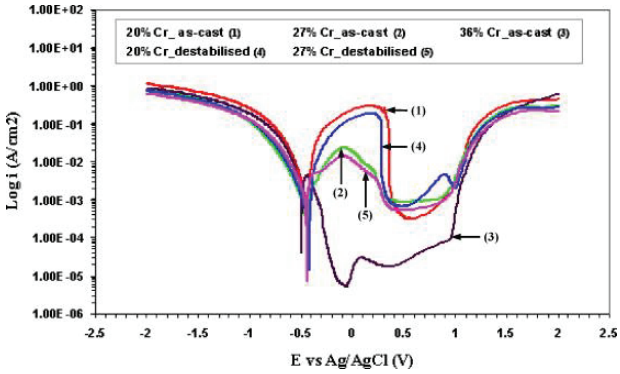

Figure 5. Anodic polarization characteristics in the as-cast and destabilized conditions of alloys 20Cr, 27Cr and 36Cr (as-cast only), in 0.5 mol. H_2SO_4 aqueous solution [49].

In order to study the influence of other strong carbide-forming elements on the microstructure and corrosion wear resistance of HHCCI, Ma et al. [50] found that as the vanadium content increased from 0 wt.% to 1.0 wt.%, the size of the carbide gradually becomes smaller and finer, from the initial block to short rod. The distribution becomes more uniform, and the corrosion wear resistance is also increasing. Because V is a strong carbide element, it is mainly distributed in carbides, and a small amount exists in the matrix. V can also refine the grains. When refining the austenite dendrites, it will make the space between the dendrites for the growth of eutectic carbides smaller, so that the carbides become finer, and the carbides formed by vanadium can also exist as heterogeneous nucleation sites to further refine the carbides. Yingchao Zhang et al. [51] studied the refinement of NbC on the M_7C_3 primary carbides of HHCCI, and the results showed that after adding 1.54 wt.%Nb element, the primary carbides in HHCCI were refined from 76μm to 40 μm. This is because the lattice mismatch of NbC (110) and M_7C_3 (001) is 5.39% and less than 6% (as shown in Table 1). Therefore, it can be used as the heterogeneous nucleation site to refine the M_7C_3 primary carbide, and its unit cell matching diagram is shown in Figure 6. Penagos et al. [52] studied the effect of Nb on the corrosion wear resistance of HCCI. The results showed that the addition of a very low content of Nb element can reduce the eutectic region between M_7C_3 carbides and promote its microstructure refinement, as the Nb content increased from 0 wt.% to 1 wt.%, the macro-hardness and micro-hardness increased by about 7%, and the corrosion wear resistance increased by 17%.

Table 1. Calculated lattice misfit values between NbC (110) and M_7C_3 (001) [51].

Matching Face	NbC(110)//M_7C_3 (001)		
[uvw]s	[100]	[110]	[111]
[uvw]n	[100]	[010]	[110]
θ	0	0	3.84
d[uvw]s	0.4469	0.6322	0.7742
d[uvw]n	0.4473	0.6982	0.8458
δ		5.39%	

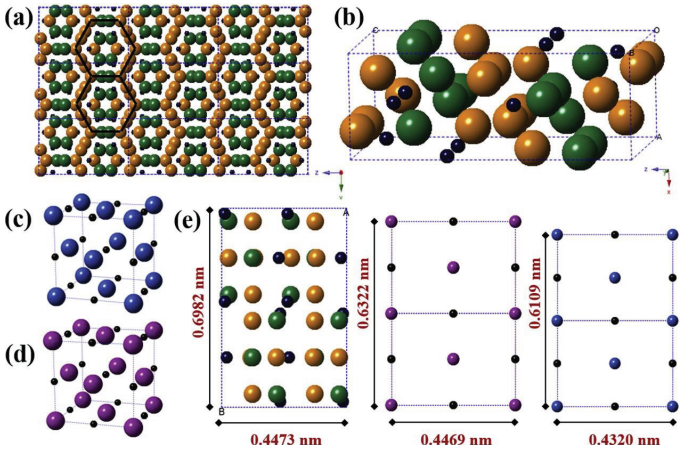

Figure 6. Schematic diagram of cells. (**a**) Polycellular M_7C_3 with Pnma structure; (**b**) monocellular M_7C_3; (**c**) monocellular TiC; (**d**) monocellular NbC; (**e**) (001) plane of M_7C_3, (110) plane of NbC and (110) plane of TiC [51].

For the alloying element Mo, the authors analyzed the effect of Mo on the corrosion wear resistance of HHCCI from the perspective of corrosion performance. Mo has been found to further enrich the passivated film in HHCCI with chromium [53] and inhibit the phenomenon of chromium deficiency in the transition zone. Mo also can improve the passivation potential of the passivation film, and strengthen the passivation film. In an acidic environment, the limited solubility of Mo and SO_4^{2-} in the solution to form $MoSO_4^{2-}$. It will be adsorbed in the weak area of the passivation film or participate in the formation of hydrated oxides to make the passivation film uniform and dense, thereby repairing the passivation film. Mo also improves the affinity of the passive film to oxygen, which will repel a part of Cl^- during the competitive adsorption process with Cl^-, protect the passivation film, and improve the pitting corrosion resistance of the material [54]. In addition to optimizing the corrosion wear resistance of HHCCI through the improvement of corrosion resistance, the influence of alloying elements on the microstructure evolution will also affect the corrosion wear resistance of HHCCI. Mo exists in the HHCCI matrix and carbide at the same time. Mo can improve the hardenability of HHCCI, and the Mo element dissolved into the matrix can increase the Ms point and promote the transformation of retained austenite into martensite. Therefore, the authors believe that Mo element is also an alloying element with excellent research prospects, which can be used to improve the corrosion wear resistance of HHCCI.

W is similar to Cr, Mo and V. It is also a strong carbide-forming element. During the solidification of the alloy, it will form M_6C, M_2C, and M_3C carbides that are uniformly dispersed in the matrix. Studies have shown that [31], as the W content increases, the carbide content in the alloy matrix will increase accordingly. During solidification, carbides will absorb a large amount of carbon in austenite during the formation process, so that

a narrow carbon-poor zone is formed between carbides and austenite. The absence of carbon increases the MS transformation temperature, making this zone transform into martensite in the subsequent cooling process, forming a carbide surrounded by martensite. Yezhe Lv et al. [55] studied the effect of W content on the structure and properties of HHCCI. The results showed that W was uniformly distributed in the matrix and carbides. With the increase of W content, the matrix hardness and the macro-hardness and wear resistance of HHCCI gradually increase. When the W content in HHCCI is 1.03 wt.%, HHCCI shows the most excellent toughness (8.23 $J \cdot cm^{-2}$), and its wear resistance is increased by 205% compared with the alloy without W %. Therefore, the authors believe that the corrosion wear resistance of HHCCI can be improved by adding a certain amount of W.

5.2. Effect of Non-Carbide Forming Elements on Corrosion Wear Resistance of HHCCI

Studies have shown [56] that adding non-carbide forming elements Cu, Si and Ni can increase the electrode potential of the matrix and significantly improve the corrosion wear resistance of HHCCI.

The corrosion wear resistance of the sample mainly depends on its mechanical properties. In order to further improve the corrosion wear resistance of HHCCI, T.Z. Li et al. [57] added trace Ni elements to HHCCI to increase the hardness of the sample and the volume of carbides. It is beneficial to improve the corrosion wear resistance of the sample, and the HHCCI with 0.09 wt.%Ni shows the most excellent corrosion wear performance. The calculation results show that the Ni atom reduces the interface energy between the carbide and the matrix interface, it reduces the activation energy of carbide nucleation, and increases the nucleation rate, thus forming fine primary carbides. Which is conducive to reducing stress concentration, reducing the probability of carbide fragmentation during the corrosion wear process, and improving the corrosion wear resistance of HHCCI.

Researchers also improved the overall mechanical properties of HHCCI carbides by adding Si elements to regulate the morphology of HHCCI carbides. G.L.F.Powell et al. [17] found that adding 7 wt.% Si could transform the microstructure of high-chromium cast iron from hypoeutectic to hypereutectic structure, the primary carbides grow preferentially along [0001]. It has been pointed out in the literature [58] that Si can be adsorbed on the preferential growth surface of carbides to refine carbides. The addition of an appropriate amount of Si can refine HHCCI carbides, improve their hardenability, and transform the matrix into martensite by increasing the Ms point. thereby obtaining HHCCI with fine carbides and martensite matrix. Moreover, the solid solution of Si element in the matrix can improve the electrode potential of the matrix, and Si element will also form a dense SiO_2 oxide film on the surface of the matrix under corrosion conditions to prevent further corrosion of the matrix and improve its corrosion wear resistance. However, the addition of excessive Si elements will cause the growth of eutectic carbides and transform the matrix into pearlite or ferrite, thereby reducing the corrosion wear resistance of HHCCI [59,60].

Cu can increase the thickness of the passivation film and repair the passivation film. Because Cu and Cr have a superposition effect, and Cu can promote the enrichment of chromium on the passivation film to passivate the cast iron again when it is corroded. Cu^{2+} has better anti-reduction, it can be enriched on the surface in the form of Cu^{2+}, thus reducing the active dissolution rate of HHCCI, and can effectively promote the formation of HHCCI passivation film. Thereby improving the corrosion wear resistance of HHCCI. To further verify the effect of copper on the corrosion wear resistance of HHCCI, Gong studied the effect of Cu on the structure and properties of HHCCI [61]. The results showed that Cu can promote the precipitation of secondary carbides in the matrix, and the wear resistance of copper-containing HHCCI is 2.6 times that of copper-free HHCCI. It can be seen from the observation of the TEM results (Figure 7) that the secondary carbides in the copper-containing HHCCI are precipitated from the matrix in a semi-coherent form, which plays a role in precipitation strengthening, thereby improving its corrosion resistance potential. On this basis, Liqiang G [62] further studied the effect of Cu on the corrosion resistance of HHCCI. Cu alloying reduced the corrosion current of HHCCI by 4 orders of

magnitude, reducing the corrosion current from 2.57×10^{-6} A/cm^2 to 7.43×10^{-10} A/cm^2. The corrosion resistance and hardness of HHCCI increase with the appropriate increase of Cu content, because Cu does not form carbides with C, and most of Cu will dissolve into the matrix to form solid solution strengthening and increase the corrosion potential. A small amount of Cu can also dissolve in Fe and enter the iron-carbon-chromium carbide, which helps to increase the hardness of the alloy appropriately. It further compared the corrosion resistance of HHCCI at pH = 1 and pH = 7, and the results showed that the corrosion current of copper-containing HHCCI (1.5 wt.%Cu) in pH = 1 acidic solution (8.50×10^{-11} A/cm^2) is less than the corrosion current (7.43×10^{-10} A/cm^2) in NaCl solution with pH = 7, which indicates that HHCCI is more suitable for application in acidic working conditions. It shows that copper-containing HHCCI has excellent corrosion resistance potential. The corrosion resistance and hardness of HHCCI increase with the appropriate increase of Cu content. Because Cu does not form carbide with C, most of the Cu will be dissolved into the matrix to strengthen the solid solution and increase the corrosion potential, and a small amount can also be dissolved in Fe to enter iron carbon chromium carbide, which is helpful to properly improve the hardness of the alloy. This shows that copper containing HHCCI has very excellent corrosion wear resistance potential. However, the specific strengthening mechanism of Cu alloying has not been explained too much. The authors believe that the hypothesis of solid solution strengthening and alloying to increase the potential of the substrate electrode is expected to be verified by first-principle calculations. In the future, it is a feasible research direction to improve the corrosion resistance of HHCCI from the aspects of solid solution strengthening and increasing the matrix potential through Cu alloying, because Cu is mainly distributed in the matrix and has the effect of expanding the γ-phase region. Appropriate Cu can refine the carbides of HHCCI, reduce the spacing, distribute intermittently and uniformly, and reduce the splitting phenomenon [50].

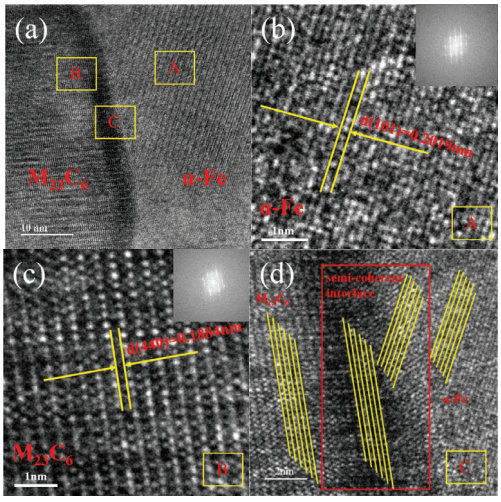

Figure 7. High-resolution TEM image and Fourier-filter images: (**a**) HR-TEM image of 1.5 wt.% Cu HHCCI after heat treatment at 1050 °C; (**b**) Fourier-filtered image of α-Fe in (**a**); (**c**) Fourier-filtered image of $M_{23}C_6$ precipitation in (**a**); (**d**) Fourier-filtered image of the boundary between α-Fe and $M_{23}C_6$ in (**a**) [61].

5.3. Other Alloy Element

N is also an alloying element that has the potential to improve the corrosion wear resistance of HHCCI. It can promote the refinement of HHCCI primary carbides, N element can also improve the hardenability of the matrix and the electrode potential. Jibo Wang et al. [63] studied the influence of different N contents on the impact wear properties of HHCCI abra-

sive grains. The results showed that as the N content increased from 0.09 wt.% to 0.19 wt.%, the primary carbides were obviously refined, the hardness increased from 18 GPa to 21 GPa. There were fewer cracks appeared during the HHCCI wear process, and the carbides changed from fracture to bending. The mismatch between (Ti, Nb) (C, N) nitrogen carbide (100) and M_7C_3 (010) was 6.15%, which indicates that (Ti, Nb) (C, N) nitrogen carbides can also serve as the heterogeneous nucleation site refinement carbides of M_7C_3. Its crystallographic relationship is shown in Figure 8. It also shows that N alloying can refine the carbides of HHCCI and improve the corrosion wear resistance of HHCCI.

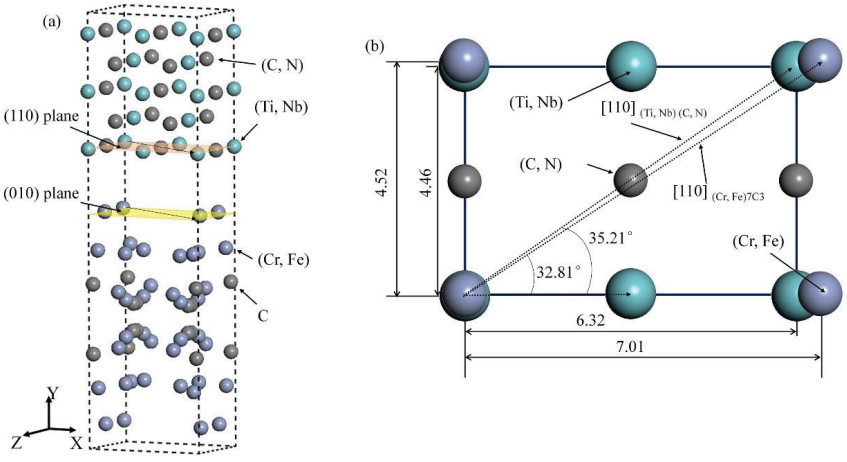

Figure 8. (**a**) Crystallographic relationship of (Ti, Nb)(C, N) and $(Cr, Fe)_7C_3$; (**b**) correspondence condition of the crystal plane (110)(Ti, Nb)(C, N) and (010)$(Cr, Fe)_7C_3$ [63].

Liujie Xu et al. [64] prepared HCCI-N with a nitrogen content of 0.38% in an environment with a nitrogen partial pressure of 0.4 Mpa. It can be seen from the TEM (Figure 9) that a sandwich structure of M_7C_3 carbide-ferrite interlayer-martensite matrix is formed at the carbide boundary. According to the Fourier (FT) change results, the inverse Fourier change (IFT) image Figure 10 is obtained, it is found that the atomic arrangement of M_7C_3 is regular. While the atomic arrangement of the interface region between M_7C_3 carbide and "α-Fe" is disordered, and there is no obvious crystal orientation relationship at the two-phase interface. The study found that the corrosion wear resistance of nitrogen-containing sample is 1.34 times that of ordinary sample, because nitrogen and chromium dissolved in the matrix improve its corrosion resistance and reduce the synergistic effect of corrosion and wear. According to literature research, nitrogen dissolved can consume H^+ in small pores or gaps on HHCCI after acid corrosion to form NH^+, which reduces the pH value in small pores and promotes passivation of small pores before expansion. Nitrogen is also enriched between the metal and the passivation film, improving corrosion resistance. Adding nitrogen to the substrate can increase the electrode potential of the substrate and enhance the self-healing ability of the passivation film, thereby improving the corrosion resistance [65]. Nitrogen can also refine the grain size of HHCCI [66], effectively increase the number of secondary carbides [67] and improve its corrosion wear resistance through solid solution strengthening [68]. Adding Ni, Mo, Cu, Si and N can increase the electrode potential of the substrate, reduce the electrode potential difference between the metal substrate and carbide, and improve the corrosion wear resistance of HHCCI. However, Ni, Mo and Cu are expensive alloying elements. Adding them to HHCCI will greatly increase the production cost of HHCCI. Si and N are both cheap elements, and they have a significant effect in increasing the electrode potential of HHCCI substrates. Therefore, it is a preferred choice to use Si and N to increase the electrode potential of the substrate in the future. However, the addition of a large amount of N will promote the appearance of

pores in HHCCI castings and reduce the comprehensive performance of HHCCI. N also has the effect of expanding the γ-phase region and improving the hardenability of HHCCI. Si is an element that shrinks the γ-phase region, adding a large amount will reduce the hardenability of HHCCI, promote the precipitation of pearlite and reduce the hardness and corrosion wear resistance of HHCCI. Therefore, the combined addition of Si and N is expected to overcome their respective defects and promote a substantial increase in the corrosion wear resistance of HHCCI.

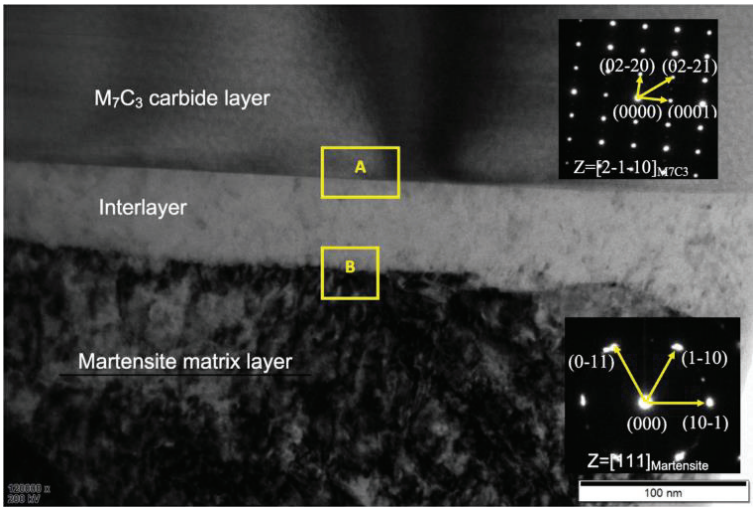

Figure 9. TEM image and selected area diffraction pattern (SADP) analysis at the boundary of eutectic carbide (A: the interface between M_7C_3 and interlayer; B: the interface between martensite and interlayer) [64].

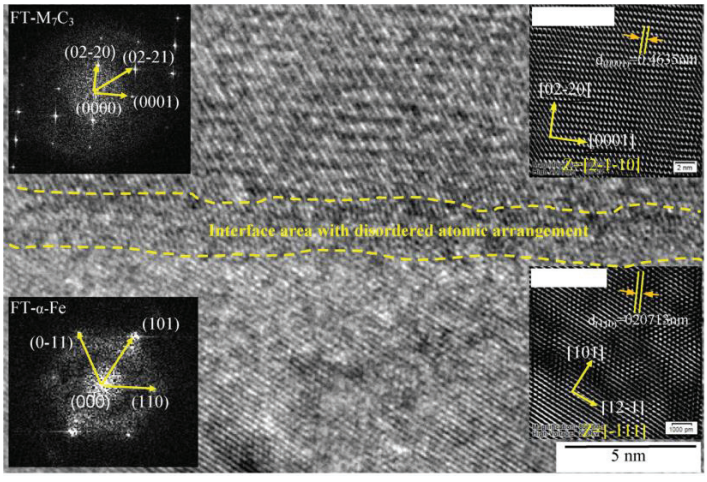

Figure 10. HRTEM image and analysis results of eutectic M_7C_3 carbide interface in area A of Figure 9 [64].

This section comprehensively analyzes the improvement potential of Cr, V, Nb, Mo, Mn, W, Ni, Cu, Si, N and other alloying elements on the corrosion wear resistance of HHCCI, and summarizes the related improvement mechanism. The authors believe that

the corrosion wear resistance of HHCCI can be effectively improved by alloying, and the alloying elements added to HHCCI mainly have three functions: solid solution strengthening (some alloying elements can increase the matrix potential), grain refinement, and improving the hardenability. The increase of Cr content can not only generate more carbides and improve wear resistance, but also allow more Cr elements to dissolve into the matrix, reduce the potential difference between the matrix and carbides, and improve the corrosion resistance of HHCCI. Comprehensive analysis shows that when the Cr/C ratio is kept around 9.65, the Cr content of HHCCI with the best corrosion wear resistance potential is 27–36 wt.%. V alloying can change the size of carbides from block to short rod, and the distribution is more uniform, which is beneficial to the improvement of corrosion wear resistance. The V content of HHCCI with the best corrosion wear resistance potential is 0.2–1.0 wt.%. The addition of Nb element can reduce the size of M_7C_3 carbides, promote the refinement of its microstructure, and improve the macro-hardness and micro-hardness and corrosion wear resistance of HHCCI. The Nb content of HHCCI with the best corrosion wear resistance potential is 1.0–1.54 wt.%. Mo alloying can generate carbides with high hardness and high melting point, which can improve the corrosion and wear resistance of HHCCI. The Mo content of HHCCI with the best corrosion wear resistance potential is 0.5–1.0 wt.%. For the Mn element, it can not only enter the carbide but also dissolve in the metal matrix. Mn is also a stable austenite element, which will strongly reduce the Ms point. The Mn content of HHCCI with the best corrosion wear resistance potential is 0.3–0.6 wt.%. In addition to the above alloying elements, elements such as Si, Cu and Ni can also be used to improve the corrosion wear resistance of HHCCI. The Si element is a non-carbide forming element, it has a strong solid solution strengthening effect, but too much Si will reduce the toughness. The Si content of HHCCI with the best corrosion wear resistance potential is 1.0–2.0 wt.%. Cu, Mo and Cr have a superposition effect, which can increase the thickness of the passivation film and repair the passivation film, and solid solution into the matrix can also increase the electrode potential. The Cu content of HHCCI with the best corrosion wear resistance potential is 0.5–1.0 wt.%. Trace Ni elements can increase the hardness of the sample and the volume fraction of carbides, which is beneficial to the improvement of the corrosion wear resistance of the sample. The Ni content of HHCCI with the best corrosion wear resistance potential is 0.05–0.1 wt.%. N alloying can significantly improve the corrosion wear resistance. The N content of HHCCI with the best corrosion wear resistance potential is 0.09–0.19 wt.%. Although the corrosion wear resistance of HHCCI can be effectively improved by alloying, the failure mechanism of HHCCI under the interaction of corrosion and wear is still unclear, and the influence of alloying elements on the corrosion and wear mechanism of HHCCI needs to be further studied. There is still great research potential to explore the mechanism of corrosion wear resistance performance by means of the first-principle calculation simulation combined with experimental demonstration.

6. Concluding Remarks

To further improve the corrosion wear resistance of HHCCI, the following aspects should be strengthened in the future:

(1) The hypereutectic structure is mainly composed of primary carbide M_7C_3 and eutectic structure ($\gamma + M_7C_3$), and its corrosion wear resistance is much higher than that of hypoeutectic high chromium cast iron. The primary carbide M_7C_3 in HHCCI is coarse and brittle, which is prone to cracking during wear. The corrosion wear resistance of HHCCI can be further improved by refining the primary carbide to improve the strength +heat treatment (with cryogenic treatment) + alloying to improve the corrosion resistance of the matrix.

(2) By adding an appropriate amount of modifying elements such as V, N, $LaAlO_3$, etc. to HHCCI, the heterogeneous nucleation sites of carbides are formed to refine carbides, and the adsorption of alloying elements on the carbide preferential growth surface is studied.

In the future, it is a direction to study the refinement of HHCCI carbides to improve the corrosion wear resistance.

(3) Under the premise of controlling the appropriate chromium and carbon content, it is more feasible to generate carbides with an appropriate volume fraction, make them oriented, and combine modification, semi-solid treatment, and pulse current treatment to refine primary carbides. The research method can effectively enhance the strength and toughness of carbides in HHCCI and improve the corrosion wear resistance of HHCCI.

(4) Transforming the HHCCI matrix into martensite through heat treatment + DCT and the precipitation of uniform secondary carbides is one of the effective means to improve the corrosion wear resistance of HHCCI. However, the influence of tempering temperature, times and holding time as well as the holding time and times of DCT on the corrosion wear resistance of HHCCI and the related problems of mechanism need to be further studied and discussed.

(5) In the future, the corrosion wear resistance potential of HHCCI can be considered from the aspect of secondary carbides, because the secondary carbides generated in HHCCI usually precipitate from the matrix in the form of coherent, semi coherent, twin, etc., playing a role in precipitation strengthening. There are two orientation relationships between $M_{23}C_6$ carbides and the matrix: cubic–cubic and non-cubic–cubic [43]. Although the toughness of $M_{23}C_6$ is 25% higher than that of M_7C_3, the formation of excessive secondary carbides, such as intergranular $M_{23}C_6$ carbides, will increase the brittleness of HHCCI. The authors believe that adopting heat treatment to allow an appropriate amount of secondary carbide precipitation can promote the transformation of the matrix and the homogenization of carbides, and improve the corrosion wear resistance potential of HHCCI.

(6) At present, there are few studies on the mechanism of alloying to improve the corrosion wear resistance of HHCCI, and there is still great research potential for the mechanism analysis of alloying to improve the corrosion resistance of HHCCI, such as copper, nitrogen, molybdenum, tungsten and other alloying elements on the corrosion wear resistance of HHCCI.

(7) Cu element can improve the corrosion resistance of HHCCI from the aspects of solid solution strengthening and increasing the matrix potential. Dissolving into the matrix plays the role of solid solution strengthening and increasing the corrosion potential, and a small amount can also solid dissolve in Fe and enter the iron-carbon-chromium carbide, which helps to improve the hardness of the alloy, but its specific strengthening mechanism is not too much to explain. The authors believe that the hypothesis that solid solution strengthening and alloying increase the potential of the substrate electrode is expected to be verified by the first-principle calculations.

(8) For the application conditions of HHCCI, the carbide and the matrix need to have sufficient interfacial bonding strength to ensure that the carbide has sufficient wear time during the corrosion wear process. The interfacial bonding strength generally depends on the atomic bonding strength between the matrix and the carbide and the microstructure at the interface, while the atomic level interface force is difficult to explain. Therefore, the first principle calculation combined with high-resolution transmission analysis is an important direction to guide the improvement of HHCCI performance in the future.

(9) The authors believe that the use of surface treatment on HHCCI in the future is also one of the important means to improve its corrosion wear resistance. The corrosion-wear-resistant material (such as SiC + C, etc.) is sprayed onto the surface of the workpiece by laser cladding or spraying in the atmosphere of high-pressure nitrogen auxiliary gas, and a dense layer and nitride with fine grains are formed on the surface, which can effectively improve the corrosion-wear-resistant performance of HHCCI [69].

(10) In addition to corrosion wear at room temperature, HHCCI treated with composites also has the potential to resist corrosion wear at high temperatures. For example, the authors believe that the cast-in insertion multi-component white cast iron prepared with HHCCI as the matrix material combined with cemented carbide WC-Co or TiC-Ni

is a new type of corrosion-wear-resistant material that can be used in high-temperature environments in the future [70].

Author Contributions: Conceptualization, writing-original draft, L.G.; analysis, writing—review and editing, H.F.; investigation, funding acquisition, X.Z. All authors have read and agreed to the published version of the manuscript.

Funding: This research was funded by National Natural Science Foundation of China (Grant number 52075010).

Data Availability Statement: All data is contained within the article.

Conflicts of Interest: The authors declare no conflict of interest.

References

1. Jain, A.-S.; Mustafa, M.I.; Sazili, M.I.I.M.; Chang, H.; Zhang, M.-X. Effects of destabilization and tempering on microstructure and mechanical properties of a hypereutectic high-chromium cast iron. *J. Mater. Sci.* **2022**, *57*, 15581–15597. [CrossRef]
2. Chen, C.; Feng, A.; Liu, B.; Wei, Y.; Song, X. Effect of quench-tempering and laser quenching on the microstructure and properties of high-chromium cast iron. *J. Mater. Res. Technol.* **2022**, *19*, 2759–2773. [CrossRef]
3. Li, P.; Yang, Y.; Shen, D.; Gong, M.; Tian, C.; Tong, W. Mechanical behavior and microstructure of hypereutectic high chromium cast iron: The combined effects of tungsten, manganese and molybdenum additions. *J. Mater. Res. Technol.* **2020**, *9*, 5735–5748. [CrossRef]
4. Sakamoto, O.M. Abrasion resistance of high Cr cast irons at an elevated temperature. *Wear* **2001**, *250*, 71–75.
5. Chung, R.J.; Tang, X.; Li, D.Y.; Hinckley, B.; Dolman, K. Abnormal erosion–slurry velocity relationship of high chromium cast iron with high carbon concentrations. *Wear* **2011**, *271*, 1454–1461. [CrossRef]
6. Chang, C.M.; Hsieh, C.C.; Lin, C.M.; Chen, J.H.; Fan, C.M.; Wu, W. Effect of carbon content on microstructure and corrosion behavior of hypereutectic Fe–Cr–C claddings. *Mater. Chem. Phys.* **2010**, *123*, 241–246. [CrossRef]
7. Tang, X.; Chung, R.; Pang, C.; Li, D.; Hinckley, B.; Dolman, K. Microstructure of high (45 wt.%) chromium cast irons and their resistances to wear and corrosion. *Wear* **2011**, *271*, 1426–1431. [CrossRef]
8. Wang, S.; Song, L.; Qiao, Y.; Wang, M. Effect of carbide orientation on impact-abrasive wear resistance of high-Cr iron used in shot blast machine. *Tribol. Lett.* **2013**, *50*, 439–448. [CrossRef]
9. Yang, D.S.; Lin, J.S.; Pen, D.J.; Hsu, F.M. The effect of directionally chilled microstructure on hypereutectic high-chromium white cast iron. *Adv. Mater. Res.* **2014**, *912–914*, 399–403. [CrossRef]
10. Ping, Z.; Zheng, B.; Tu, X.; Li, W. Application of directional solidification technology in high chromium cast iron. *Casting* **2021**, *70*, 899–905.
11. Coronado, J.J. Effect of (Fe, Cr) $_7C_3$ carbide orientation on abrasion wear resistance and fracture toughness. *Wear* **2011**, *270*, 287–293. [CrossRef]
12. Coronado, J. Effect of load and carbide orientation on abrasive wear resistance of white cast iron. *Wear* **2011**, *270*, 823–827. [CrossRef]
13. Ye, X.; Jiang, Y.; Li, Z.; Zhou, R.; Qi, T. Microstructure and corrosion wear properties of directionally solidified high chromium cast iron Cr28. *Cast. Technol.* **2006**, *27*, 935–938.
14. Jain, A.-S.; Chang, H.; Tang, X.; Hinckley, B.; Zhang, M.-X. Refinement of primary carbides in hypereutectic high-chromium cast irons: A review. *J. Mater. Sci.* **2021**, *56*, 999–1038. [CrossRef]
15. Yang, D.S.; Lei, T.S. Investigating the Influence of Mid-Chilling on Microstructural Development of High-Chromium Cast Iron. *Mater. Manuf. Process.* **2011**, *27*, 919–924. [CrossRef]
16. Liu, Q.; Zhang, H.; Wang, Q.; Zhou, X.; Joensson, P.G.; Nakajima, K. Effect of Cooling Rate and Ti Addition on the Microstructure and Mechanical Properties in As-cast Condition of Hypereutectic High Chromium Cast Irons. *ISIJ Int.* **2012**, *52*, 2210–2219. [CrossRef]
17. Powell, G.; Carlson, R.A.; Randle, V. The morphology and microtexture of M_7C_3 carbides in Fe-Cr-C and Fe-Cr-C-Si alloys of near eutectic composition. *J. Mater. Sci.* **1994**, *29*, 4889–4896. [CrossRef]
18. Yilmaz, S.O.; Teker, T. Effect of TiBAl inoculation and heat treatment on microstructure and mechanical properties of hypereutectic high chromium white cast iron. *J. Alloys Compd.* **2016**, *672*, 324–331. [CrossRef]
19. Zhi, X.; Xing, J.; Fu, H.; Gao, Y. Effect of titanium on the as-cast microstructure of hypereutectic high chromium cast iron. *Mater. Charact.* **2008**, *59*, 1221–1226. [CrossRef]
20. Ruan, M. Optimization of the Structure and Properties of Wear-Resistant Steel with Rare Earth Based Composite Modifier. Master's Thesis, Wuhan University of Science and Technology, Wuhan, China, 2018; pp. 67–68.
21. Li, R.; Jiang, Y.; Zhou, R. Preparation and Structure of Semi solid Slurry of Hypereutectic High Chromium Cast Iron. *Spec. Cast. Nonferrous Alloy.* **2005**, 270–272. [CrossRef]
22. Geng, B.; Zhou, R.; Li, L.; Lv, H.; Li, Y.; Bai, D.; Jiang, Y. Change in primary (Cr, Fe)$_7C_3$ carbides induced by electric current pulse modification of hypereutectic high chromium cast iron melt. *Materials* **2018**, *12*, 32. [CrossRef] [PubMed]

23. Qin, R. Study on Nonequilibrium Transition under the Action of Electric Pulse. Ph.D. Thesis, Institute of Metals, Chinese Academy of Sciences, Shenyang, China, 1996; pp. 1–10.
24. Bai, D.; Li, L.; Zhou, R.; Lv, H.; Jiang, Y.; Zhou, R. Effect of pulse current treatment on solidification structure of hypereutectic high chromium cast iron. *J. Mater. Heat Treat.* **2016**, *37*, 76–80.
25. Bai, D. Research on Microstructure Evolution of Hypereutectic High Chromium Cast Iron under Pulse Current. Master's Thesis, Kunming University of Science and Technology, Kunming, China, 2017; pp. 63–64.
26. Kang, M. Effect of Pulse Current Treatment on the Distribution of Structural Elements and Properties of Hypereutectic High Chromium Cast Iron. Master's Thesis, Kunming University of Science and Technology, Kunming, China, 2016; pp. 59–60.
27. Chatterjee, S.; Pal, T.K. Wear behaviour of hardfacing deposits on cast iron. *Wear* **2003**, *255*, 417–425. [CrossRef]
28. Da, L.; Liu, L.; Zhang, Y.; Ye, C.; Ren, X.; Yang, Y.; Yang, Q. Phase diagram calculation of high chromium cast irons and influence of its chemical composition. *Mater. Des.* **2009**, *30*, 340–345.
29. Chang, K.K.; Lee, S.; Jung, J.Y. Effects of heat treatment on wear resistance and fracture toughness of duo-cast materials composed of high-chromium white cast iron and low-chromium steel. *Metall. Mater. Trans. A* **2006**, *37*, 633–643.
30. Zhi, X.; Xing, J.; Gao, Y.; Fu, H.; Peng, J.; Bing, X. Effect of heat treatment on microstructure and mechanical properties of a Ti-bearing hypereutectic high chromium white cast iron. *Mater. Sci. Eng. A* **2008**, *487*, 171–179. [CrossRef]
31. Anijdan, S.M.; Bahrami, A.; Varahram, N.; Davami, P. Effects of tungsten on erosion–corrosion behavior of high chromium white cast iron. *Mater. Sci. Eng. A* **2007**, *454*, 623–628. [CrossRef]
32. Zhao, Z.; Song, R.; Zhang, Y.; Yu, P.; Pei, Y. Co-orientation relationship between secondary carbides and adjacent ferrite after quenching and tempering in high chromium cast iron. *Vacuum* **2021**, *184*, 109911. [CrossRef]
33. Karantzalis, A.E.; Lekatou, A.; Diavati, E. Effect of Destabilization Heat Treatments on the Microstructure of High-Chromium Cast Iron: A Microscopy Examination Approach. *J. Mater. Eng. Perform.* **2009**, *18*, 1078. [CrossRef]
34. Rhp, A.; Ks, A.; Kk, A.; Tt, A.; Ms, B.; Hh, C.; Ji, C. Erosive wear characteristics of high-chromium based multi-component white cast irons. *Tribol. Int.* **2021**, *159*, 106982.
35. Taub, A.; De Moor, E.; Luo, A.; Matlock, D.K.; Speer, J.G.; Vaidya, U. Materials for automotive lightweighting. *Annu. Rev. Mater. Res.* **2019**, *49*, 327–359. [CrossRef]
36. Yang, H.-S.; Jun, W.; Bao-Luo, S.; Hao-Huai, L.; Sheng-Ji, G.; Si-Jiu, H. Effect of cryogenic treatment on the matrix structure and abrasion resistance of white cast iron subjected to destabilization treatment. *Wear* **2006**, *261*, 1150–1154. [CrossRef]
37. Bensely, A.; Prabhakaran, A.; Lal, D.M.; Nagarajan, G. Enhancing the wear resistance of case carburized steel (En 353) by cryogenic treatment. *Cryogenics* **2005**, *45*, 747–754. [CrossRef]
38. Zhirafar, S.; Rezaeian, A.; Pugh, M. Effect of cryogenic treatment on the mechanical properties of 4340 steel. *J. Mater. Process. Technol.* **2007**, *186*, 298–303. [CrossRef]
39. Yan, Z.; Liu, K.; Eckert, J. Effect of tempering and deep cryogenic treatment on microstructure and mechanical properties of Cr–Mo–V–Ni steel. *Mater. Sci. Eng. A* **2020**, *787*, 139520. [CrossRef]
40. Liu, H.; Wang, J.; Yang, H.; Shen, B. Effects of cryogenic treatment on microstructure and abrasion resistance of CrMnB high-chromium cast iron subjected to sub-critical treatment. *Mater. Sci. Eng. A* **2008**, *478*, 324–328. [CrossRef]
41. Liu, H.-H.; Wang, J.; Shen, B.-L.; Yang, H.-S.; Gao, S.-J.; Huang, S.-J. Effects of deep cryogenic treatment on property of 3Cr13Mo1V1. 5 high chromium cast iron. *Mater. Des.* **2007**, *28*, 1059–1064. [CrossRef]
42. Cui, J.; Chen, L. Microstructure and abrasive wear resistance of an alloyed ductile iron subjected to deep cryogenic and austempering treatments. *J. Mater. Sci. Technol.* **2017**, *33*, 1549–1554. [CrossRef]
43. Chen, G.; Rahimi, R.; Harwarth, M.; Motylenko, M.; Xu, G.; Biermann, H.; Mola, J. Non-cube-on-cube orientation relationship between $M_{23}C_6$ and austenite in an austenitic stainless steel. *Scr. Mater.* **2022**, *213*, 114597. [CrossRef]
44. Thornton, R.; Slatter, T.; Jones, A.H.; Lewis, R. The effects of cryogenic processing on the wear resistance of grey cast iron brake discs. *Wear* **2011**, *271*, 2386–2395. [CrossRef]
45. He, F. Cryogenic Treatment and Properties of High Chromium Cast Iron. Master's Thesis, Fuzhou University, Fuzhou, China, 2003.
46. Sarkar, T.; Mukherjee, M.; Pal, T.K. Effect of Cu addition on microstructure and hardness of As-Cast and heat-treated high-Cr cast iron. *Trans. Indian Inst. Met.* **2018**, *71*, 1455–1461. [CrossRef]
47. Inthidech, S.; Sricharoenchai, P.; Matsubara, Y. Effect of Alloying Elements on Heat Treatment Behavior of Hypoeutectic High Chromium Cast Iron. *Mater. Trans.* **2006**, *47*, 72–81. [CrossRef]
48. Zumelzu, E.; Goyos, I.; Cabezas, C.; Opitz, O.; Parada, A. Wear and corrosion behaviour of high-chromium (14–30% Cr) cast iron alloys. *J. Mater. Process. Technol.* **2002**, *128*, 250–255. [CrossRef]
49. Wiengmoon, A.; Pearce, J.; Chairuangsri, T. Relationship between microstructure, hardness and corrosion resistance in 20 wt.% Cr, 27 wt.% Cr and 36 wt.% Cr high chromium cast irons. *Mater. Chem. Phys.* **2011**, *125*, 739–748. [CrossRef]
50. Ma, J.; Zhang, Y.; Yang, Y.; Wang, G. Effect of vanadium and copper on as cast structure and properties of high alloy white cast iron. *Cast. Technol.* **2007**, *28*, 5.
51. Zhang, Y.; Song, R.; Pei, Y.; Wen, E.; Zhao, Z. The formation of TiC–NbC core-shell structure in hypereutectic high chromium cast iron leads to significant refinement of primary M_7C_3. *J. Alloys Compd.* **2020**, *824*, 153806. [CrossRef]
52. Penagos, J.J.; Pereira, J.; Machado, P.; Albertin, E.; Sinatora, A. Synergetic effect of niobium and molybdenum on abrasion resistance of high chromium cast irons. *Wear* **2017**, *376*, 983–992. [CrossRef]

53. Ye, C.; Liu, T.; Huang, W.; Zhou, C. Bare metal passivation characteristics of 0Cr18Ni9 austenitic stainless steel in low concentration sodium chloride solution. *J. Nanjing Univ. Technol.* **1999**, *21*, 52–55.
54. Zhang, S. Discussion on Wear and Corrosion Resistance of High Chromium Cast Iron A49. *Cast. Equip. Process* **2013**, *7*. [CrossRef]
55. Lv, Y.; Sun, Y.; Zhao, J.; Yu, G.; Shen, J.; Hu, S. Effect of tungsten on microstructure and properties of high chromium cast iron. *Mater. Des.* **2012**, *39*, 303–308. [CrossRef]
56. Alamdari, H.; Couture, A.; Fiset, M. The effect of nickel, silicon and austenite deep-freezing treatment on the microstructure and wear properties of high chromium white iron containing niobium. *Int. J. Cast Met. Res.* **1998**, *11*, 89–95. [CrossRef]
57. Li, T.; Li, L.; Lu, H.; Parent, L.; Tian, H.; Chung, R.; Li, D. Effect of trace Ni on the resistance of high-Cr cast iron to slurry erosion. *Wear* **2019**, *426*, 605–611. [CrossRef]
58. Zhi, X.; Xing, J.; Fu, H.; Gao, Y. Effect of fluctuation and modification on microstructure and impact toughness of 20 wt.% Cr hypereutectic white cast iron. *Mater. Sci. Eng. Technol.* **2008**, *39*, 391–393. [CrossRef]
59. Azimi, G.; Shamanian, M. Effects of silicon content on the microstructure and corrosion behavior of Fe–Cr–C hardfacing alloys. *J. Alloys Compd.* **2010**, *505*, 598–603. [CrossRef]
60. Yu, Z.; Qiang, J.; Li, H. Corrosion behavior of high silicon cast iron in various environments. *J. Xi'an Univ. Sci. Technol.* **2007**, *27*, 69–72.
61. Liqiang, G.; Hanguang, F.; Xiaohui, Z. Microstructure and properties of Cu-bearing hypereutectic high chromium cast iron. *Mater. Charact.* **2022**, *195*, 112546. [CrossRef]
62. Liqiang, G.; Hanguang, F.; Xiaohui, Z. First-principles study on corrosion resistance of copper-bearing hypereutectic high chromium cast iron. *Mater. Today Commun.* **2022**, *33*, 104345.
63. Wang, J.; Liu, T.; Zhou, Y.; Xing, X.; Liu, S.; Yang, Y.; Yang, Q. Effect of nitrogen alloying on the microstructure and abrasive impact wear resistance of Fe-Cr-C-Ti-Nb hardfacing alloy. *Surf. Coat. Technol.* **2017**, *309*, 1072–1080. [CrossRef]
64. Xu, L.; Wang, F.; Lu, F.; Zhou, Y.; Wei, S. Microstructure and erosion wear properties of high chromium cast iron added nitrogen by high pressure in alkaline sand slurry. *Wear* **2021**, *476*, 203655. [CrossRef]
65. Gelfi, M.; Pola, A.; Girelli, L.; Zacco, A.; Masotti, M.; Vecchia, G.L. Effect of heat treatment on microstructure and erosion resistance of white cast irons for slurry pumping applications. *Wear* **2019**, *428*, 438–448. [CrossRef]
66. Liu, S.; Zhang, H.; Ding, H.; Guo, J. Improving impact toughness of a high chromium cast iron regarding joint additive of nitrogen and titanium. *Mater. Des.* **2016**, *90*, 958–968. [CrossRef]
67. Guitar, M.A.; Suárez, S.; Prat, O.; Guigou, M.D.; Gari, V.; Pereira, G.; Mücklich, F. High Chromium Cast Irons: Destabilized-Subcritical Secondary Carbide Precipitation and Its Effect on Hardness and Wear Properties. *J. Mater. Eng. Perform.* **2018**, *27*, 3877–3885. [CrossRef]
68. Lu, F.; Wei, S.; Xu, L.; Zhou, Y.; Wang, X. Investigation on erosion-wear behaviors of high-chromium cast iron with high nitrogen content in salt–sand slurry. *Mater. Res. Express* **2019**, *6*, 106558. [CrossRef]
69. Yilbas, B.S.; Toor, I.; Karatas, C.; Malik, J.; Ovali, I. Laser treatment of dual matrix structured cast iron surface: Corrosion resistance of surface. *Opt. Lasers Eng.* **2015**, *64*, 17–22. [CrossRef]
70. Kusumoto, K.; Shimizu, K.; Efremenko, V.G.; Hara, H.; Shirai, M.; Purba, R. High-temperature erosive wear characteristics and bonding requirements of hard carbides cast-in insertion multi-component white cast iron. *Wear* **2021**, *476*, 203672. [CrossRef]

metals

MDPI

Article

Hardness Prediction in Quenched and Tempered Nodular Cast Iron Using the Hollomon-Jaffe Parameter

Fidel Salas Vicente [1,*], Javier Carcel Carrasco [2], Raquel Fernández Antoni [3], Juan Carlos Ferrero Taberner [1] and Manuel Pascual Guillamón [1]

[1] Mechanics and Materials Engineering Department, Universitat Politècnica de València, 12412 Valencia, Spain; juaferta@doctor.upv.es (J.C.F.T.); mpascual@mcm.upv.es (M.P.G.)
[2] Architectural Building Department, Universitat Politècnica de València, 12412 Valencia, Spain; fracarc1@csa.upv.es
[3] ETSID, Universitat Politècnica de València, 12412 Valencia, Spain; raquel96f@gmail.com
* Correspondence: fisavi@doctor.upv.es; Tel.: +34-963-877-628

Abstract: The Hollomon-Jaffe parameter is usually used to stablish a equivalence between time and temperature in a tempering treatment, but not to predict the harness of the alloy after the treatment. In this paper this last possibility has been studied. A group of cast iron samples was annealed and cooled at different rates in order to obtain samples with three different hardness values. These samples were tempered using different times and temperatures. The Hollomon-Jaffe parameter was calculated for each case and a relationship based on a logistic function between that parameter and the final hardness was stablished. This relationship was found to depend on the initial hardness and the lowest hardness achievable.

Keywords: Hollomon-Jaffe parameter; hardness; cast iron; quenching; tempering

Citation: Salas Vicente, F.; Carcel Carrasco, J.; Fernández Antoni, F.; Ferrero Taberner, J.C.; Pascual Guillamón, M. Hardness Prediction in Quenched and Tempered Nodular Cast Iron Using the Hollomon-Jaffe Parameter. *Metals* **2021**, *11*, 297. https://doi.org/10.3390/met11020297

Academic Editors: Annalisa Fortini and Chiara Soffritti

Received: 5 January 2021
Accepted: 3 February 2021
Published: 9 February 2021

1. Introduction

The heat treatment known as tempering, which consists in heating the hardened material to a temperature below the lower critical temperature, is a common procedure carried out after quenching in order to improve toughness and ductility of an iron alloy with martensitic microstructure, including welds [1–3] and the newest generations of steels [4,5]. Although the cost is a hardness reduction, the benefits clearly outweigh the inconveniences as the material properties are adapted to the in-service demands. Furthermore, the combination of a quenching and tempering treatment is technically a lot easier to perform than a quenching where the cooling rate must be accurately controlled or a certain temperature must be maintained during a certain period of time (e.g., austempering).

The two main parameters of the process are the temperature and the time the material is held at that temperature, being those two parameters complementary and interchangeable. This means a lower temperature can be compensated by a longer soaking time and a higher temperature should be accompanied by a lower soaking time if the same hardness reduction is to be obtained. Several equations have been proposed as a means to study the combined effect of time and temperature and other variables [6–8], although the most known and used worldwide is the Hollomon-Jaffe equation [9], which is expressed as:

$$TP = \frac{T}{1000} \cdot (C + \log(t)) \quad (1)$$

where TP is the Hollomon-Jaffe parameter (also known as the Larson-Miller [10] or the tempering parameter), T is the temperature in kelvin, t is the soaking time in hours and C is a constant. This equation was derived from the known Arrhenius equation [11], which in turn is the simplest form of the Van't Hoff equation [12,13]. The importance of Equation (1) lies in

the fact that there is a relationship between the value of TP and the decrease in hardness, which, in turn, relates to the mechanical properties of the material.

The selection of a correct value for constant C in Equation (1) can be important for the use of the Hollomon-Jaffe parameter. Initially, it was proposed a dependence of C with the carbon content of the steel and a mean value of 20 if time was expressed in hours was proposed [14] shortly after. Although this value has been widely used [15–18] even for new steels [19,20], other values have also been proposed for different alloys, basically through the fit of experimental data [16,21–23]. Even a negligible influence of the value of C in the applicability of the tempering parameter has been suggested [24], which could explain the aforementioned wide and appropriate use of a value of 20 for C.

Nevertheless, some authors have stated that the use of the Hollomon-Jaffe parameter is not suitable for all iron alloys [25].

Cast irons are iron alloys with a high carbon content that solidify with an eutectic and are used to manufacture metallic elements using the casting technology. The vast majority of those alloys are characterized by a microstructure of graphite in a ferrous matrix and can be subjected to heat treatments such as quenching, although their high carbon content imposes some limitations and oil quenching is always used except for surface hardening, when water can also be used. As the combination of quenching and annealing is cheaper and more controllable than processes like austempering or martempering, it should be preferred if the mechanical characteristics that provide an austempering are not needed or other problems like cracking during quenching are not a drawback.

The main aim of this work has been to study the applicability of the Hollomon-Jaffe parameter TP on the tempering of nodular cast iron after quenching, to determine the best value for the constant C and to use TP to predict the hardness of the samples after a hardening and tempering treatment. The results show this parameter is useful in the study of the tempering process over a wide range of C values and that the final hardness of the cast iron can be estimated from the initial hardness of the alloy and the Hollomon-Jaffe parameter.

2. Materials and Methods

The material used in this investigation was a trapezoidal bar with a section of 3.5 cm^2. This bar was made of a GJS-400-15 as-cast nodular iron alloy whose composition can be seen in Table 1. Its microstructure is shown in Figure 1. It contains both nodular and vermicular graphite (G) -around 70% nodular- in a ferritic-pearlitic matrix where pearlite accounts for 26% of the matrix. Its carbon equivalent (CE), calculated using Equation (2) [26] ranges from 3.93 to 4.57.

$$CE = \%C + 0.28 \cdot \%Si + 0.007 \cdot \%Mn + 0.303 \cdot \%P + 0.033 \cdot \%Cr + 0.092 \cdot \%Cu + 0.011 \cdot \%Mo + 0.054 \cdot \%Ni \quad (2)$$

The hardness of this alloy was 87.6 HRB (181.7 HV), what implies a minimum ultimate tensile strength of 390 MPa and a minimum yield strength of 250 MPa according to the specifications of EN 1563. The minimum elongation for this cast iron is 15%.

Table 1. Cast iron composition.

C	Si	Mn	S	P	Mg	CE
3.25–3.70	2.40–3.00	0.10–0.30	0.005–0.020	0.015–0.08	0.04–0.07	3.93–4.57

The bar was cut into samples of 15 mm width. These samples were separated into three groups of 20 samples each one in order to obtain three different hardness groups after a heat treatment:

- Group 1: Samples were austenized at 880 °C for 15 min and quenched in water. Oil is usually preferred so as to prevent cracking, but the small size of the samples avoided that problem even when quenching in water.

- Group 2: Samples were austenized at 880 °C for 15 min and cooled under air flow (24 m/s approximately) at room temperature. This airflow was obtained using two small air blowers at 100 mm from the samples.
- Group 3: Samples were austenized at 880 °C for 5 h and quenched in water. This long period of treatment leaded to a partial dissolution of the cementite in the pearlitic fraction of the matrix, which becomes graphitized. The resulting lower martensite content of the matrix after quenching implies also a lower hardness than for group 1.

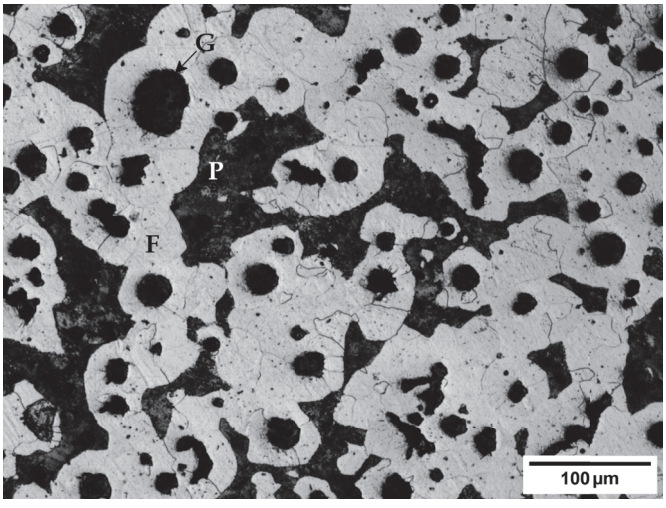

Figure 1. Microstructure of the alloy before any heat treatment. G: Graphite; F: Ferrite; P: Pearlite.

The applied austenizing treatments do not follow the usual recommendations of around 1 h/25 mm of section [27], so a complete austenization was not guaranteed for the whole samples. Nevertheless, some exploratory quenching tests were done at 880 °C and water quenching with soaking times of 10, 15, 20, 25 and 30 min and, except for the 10-min samples, all of them showed the same mean hardness at the surface. As the objective was only to obtain 3 different groups of samples with different hardness at the surface and not to obtain an homogenized or fully austenized microstructure, the lowest soaking time congruent with the objective was selected.

After quenching, the samples were tempered using different combinations of time and temperature. In total, 20 combinations were tested, according to Table 2. In order to calculate the value of the Hollomon-Jaffe parameter, a value of 20 was supposed for *C*.

As can be seen in Table 2, the selected values of temperature and time cover a range that goes from 12.3 to 22.6. In this range the values for one temperature partly overlaps with the values of the previous temperature.

Once the tempering treatment was finished, the samples were cooled in water to avoid a further evolution of the microstructure.

The hardness of the quenched and tempered samples was, after grinding using 220 and 500 grit sandpaper, measured using the Rockwell-C or Rockwell-B scales, depending on the hardness of the samples. These values were converted to the Vickers scale to facilitate a better comparability.

Finally, the samples were polished and etched using Nital-3 (3% HNO_3 in ethanol) and its microstructure studied using light microscopy.

Table 2. Tested combinations of time and temperature. The tempering parameter *TP* was calculated using *C* = 20.

Temperature (°C)	Time (Hours)	*TP*	Temperature (°C)	Time (min)	*TP*
400	0.17	12.3	600	0.17	15.9
400	0.33	12.7	600	0.33	16.5
400	1	13.5	600	1	17.5
400	5	14.5	600	5	18.9
400	24	15.6	600	24	20.2
500	0.17	14.1	700	0.17	17.7
500	0.33	14.6	700	0.33	18.4
500	1	15.5	700	1	19.5
500	5	16.7	700	5	21.0
500	24	17.9	700	24	22.6

3. Results

3.1. Microstructure and Hardness after Quenching

The structure of group 1 samples after quenching in water can be seen in Figure 2. Quenching in water generates a mixed matrix microstructure, mainly martensitic (M), but also containing areas of lower bainite (B) and ferrite (F), still present due to an incomplete austenization. Each one of these areas has a different hardness: 801 ± 75 HV0.1 for the martensitic areas, 620 ± 52 HV0.1 for the bainitic areas and 180 ± 34 HV0.05 for the ferrite grains. The mean hardness of the quenched samples was 54 ± 3 HRC (592 HV). This last value averages the effect of the different components of the microstructure as the size of the indentations done on the samples cover all of them.

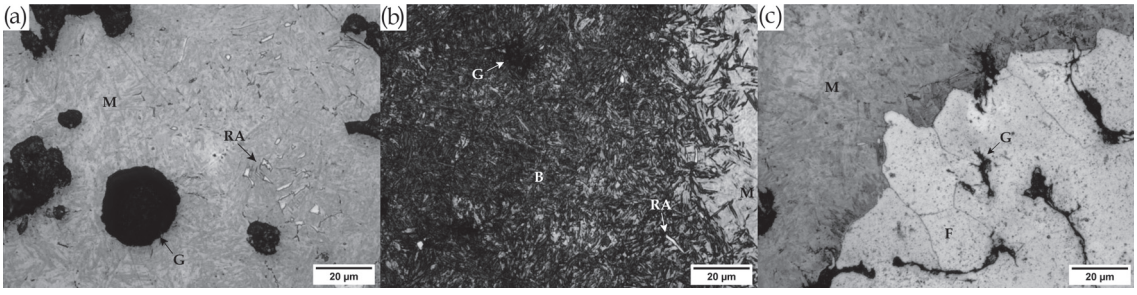

Figure 2. Microstructure of the samples quenched in water after 15 min of annealing at 880 °C. (**a**) Martensite with some retained austenite. (**b**) Bainite next to a martensitic area. (**c**) Ferrite grains and martensite. G: Graphite; F: Ferrite; M: Martensite; B: Bainite; RA: Retained austenite.

When the sample is quenched under a forced airflow the cooling rate is not high enough to produce a highly hardened microstructure, although an increase of 110 HV units is obtained when compared to the untreated cast iron. In this case the microstructure of the matrix (Figure 3) consists mainly of a mixture of fine pearlite (P) and ferrite (F) with a mean hardness of 28.6 ± 1 HRC (291 HV), although some retained austenite (RA) can still be found.

The structure that is obtained after a water quenching if the sample is maintained 5 h at 880 °C in the oven consists of martensite islands in a ferritic matrix (Figure 4). The higher proportion of ferrite in these samples when compared to the original microstructure indicates the 5 h the samples have been soaked at 880 °C had a ferritizing effect, resulting in the partial conversion of the pearlitic cementite to ferrite and graphite. Furthermore, a partial decarburization process took place at the surface of the samples due to the high temperature of the oven [28], as can be seen at the lower-left part of Figure 4 as round areas corresponding to the decarburized graphite nodules (DGN). In this case, the combination of ferrite and martensite gave the quenched samples a hardness of 42 ± 3 HRC (420 HV).

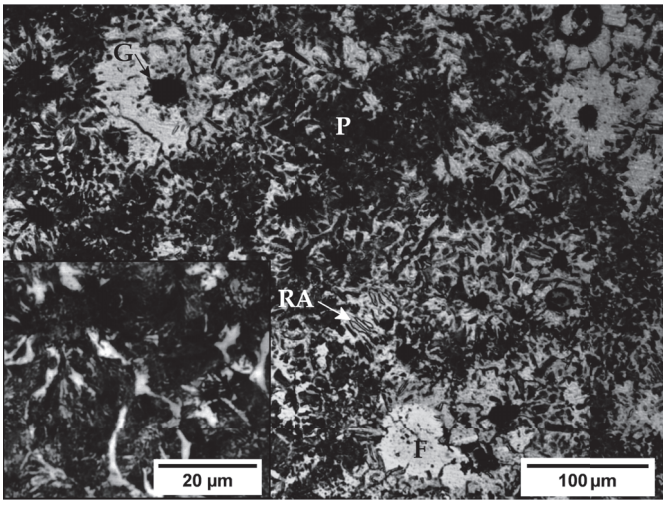

Figure 3. Microstructure of the samples cooled under forced air flow after 15 min of annealing at 880 °C. G: Graphite; F: Ferrite; P: Pearlite; RA: Retained austenite.

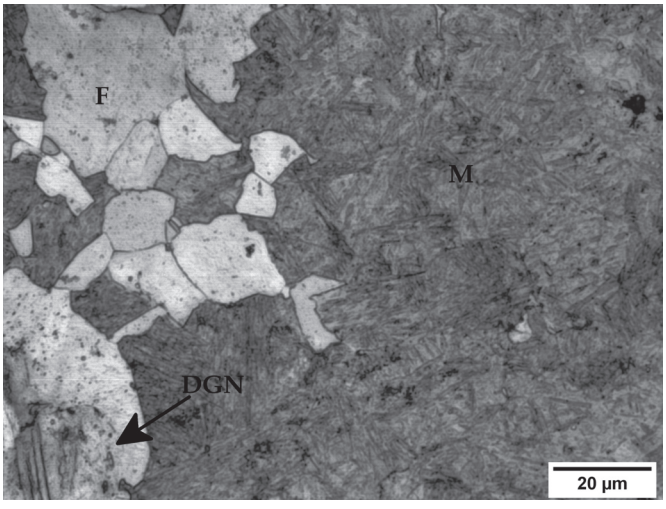

Figure 4. Microstructure of the samples quenched in water after 5 h of annealing at 880 °C. The fraction of ferrite is much higher than shown in the figure. DGN: Decarburized graphite nodule; F: Ferrite; M: Martensite.

3.2. Hardness Evolution during Tempering

Figure 5 shows the hardness measured for each sample after the quenching and tempering heat treatments as a function of temperature and time. The largest part of the hardness reduction takes place during the first hour, with a higher reduction rate during the first 10 min. After 1 h, the hardness values decrease very slowly or stabilize. This behaviour is expected due to the logarithmical relation between time and hardness in definition of the Hollomon-Jaffe parameter. This logarithmic relationship implies the need of a 10-fold increase of time in order to double the hardness decrease. The dependence with temperature is linear and that linearity can be seen in Figure 5 despite the effect of data dispersion.

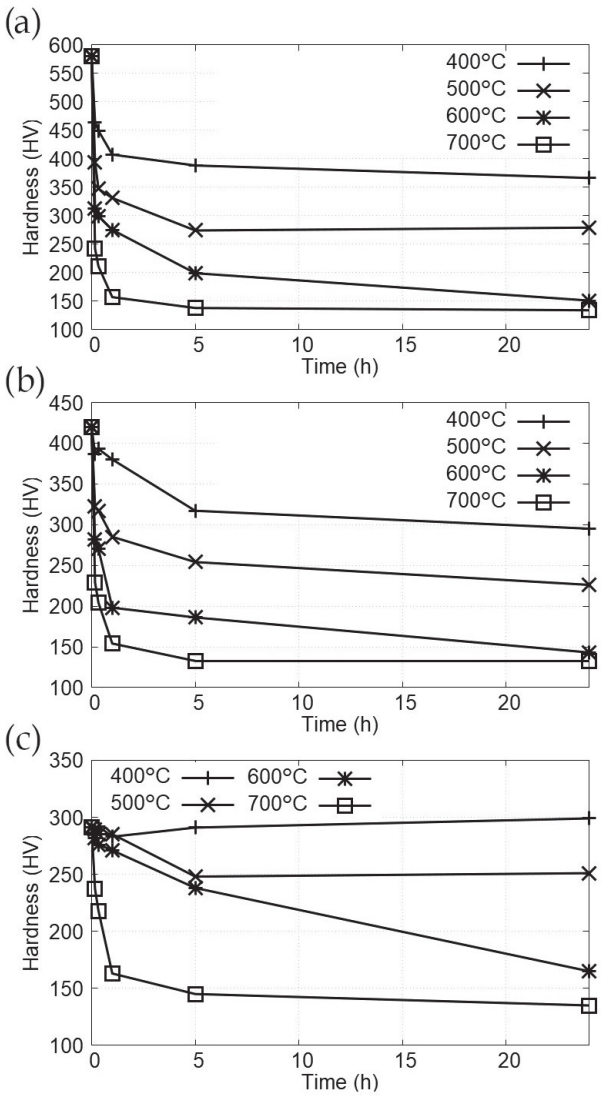

Figure 5. Evolution of hardness with time and temperature (**a**) Samples quenched in water. (**b**) Samples cooled under air flow. (**c**) Samples quenched in water after 5 h at 880 °C.

4. Discussion

4.1. Hardness and the Tempering Parameter

A better way of correlating time and temperature with hardness is the use of the Hollomon-Jaffe parameter. If hardness is plotted against the tempering parameter using $C = 20$, Figure 6 is obtained. In that graphic, the initial hardness of the quenched samples is represented by a horizontal line at the Y-axis.

According to Figure 6, the hardness decrease follows approximately the same curve independently of the initial hardness, but only once the tempering parameter is high enough to produce a noticeable change in the microstructure and the hardness. That point seems to be dependent of the initial hardness value as a tempering parameter equal to 16 is needed to see a reduction in hardness when the initial microstructure is a mixture of ferrite and fine pearlite (291 HV), but the hardness reduction is clear for the more hardened

samples (580 HV) with a value of the tempering parameter of 12. The need for a minimum value of TP in order to obtain noticeable changes is also found in the literature [29,30].

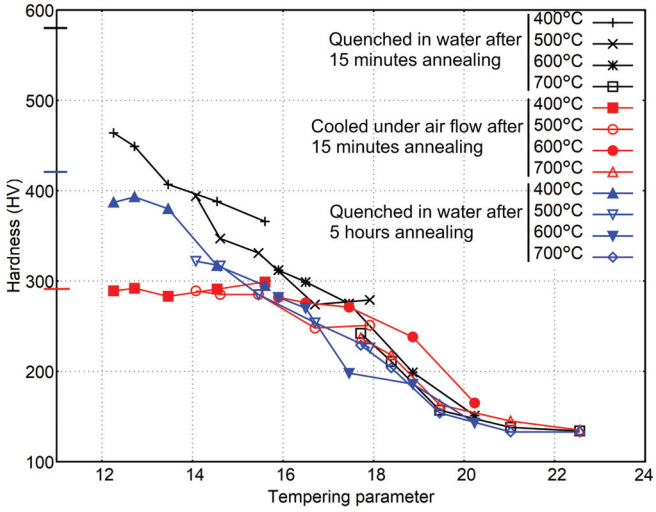

Figure 6. Evolution of hardness with the tempering parameter.

Regarding the value of C, the Hollomon-Jaffe parameter is mainly used on the linear part of the curve that represents the evolution of hardness. To obtain the best fit to the data points, a linear fit was done using all the points of group 1 samples except the one corresponding to the highest TP as that point no longer follows a linear evolution. The best fit was found with $C = 24.57$ ($R^2 = 0.981$). Nevertheless, other C values give very good results.

Figure 7 shows the value of R^2 when different values of C are used. As that figure shows, the range of values from which C can be chosen and still have a coefficient of determination R^2 over 0.95 goes from 17 to 39, what explains the different values proposed by different authors or the aforementioned negligible influence of C in the applicability of the tempering parameter [24]. Evidently, the value of TP will change with C.

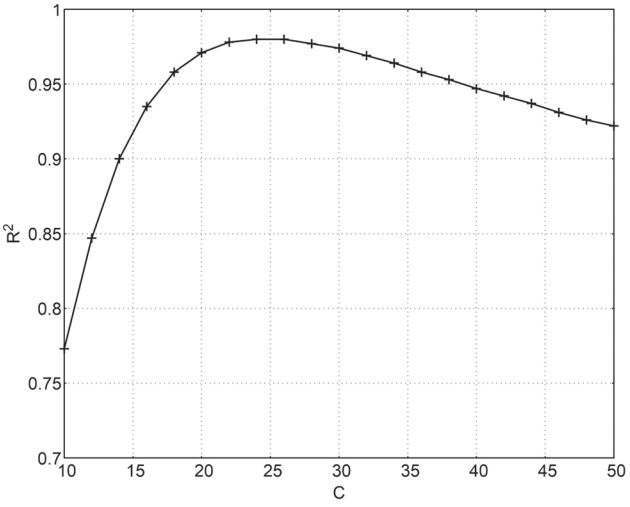

Figure 7. Coefficient of determination R^2 for different values of C.

In this case, as the use of $C = 20$ gives good results ($R^2 = 0.971$), it was decided to maintain that value in pursuit of a better comparability with bibliographic results.

It's important to note that the evolution of hardness, and also of the microstructure, depends on three diffusion processes: tempering of martensite, ferritization and decarburization of the outer layer of the samples, but despite the combination of these processes, the tempering parameter remains suitable to study the changes due to tempering.

4.2. Microstructure Evolution

The evolution of the microstructure is shown in Figure 8 for the samples of group 1, the more hardened ones. The microstructure shows tempered martensite until the tempering parameter reaches a value near 18, when the decomposition of martensite has progressed and the microstructure is composed of globular carbides in a ferritic matrix along with nodular and compacted graphite. Thenceforth, the ferritizing process dissolves those carbides to produce, for the highest values of the tempering parameter, a fully ferritic microstructure. Furthermore, decarburization also takes place and nodular and compacted graphite disappear from the outer layers of the samples, leaving footprints [31] that can be seen clearly in Figure 8f.

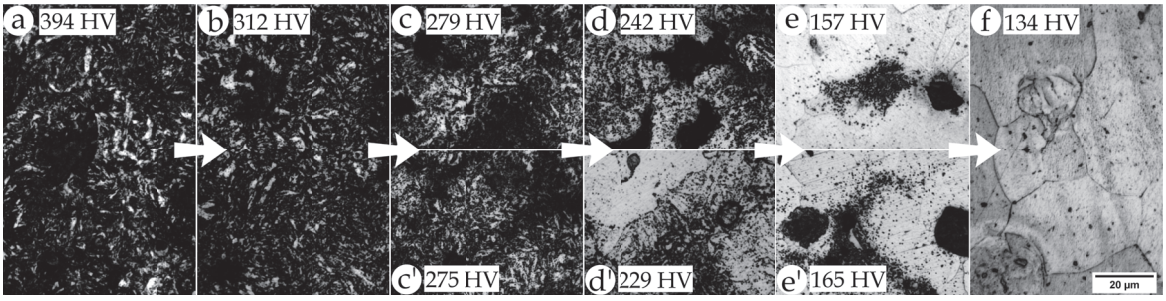

Figure 8. Evolution of hardness with the tempering parameter (**a**) $TP = 14.1$, group 1, 10 min at 500 °C. (**b**) $TP = 15.9$, group 1, 10 min at 600 °C. (**c**) $TP = 17.9$, group 1, 24 h at 500 °C. (**c'**) $TP = 17.5$, group 1, 1 h at 600 °C. (**d**) $TP = 17.7$, group 1, 10 min at 700 °C. (**d'**) $TP = 17.7$, group 3, 10 min at 700 °C. (**e**) $TP = 19.5$, group 1, 1 h at 700 °C. (**e'**) $TP = 19.5$, group 2, 24 h at 600 °C. (**f**) $TP = 22.6$, group 1, 24 h at 700 °C. All figures at ×400.

Although Figure 8 shows the evolution of the harder group of samples, the microstructure of the other groups follow a similar evolution once the decomposition of the microstructure has begun. In fact, Figure 8d' and Figure 8e' correspond to group 3 and group 2 and have been introduced to show the similarity in the microstructure for similar values of TP and hardness despite having initial different microstructures. Figure 8c,c' and Figure 8d,d' have similar values of the tempering parameter, nevertheless, the microstructure has evolved a bit more on Figure 8d,d', which have lower hardness, perhaps this behaviour is due to a slight higher influence of temperature than time that is not covered by the formula of the Hollomon-Jaffe parameter. Evidently, that could not be the case, but the different series of points in Figure 6 tend to show that, for similar TP values, the samples with higher temperatures and lower times tend to have lower hardness than the samples with lower temperatures and higher times.

4.3. Prediction of Hardness Using the Tempering Parameter

Despite minor inconsistencies that could be due to small mistakes during the procedure of tempering and quenching or, simply, to statistical dispersion of the results, the Hollomon-Jaffe parameter TP fulfils its role and combines the effect of tempering temperature and time for the tested nodular cast iron. In this case TP has also been use as a means to predict the hardness of a tempered sample. In order to do that, some points were taken into account:

- Low values of the tempering parameter will not produce any change in the microstructure of the samples.
- The curve that represents the evolution of hardness with *TP* is limited by the initial hardness and the hardness of the softer microstructure achievable, a fully ferritic matrix in this case.

Considering these restrictions, the chosen function to fit the data as a function of *TP* was based in the logistic function, which is a sigmoid function:

$$H = A - \frac{B}{1 + e^{-D \cdot (TP - E)}} \quad (3)$$

where *A*, *B*, *D* and *E* are the fitting variables. Usually, a linear relationship between *TP* and hardness would be used, but this function has been preferred as a means to extend its validity over all values of *HP*.

Some considerations must be made now regarding the function:

- Without any tempering (*TP* = 0), the hardness remains unchanged. Mathematically, for the chosen function, this implies that for $-\infty$ A equals the initial hardness, H_0.
- It can be supposed that for a infinite value of *TP*, the hardness will be the lowest of the values obtained after tempering the samples, H_f. This implies, taking into account the previous restriction, that $B = H_0 - H_f$.

So, the values of *A* and *B* can be directly calculated from the initial and the lowest attainable hardness (133 HV) and the only remaining variables are *D* and *E*, both of them needed to fit the width and position of the transition from H_0 to H_f.

The fitted functions for each one of the groups are represented in Figure 9. Each group of samples follows a different curve, which is to be expected, but there is some linearity that is shared between the 3 groups and provide an estimation for the hardness values of the quenched samples independently of the initial hardness. The range where this happens is marked in Figure 9. The values of coefficients *D* and *E* should also be dependent on H_0 and H_f and both decline as $H_0 - H_f$ increases (see Figure 10).

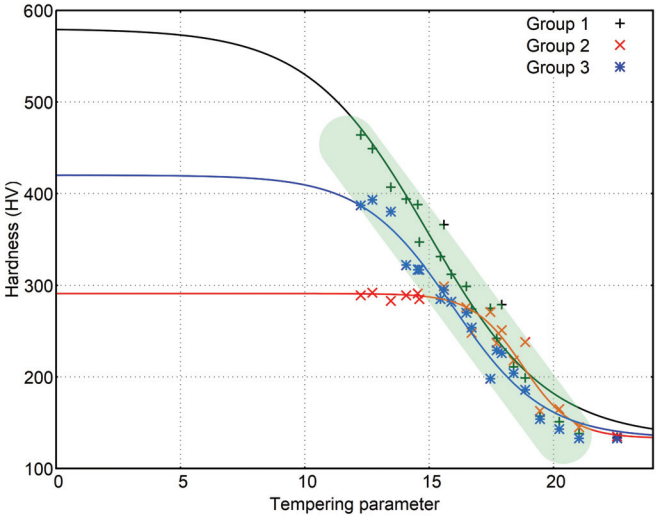

Figure 9. Mathematical relation between *TP* and hardness for the 3 groups of samples. Coefficients *D* and *E* are 0.417 and 14.97 for group 1, 1.000 and 18.76 for group 2 and 0.546 and 15.96 for group 3.

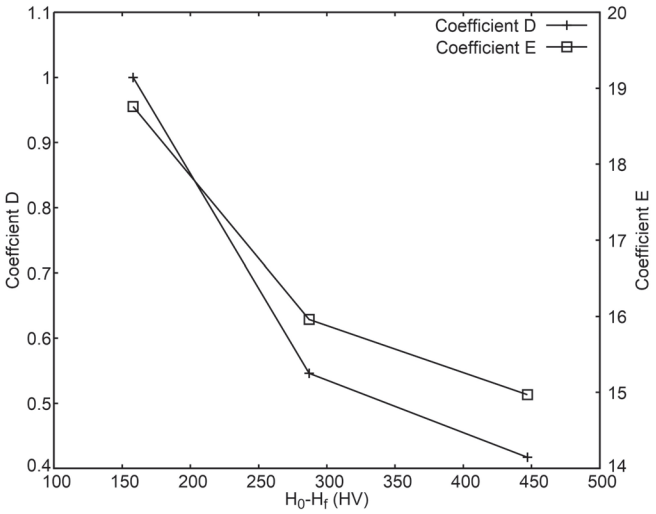

Figure 10. Coefficients D and E as a function of $H_0 - H_f$.

The fitted functions provide other insights as they show clearly how the onset of the decrease in hardness requires higher values of TP as the initial hardness lowers. That value of TP seems to coincide with the point where the curve reaches the area of linearity. This fact could be used to estimate the minimum TP needed to produce a change in a hardened sample using data obtained from samples with other hardness. If the onset of change is supposed to be related to the loss of 5% of the initial hardness, the following values are obtained for TP: 8.3, 16.3 and 11.0.

The end of the tempering could be estimated the same way. Supposing it ends when hardness reaches 105% of H_f, the functions give the following values for TP: 25.05, 22.81 and 21.88.

5. Conclusions

The following conclusions can be extracted from the study of the results:

- The tempering of three groups of hardened nodular cast iron, each one with a different initial harness, has shown the Hollomon-Jaffe is suitable for this alloy even when there are more than one diffusion process (tempering of martensite, ferritization and decarburization).
- The constant C of the Hollomon-Jaffe parameter can be chosen from a wide range of values without affecting noticeably the applicability od TP. The common choice $C = 20$ gives, in this case, good results.
- The evolution of hardness relates with that of the microstructure. These changes follow, roughly, the following sequence: tempering of martensite, ferritizing and decarburization.
- The onset of microstructure and hardness changes depends on the initial hardness of the samples. The changes begins at lower TP values as initial harness increases.
- Once hardness has begun decreasing, the evolution follows approximately the same linear evolution regardless of the initial hardness.
- Hardness evolution can be predicted using a logistic function, which can also be used to predict the onset of hardness changes.
- Coefficients D and E of the mentioned function show a similar dependence on H_0 and H_f.

Author Contributions: Conceptualization, F.S.V. and M.P.G.; methodology, F.S.V.; validation, M.P.G.; formal analysis, R.F.A., J.C.F.T. and F.S.V.; investigation, R.F.A. and J.C.F.T.; data curation, R.F.A. and J.C.F.T.; writing—original draft preparation, F.S.V. and R.F.A.; writing—review and editing, F.S.V. and J.C.C. All authors have read and agreed to the published version of the manuscript.

Funding: This research received no external funding.

Data Availability Statement: Data can be obtained from the authors.

Conflicts of Interest: The authors declare no conflict of interest.

References

1. Sun, Y.; Obasi, G.; Hamelin, C.; Vasileiou, A.; Flint, T.; Francis, J.; Smith, M. Characterisation and modelling of tempering during multi-pass welding. *J. Mater. Process. Technol.* **2019**, *270*, 118–131. [CrossRef]
2. Dai, T.; Thodla, R.; Kovacs, W., III; Tummala, K.; Lippold, J. Effect of Postweld Heat Treatment on the Sulfide Stress Cracking of Dissimilar Welds of Nickel-Based Alloy 625 on Steels. *Corrosion* **2019**, *75*, 641–656. [CrossRef]
3. Liu, G.; Yang, S.; Han, W.; Zhou, L.; Zhang, M.; Ding, J.; Dong, Y.; Wan, F.; Shang, C.; Misra, R. Microstructural evolution of dissimilar welded joints between reduced-activation ferritic-martensitic steel and 316L stainless steel during the post weld heat treatment. *Mater. Sci. Eng. A* **2018**, *722*, 182–196. [CrossRef]
4. Cheng, G.; Choi, K.S.; Hu, X.; Sun, X. Predicting Deformation Limits of Dual-Phase Steels Under Complex Loading Paths. *JOM* **2017**, *69*, 1046–1051. [CrossRef]
5. Blesi, B.W.; Smith, C.; Matlock, D.K.; De Moor, E. Bake Hardening Behavior of DP, TBF, and PHS Steels with Ultimate Tensile Strengths Exceeding 1 GPa. *SAE Int. J. Adv. Curr. Pract. Mobil.* **2020**, *2*, 3203–3218.
6. Murphy, S.; Woodhead, J.H. An investigation of the validity of certain tempering parameters. *Metall. Mater. Trans. B* **1972**, *3*, 727–735. [CrossRef]
7. Canale, L.C.; Yao, X.; Gu, J.; Totten, G.E. A historical overview of steel tempering parameters. *Int. J. Microstruct. Mater. Prop.* **2008**, *3*, 474. [CrossRef]
8. Gomes, C.; Kaiser, A.L.; Bas, J.P.; Aissaoui, A.; Piette, M. Predicting the mechanical properties of a quenched and tempered steel thanks to a "tempering parameter". *Mater. Trans.* **2010**, *107*, 293–302. [CrossRef]
9. Hollomon, J. Time-temperature relations in tempering steel. *Trans. AIME* **1945**, *162*, 223–249.
10. Larson, F.R. A time-temperature relationship for rupture and creep stresses. *Trans. ASME* **1952**, *74*, 765–775.
11. Arrhenius, S. Über die Dissociationswärme und den Einfluss der Temperatur auf den Dissociationsgrad der Elektrolyte. *Z. Phys. Chem.* **1889**, *4*, 96–116. [CrossRef]
12. Van't Hoff, J.H. *Etudes de Dynamique Chimique*; Muller: Amsterdam, The Netherlands, 1884; Volume 1.
13. Laidler, K. Chemical kinetics and the origins of physical chemistry. *Arch. Hist. Exact Sci.* **1985**, *32*, 43–75. [CrossRef]
14. Roberts, G.; Grobe, A.; Moersch, C. The tempering of high alloy tool steels. *Trans. Am. Soc. Met.* **1947**, *39*, 521–548.
15. Virtanen, E.; Tyne, C.V.; Levy, B.; Brada, G. The tempering parameter for evaluating softening of hot and warm forging die steels. *J. Mater. Process. Technol.* **2013**, *213*, 1364–1369. [CrossRef]
16. Zikeev, V.; Kornyushchenkova, Y.V.; Izvol'skii, V. Influence of the temperature-time parameter of tempering on the properties of 18Kh1G1MF steel resistant to hydrogen embrittlement. *Met. Sci. Heat Treat.* **1984**, *26*, 99–101. [CrossRef]
17. Revilla, C.; López, B.; Rodriguez-Ibabe, J. Carbide size refinement by controlling the heating rate during induction tempering in a low alloy steel. *Mater. Des. (1980–2015)* **2014**, *62*, 296–304. [CrossRef]
18. Hodgson, D.; Dai, T.; Lippold, J. Transformation and tempering behavior of the heat-affected zone of 2.25 Cr-1Mo steel. *Weld. J.* **2015**, *94*, *250–256*.
19. Kamp, A.; Celotto, S.; Hanlon, D. Effects of tempering on the mechanical properties of high strength dual-phase steels. *Mater. Sci. Eng. A* **2012**, *538*, 35–41. [CrossRef]
20. Mahadevan, S.; Manojkumar, R.; Jayakumar, T.; Das, C.R.; Rao, B.P.C. Precipitation-Induced Changes in Microstrain and Its Relation with Hardness and Tempering Parameter in 17-4 PH Stainless Steel. *Metall. Mater. Trans. A* **2016**, *47*, 3109–3118. [CrossRef]
21. Shlyakman, B.M.; Yampolskii, O.N.; Ratushev, D.V. A method for determining constant C in the Hollomon parameter. *Met. Sci. Heat Treat.* **2010**, *52*, 451–453. [CrossRef]
22. Paul, V.T.; Saroja, S.; Albert, S.; Jayakumar, T.; Kumar, E.R. Microstructural characterization of weld joints of 9Cr reduced activation ferritic martensitic steel fabricated by different joining methods. *Mater. Charact.* **2014**, *96*, 213–224. [CrossRef]
23. Shrestha, T.; Alsagabi, S.; Charit, I.; Potirniche, G.; Glazoff, M. Effect of Heat Treatment on Microstructure and Hardness of Grade 91 Steel. *Metals* **2015**, *5*, 131–149. [CrossRef]
24. Janjusevic, Z.; Gulisija, Z.; Mihailovic, M.; Pataric, A. The investigation of applicability of the Hollomon-Jaffe equation on tempering the HSLA steel. *Chem. Ind. Chem. Eng. Q.* **2009**, *15*, 131–136. [CrossRef]
25. Murry, G. évolution de la dureté des aciers de traitement thermique au cours du revenu après trempe incomplète. *Rev. Métall.* **1977**, *74*, 665–672. [CrossRef]

26. Stefanescu, D.; Lacaze, J. *ASM Handbook, Volume 1A, Cast Iron Science and Technology*; Chapter Thermodynamics Principles as Applied to Cast Iron; ASM International: Materials Park, OH, USA, 2017; pp. 31–45.
27. *ASM Handbook, Volume 4—Heat Treating*; ASM International: Materials Park, OH, USA, 1991.
28. Yamada, S.; Goto, S.; Aso, S.; Komatsu, Y.; Konno, T. Growth mechanism of decarburized layer in spheroidal cast iron. *J. Jpn. Foundry Eng. Soc.* **2001**, *73*, 219–224.
29. Dai, T.; Lippold, J. Tempering behavior of the fusion boundary region of an F22/625 weld overlay. *Weld. J.* **2017**, *96*, 467–480.
30. Hoja, S.; Hoffmann, F.; Steinbacher, M.; Zoch, H.W. Investigation of the Tempering Effect during Nitriding. *HTM J. Heat Treat. Mater.* **2018**, *73*, 335–343. [CrossRef]
31. Yamaguchi, Y.; Kiguchi, S.; Sumimoto, H.; Nakamura, K. Effect of graphite morphology on decarburized cast iron. *Int. J. Cast Met. Res.* **2003**, *16*, 137–142. [CrossRef]

metals

MDPI

Article

Solidification Pattern of Si-Alloyed, Inoculated Ductile Cast Irons, Evaluated by Thermal Analysis

Iuliana Stan, Denisa Anca *, Stelian Stan and Iulian Riposan

Materials Science and Engineering Faculty, Politehnica University of Bucharest, 060042 Bucharest, Romania; iuliana.stan@upb.ro (I.S.); constantin.stan@upb.ro (S.S.); iulian.riposan@upb.ro (I.R.)
* Correspondence: denisa_elena.anca@upb.ro

Abstract: The solidification cooling curve itself as well as its first derivative, and related temperatures, reported to the calculated equilibrium temperatures in stable and metastable solidification systems, are used to predict the solidification characteristics of the cast iron. Silicon, as the most representative cast iron element, and inoculation, as graphitizing metallurgical treatment, have a major influence on the transition from the liquid to the solid state. Six experimental programs are performed, with Si content typically for non-alloyed (<3.0% Si), low (3.0–3.5% Si) and medium alloyed (4.5–5.5% Si) ductile cast irons, as Si-content increasing, and inoculation simultaneous effects. Silicon is an important influencing factor, but the base and minor elements also affect the equilibrium eutectic temperatures, much more in the Fe-C-Si-*Xi* stable system (15–20 °C) than in the metastable system (5–10 °C), comparing with their calculation based only on a Si effect (Fe-C-Si system). The highest positive effect of inoculation is visible in non-Si alloyed cast irons (2.5% Si): 9–15 °C for the eutectic reaction and 3 to 4 times increased at the end of solidification (37–47 °C). Increased Si content decreases inoculation power to 7–9 °C for low alloying grade (up to 3.5% Si), with the lowest contribution at more than 4.5% Si (0.3–2.0 °C). 2.5–3.5% Si ductile cast irons are more sensitive to high solidification undercooling, especially at the end of solidification (but with a higher efficiency of inoculation), compared to 4.5–5.5% Si ductile cast irons, at a lower undercooling level, and at lower inoculation contribution, as well.

Keywords: ductile cast iron; solidification; eutectic reaction; end of solidification; stable system; metastable system; cooling curve analysis; silicon alloying; inoculation; eutectic undercooling

Citation: Stan, I.; Anca, D.; Stan, S.; Riposan, I. Solidification Pattern of Si-Alloyed, Inoculated Ductile Cast Irons, Evaluated by Thermal Analysis. *Metals* **2021**, *11*, 846. https://doi.org/10.3390/met11050846

Academic Editor: Annalisa Fortini

Received: 20 April 2021
Accepted: 14 May 2021
Published: 20 May 2021

1. Introduction

By free carbides avoiding and ferrite promoting, silicon has an important contribution to reach high ductility and toughness characteristics, accompanied by the best machinability conditions. The presence of the silicon atoms inside the ferrite structure contributes to increasing the tensile strength *Rm* ((+128 MPa)/% Si—maximum reached at 4.2–4.4% Si), the yield strength $Rp_{0.2}$ ((+118 MPa)/% Si—maximum reached at 4.6–4.8% Si), and the Brinell hardness ((+45 HB)/% Si—for 2.5–6% Si (150 HB to 310 HB), but with a drastic decrease of elongation *A* ((−5% *A*)/% Si)—at less than 4.3% Si, and (−30% *A*)/% Si, for 4.3% up to 4.8% Si) of the ferritic ductile cast irons [1].

In 3.2–4.3% Si ductile cast irons, the unstable mixed ferrite-pearlite matrix is replaced with more predictable and controllable ferritic grades, at a reduced hardness variation (±4 HB), increased cutting tool life, and better mechanical properties (*Rm* = 450–650 MPa; $Rp_{0.2}$ = 350–500 MPa; *A* = 10–20%); these materials are usually used in the automotive industry. Silicon (4–6% Si), and Si-Mo (2.5–5.5% Si, and 0.2–2.0% Mo) alloyed ductile cast irons are characterized by a high resistance to oxidation and corrosion at high temperatures. Molybdenum addition favors superior mechanical properties, especially at high temperatures (*Rm* = 400–650 MPa; $Rp_{0.2}$ = 250–550 MPa; *A* = 3–12%), typically for exhausted applications [2–4].

Inoculation, an important metallurgical treatment, is applied to the liquid cast iron, usually after the Mg-treatment to forestall solidification at an excessive eutectic undercooling degree, favorable for carbides occurrence or/and undesired graphite morphologies. In this way, it is possible to obtain an as-cast structure without free carbides (promoters of bad machinability and brittleness) and with a high quality graphite shape (the best expected graphite morphology specifically for each cast iron type, at a lower size and a higher nodule count).

Inoculation is recorded by addition of 0.05–1.0 wt.% alloy (inoculant, FeSiAl*X*, where *X* = Ca, Ba, Sr, RE, etc.) in the tapped iron melt (1300–1500 °C). The main objective of this treatment is to promote active compounds (microns scale) in the iron melt, to act as active graphite nucleation sites, at a lower eutectic undercooling, by improving the existent nucleation sites or/and by promoting new nucleation sites.

Factors influencing inoculation efficiency mainly refer to charge materials (pig iron/steel scrap ratio, recarburizers, preconditioners), melting furnace thermal regime, base iron chemical composition (Si, Mn, S) and iron residuals (Al, Ti, O, N), inoculating elements, inoculant type, inoculation procedure, holding time, pouring procedure, and casting characteristics [5].

Thermal (cooling curve) analysis is usually used to evaluate the solidification pattern of ductile cast irons, in terms of the prediction of eutectic undercooling, important for free carbide formation sensitivity, different graphite morphologies occurrence and the end of solidification defects (inter-eutectic cells free carbides and micro-shrinkage).

Important events on the cooling curve (the lowest and the highest eutectic temperatures and the temperature on the end of solidification), and on its first derivative (maximum recalescence rate, the lowest level at the end of solidification, different graphitizing factors) offer important information on the solidification pattern of ductile iron castings. The referring of these events to the equilibrium temperatures in the stable and metastable Fe-C systems offers more data on the specifics of primary structure characteristics [6–8].

The main objective of the present paper is to evaluate by thermal (cooling curve) analysis the solidification pattern of ductile cast irons, non-Si alloyed (<3.0% Si), low (3.0–3.5% Si), and medium Si alloyed (4.5–5.5% Si), as silicon content increases, while inoculation application effects present simultaneously on the cooling curves events.

2. Materials and Methods

Six experimental programs are performed, for three groups of ductile cast irons, with silicon content typically for non-alloyed (2.4–2.6% Si), lower limit (3.15–3.45% Si, low alloying grade), and upper limit (4.5–5.5% Si, medium alloying grade) of High-Si ductile cast irons (two programs for each group) (Table 1, Figure 1).

More information on some experimental programs and previous reported results are available in our previous published papers: Program I [8], Program II [2], Program III [9], Program IV [10], and Program V [11]. New obtained data are added to selected data from these previous papers, in order to have a coherent evaluation of the simultaneous influence of silicon and inoculation, for the entire range of silicon content in non-and Si alloyed ductile cast irons for applications involving mechanical properties and oxidation resistance, such as for the automotive industry.

Charge materials include steel scrap, ductile iron returns, ferrosilicon and recarburizer, typically used for commercial ductile irons production. Experimental cast irons, obtained by electric melting (10 kg—coreless induction furnace, 8000 Hz frequency, graphite crucible, 1500–1550 °C superheating), are subjected to a nodularization treatment (Tundish-Cover technique, 1.5–2.5 wt.% FeSiCaMgRE treatment alloys), followed by a FeSi-based alloys inoculation (Ca, Ba, Ce, Al as active elements), ladle and in-mold inoculation.

Table 1. Experimental programs parameters.

Pr *	Si Content (%)	Mg-Treatment ** (Nodularization)	Inoculation (Graphitization)
I	2.48	2.0 wt.% FeSiCaMgRE Tundish Cover Ladle	0.5 wt.% Ca, Ce, S, O-FeSi Pouring Ladle
II	2.55	2.0 wt.% FeSiCaMgRE Tundish Cover Ladle	0.3 wt.% Ca, Ce, S, O-FeSi Pouring Ladle
III	3.15	2.0 wt.% FeSiCaMgRE Tundish Cover Ladle	0.5 wt.% Ca, Ba, Al-FeSi Pouring Ladle
IV	3.44	2.5 wt.% FeSiCaMgRE Tundish Cover Ladle	0.5 wt.% Ca, Ba, Al-FeSi Pouring Ladle
V	4.55	1.5 wt.% FeSiCaMgRE Tundish Cover Ladle	0.1 wt.% Ca, Ba, Al-FeSi In-mold, Quick-Cup^{TM}
VI	5.25	1.5 wt.% FeSiCaMgRE Tundish Cover Ladle	0.1 wt.% Ca, Ba, Al-FeSi In-mold, Quick-Cup^{TM}

* Pr—Experimental Program; ** RE—Rare Earth Elements.

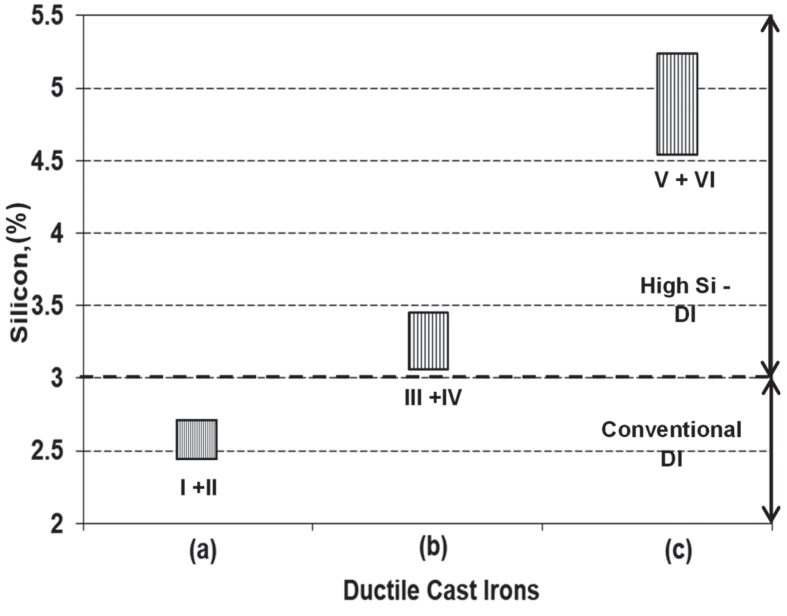

Figure 1. Representative groups of experimental programs (Table 1) (**a**) non-Si alloyed; (**b**) low-Si alloyed; (**c**) medium-Si alloyed).

Mg-treatment alloys include 43–46% Si, 6–10% Mg, 1–2% Ca, 0.8–1.5% Al, Fe-bal. Ca, Ba, Al-FeSi alloys (0.94–1.0% Ca, 1.0–1.68% Ba, 0.96–1.1% Al, 72.6–75% Si, Fe-bal) and Ca, Ce, S, O-FeSi alloys (70–76% Si, 0.75–1.25% Ca, 0.75–1.25% Al, 1.5–2.0% RE, and less than O and S-bearing compounds) [5] are selected as inoculants.

In ductile iron production, both the ladle and in-mold inoculation techniques are used. For higher silicon content ductile cast irons (>4% Si), trials V and VI, inoculation was recorded just in the ceramic cup, and used for thermal (cooling curve) analysis, as this inoculation technique is known to have the highest efficiency. This is considered necessary for high Si content ductile irons, according to the previously obtained results [2].

A SPECTROLAB high-end spectrometer (SPECTROLAB, Sylmar, CA, USA) with hybrid optic (photomultiplier tubs (PMT) and CCD (Spectroscopic Charge Coupled Device detection system) detectors simultaneously are used for high precision metal analysis. The instrument achieves detection limits below 1 mg/kg.

The present paper focuses on the thermal (cooling curve) analysis (standard QuickCup^{TM} (Heraeus Electro-Nite International, Houthalen, Belgium) thermal analysis) [12] of the Mg-treated liquid cast irons, before and after the inoculation process. Un-inoculated and inoculated iron melts are poured in standard ceramic cups (7.3 mm cooling modulus), including a thermocouple for thermal (cooling curve) analysis of the solidification process. Cooling modulus is the ratio between the volume and the total surface area of castings; it expresses the capacity to transfer the heat from casting through the mold media, outwardly. A lower cooling modulus value leads to a higher solidification cooling rate, with important effects on the eutectic and eutectoid structure formation and characteristics.

3. Results and Discussion

3.1. Chemical Composition

Base (C, Si, Mn, P, S), nodularizing (Mg, Ce, La), inoculating (Ca, Al, Zr) and minor (Ti, As, Sn, Sb, Pb, Bi, V, Cu, Ni, Cr, Co, Mo, Nb, W) elements, usually present in the commercial cast irons are analyzed (Tables 2 and 3).

Table 2. Base chemical composition and chemistry control factors.

Pr *	Chemical Composition (wt.%)							Chemistry Control Factors		
	C	Si	Mn	P	S	Al	Mg	*CE* ** (%)	*K* ***	*Px* ****
I	3.32	2.48	0.50	0.04	0.011	0.014	0.045	4.11	0.89	2.35
II	3.20	2.55	0.38	0.013	0.015	0.014	0.032	4.03	0.90	1.94
III	3.65	3.15	0.10	0.013	0.004	0.002	0.049	4.60	1.38	0.47
IV	3.37	3.44	0.44	0.05	0.020	0.015	0.032	4.43	0.87	0.23
V	3.33	4.55	0.22	0.04	0.012	0.0054	0.035	4.65	1.59	1.72
VI	3.46	5.25	0.22	0.04	0.010	0.0065	0.045	5.05	1.66	1.52

* Pr—Experimental Program, ** *CE*—Equation (1); *** *K*—Equation (2); **** *Px*—Equation (3).

Table 3. Minor elements.

Pr *	Chemical Composition ** (wt.%)										
	Ti	As	Sn	Sb	Pb	Bi	V	Cu	Ni	Cr	Mo
I	0.013	0.003	0.004	0.001	0.0002	0.002	0.004	0.055	0.044	0.048	0.010
II	0.013	0.003	0.005	0.0009	0.0002	0.002	0.005	0.06	0.040	0.050	0.020
III	0.005	0.005	0.005	0.005	0.002	0.002	0.016	0.02	0.072	0.080	0.050
IV	0.0063	0.006	0.005	0.0015	0.0002	0.002	0.004	0.067	0.050	0.078	0.010
V	0.0067	0.019	0.015	0.040	0.003	0.001	0.008	0.17	0.10	0.050	0.070
VI	0.0073	0.020	0.013	0.019	0.004	0.0009	0.011	0.11	0.064	0.094	0.042

* Pr—Experimental Program, ** Other elements (wt.%): 0.004–0.015 Co, 0.002–0.006 Nb, 0.0002–0.008 W, 0.01–0.025 Zr, 0.0004–0.018 Ce, 0.0001–0.006 La, 0.004–0.016 Ca.

As chemistry control factors, carbon equivalent (*CE*, Equation (1)), antinodularizing factor (*K*, Equation (2)) [13] and pearlite promoting factor (*Px*, Equation (3)) [13] are considered.

$$CE = \%\,C + 0.3(\%\,Si + \%\,P) + 0.4(\%\,S) - 0.027(\%\,Mn) \quad (1)$$

$$K = 4.4(\%\,Ti) + 2.0(\%\,As) + 2.4(\%\,Sn) + 5.0(\%\,Sb) + 290(\%\,Pb) + 370(\%\,Bi) + 1.6(\%\,Al) \quad (2)$$

$$Px = 3(\%\ \mathrm{Mn}) - 2.65(\%\ \mathrm{Si} - 2) + 7.75(\%\ \mathrm{Cu}) + 90(\%\ \mathrm{Sn}) + 357(\%\ \mathrm{Pb}) + 333(\%\ \mathrm{Bi}) + 20.1(\%\ \mathrm{As}) + 9.60\ (\%\ \mathrm{Cr}) + 71.7(\%\ \mathrm{Sb}) \quad (3)$$

For 2.48–5.25% Si and 3.20–3.65% C, the experimental cast irons are characterized by a large range carbon equivalent *CE* = 4.03–5.05%: slightly hypo-eutectic position for conventional, non-Si alloyed cast irons (2.48–2.55% Si, 4.03–4.11% *CE*), hyper-eutectic position (*CE* = 4.43–4.60%) for a lower limit Si-alloyed cast irons (3.15–3.45% Si) and a strong hyper-eutectic behavior (*CE* = 4.65–5.05%) for the upper limit of Si-alloying ductile cast irons (4.55–5.25% Si). A residual magnesium level is typical for ductile cast irons (0.032–0.045% Mg_{res}), with a supplementary nodularization contribution of 0.0004–0.018% Ce_{res} and 0.0001–0.006% La_{res}.

Minor elements presence and content are typical for medium quality commercial ductile cast irons, characterized by an upper limit of antinodularizing factor *K*, Equation (2) (0.87–1.66). Equation (2) illustrates the influence and establishes a rank of some important elements, starting with aluminum (having the lowest detrimental effect), followed by tin and arsenic, titanium and antimony, up to the most hazardous elements, lead and bismuth. According to Thielman, in magnesium-treated irons, the complex antinodularizing factor *K* should not exceed 1.0 [13]. The presence of rare earth elements (Ce, La) in the final chemical composition is quite useful to counteract the negative effect of antinodularizing elements, as the *K* factor exceeds the 1.0 level [5].

Pearlite promoting factor *Px* (Equation (3)) is normally decreased by silicon content increasing, but it is increased by Mn and many minor elements, which could decrease or just counteract the silicon effect. According to the data in Tables 2 and 3, at the normal content of silicon (2.5% Si), cast irons are characterized by *Px* = 1.94–2.35, typically for ferritic-pearlitic cast irons. Higher silicon content for the second group (3.15–3.44% Si) and a lower level of minor elements leads to very low *Px* values (0.23–0.47), favorable for the ferritic structure. Despite the highest content of silicon (4.55–5.25% Si), the third group is characterized by an intermediate *Px* level (1.52–1.72), due to the higher incidence of presence of the minor elements. Then it could be concluded that the favorable effect of high silicon content in ferrite formation allows the tolerance of higher amounts of pearlite and carbide stabilizing elements in the chemical composition of the High-Si ductile cast irons [1,2,14,15].

3.2. Thermal (Cooling Curve) Analysis

The well-known Fe-C phase diagram is obtained in equilibrium conditions, with very pure materials, without minor elements, under vacuum melting and at very slow cooling rate (0.5–2.5 °C/min or 0.008–0.04 °C/s). On the contrary, the commercial cast irons solidified in non-equilibrium conditions in the foundry industry, as a result of the complex chemistry (usually more than 30 elements, see Tables 2 and 3), involving different charge materials and industrial melting procedures, with more than ten times higher castings solidification rate (>0.4 °C/s) [5,16].

As a result, the solidification process will be more complicated, strongly influenced by the cast iron chemical composition, characteristics of charge materials, melting parameters, metallurgical treatment applied to the molten iron, pouring parameters, castings characteristics, mold and core media, etc. Generally, the real Fe-C phase diagram is modified, in terms of representative temperatures and carbon concentration, while the solidification process is performed at a higher undercooling. Representative in this respect is the solidification cooling curve. A typical system of cooling curves [$T = f(t)$] and its first derivative [$dT/dt = f(t)$] is presented in Figure 2, referring to the Program I, Table 1.

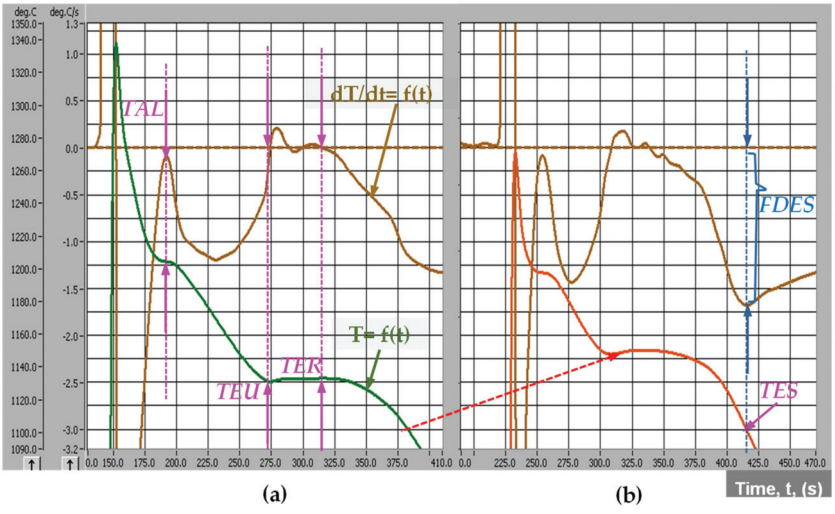

Figure 2. Typical cooling curves [T = f(t)] and their first derivative [dT/dt = f(t)] of un-inoculated (**a**) and inoculated (**b**) ductile cast irons (Program I, Table 1, *CE* = 4.11%) (*TAL*—temperature of austenitic liquidus; *TEU*—the lowest and *TER*—the highest eutectic temperatures; *TES*—temperature at the end of solidification; FDES—the lowest peak on the first derivative at the end of solidification).

The starting formation of the solid phase, as primary austenite, is clear marked by *TAL* (temperature of the austenitic liquidus) (Figure 2a), as a result of the heat released during austenite formation. It is corresponding to the zero level on the first derivative curve, and according to the hypo-eutectic position of this cast iron (*CE* = 4.11%). For hyper-eutectic cast irons, the primary graphite will be the first formed solid phase, corresponding to the *TGL*-temperature of the graphitic liquidus, usually less obvious on the cooling curve, due to the lower heat released during the graphite formation, comparing to the austenite.

TEU represents the lowest and *TER* the highest eutectic temperature on the cooling curve, both of them corresponding to zero level on the first derivative of the cooling curve (Figure 2a). Solid eutectic (austenite + graphite) formation means heat release, which could compensate for the lost heat; this process is usually expressed by a limited increasing temperature (from *TEU* up to *TER*), representing the eutectic recalescence. The temperature of the end of solidification (*TES*) corresponds to the lowest position of the first derivative at the end of solidification, *FDES* (Figure 2b).

Important information on the primary structure, especially expressed by carbides to graphite transition in the first part of eutectic reaction and on the results of the solidification of the last liquid iron in the areas between the eutectic cells (carbides, micro-shrinkage) could be obtained. This is possible if *TEU*, *TER* and *TES* parameters are reported to the eutectic equilibrium temperatures in graphitic (stable—T_{st}) and carbidic (metastable—T_{mst}) Fe-C systems. These temperatures have fixed values in the binary Fe-C system, but variable levels, depending on the presence, the content and the specific influence factor of other elements, which affect the carbon solubility in the liquid iron (Figure 3).

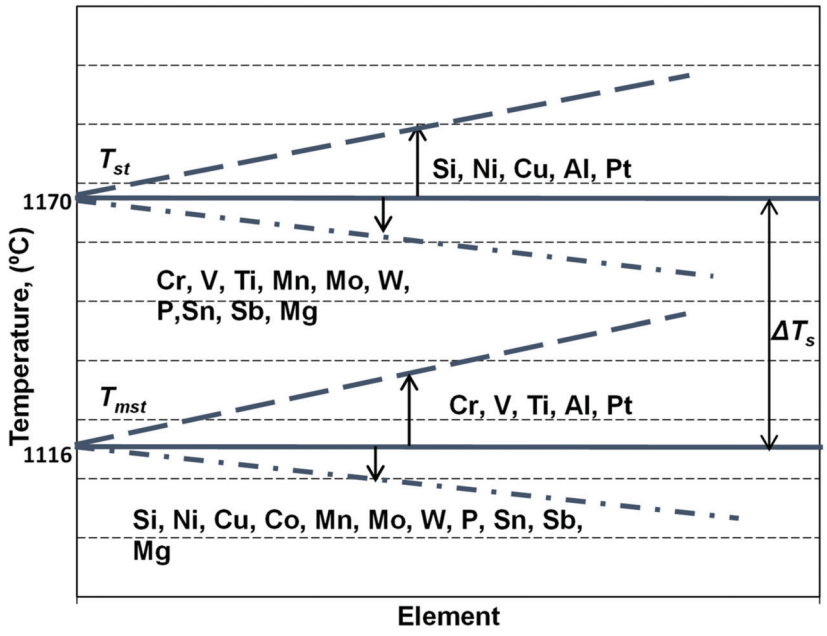

Figure 3. The influence of the chemical composition on the stable (T_{st}) and metastable (T_{mst}) eutectic temperatures in cast irons, as for the Fe-C-Si-*Xi* system alloys.

The simplest approach of a commercial cast iron is in a ternary system, as in the Fe-C-Si alloy, with silicon as an important influencing factor for T_{st} and T_{mst} evaluation, according to Equations (4) and (5) [17]. However, as the more realistic approach of a commercial cast iron is in the Fe-C-Si-*Xi* system, more complex equations, including the most important influencing elements in the chemical composition of commercial ductile cast irons are necessary, such as expressed by Equations (6) and (7) [18,19].

Recently [8] it was found that it is possible to have different values for T_{st} and T_{mst}, for a defined value of the silicon content. For this reason, T_{st} and T_{mst} parameters were calculated for both Fe-C-Si and Fe-C-Si-*Xi* systems, using the chemical composition included in Tables 2 and 3, by considering only silicon (S-series) and the full chemistry of the experimental cast irons (K-series) (Table 4, Figure 4).

Table 4. Calculated equilibrium eutectic temperatures T_{st} and T_{mst}.

Pr *	Si (%)	T_{st} (°C)		T_{mst} (°C)		$\Delta T_s = T_{st} - T_{mst}$ (°C)		ΔT_{st} (°C) (S–K)	ΔT_{mst} (°C) (S–K)
		S **	K ***	S	K	S	K		
I	2.48	1169.60	1151.80	1117.20	1106.60	52.40	45.20	17.80	10.60
II	2.55	1170.09	1153.40	1116.40	1106.70	53.69	46.70	17.55	9.70
III	3.15	1174.11	1161.03	1109.20	1105.01	64.91	56.02	13.08	4.19
IV	3.44	1176.05	1160.71	1105.72	1100.15	70.33	60.56	15.34	5.57
V	4.55	1183.49	1165.72	1092.40	1086.21	91.09	79.51	17.77	6.19
VI	5.25	1188.18	1169.17	1084.00	1079.11	104.18	90.06	19.01	4.89

* Pr—Experimental Program, ** *S*—Equations (4) and (5); *** *K*—Equations (6) and (7).

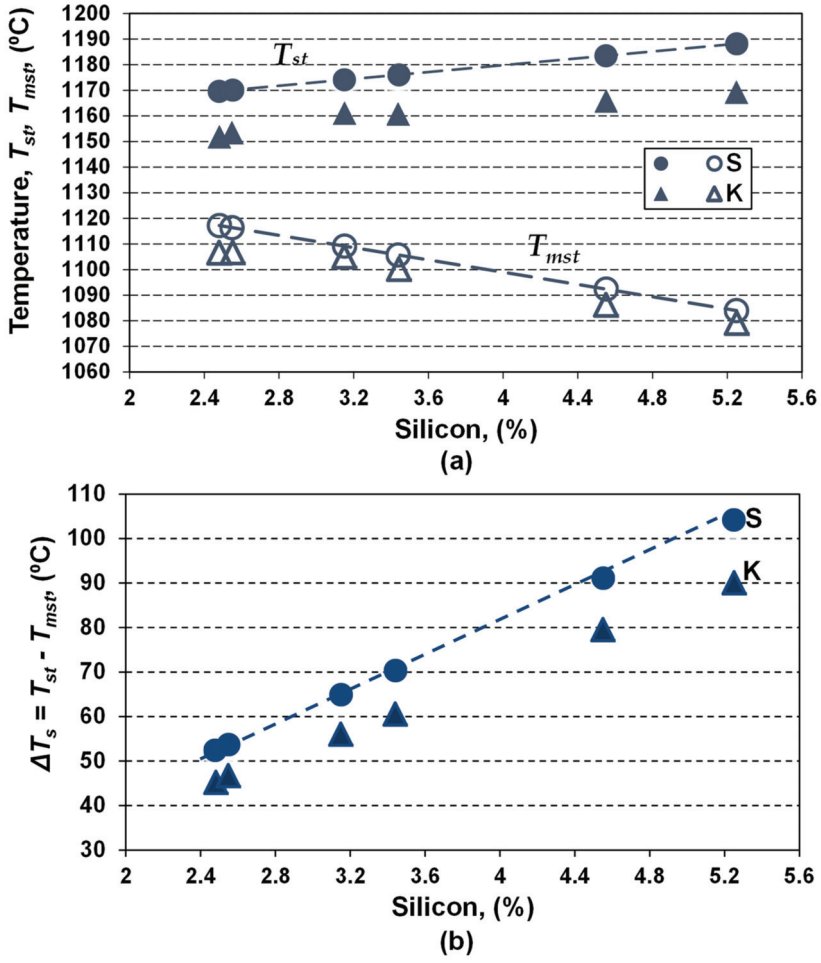

Figure 4. Influence of Si content on the T_{st} and T_{mst} eutectic temperatures (**a**) and the eutectic interval ΔT_s (**b**), for only Si effect (series S, Equations (4) and (5)) and complex chemical composition (series K, Equations (6) and (7)).

Silicon appears to have the most important effect, leading to the increasing of T_{st} and decreasing of T_{st} temperatures, and, consequently, enlarging the T_{st}–T_{mst} (ΔT_s) interval two times, as silicon increased from 2.5% up to 5.25% (series S).

For the real chemistry (series K), characterized by a multitude of elements, silicon remains the main influencing factor, but the results are affected by the presence of other elements.

$$T_{st} = 1153\ (^{\circ}C) + 6.7\ (\%\ Si) \quad (4)$$

$$T_{mst} = 1147\ (^{\circ}C) - 12\ (\%\ Si) \quad (5)$$

$$T_{st[TEG]} = 1149.1\ (^{\circ}C) + 4.7\ (\%\ Si) - 4.0\ [\%Sol.\ Mn] - 44\ (\%\ P) + 2.7\ (\%\ Cu) + 1.0\ (\%\ Ni) + 1.8\ (\%\ Co) + 13.9\ (\%\ Al) - 17.7\ (\%\ Mo) - 10.5\ (\%\ Cr) - 9.3\ (\%\ Sn) - 5.2\ (\%\ Sb) - 6.1\ (\%\ W) - 3.7\ (\%\ Nb) - 14.8\ (\%\ V) - 80.3\ (\%\ B) \quad (6)$$

$$T_{mst[TEC]} = 1142.6\ (^{\circ}C) - 11.6\ (\%\ Si) - 0.75\ [\%\ Sol.\ Mn] - 46.2\ (\%\ P) - 1.4\ (\%\ Cu) - 1.1\ (\%\ Ni) - 0.7\ (\%\ Co) - 1.8\ (\%\ Al) - 14.5\ (\%\ Mo) + 5.9\%\ Cr) - 6.0\ (\%\ Sn) - 5.1\ (\%\ Sb) - 2.8\ (\%\ W) + 0\ (\%\ Nb) + 3.3\ (\%\ V) - 26.0\ (\%\ B) \quad (7)$$

The base and minor elements affect the equilibrium eutectic temperatures, much more in the Fe-C-Si-*Xi* stable system (T_{st}, 15–20 °C) than in the metastable system (T_{mst}, 5–10 °C), comparing with their calculation as only the Si effect (Fe-C-Si), where the highest values resulted. It is found that if the pearlite formation potential is higher, as effects of Mn and some minor elements (Cu, Sn, Pb, Bi, As, Cr, Sb), the higher is the affectation of T_{st} and T_{mst}, obtained only as a Si effect. Factors of the cumulative effects of the base and minor elements, used to offer useful information such as on pearlite promoting (*Px*, Equations (4) and (5)) or on antinodularizing action (*K*, Equations (6) and (7)) (Tables 2 and 3) appear to also offer information on the T_{st} and T_{mst} affectation. Figure 5 shows the effect of *Px* (Figure 5a) and *K* (Figure 5b) on the difference between equilibrium temperatures in a stable system ($\Delta T_{st(S\text{-}K)} = T_{st(S)} - T_{st(K)}$) and a metastable system ($\Delta T_{mst(S\text{-}K)} = T_{mst(S)} - T_{mst(K)}$), calculated in *S* (only Si effect) and *K* (full chemistry effect) series.

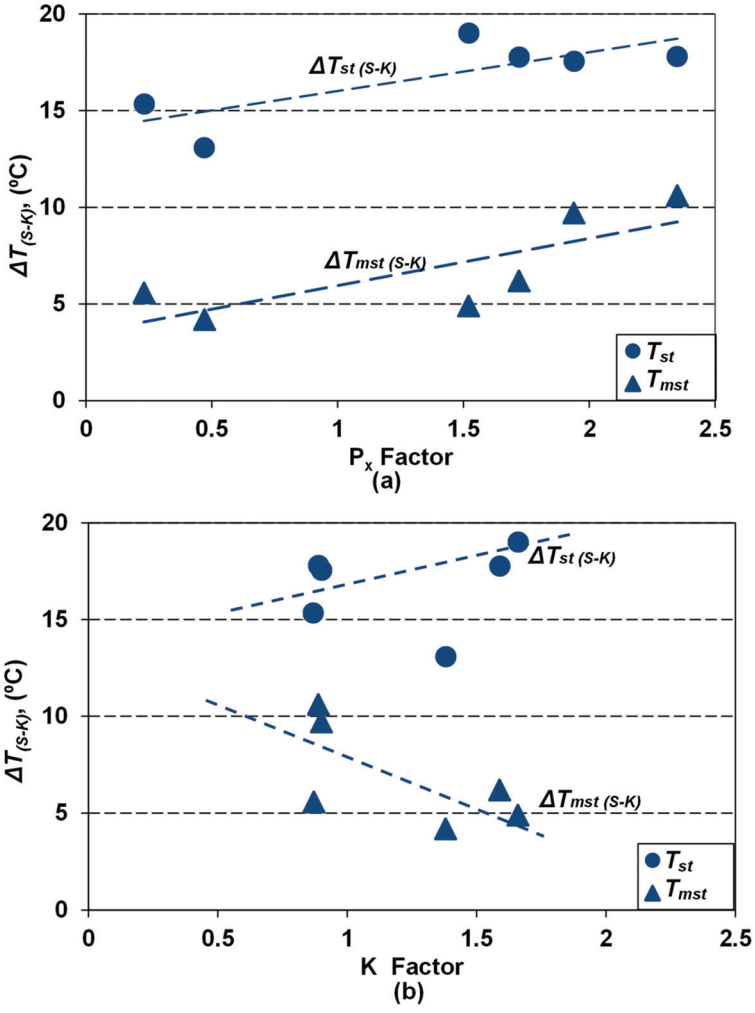

Figure 5. Influence of pearlite promoting factor *Px* (**a**) and antinodularizing factor *K* (**b**) on the difference between equilibrium eutectic temperatures ($\Delta T_{st(S\text{-}K)}$, $\Delta T_{mst(S\text{-}K)}$) calculated only as Si influence (S series) and full chemistry (K series).

Elements promoting pearlite, with a cumulative effect expressed by the *Px* factor, act to increase the difference between both the considered eutectic temperatures ($T_{(S-K)}$), practically with the same power. The $\Delta T_{(S-K)}$ factor for high purity cast iron ($Px < 0.5$) reached 4–5 °C for T_{mst} and 13–15 °C for T_{st}, but it will reach 10 °C for T_{mst} and 20 °C for T_{st}, for $Px > 2.0$, respectively.

Elements known with an antinodularizing action, with a cumulative effect expressed by the *K* factor, have different effects on the considered eutectic temperatures (Figure 5b). Factor $\Delta T_{mst(S-K)}$ decreases (from 5–10 °C up to 4–5 °C) by transition from medium pure cast iron ($K < 1.0$) to lower purity cast iron ($K = 1.5–2.0$). The $\Delta T_{st(S-K)}$ factor has an un-conclusive evolution.

Table 5 summarizes the results obtained in thermal (cooling curve) analysis, as selected representative temperatures on the cooling curve, characteristics to the eutectic reaction and the end of solidification, and the undercooling degrees referring to the stable and metastable equilibrium eutectic temperatures, as effects of silicon alloying and inoculation application.

Table 5. Representative parameters of thermal (cooling curve) analysis.

Pr *	Si (%)	Iron	*TEU* (°C)	*TER* (°C)	*TES* (°C)	ΔT_m (°C)	ΔT_1 (°C)	ΔT_2 (°C)	ΔT_3 (°C)	ΔTEU (°C)	ΔTES (°C)
I	2.48	UI ** Inoc ***	1128.4 1142.4	1129.9 1145.1	1050.9 1087.5	23.4 9.4	21.8 35.8	23.3 38.5	−55.7 −19.1	14.0	36.6
II	2.55	UI Inoc	1136.6 1145.8	1136.8 1147.7	1050.4 1097.6	16.8 7.6	28.9 39.1	30.1 41.0	−56.3 −9.1	9.2	47.2
III	3.15	Inoc	1144.53	1156.01	1107.17	16.5	39.52	51.0	2.16		
IV	3.44	UI Inoc	1138.34 1145.97	1141.16 1150.07	1089.03 1098.17	22.37 14.74	38.19 45.82	41.01 49.92	−11.1 −1.98	7.63	9.14
V	4.55	UI Inoc	1156.1 1157.9	1156.6 1158.6	1104.4 1106.7	9.62 7.82	69.89 71.69	70.39 72.39	18.9 20.5	1.8	2.3
VI	5.25	UI Inoc	1156.7 1157.3	1158.9 1158.9	1106.2 1106.5	12.47 11.87	77.59 78.19	79.79 79.79	27.09 27.39	0.6	0.3

* Pr—Experimental Program, ** UI—non-inoculation; *** Inoc—inoculation.

Figure 6 shows the influence of the silicon content and applied inoculation on the representative temperatures characterizing the eutectic formation and the end of solidification, showing: the lowest eutectic reaction temperature (*TEU*), the highest (recalescence) eutectic reaction temperature (*TER*), and the temperature of the end of solidification (*TES*).

Both the silicon content and the inoculation act as favorable influencing factors by increasing all these temperatures, but at different powers depending on the considered temperature and the silicon alloying grade in ductile cast irons, respectively.

Increasing the silicon content from 2.5% up to 5.25% in the present experimental programs leads to increasing the representative temperatures, in both non-inoculated and inoculated ductile cast irons (UI/Inoc): *TEU* (from 1128.4 °C to 1156.7 °C/from 1142.4 to 1157.9°C), *TER* (from 1129.9 °C to 1158.9 °C/from 1145.1 °C to 1158.9 °C) and *TES* (from 1050.4 °C to 1106.2 °C/from 1097.5 °C to 1106.7 °C). The power of increasing the silicon is higher in less than 4.0% Si comparing with the highest silicon content range.

The highest effect of inoculation is visible in non-Si alloyed cast irons (2.5% Si): ΔTEU = 9–14 °C, ΔTER = 11–15 °C and is 3 to 4 four times higher for *TES* (ΔTES = 37–47 °C). For the low level silicon alloying grade (3.15–3.45% Si) beneficial inoculation effect, expressed by temperatures increasing, it is reduced at 7 °C order for *TEU* and *TER* and 9 °C for *TES*, respectively. The highest alloying grade (4.55–5.25% Si) ductile cast irons are characterized by the lowest contribution of inoculation, expressed by ΔTEU = 0.6–1.8 °C, ΔTER = 0–2 °C and ΔTES = 0.3–2.3 °C.

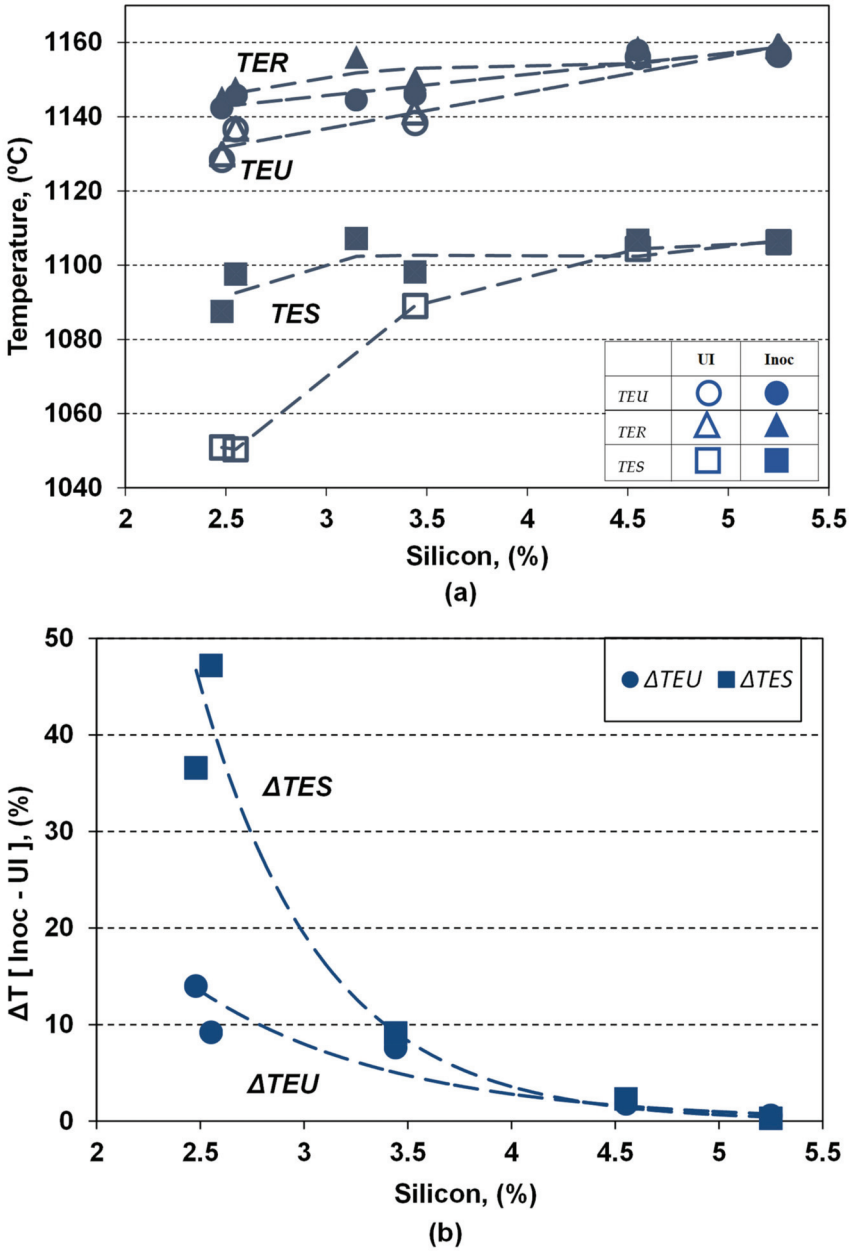

Figure 6. Influence of the silicon content and inoculation on the *TEU*, *TER* and *TES* temperatures (**a**) and the difference between the inoculated and non-inoculated ductile cast irons (Δ*TEU*, Δ*TES*) (**b**).

The representative temperatures *TEU*, *TER* and *TES* could offer useful information especially if they are compared with equilibrium eutectic temperatures, in a stable (graphitic) system T_{st} and in a metastable (carbidic) system T_{mst}. Positions of these temperatures referring to the T_{st}–T_{mst} interval are expressed by a specific undercooling degree.

The most important parameters are illustrated by Equations (8)–(11):

$$\Delta T_m = T_{st} - TEU \quad (8)$$

$$\Delta T_1 = TEU - T_{mst} \quad (9)$$

$$\Delta T_2 = TER - T_{mst} \quad (10)$$

$$\Delta T_3 = TES - T_{mst} \quad (11)$$

The highest eutectic undercooling ΔT_m, as the difference between stable equilibrium eutectic temperature T_{st} and the lowest temperature level on the cooling curve *TEU* offers information on the real undercooling necessary for starting the eutectic reaction. Generally, the higher ΔT_m is, the higher is the possibility to form free carbides in the first stage of solidification. But the certitude of the free carbides formation, in specific solidification conditions, could be obtained only if this parameter is higher than the $\Delta T_s = T_{st}–T_{mst}$ interval.

This means that the eutectic reaction will start below T_{mst} with carbides formation, but without information on the end of the eutectic reaction, when the temperature increased, due to the heat released as solid eutectic formation. Also, no information on it is happened at the end of solidification, in non-equilibrium conditions, specifically for iron castings production in the foundry industry.

Information on these important characteristics of the cast iron solidification could also be obtained by comparing *TEU*, *TER* and *TES* with T_{mst}, resulting in an undercooling degree ΔT_1, ΔT_2 and ΔT_3, respectively. As free carbides could be formed only if the eutectic reaction temperatures are lower than T_{mst}, and graphite is promoted if these temperatures are above T_{mst}, negative values mean carbides and positive values mean graphite, at the beginning of the eutectic reaction (ΔT_1) and at the end of this reaction (ΔT_2), respectively.

Total graphitic structure is illustrated by positive values and total carbidic structure (white cast iron) by negative values, for both ΔT_1 and ΔT_2 parameters. Mottled cast iron is characterized by carbides formation at the beginning of the eutectic reaction (ΔT_1 is negative) and graphite at the end of eutectic reaction (ΔT_2 is positive). The sensitiveness of iron castings to form undesirable defects at the end of solidification, such as free carbides and micro-shrinkage in the areas between eutectic cells is expressed by the ΔT_3 undercooling degree: the higher (more negative) is ΔT_3, the higher is the occurrence of these undesirable events.

Figure 7 shows the variation of the representative undercooling degrees, reporting to T_{st} (ΔT_m) and T_{mst} (ΔT_1, ΔT_2, ΔT_3) as effect of silicon content and inoculation application. Silicon favors the increasing of T_{st} and decreasing of T_{mst} ($\Delta T_s = T_{st}–T_{mst}$ enlargement) (Figure 4), and, at the same time, the increasing of *TEU*, *TER* and *TES* parameters (Figure 6). As a result, the undercooling behavior during solidification will be influenced by both of these effects. T_{st} and T_{mst} are considered to be the effects of all the identified elements in the final chemical composition of tested ductile cast irons (K series), including not only silicon influence, but also the complex behavior of the other elements (Figure 2).

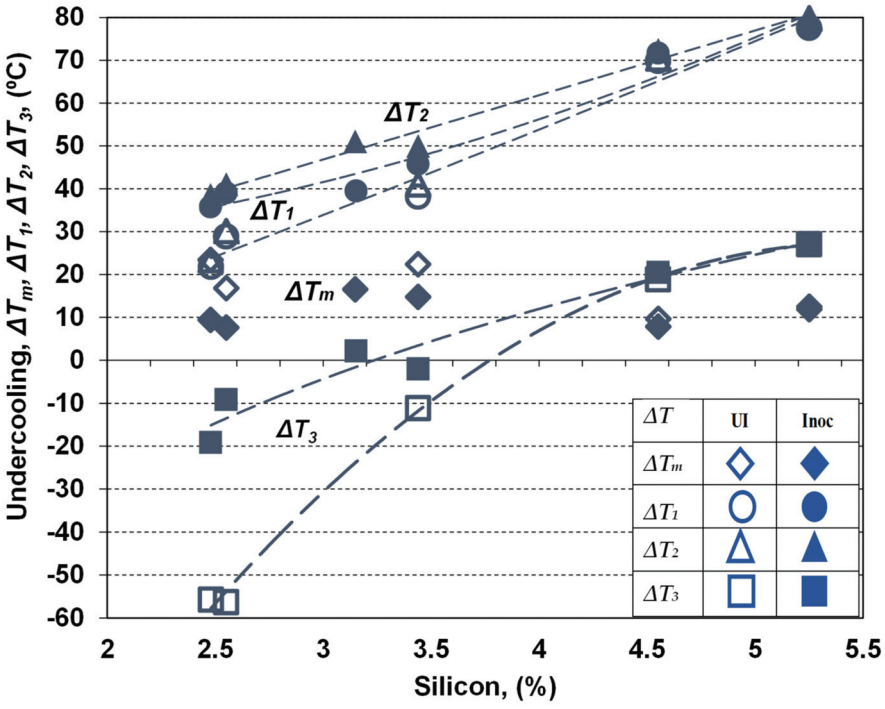

Figure 7. The variation of representative undercooling degrees, reporting to T_{st} (ΔT_m) and T_{mst} (ΔT_1, ΔT_2, ΔT_3) as the effect of silicon content and inoculation application.

Generally, silicon contributes to ΔT_m decreasing and ΔT_1, ΔT_2 and ΔT_3 (less negative) increasing, with supplementary positive contribution of inoculation in the same direction. The highest undercooling degrees characterize the non-Si alloyed ductile cast irons (2.5% Si), while the silicon alloying leads to decreasing the undercooling degrees, on the entire solidification time, but in a different way for eutectic reaction and at the end of solidification, and for non-inoculated and inoculated Mg-treated cast irons, respectively.

The lower limit of Si-alloyed cast irons (3.15–3.45% Si) are characterized by 1.4–1.6 times higher eutectic undercooling, with 2–3 times beneficial effects for the higher silicon level (4.55–5.25% Si). The positive effect of silicon alloying is higher for non-inoculated cast irons, and especially at the end of solidification.

Inoculation has an important contribution to reduce the undercooling degree; ΔT_m reached a lower level and ΔT_1, ΔT_2 and ΔT_3 reached a higher level, respectively. From this point of view, this metallurgical treatment is very important for the non-Si alloyed ductile cast irons; it is visible for less than 3.5% Si (medium range), but with only a small contribution for more than 4.5% Si.

A special remark for the undercooling at the end of solidification (ΔT_3): it becomes positive for more than 4% Si non-inoculated and 3.2% Si inoculated ductile cast irons.

The cumulative effects of silicon alloying and inoculation could also be expressed by the ratio between the highest eutectic undercooling reporting to the stable eutectic temperature (ΔT_m) and the eutectic interval in stable and metastable systems, $\Delta T_s = T_{st} - T_{mst}$ (Figure 8). This ratio is at the 0.4–0.5 level for non-inoculated and 0.15–0.20 for inoculated, 2.5% Si ductile cast irons, but it is decreased up to 0.12–0.14 and 0.10–0.13, respectively, for the highest silicon content.

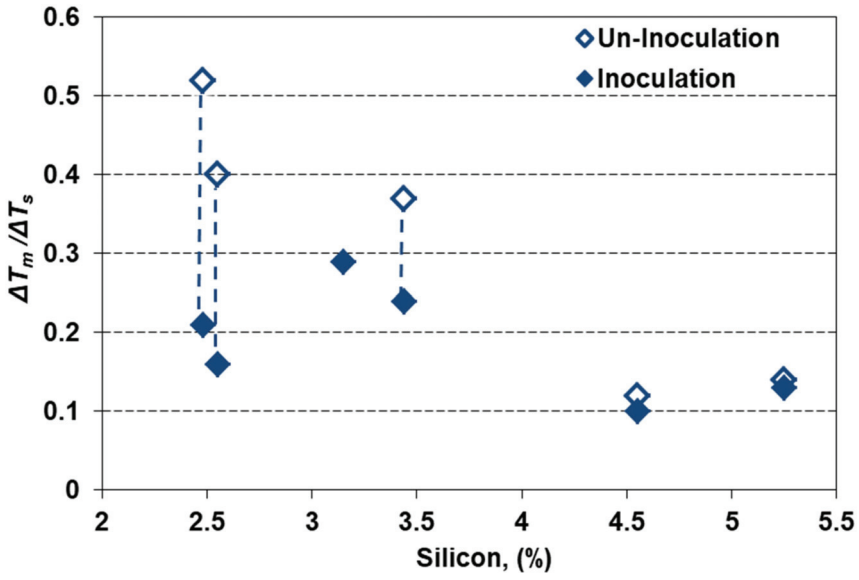

Figure 8. The cumulative effects of silicon alloying and inoculation on the eutectic undercooling level.

Generally, the $\Delta T_m/\Delta T_s$ ratio is strongly affected by inoculation for less than 3.5% Si, but at a lower level, and less affected by inoculation for more than 4.5% Si. The 2.5–3.5% Si ductile cast irons are more sensitive to high solidification undercooling (but with a higher efficiency of inoculation), comparing to 4.5–5.5% Si cast irons, at a lower undercooling level (but also at a lower inoculation effect). In high Si-ductile cast irons (especially for more than 4% Si) the main objective of inoculation is not carbides avoiding, but the improvement of the nodular graphite compactness degree (affected by Si) [2,11,20].

It was found that the solidification time has a significant effect on the microstructure and mechanical properties of solution strengthened ferritic ductile iron. In particular, it has been found that with increasing solidification times, the microstructure becomes coarser and the presence of defects increases. Moreover, the lower the cooling rate, the lower the measured tensile and fatigue properties [21]. A recent work [22] found that the melt quality is closely associated with the resultant morphology and number of austenite dendrites, graphite nodules, and matrix structure, in thin-walled ductile iron castings.

4. Conclusions

The present paper evaluates by a thermal (cooling curve) analysis the solidification pattern of ductile cast irons, non-Si alloyed (<3.0% Si), low (3.0–3.5% Si) and medium Si alloyed (4.5–5.5% Si), as silicon content increases and inoculation is applied with simultaneous effects. The following conclusions could be drawn.

- Chemical analysis focuses not only on the base elements but also on the minor elements, such as their cumulative effects such as the pearlite formation sensitiveness, antinodularizing action and on the values of eutectic temperatures in stable (graphitic) and metastable (carbidic) Fe-C-Si-*Xi* systems.
- Silicon is an important influencing factor, but the base and minor elements affect the equilibrium eutectic temperatures, inclusively at high Si-content, much more in the Fe-C-Si-*Xi* stable system (ΔT_{st} = 15–20 °C) than in the metastable system (ΔT_{mst} = 5–10 °C), comparing their calculations with only the Si effect (Fe-C-Si system), where the highest values resulted.
- It is found that higher is the pearlite formation potential (*Px*), the higher is the affectation of T_{st} and T_{mst}, obtained only as a Si effect: from 4–5 °C for T_{mst} and 13–15 °C

for T_{st} in high purity cast iron ($Px < 0.5$) up to 10 °C for T_{mst} and 20 °C for T_{st}, for $Px > 2.0$.

- Elements known to have an antinodularizing action, with cumulative effect expressed by K factor, decrease T_{mst} (from 5–10 °C up to 4–5 °C) by transition from a medium pure cast iron ($K < 1.0$) to a lower purity cast iron ($K = 1.5–2.0$), without a conclusive evolution for T_{st}.
- Both Si-content and inoculation act as favorable influencing factors, by increasing the representative temperatures and decreasing the undercooling degrees for the eutectic reaction and at the end of solidification, but at a different power depending on the considered temperature and the Si-alloying grade.
- The highest positive effect of inoculation is visible in non-Si alloyed cast irons (2.5% Si): 9–15 °C for the eutectic reaction and 3 to 4 times increased at the end of solidification (37–47 °C). Increased Si content decreases the inoculation power to 7–9 °C for a low alloying grade (up to 3.5% Si), with the lowest contribution at more than 4.5% Si (0.3–2.0 °C).
- Si favors increasing of the eutectic interval (T_{st}–T_{mst}), and, at the same time, the increasing of temperatures for the eutectic reaction and, at the end of solidification, with other elements contribution, as well. As a result, the undercooling behavior during solidification will be influenced by both effects.
- The highest undercooling characterizes the non-Si alloyed cast irons, while the lower limit of Si-alloyed cast irons are characterized by 1.4–1.6 times lower eutectic undercooling, with 2–3 times higher beneficial effect for the higher Si level. The positive effect of Si-alloying is higher for non-inoculated cast irons, and especially at the end of solidification.
- Inoculation has an important contribution to reduce the undercooling degree, being very important for the non-Si alloying, visible for less than 3.5% Si, but with only a small contribution for more than 4.5% Si. A special remark for the undercooling at the end of solidification, which becomes positive for more than 4% Si non-inoculated and 3.2% Si inoculated ductile cast irons.
- 2.5–3.5% Si ductile cast irons are more sensitive to high solidification undercooling (but with a higher efficiency of inoculation), comparing to 4.5–5.5% Si cast irons, at a lower undercooling level (but also at a lower inoculation effect). In high Si-ductile cast irons (especially for more than 4% Si) the main objective of inoculation is not carbides avoiding, but the improvement of the nodular graphite compactness degree (affected by Si). This could be important especially in the furan resin molding technique, where Sulphur in P-toluenesulphonic acid (PTSA), usually is used as the hardener, has been identified as an important factor causing graphite degeneration [23].

Author Contributions: I.S., D.A., S.S. and I.R. contributed equally in conceiving, designing and performing the experiments; analyzing the data; and writing the paper. All authors have read and agreed to the published version of the manuscript.

Funding: This research received no external funding.

Data Availability Statement: Not applicable.

Conflicts of Interest: The authors declare no conflict of interest.

References

1. Stets, W.; Loblich, H.; Gassner, G.; Schumacher, P. Solution Strengthened Ferritic Ductile Cast Iron According DIN EN1563:2012–Properties, Production and Application. In Proceedings of the "Keith Millis" Symposium on Ductile Iron, Nashville, TN, USA, 15–17 October 2013; pp. 283–292.
2. Stan, S.; Riposan, I.; Chisamera, M.; Barstow, M. Solidification Pattern of Silicon Alloyed Ductile Cast Irons. In Proceedings of the 122nd AFS Metalcasting Congress, Fort Worth, TX, USA, 3–5 April 2018; pp. 18–22.
3. EN 1563 Founding—Spheroidal Graphite Cast Irons. Available online: https://www.en-standard.eu/csn-en-1563-founding-spheroidal-graphite-cast-irons/ (accessed on 13 March 2021).

4. Automotive Ductile Iron Castings for High Temperature Applications J2582_200406. Available online: https://www.sae.org/standards/content/j2582_200406/ (accessed on 13 March 2021).
5. Riposan, I.; Skaland, T. Modification and Inoculation of Cast Iron. In *Cast Iron Science and Technology Handbook*; Stefanescu, D.M., Ed.; American Society of Materials: Materials Park, OH, USA, 2017; pp. 160–176.
6. Stefanescu, D.M. Thermal Analysis-Theory and Applications in Metalcasting. *Int. J. Metalcasting* **2015**, *9*, 7–22. [CrossRef]
7. Sparkman, D. Microstructure by Thermal Analysis. *AFS Trans.* **2011**, *119*, 413–419.
8. Cojocaru, A.M.; Riposan, I.; Stan, S. Solidification Influence in the Control of Inoculation Effects in Ductile Cast Irons by Thermal Analysis. *J. Therm. Anal. Calorim.* **2019**, *138*, 2131–2143. [CrossRef]
9. Anca, D.; Chisamera, M.; Stan, S.; Stan, I.; Riposan, I. Sulfur and Oxygen Effects on High-Si Ductile Iron Casting Skin Formation. *Coatings* **2020**, *10*, 618. [CrossRef]
10. Anca, D.; Chisamera, M.; Stan, S.; Riposan, I. Graphite Degeneration in High Si, Mg-Treated Iron Castings—Sulfur and Oxygen Addition Effects. *Int. J. Met.* **2019**, *14*, 663–671. [CrossRef]
11. Riposan, I.; Stefan, E.; Stan, S.; Pana, N.R.; Chisamera, M. Effects of Inoculation on Structure Characteristics of High Silicon Ductile Cast Irons in Thin Wall Castings. *Metals* **2020**, *10*, 1091. [CrossRef]
12. QuiK-Cup®QuiK-Lab®E Thermal Analysis of Cast Iron. Available online: https://www.heraeus.com/media/media/hen/media_hen/products_hen/iron/QuikLabE_QuikCup_EN_lowres.pdf (accessed on 13 March 2021).
13. Thielemann, T. Zur Wirkung van Spurenelementen in Gusseisen mit Kugelgraphit [Effects of trace elements in nodular graphite cast irons]. *Giessereitechnik* **1970**, *16*, 16–24.
14. Dommaaschk, C. Chances and Limits of High Silicon Ductile Iron. In Proceedings of the WFO Technical Forum, Gauteng, Africa, 14–17 March 2017.
15. Hammersberg, P.; Hamberg, K.; Bjorkegren, L.E.; Lindkvist, J.; Borgstrom, H. Sensitivity to Variation of Tensile Properties of High Silicon Ductile Iron. *Mater. Sci. Forum* **2018**, *925*, 280–287. [CrossRef]
16. Zhou, J. Colour Metallurgy of Cast Iron. *China Foundry* **2009**, *6*, 57–69.
17. Sillen, R.V. Novacast Technologies. 2006. Available online: www.novacast.se (accessed on 10 December 2006).
18. Kanno, T.; Iwami, Y.; Kang, I. Prediction of Graphite Nodule Count and Shrinkage Tendency in Ductile Cast Iron With 1 Cup Thermal Analysis. *Int. J. Metalcast.* **2017**, *11*, 94–100. [CrossRef]
19. Kanno, T.; Fukuda, Y.; Morinaka, M.; Nakae, H. Effect of Alloying Elements on Graphite and Cementite Eutectic Temperature of Cast Iron. *J. JFS.* **1998**, *70*, 465–470.
20. Stan, S.; Riposan, I.; Chisamera, M.; Stan, I. Solidification Characteristics of Silicon Alloyed Ductile Cast Irons. *J. Mater. Eng. Perform.* **2019**, *28*, 278–286. [CrossRef]
21. Borsato, T.; Ferro, P.; Berto, F.; Carollo, C. Effect of Solidification Time on Microstructural, Mechanical and Fatigue Properties of Solution Strengthened Ferritic Ductile Iron. *Metals* **2019**, *9*, 24. [CrossRef]
22. Gorny, M.; Kawalec, M.; Sikora, G.; Olejnik, E.; Lopez, H. Primary Structure and Graphite nodules in Thin-Walled High-Nickel Ductile Iron Castings. *Metals* **2018**, *8*, 649. [CrossRef]
23. Ivan, N.; Chisamera, M.; Riposan, I. Graphite Degeneration In the Surface Layer of Ductile Iron Castings. *Int. J. Cast Met. Res.* **2013**, *26*, 138–142. [CrossRef]

metals

MDPI

Article

Microstructural Evolution as a Function of Increasing Aluminum Content in Novel Lightweight Cast Irons

Alejandro Obregon [1,*], Jon Mikel Sanchez [1,*], David Eguizabal [1,*], Jose Carlos Garcia [1], Gurutze Arruebarrena [2], Iñaki Hurtado [2], Ion Quintana [3] and Patxi Rodriguez [3]

[1] TECNALIA, Basque Research and Technology Alliance (BRTA), 48160 Derio, Spain; josecarlos.garcia@tecnalia.com
[2] Faculty of Engineering, Mondragon Unibertsitatea, 20500 Arrasate/Mondragon, Spain; garruebarrena@mondragon.edu (G.A.); ihurtado@mondragon.edu (I.H.)
[3] Materials & New Technologies, Fagor Ederlan Group, EDERTEK Technology Centre, Fagor Ederlan Group, 20500 Arrasate/Mondragon, Spain; i.quintana@edertek.es (I.Q.); p.rodriguez@edertek.es (P.R.)
* Correspondence: alejandro.obregon@tecnalia.com (A.O.); jonmikel.sanchez@tecnalia.com (J.M.S.); david.eguizabal@tecnalia.com (D.E.)

Abstract: In the context of the development of new lightweight materials, Al-alloyed cast irons have a great potential for reducing the weight of the different part of the vehicles in the transport industry. The correlation of the amount of Al and its effect in the microstructure of cast irons is not completely well established as it is affected by many factors such as chemical composition, cooling rate, etc. In this work, four novel lightweight cast irons were developed with different amounts of Al (from 0 wt. % to 15 wt. %). The alloys were manufactured by an easily scalable and affordable gravity casting process in an induction furnace, and casted in a resin-bonded sand mold. The microstructural evolution as a function of increasing Al content by different microstructural characterization techniques was studied. The hardness of the cast irons was measured by the Vickers indentation test and correlated with the previously characterized microstructures. In general, the microstructural evolution shows that the perlite content decrease with the increment of wt. % of Al. The opposite occurs with the ferrite content. In the case of graphite, a slight increment occurs with 2 wt. % of Al, but a great decrease occurs until 15 wt. % of Al. The addition of Al promotes the stabilization of ferrite in the studied alloys. The hardness obtained varied from 235 HV and 363 HV in function of the Al content. The addition of Al increases the hardness of the studied cast irons, but not gradually. The alloy with the highest hardness is the alloy containing 7 wt. % Al, which is correlated with the formation of kappa-carbides and finer perlite.

Keywords: cast iron; microstructure; casting; modelling; light-weighting; hardness

Citation: Obregon, A.; Sanchez, J.M.; Eguizabal, D.; Garcia, J.C.; Arruebarrena, G.; Hurtado, I.; Quintana, I.; Rodriguez, P. Microstructural Evolution as a Function of Increasing Aluminum Content in Novel Lightweight Cast Irons. *Metals* **2021**, *11*, 1646. https://doi.org/10.3390/met11101646

Academic Editor: Cristiano Fragassa

Received: 15 September 2021
Accepted: 14 October 2021
Published: 18 October 2021

1. Introduction

Weight reduction has become an important element to reduce greenhouse gas emissions in the transport industry. A great deal of effort is being made in the development of novel materials with improved mechanical and/or physical properties, with light weight as the main goal. The transport industry depends on the development of new lightweight materials to optimize the fuel consumption of the next generation of vehicles. Therefore, with the goal of complying with global vehicle emissions regulations, the research focus is on the development of new materials to replace traditional alloys for reducing energy consumption and, thereby, gas emissions (NOx, CO_2, etc.). In addition, new materials should not compromise structural properties, or contribute to significant cost increases. In this way, novel materials such as complex concentrated alloys, medium/high entropy alloys, aluminum-based hybrid composites, etc. has been developed in the last years [1–5].

As steels are alloys mainly formed by one of the most abundant elements in the Earth's crust, and the most used engineering alloys; the development of new lightweight steels

have become a hot topic in materials science. Hence, novel lightweight steels with improved specific strength and/or ductility have been developed, by alloying light elements such as Al or Si [6–12]. On the other hand, few investigations have been carried out to develop novel lightweight cast irons. To date, the strategy most employed is to develop high-strength lightweight cast irons by alloying a large amount of Al. Approximately, the density of traditional cast irons can be decreased to a value below 7 g/cm^3 by alloying ~5 wt. % Al and near 6 g/cm^3 by alloying ~15 wt. % Al [13,14]. In addition, cast irons meet one of the previously mentioned requirements for light weighting at a reasonable cost. Depending on its concentration, the introduction of Al in cast iron has a significant effect on the microstructure of the alloy, as well as on the mechanical properties [15].

Some research has been done to correlate the amount of Al and its effect in the microstructure. The correlation of the amount of Al and its effect in the microstructure of cast irons is not completely well established as it is affected by many factors such as chemical composition, cooling rate, inoculation and melting treatments [16,17]. For example, Ibrahim et al. [18] concluded that increasing Al content within a certain range up to 4 wt. % facilitated the cast iron graphitization, but its further increase suppressed the graphite precipitation and promoted the formation of carbides. On the other hand, Gumienny et al. [19] concluded that Al with a concentration of up to 2.4 wt.% in compacted graphite iron exhibits graphitizing properties, above this concentration it is a carbide-forming element. In the same research, it was also pointed out that with an Al content higher than 8 wt. % the $AlFe_3C_{0.5}$ carbide is precipitated, and that a concentration higher than 3.1 wt. % of Al causes carbide spheroidization in the eutectoid mixture, replacing cementite by κ-carbides (kappa-carbides). Shayesteh-Zeraati et al. [20] studied Al-alloyed ductile cast iron containing 0.48 wt. %, 4.88 wt. % and 6.16 wt. % Al. The results showed that increasing the Al content leads to the decrease of free ferrite and carbides, as well as an increase in the pearlite volume fraction. In the same research, also was reported that increasing the Al content, more intermetallic compounds (Al_6Fe, $AlFe_3C_{0.5}$, Fe_3Al and FeAl) were stabilized.

The complexity of the metallurgy of lightweight cast irons is not only due to the addition of Al, but also to other secondary elements such as Si. For example, Si is well known as an important influencing factor in the solidification of ductile cast irons [21]. As the addition of Al promotes the graphitization of the alloy, Si is employed to avoid metastable iron carbide solidification in gray cast iron [21]. In addition, Kasvayee et al. [22] showed that graphite content, graphite nodule count and ferrite fraction were increased by increasing the Si content, resulting in an increase in yield strength.

Although the aforementioned metallurgical complexity of lightweight cast irons, several benefits have been reported in the mechanical and physical properties, especially in terms of hardness, which is the most studied property. Takamori et al. [23] studied several Al-alloyed cast irons with 3.2 wt. % C, from 1.6 wt. % to 2.4% Si, and from 0 wt. % to 20 wt. % Al. It was concluded that the addition of 12 wt. % of Al improved wear resistance due to the precipitation of carbides but deteriorated the damping capacity. Furthermore, the addition of over 6 wt. % of Al improved the heat resistance, and a content over 20 wt. % produced non-magnetic anticorrosion alloys. The wear resistance also was improved by increasing the Al content in ductile irons, specifically in the alloys containing 2.29 wt. %, 3.02 wt. %, and 3.74 wt. % Al [24]. Ibrahim et al. [18] studied the hardness, oxidation resistance and damping capacity of Al-alloyed (up to 16 wt. % Al) ductile and white cast irons. The hardness was increased up to 500 HV in alloys containing 9 wt. %, 13 wt. % and 14 wt. %. Al, it was attributed to the formation of FeAl, $AlFe_3C$ and Fe_3Al compounds. The oxidation resistance was enhanced by increasing Al content to 5.8 wt. % due to the formation of Al_2O_3. Finally, the damping capacity also was improved in the same alloys, especially in the alloys with 2.6 wt. % and 16.0 wt. %Al. In another work [20], the Fe-3.7C-0.5Al-1.0Si, Fe-3.4C-4.9Al-1.2Si and Fe-3.2C-6.2Al-1.2Si cast irons were studied, obtaining higher hardness values as a function of increasing Al content, 305 HV, 377 HV and 411 HV respectively. Aguado et al. [21] improved the standard properties of Fe-C–Si grey cast irons,

obtaining a strength of 466 MPa and hardness up to 260 HV for an iron with 3.08 wt. % C, 3.15% Al and 0.16 wt. % Si. Recently, the tribological properties of Al-alloyed ductile cast irons were studied, the best wear properties was achieved by the 4 wt. % Al-alloyed nodular cast iron [25]. In the same work, the hardness of the EN-GJS-400–15 grade was augmented in function of increasing the amount of Al, obtaining the highest hardness value in the alloy containing 4 wt. % of Al.

Therefore, the aforementioned properties of the lightweight cast irons make them very interesting alloys for the automotive industry, especially as brake disc material, engine gears, pump housings, etc. Motivated by the above concerns, and because of the great potential that lightweight cast iron to reduce the density and overpass the mechanical properties of traditional cast irons, this study developed four novel Fe-Al-C-Si lightweight gray cast iron alloys. The microstructural evolution of EN-GJL-HB195 grade cast iron alloyed with Al between 0 wt. % and 15 wt. % was studied by different characterization techniques, and the hardness values were obtained for each alloy. It should be mentioned that the alloys were manufactured by easily scalable gravity casting process, and the use of expensive or scarce elements was avoided.

2. Materials and Methods

2.1. Calculation of Equilibrium Phase Diagram

The software Thermo-Calc (v. 2020, Thermo-Calc Software AB, Stockholm, Sweden) [26] in conjunction with the TCFE6 thermodynamic database was used for calculations of the equilibrium phases as a function of temperature.

2.2. Materials Preparation

For the preparation of gray cast irons with different percentages of Al, a 20 kg medium frequency induction furnace VIP-I (Inductotherm Corp., Rancocas, VT, USA) was used. As charge material, 14 kg of low alloying steel scrap was used. Once the charge material was melted, the chemical composition was adjusted to the target composition by using FeSi (75 wt. % Si, 0.073 wt. % C, 0.01 wt. % S, 0.019 wt. % P) and graphite (99 wt. % C). After adjusting, the melt was overheated to ~1500 °C and the elemental composition of the molten bath was analyzed using optical emission spectrometry (OES) before alloying Al, and the results are shown in Table 1.

Table 1. Elemental composition of the molten bath before alloying obtained by optical emission spectrometry (OES).

Fe	C	Si	Mn	Cr	Ni	Mo	Cu	Sn	P	S
Bal.	3.12	2.0	0.63	0.15	0.06	0.01	0.09	0.01	0.02	0.03

After that, pure Al (99 wt. %) was added to obtain the targets compositions with different predetermined amounts of Al (0 wt. %, 2 wt. %, 7 wt. %, and 15 wt. %, referred to as 0-Al, 2-Al, 7-Al and 15-Al, respectively). When the target composition of each alloy was obtained, the alloys were individually casted in a resin-bonded sand mold. Approximately 500 g of each alloy was obtained in a cylindrical (Ø 20 × 50 mm) sample.

2.3. Microstructural and Elemental Characterization

Before casting, Thermal Analysis (TA) samples were poured into standard QuiK-Cup® sand cups. The data for TA was collected using a high-speed National Instruments Data Acquisition System. The final chemical composition of the four alloys was determined by ICP.

The samples for optical microscopy (OM) and the microhardness test were cut from the bulk samples and prepared according to standard metallographic procedures, by hot mounting in conductive resin, grinding, and polishing. Graphite distribution type and amount (area %) were defined using image analysis computer tools. Afterward, the samples were etched with Nital 5 (5% nitric acid, 95% ethanol) to reveal the matrix structure.

Microstructural identification, shape classification and terminology have been carried out according to standard UNE-EN ISO 945-1.

The X-ray diffraction (XRD) equipment used to characterize the crystal structures of the alloys was a model D8 ADVANCE (BRUKER, Karlsruhe, Germany), with Cu Kα radiation, operated at 40 kV and 30 mA. The diffraction diagrams were measured at the diffraction angle 2 θ, range from 10° to 90° with a step size of 0.05°, and 5 s/step. The powder diffraction file (PDF) database 2008 was applied for phase identification. The microstructure, the different regions and the averaged overall chemical composition of each sample were investigated by an optic microscope model DMI5000 M (LEICA Microsystems, Wetzlar, Germany) and a scanning electron microscope (SEM), equipped with an energy-dispersive X-ray spectrometry (EDS) model JSM-5910LV (JEOL, Croissy-sur-Seine, France). The quantitative analysis of volume fractions of different phases was performed for each chemical composition and the average values were calculated using image analysis software.

2.4. Mechanical Characterization

Vickers hardness FM-700 model (FUTURE-TECH, Kawasaki, Japan) was employed on the polished sample surface using a 10 kg load, applied for 10 s. At least five random individual measurements were made.

3. Results and Discussion

3.1. Thermodynamic Equilibrium Phase Diagram of the Alloys

In Figure 1 the equilibrium phase diagram of the elemental composition (Table 1) of the alloy with a variable Al content is plotted. For the sake of simplicity of the diagram, only the principal elements (Fe-C-Si-Mn-Al) were taken in account in the thermodynamic calculations. The as-cast microstructures of each alloy subsequently observed by OM were correlated with the mass percent of Al in the diagram. The microstructural evolution of the samples with 0 wt. % (0-Al), 2 wt. % (2-Al), 7 wt. %. (7-Al) and 15 wt. %. (15-Al) of Al are further discussed in the following section.

As can be seen in Figure 1, the thermodynamic calculations suggested that the phase diagram can be roughly classified in four different regions in function of the wt. % of Al and the stable phases. Firstly, in the region (Region A, highlighted in green) with the lowest wt. % of Al (from 0~6 wt. % Al), the major stable phases are FCC (austenitic matrix), BCC (ferritic matrix), graphite and M_7C_3 carbides. The M_7C_3 carbide phase is only stable at temperatures below 381 °C.

The line designated as "Kappa line" (dark blue line), separates Region A (FCC, BCC, graphite and M_7C_3) and Region B (highlighted in blue). In Region B (between ~6 wt. % and ~9 wt. % Al), the kappa-carbide phase is in thermodynamic equilibrium. The kappa phase was thermodynamically described in Al-C-Fe system [27], and was considered as a high-temperature phase in Fe-C-Al alloys [28].

BCC, graphite and M_7C_3 phases. The major subregion in this range indicates the stabilization of BCC + graphite + kappa over wide range of temperatures and up to 15 wt. % of Al, especially at high temperatures.

Then, in the range from ~9 wt. % to ~13 wt. % Al (Region C, highlighted in yellow) there is a significant qualitative change in the stable phases in the diagram. This region is distinguished from Region 2 by a light brown line. When the amount of Al is over 9.4 wt. %, and at temperatures below 730 °C graphite is not in thermodynamic equilibrium. There are two different subregions, the stable phases are BCC + kappa and BCC + kappa + M_7C_3 (up to ~11.2 wt. % Al), respectively.

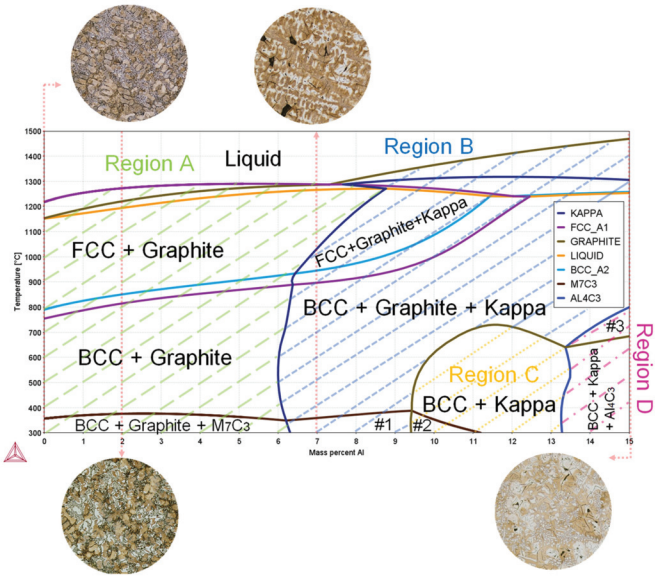

Figure 1. Phase diagram of the nominal composition of the Fe-3.1C-2.0Si-0.6Mn alloy with variable wt.% of Al correlated with the etched microstructures subsequently observed by OM (#1 = BCC + Graphite + kappa + M_7C_3; #2 = BCC + kappa + M_7C_3; #3 = BCC + kappa + M_7C_3 + Al_4C_3).

Finally, in Region D (highlighted in pink) in the range between 13–15 wt. % Al (delimited by the bright blue line), there are two different subregions. In the first one (denoted as #3 in the diagram), above 13.4 wt. % Al and between 632~800 °C, the stable phases are BCC + kappa + Al_4C_3. In the second one, above 13.4 wt. % Al and below 632 °C the stable phases are BCC + kappa + Al_4C_3. Therefore, when the amount of Al is over ~13 wt. %, Al_4C_3 carbides also are stabilized at temperatures below ~800 °C.

Therefore, from the thermodynamic calculations, graphite is not expected to be in thermodynamic equilibrium in Region C and Region D. In addition, increasing the Al content promotes the formation of M_7C_3, kappa and Al_4C_3 phases.

Since the alloys were thermodynamically modelled with the goal of the development of novel lightweight materials, the densities at room temperature of the selected alloys were calculated by Thermo-Calc. The calculated densities are from 7.22 g/cm^3 (Al-free alloy, 0-Al) to 6.05 g/cm^3 for the alloy containing 15 wt. % Al (15-Al). The densities of the alloys are further discussed in Section 3.4 (Hardness of the Samples).

3.2. Alloy Composition and Microstructure of the Cast Samples

The chemical composition of the studied cast irons obtained by ICP is summarized in Table 2. The result obtained by OES (Table 1) and ICP in 0-Al alloy shows good agreement.

Table 2. Elemental composition of Al-alloyed cast irons in wt. % obtained by ICP.

Alloy	Fe	C	Al	Si *	Mn	P	S	Cr	Ni	Mo	Cu
0-Al	Bal.	3.19	0.01	2.53	0.65	0.02	0.02	0.15	<0.10	<0.10	0.10
2-Al	Bal.	3.04	1.80	2.83	0.66	0.02	0.02	0.18	<0.10	<0.10	0.10
7-Al	Bal.	2.85	7.30	2.74	0.62	0.02	0.02	0.16	<0.10	<0.10	0.09
15-Al	Bal.	2.65	15.0	2.33	0.55	0.02	0.02	0.16	<0.10	<0.10	0.09

* The content of Si was estimated by SEM + EDS.

The XRD patterns in Figure 2 showed the formation of graphite and BCC phases in 0-Al and 2-Al cast irons, which demonstrates good agreement with CALPHAD (CALculation of PHAse Diagrams) in Figure 1. On the other hand, the XRD peaks of the 7-Al alloy

indicates the stabilization of BCC, graphite and kappa-carbides ($AlFe_3C_{0.5}$) as a function of increasing aluminum content. The indexed phases showed good agreement with the major subregion (BCC + graphite + kappa) in Region B obtained by CALPHAD calculations. Finally, in 15-Al cast iron, the peaks corresponding to kappa carbides, graphite and BCC phases also were indexed. The indexed peaks also showed good agreement with the major subregion in Region B.

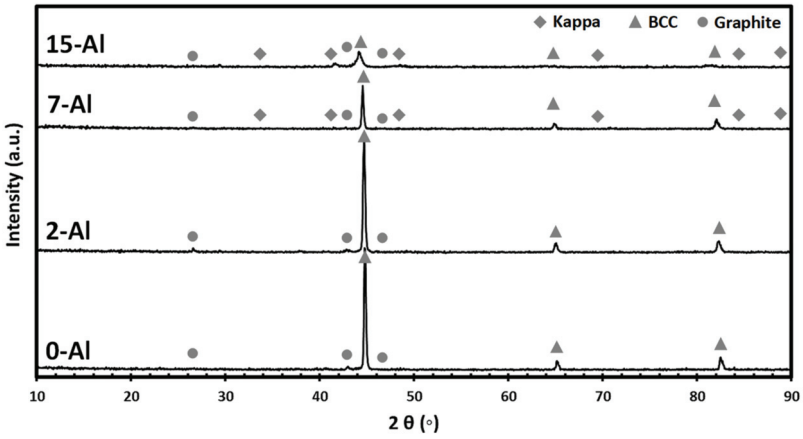

Figure 2. X-ray diffraction (XRD) patterns of the developed cast irons.

In Figure 3 the etched OM (a, d, g and j) and SEM images for each of the studies alloys are shown. Images confirmed the formation of two phases. Thus, the microstructure of 0-Al alloy in Figure 3a–c displays a "D" type morphology that indicates an overcooled graphite. The fine graphite flakes are uniformly distributed in a pearlitic matrix, and a low fraction of ferrite.

In Figure 3d–f the microstructure of 2-Al cast iron shows a "D"/"E" type distribution that indicate an overcooled graphite and low carbon equivalent. The alloy also displays a pearlitic microstructure with some ferrite, which agrees with the results obtained by XRD.

In Figure 3j–l, the microstructure of 7-Al displays ferritic matrix with dispersed perlite. The graphite flakes show a large morphology that indicates the presence of primary graphite. The microstructure also shows a "D"/"E" type distribution that indicate an overcooled graphite and low carbon equivalent. The microstructure also shows the stabilization of kappa carbides, demonstrating good agreement with the results obtained by XRD.

Finally, in Figure 3j–l the microstructure of 15-Al shows similar pattern to alloy containing 7 wt. %. Al, but the graphite shows coarser morphology.

To determine the effect of Al on the graphite morphology of the cast iron, the non-etched OM of the alloys are shown in Figure 4. The microstructures show that the perlite content decrease with the increment of wt. % of Al. The opposite occurs with the ferrite.

In the case of graphite, a slight increment occurs with 2 wt. % of Al, but a great decrease occurs until 15 wt. % of Al. This indicates that Al in low quantity is a graphite stabilizer. On the other hand, as the quantity of Al increases, it becomes a carbide former with a subsequent reduction in the amount of graphite.

The quantitative results of the volume fraction of the characterized phases of the studied alloys obtained by image analysis are summarized in Table 3. The analysis of ferrite volume fraction for 7-Al and 15-Al are not only for ferrite. Due to the uncertainty of the method to distinguish between both phases, ferrite and kappa-carbides are quantified together.

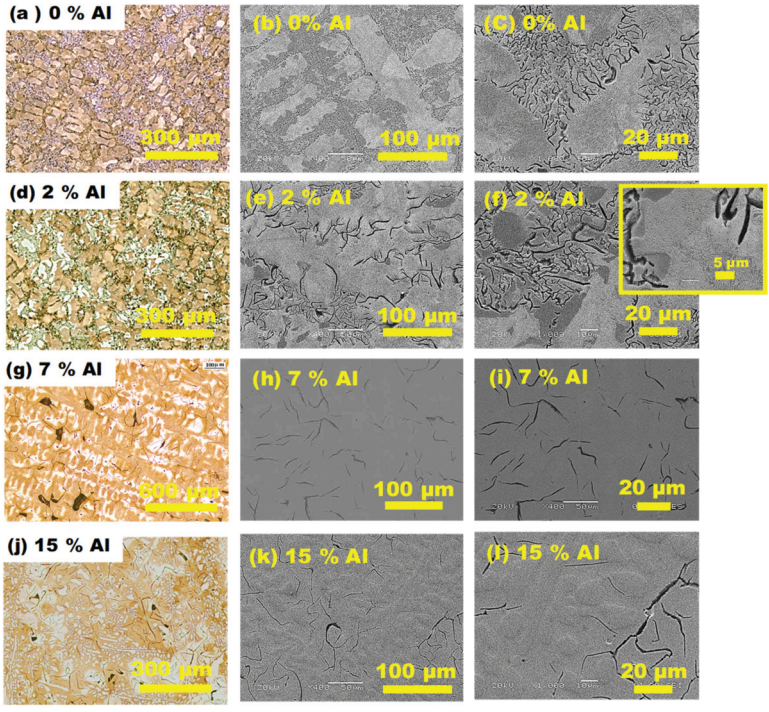

Figure 3. (**a**–**c**) Etched optical microscopy (OM) and SEM images of 0-Al; (**d**–**f**) etched OM and SEM images of 2-Al; (**g**–**i**); etched OM and SEM images of 7-Al and (**j**–**l**) etched OM and SEM images of 15-Al.

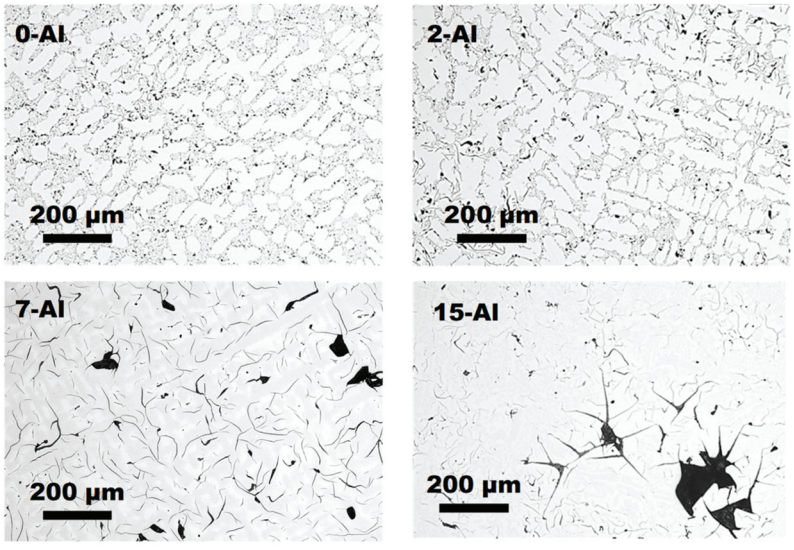

Figure 4. Effect of Al on the graphite morphology in the microstructure of alloys containing 0 wt.%, 2 wt.%, 7 wt.% and 15 wt.% Al.

Table 3. Phase volume fraction of the studied alloys.

Alloy	Ferrite (%)	Graphite (%)	Perlite (%)
0-Al	9.2	8.1	82.7
2-Al	15.5	8.6	75.9
7-Al	26.9 *	7.1	66.0
15-Al	36.1 *	5.5	56.8

* Ferrite + kappa-carbides.

3.3. Analysis of the Cooling Curves

The solidification properties of the studied cast irons were obtained by TA of the solidification curves and its derivatives. In Figure 5 the cooling curves of the studied cast irons are shown. For the sake of simplicity, only the solidification curves are plotted.

As can be seen from the solidification curves, the solidification changes from a completely hypoeutectic to a relative eutectic behavior, with a recalescence that remains stable at the eutectic temperature for nearly 26 s in the alloy containing 15 wt. % of Al. In the alloy containing 7 wt. % Al no recalescence is observed, and the temperature does not stop falling at any time, indicating low graphitic precipitation.

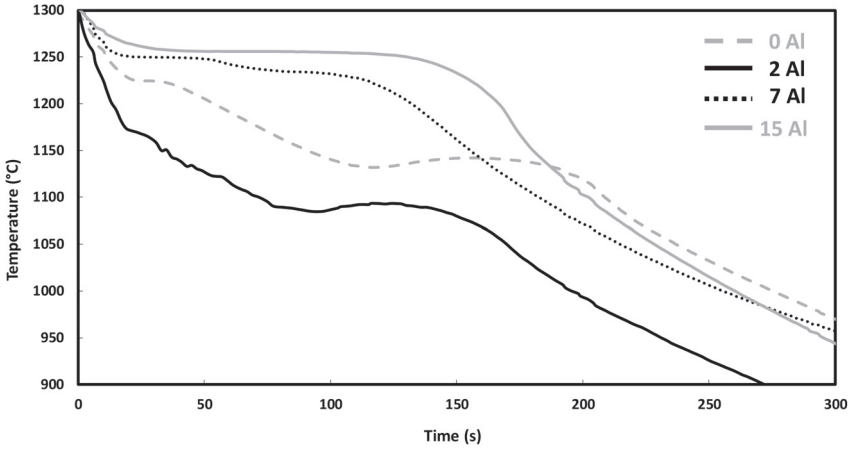

Figure 5. The cooling curves of the studied cast irons.

In conventional TA of standard grade cast irons there are two important points in the interpretation of the cooling curves, known as low and high eutectic points. These points also are known as eutectic undercooling and eutectic recalescence, respectively. From these points, characteristics of the free graphite forming can be defined, as well as important aspects of the quality of the cast irons. The recalescence parameter is known as the difference between both eutectic points and is assessed as one of the key parameters of the metallurgical quality of the cast irons.

Even though in Fe-Al system there is no similar eutectic point for the studied alloys (at 7 wt. %. Al a similar region can be identified, but with different definition and geometry from one of the cast irons), the cooling curves show similar evolution than standard cast iron ones, probably due to the Fe–C relation.

To analyze the cooling curves obtained in this work, these points with similarities with conventional low and high eutectic points have been defined as eutectic undercooling and eutectic recalescence points. Finally, the recalescence was defined as the difference between them. Therefore, the aforementioned points, the liquidus temperature (T_{liq}) and solidus temperature (T_{sol}) are shown in Table 4.

Table 4. Solidification properties of the cooling curves.

Alloy	Liquidus (°C)	Solidus (°C)	Eutectic Undercooling (°C)	Eutectic Recalescence (°C)	Recalescence	Time (s)
0-Al	1224	1082	1132	1142	10	39
2-Al	1168	1044	1084	1093	9	29
7-Al	1250	1170	–	–	–	–
15-Al	1264	1179	1256	1256	0	26

3.4. Hardness of the Samples

The bulk hardness of the studied alloys was studied on Vickers hardness tester under the load of 10 kg. The mean values with the standard deviation are summarized in Table 5. The addition of Al increases the hardness of the alloys, but not gradually, as the alloy with the highest hardness is 7-Al. This is correlated with the formation of kappa phase and finer perlite.

Table 5. Hardness, calculated density and specific hardness of the studied cast irons.

Alloy	Hardness (HV 10)	Density (g/cm^3)	Specific Hardness (HV/g·cm^{-3})
0-Al	235 ± 14	7.22	32.5
2-Al	251 ± 15	7.04	35.6
7-Al	363 ± 06	6.62	54.8
15-Al	334 ± 25	6.05	55.2

Since the alloys were designed with the goal of the development of novel lightweight materials, the densities at room temperature of the developed alloys also were calculated by Thermo-Calc in Table 5. The densities are between 7.22 g/cm^3 (0-Al) and 6.05 g/cm^3 for the alloy containing 15 wt. % Al (15-Al). Furthermore, the specific hardness of 15-Al cast iron is the highest of the results obtained. This is due to a combination of low density and high hardness of the alloy.

A comparison of the hardness and calculated density at room temperature of the developed cast irons with related works in the field [18,20,21,25] is given in Figure 6. As can be seen, the 0-Al cast iron showed a density of 7.22 g/cm^3 and a hardness value of 235 ± 14 HV 10, which is in accordance with the typical range between 186–247 HV of the EN-GJL-HB195 grade cast iron. The developed alloys showed good agreement in terms of hardness and density with previously published works. It should be noted that 15-Al cast iron shows quite similar properties to Fe-3.0C-16.0Al-2.2Si cast iron [18].

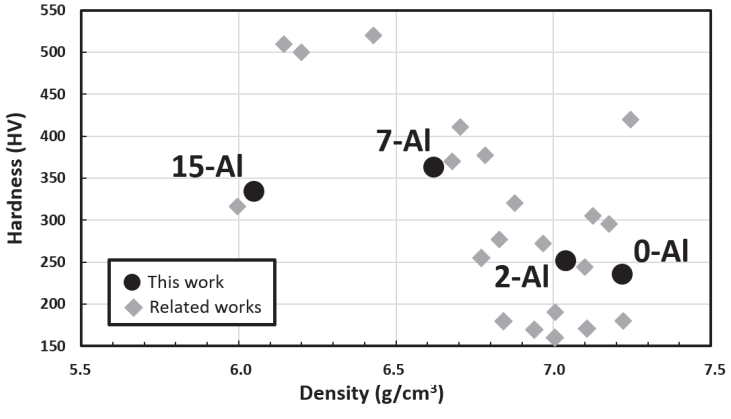

Figure 6. Materials property space for hardness vs. calculated density at room temperature of manufactured cast irons and related works, data from [18,20,21,25].

4. Conclusions

In this work, the microstructural evolution and hardness of four lightweight cast irons as a function of increasing aluminum content (from 0 wt. % to 15 wt. %) was studied. The alloys were manufactured by an easily scalable and affordable gravity casting process. The following conclusions were obtained:

- The phase diagram of the alloys in function of the wt. % of Al can be divided in four regions in function of the stable phases. From the phase diagram, graphite is not expected to be in thermodynamic equilibrium over 9,4 wt. % Al at low temperatures (Region C and D). But the observed microstructures showed the formation of graphite, which means that thermodynamic equilibrium of 15-Al is over ~800 °C (Region B).
- From thermodynamic calculations, the increasing of the Al content also promotes the formation of M_7C_3, kappa-carbides and Al_4C_3 phases. Al_4C_3 carbides are in thermodynamic equilibrium when the amount of Al is over ~13 wt. %. Therefore, according to thermodynamic calculations, there is a limit as to where, in addition to Al_4C_3 phase, kappa-carbides are also stabilized.
- The microstructure of 0-Al alloy is formed by a fine graphite flakes distributed in a pearlitic matrix, and a low fraction of ferrite. The microstructure of 2-Al alloy also shows a pearlitic matrix with ferrite, but "D"/"E" type distribution with overcooled graphite. The microstructure of 7-Al alloy is formed by a ferritic matrix with dispersed perlite. The graphite flakes show a large morphology that indicates the presence of primary graphite. The microstructure also shows the stabilization of kappa-carbides. The microstructure of 15-Al graphite shows a similar pattern to alloy containing 7 wt. %. Al, but the graphite shows coarser morphology.
- The microstructures show that the perlite content decrease with the increment of wt. % of Al. The opposite occurs with the ferrite. In the case of graphite, a slight increment occurs with 2 wt. % of Al, but a great decrease occurs until 15 wt. % of Al.
- The cooling curves of the studied cast irons shows that recalescence is not observed in 7-Al cast iron. The solidification changes from a hypoeutectic to a eutectic behavior, with a recalescence that remains stable at the eutectic temperature in 15-Al cast iron.
- The addition of Al increases the hardness of the studied cast irons, but not gradually. The alloy with the highest hardness is 7-Al, which is correlated with the formation of kappa carbides and finer perlite.
- The obtained properties showed good consistency in terms of hardness vs. density with related works in the field.

As a future work, based on the obtained results, it is suggested the manufacturing of alloys containing 7 wt. % and 15 wt. % or more Al, to further study the mechanical properties. Specifically, it can be interesting the intensive study of the tribological properties of high Al-alloyed ($\geq$7 wt. % Al) cast irons.

Author Contributions: Conceptualization, J.M.S.; Formal analysis, A.O.; Funding acquisition, D.E.; Investigation, J.M.S., J.C.G., G.A. and I.H.; Methodology, A.O.; Project administration, I.Q.; Resources, P.R.; Supervision, D.E., J.C.G., G.A., I.H., I.Q. and P.R.; Validation, D.E. and J.C.G.; Writing—original draft, J.M.S.; Writing—review and editing, J.M.S. All authors have read and agreed to the published version of the manuscript.

Funding: This work has been partially funded by the Basque Government through the project Elkartek LION: KK-2019/00040.

Data Availability Statement: Data presented in this article is available on request from the corresponding author.

Conflicts of Interest: The authors declare no conflict of interest.

References

1. Mitrica, D.; Badea, I.C.; Olaru, M.T.; Serban, B.A.; Vonica, D.; Burada, M.; Geanta, V.; Rotariu, A.N.; Stoiciu, F.; Badilita, V.; et al. Modeling and experimental results of selected lightweight complex concentrated alloys, before and after heat treatment. *Materials* **2020**, *13*, 4330. [CrossRef] [PubMed]
2. Tun, K.S.; Charadva, V.; Gupta, M. Lightweight medium entropy magnesium alloy with exceptional compressive strength and ductility combination. *J. Mater. Eng. Perform.* **2021**, *30*, 2422–2432. [CrossRef]
3. Chandel, R.; Sharma, N.; Bansal, S.A. A review on recent developments of aluminum-based hybrid composites for automotive applications. *Emergent Mater.* **2021**, 1–15. [CrossRef]
4. Wallerstein, D.; Salminen, A.; Lusquiños, F.; Comesaña, R.; García, J.D.V.; Rodríguez, A.R.; Badaoui, A.; Pou, J. Recent developments in laser welding of aluminum alloys to steel. *Metals* **2021**, *11*, 622. [CrossRef]
5. Zhou, B.; Liu, B.; Zhang, S. The advancement of 7xxx series aluminum alloys for aircraft structures: A review. *Metals* **2021**, *11*, 718. [CrossRef]
6. Kaltzakorta, I.; Gutierrez, T.; Elvira, R.; Jimbert, P. Manufacturing and forging issues encountered while upscaling 1.3C30Mn10Al-austenitic and 0.65C12Mn-duplex low-density steels. *Mater. Manuf. Process.* **2021**, 1–12. [CrossRef]
7. Moon, J.; Ha, H.Y.; Kim, K.W.; Park, S.J.; Lee, T.H.; Kim, S.D.; Jang, J.H.; Jo, H.H.; Hong, H.U.; Lee, B.H.; et al. A new class of lightweight, stainless steels with ultra-high strength and large ductility. *Sci. Rep.* **2020**, *10*, 1–10. [CrossRef] [PubMed]
8. Liu, D.; Ding, H.; Han, D.; Cai, M.; Lee, Y.K. Microstructural evolution and tensile properties of Fe–11Mn–10Al-1.2C medium-Mn lightweight steel. *Mater. Sci. Eng. A* **2020**, *797*, 140256. [CrossRef]
9. Wang, Z.; Lu, W.; Zhao, H.; He, J.; Wang, K.; Zhou, B.; Ponge, D.; Raabe, D.; Li, Z. Formation mechanism of κ-carbides and deformation behavior in Si-alloyed FeMnAlC lightweight steels. *Acta Mater.* **2020**, *198*, 258–270. [CrossRef]
10. Kaltzakorta, I.; Gutiérrez, T.; Elvira, R.; Guraya, T.; Jimbert, P. Low density steels for forging. *Mater. Sci. Forum* **2018**, *941*, 287–291. [CrossRef]
11. Chen, S.; Rana, R.; Haldar, A.; Ray, R.K. Current state of Fe-Mn-Al-C low density steels. *Prog. Mater. Sci.* **2017**, *89*, 345–391. [CrossRef]
12. Kaltzakorta, I.; Gutierrez, T.; Elvira, R.; Jimbert, P.; Guraya, T. Evolution of microstructure during isothermal treatments of a duplex-austenitic 0.66C11.4Mn.9.9Al low-density forging steel and effect on the mechanical properties. *Metals* **2021**, *11*, 214. [CrossRef]
13. Pero-Sanz Elorz, J.A.; Fernández González, D.; Verdeja González, L.F. *Physical Metallurgy of Cast Irons*; Springer: Cham, Switzerland, 2018.
14. Verhoeven, J.D. Cast Irons. In *Steel Metallurgy for the Non-Metallurgist*; ASM International: Novelty, OH, USA, 2019.
15. Davis, J.R. (Ed.) *ASM Specialty Handbook: Cast Irons*; ASM International: Materials Park, OH, USA, 1996.
16. Bourdie, J.; Bruneseaux, F.; De Parseval, P.; Gouy, S.; Laffont, L.; Lacaze, J. Effect of cooling rate and aluminium addition on graphite growth during solidification and graphitization. *Mater. Sci. Forum* **2018**, *925*, 20–27. [CrossRef]
17. Haque, M.M.; Young, J.M. Production of spheroidal graphite aluminium cast iron and the factors affecting it. *J. Mater. Process. Technol.* **1995**, *55*, 186–192. [CrossRef]
18. Ibrahim, M.M.; Mourad, M.M.; Nofal, A.A.; Farahat, A.I.Z. Microstructure, hot oxidation resistance and damping capacity of Al-alloyed cast iron. *Int. J. Cast Met. Res.* **2017**, *30*, 61–69. [CrossRef]
19. Gumienny, G.; Kurowska, B.; Klimek, L. Aluminium in compacted graphite iron. *China Foundry* **2020**, *17*, 137–143. [CrossRef]
20. Shayesteh-Zeraati, A.; Naser-Zoshki, H.; Kiani-Rashid, A.R. Microstructural and mechanical properties (hardness) investigations of Al-alloyed ductile cast iron. *J. Alloys Compd.* **2010**, *500*, 129–133. [CrossRef]
21. Aguado, E.; Ferrer, M.; Larrañaga, P.; Stefanescu, D.M.; Suárez, R. The effect of the substitution of silicon by aluminum on the properties of lamellar graphite iron. *Int. J. Met.* **2019**, *13*, 536–545. [CrossRef]
22. Kasvayee, K.A.; Ghassemali, E.; Svensson, I.L.; Olofsson, J.; Jarfors, A.E.W. Characterization and modeling of the mechanical behavior of high silicon ductile iron. *Mater. Sci. Eng. A* **2017**, *708*, 159–170. [CrossRef]
23. Takamori, S.; Osawa, Y.; Halada, K. Aluminum-alloyed cast iron as a versatile alloy. *Mater. Trans.* **2002**, *43*, 311–314. [CrossRef]
24. Adebayo, A.O.; Oyetunji, A.; Alaneme, K.K. Microstructural characteristics, mechanical and wear behaviour of aluminium-alloyed ductile irons subjected to two austempering processes. *Acta Polytech.* **2020**, *60*, 185–196. [CrossRef]
25. Sandikoglu, A.; Gecu, R. Microstructural, mechanical and tribological characterization of aluminum-alloyed ductile cast irons based on aluminum content. *J. Alloys Compd.* **2021**, *879*, 160428. [CrossRef]
26. Andersson, J.O.; Helander, T.; Höglund, L.; Shi, P.; Sundman, B. Thermo-Calc & DICTRA, computational tools for materials science. *Calphad Comput. Coupling Phase Diagrams Thermochem.* **2002**, *26*, 273–312. [CrossRef]
27. Zheng, W.; He, S.; Selleby, M.; He, Y.; Li, L.; Lu, X.G.; Ågren, J. Thermodynamic assessment of the Al-C-Fe system. *Calphad* **2017**, *58*, 34–49. [CrossRef]
28. Cheng, W.C.; Song, Y.S.; Lin, Y.S.; Chen, K.F.; Pistorius, P.C. On the eutectoid reaction in a quaternary Fe-C-Mn-Al alloy: Austenite → ferrite + kappa-carbide + M23C6 carbide. *Metall. Mater. Trans. A Phys. Metall. Mater. Sci.* **2014**, *45*, 1199–1216. [CrossRef]

metals

MDPI

Article

Strain-Controlled Fatigue Behavior of a Nodular Cast Iron in Real Off-Highway Axles: Effects of Casting Skin and Strain Ratio

Federico Scacco, Alberto Campagnolo, Mattia Franceschi and Giovanni Meneghetti *

Department of Industrial Engineering, University of Padova, Via Venezia 1, 35131 Padova, Italy; federicoscacco93@gmail.com (F.S.); alberto.campagnolo@unipd.it (A.C.); mattia.franceschi@phd.unipd.it (M.F.)
* Correspondence: giovanni.meneghetti@unipd.it; Tel.: +39-049-8276751

Abstract: Nodular cast irons are widely adopted in off-highway vehicles, since they allow to obtain components with complex shapes as well as good mechanical properties. However, the fatigue strength of such components is a major issue, which is typically addressed by adopting the strain-life approach, since it considers the local strains at stress concentrators where fatigue cracks are prone to initiate. In the fatigue design of off-highway components, the detrimental effect of casting skin, due to both surface and subsurface features, must be accounted for in all cases where machining is not needed. Moreover, the local strain ratio at stress raisers can be different from the nominal one due to forward plasticity. In this paper, static tensile as well as strain-controlled fatigue tests have been executed on specimens taken from real EN-GJS-450-10 off-highway axles. Static tensile tests have been performed on specimens with machined surfaces, while fatigue tests at a strain ratio equal to −1 have been carried out on specimens with surfaces in both machined and as-cast conditions. In addition, machined specimens have been tested at strain ratios equal to 0.1 and 0.5 to investigate the material sensitivity to the mean strain. Finally, the high-cycle downgrading effect of the casting skin has been evaluated, and experimental data of machined specimens tested at different strain ratios have been summarized by using the Smith–Watson–Topper expression.

Keywords: nodular cast iron; off-highway axles; strain-controlled fatigue; strain ratio; casting skin

Citation: Scacco, F.; Campagnolo, A.; Franceschi, M.; Meneghetti, G. Strain-Controlled Fatigue Behavior of a Nodular Cast Iron in Real Off-Highway Axles: Effects of Casting Skin and Strain Ratio. *Metals* **2022**, *12*, 426. https://doi.org/10.3390/met12030426

Academic Editors: Annalisa Fortini and Chiara Soffritti

Received: 18 January 2022
Accepted: 22 February 2022
Published: 28 February 2022

1. Introduction

Nodular cast irons are preferred materials for manufacturing axles of off-highway vehicles because their complex shape can be manufactured at affordable costs and with adequate mechanical properties for structural applications. However, such components must withstand severe cyclic loadings during the in-service conditions; therefore, reliable material data and approaches are necessary to design against fatigue.

Several papers in the literature have been devoted to investigate the fatigue behavior of nodular cast irons, providing both material data and fatigue criteria, among them: stress-life approaches [1–6], fracture-mechanics-based methodologies [7–12], and strain-life approaches [13–16]. In the context of the fatigue design of off-highway axles made of nodular cast irons, the strain-life approach is widely employed, since it considers the local strains at stress concentrators where fatigue cracks are prone to initiate.

According to the experimental data collected in the literature, the mechanical properties of nodular cast irons, and particularly the fatigue resistance, are strongly influenced by the microstructure. The latter depends on the chemical composition, technological processes, heat treatments, geometry of the raw cast, and also the locations where specimens are taken.

Another relevant microstructural feature in nodular cast iron components is the casting skin, which represents the rim zone of the casting and can lead to a detrimental effect on the fatigue strength, not only for the high surface roughness but also for the deviating

microstructure, since discontinuities such as inhomogeneous microstructures (e.g., decarburization or graphite degeneration and a ferritic or pearlitic rim, imperfections, pores, defects, and/or sand inclusions coming from the mold) are typically concentrated there [2]. The influence of the casting skin on the fatigue strength of cast iron components has been widely investigated in the recent literature [9,17–25]. This effect must be accounted for in the fatigue design of components where machining is not needed, such as the case of axles of off-highway vehicles.

Dealing with the loading condition, strain-controlled fatigue tests for material characterization are usually performed under completely reversed strains, that is, at a strain ratio $R_\varepsilon = -1$. However, strain ratios different from -1 are typically present in the critical locations of axles of off-highway vehicles, especially at stress raisers where the local strain ratio could be different from the nominal one due to forward plasticity. To treat such cases, on one hand, mean stress/strain corrections [4,26] have been proposed to correct the strain-life fatigue approach, where the material parameters are calibrated on experimental results generated under push-pull, strain-controlled fatigue loading. On the other hand, the mean stress/strain sensitivity is a material-dependent feature [27]; therefore, it should be experimentally investigated through dedicated fatigue tests, as performed in [28–30], dealing with nodular cast irons.

In the present paper, specimens taken from real off-highway axles and made of nodular cast iron EN-GJS-450-10 have been tested to investigate previous topics relevant to the fatigue design of off-highway axles. In the relevant literature, to the best of the authors' knowledge, there is a scarcity of experimental results relevant to the fatigue behavior of EN-GJS-450-10 nodular cast iron. In fact, only the works by Heinrietz and Hesseler [31] and Bleicher et al. [29] provided experimental results generated by testing EN-GJS-450-10 nodular cast iron under stress-controlled fatigue loading, while Bleicher et al. [29] also provided experimental results generated under strain-controlled fatigue loading, but only at a strain ratio $R_\varepsilon = -1$. Moreover, no research work has been devoted to the specific topics of the casting skin and strain ratio effects on the fatigue strength of EN-GJS-450-10 nodular cast iron. In this context, the present work aims at filling these gaps. To do this, specimens with either machined or as-cast surfaces have been fatigue tested under strain-control loading to determine the high-cycle downgrading factor due to the cast skin effect. Finally, machined specimens have been fatigue tested under different strain ratios to analyze the influence of the mean strain.

2. Materials and Methods

2.1. Specimens' Position

The analyzed material is a ferritic-pearlitic nodular cast iron, EN-GJS-450-10. Specimens were taken from a real off-highway axle, in order to include the effects of the manufacturing processes. Figure 1 shows the overall geometry of the axle along with the definition of the upper, central, and lower regions. Specimens were located in the wall thickness of the axle; more precisely, cylindrical specimens were taken from the radiused lower-right region, while flat specimens with the casting skin have been taken from the straight, lower-central region, as highlighted in Figure 1. The specimens' geometry will be presented in the following sections.

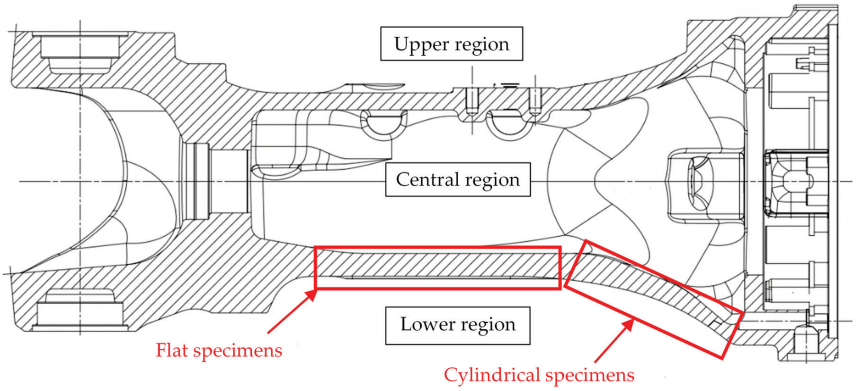

Figure 1. Regions of the axle where samples were taken.

2.2. Metallographic Analyses and Hardness Measurements on the Axle

Metallographic analyses and Brinell hardness measurements according to [32,33] have been performed on three regions of the real off-highway axle as defined in Figure 2. The microstructure was observed with an Olympus BX51M optical microscope, while hardness has been measured by using a Wolpert UH3001 tester. Figure 3 shows the microstructures before and after Nital 4% etching, which allow one to classify the shape and size of graphite nodules and to define the composition of the matrix on the basis of a visual inspection, according to [32]. Table 1 summarizes the obtained results, while Table 2 reports the Brinell hardness measurements. As a result, graphite nodules have a regular spheroidal shape (shape VI [32]), with a diameter typically in the range between 15 μm and 60 μm (size 6/7 [32]); the matrix is approximately composed half by ferrite and half by pearlite, and the average Brinell hardness is between 182 and 186.

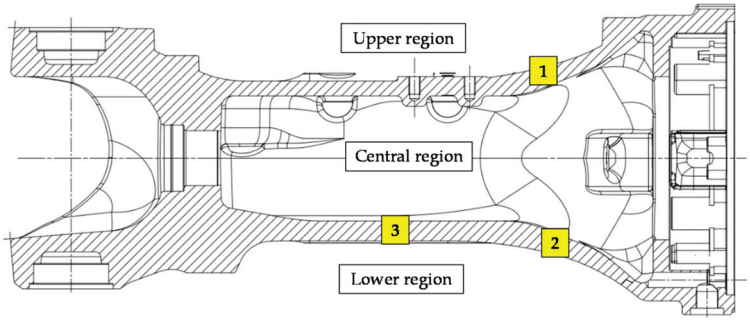

Figure 2. Regions of the axle where metallographic analyses and Brinell hardness measurements have been performed.

Table 1. Size and shape of graphite nodules and matrix composition in the regions of the axle defined in Figure 2 according to ISO 945-1:2018 [32].

Region	Shape # and Size * of Graphite Nodules	Matrix Composition
1	VI-7 Spheroidal graphite	ferritic (50%)–pearlitic (50%)
2	VI-6/7 Spheroidal graphite	ferritic (50%)–pearlitic (50%)
3	VI-7 Spheroidal graphite	ferritic (50%)–pearlitic (50%)

shape of graphite nodules: VI corresponds to regular spheroidal graphite. * size of graphite nodules: 6 corresponds to a diameter in the range between 30 μm and 60 μm, and 7 to a diameter in the range between 15 μm and 30 μm.

Table 2. Brinell hardness [33] measured in the regions of the axle defined in Figure 2.

Region	HBW—Test 1	HBW—Test 2	HBW—Test 3	HBW—Average	HBW—Standard Deviation
1	182	182	183	182.3	0.577
2	182	184	183	183.0	1.000
3	185	187	187	186.3	1.155

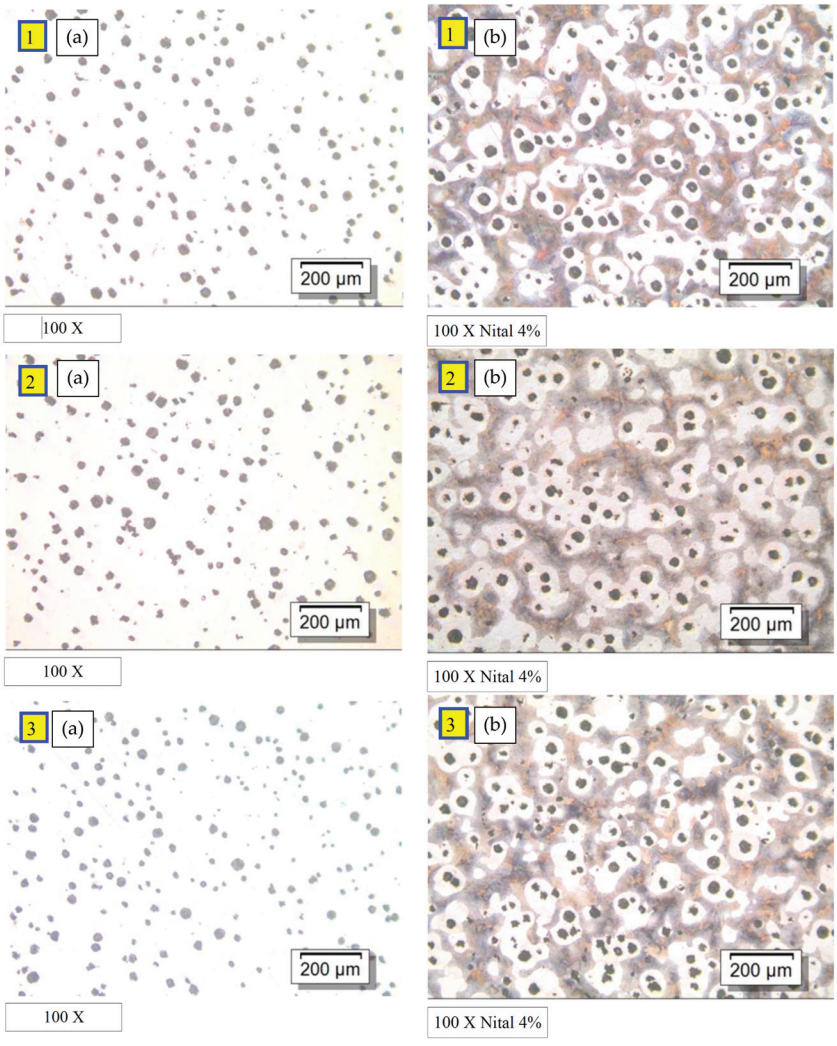

Figure 3. Microstructures (**1a**), (**2a**), (**3a**) before and (**1b**), (**2b**), (**3b**) after Nital 4% etching as analysed in regions 1, 2 and 3 of the axle (see Figure 2), respectively. Size of graphite nodules and matrix type.

2.3. Static and Fatigue Testing: Parameters and Specimens' Geometry

Static tensile tests and strain-controlled fatigue tests have been performed at room temperature by adopting an MTS 858 MiniBionix II axial servo-hydraulic testing machine (MTS, Eden Prairie, MN, USA), with a load capacity of 15 kN and equipped with an MTS TestStar IIm controller. The uniaxial extensometer MTS 634.12F-24 with gauge length of 25 mm has been adopted to measure the axial strain.

Static tensile tests have been performed on plain cylindrical specimens with machined surface (Figure 4) by applying a displacement rate equal to 0.5 mm/min under displacement control according to ISO 6892-1:2016 [34]. All in all, seven specimens have been tested. The MTS controller acquired the applied load from the load cell of the testing machine and the strain from the extensometer during each static test. After each test, the static Young's modulus E_s, the engineering proof stress $\sigma_{p,0.2}$, the engineering tensile strength σ_R, the elongation after fracture A%, and the reduction of area Z% have been derived.

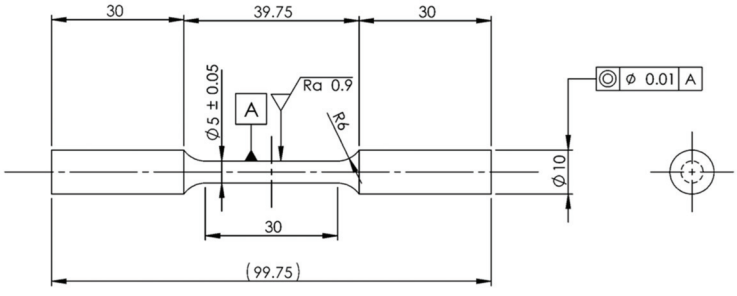

Figure 4. Geometry of plain cylindrical specimens tested under static tensile loading (dimensions are in mm). Specimens have been taken from the axle (see Figure 1 and region 2 of Figure 2), and after that, the cylindrical surface has been machined (Ra = 0.9 μm).

Fatigue tests have been performed on plain cylindrical specimens with machined surface (Figure 5) by imposing a sinusoidal wave form under closed-loop total strain control mode according to ISO 12106:2017 [35]. In more detail, the cylindrical surface of the specimens has been machined by fine turning and then polished with fine emery papers to achieve a roughness of Ra = 0.9 μm. It is worth noting that specimens adopted for static tensile tests (Figure 4) have a smaller cross-section area as compared to that of specimens adopted in the fatigue tests (Figure 5). In fact, the diameter of the tested specimens has been properly selected to keep the maximum applied load below the load capacity of the testing machine (i.e., 15 kN). A nominal strain ratio R_ε (defined as the ratio between the minimum and the maximum applied strain) equal to −1, 0.1, and 0.5 has been adopted in the tests to investigate the material sensitivity to the mean strain. In more detail, $R_\varepsilon = -1$ is typically the reference strain ratio, as suggested also by ISO 12106:2017 [35]; while $R_\varepsilon = 0.1$ and 0.5 are of interest for the specific application of real off-highway axles. In fact, strain ratios R_ε approximately equal to 0.1 and 0.5 have been derived by both strain gauge measurements and elastic-plastic FE calculations performed close to the actual crack initiation location in real off-highway axles under two different in-service loading conditions. Test frequencies between 0.2 and 1 Hz have been adopted. During each fatigue test, the hysteresis loops have been measured by taking advantage of the signals acquired by the MTS controller from the load cell and the extensometer. Stabilised hysteresis loops have been defined at half the fatigue life of each specimen [35,36]. Long-run tests up to $2 \cdot 10^6$ cycles in the elastic regime have been performed by switching to load-controlled mode and by adopting a test frequency of 15–18 Hz [36]. Fatigue tests have been interrupted when either specimen complete separation or run out condition, defined at $2 \cdot 10^6$ cycles, occurred.

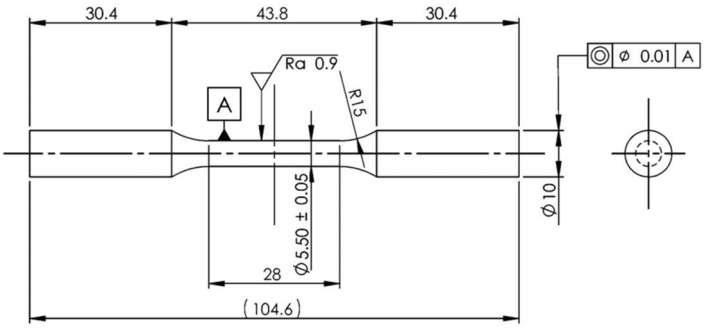

Figure 5. Geometry of plain cylindrical specimens tested under strain-controlled fatigue loading (dimensions are in mm). Specimens have been taken from the axle (see Figure 1 and region 2 of Figure 2), and after that, the cylindrical surface has been machined (Ra = 0.9 μm).

To investigate the detrimental effect of the casting skin, strain-controlled fatigue tests have been performed again under total strain control mode on plain flat specimens with three surfaces machined by milling to achieve a roughness of Ra = 0.4 μm, while one has been kept as-cast (Figure 6). A nominal strain ratio $R_\varepsilon = -1$ has been adopted, and other testing parameters are kept the same as described above for cylindrical machined specimens.

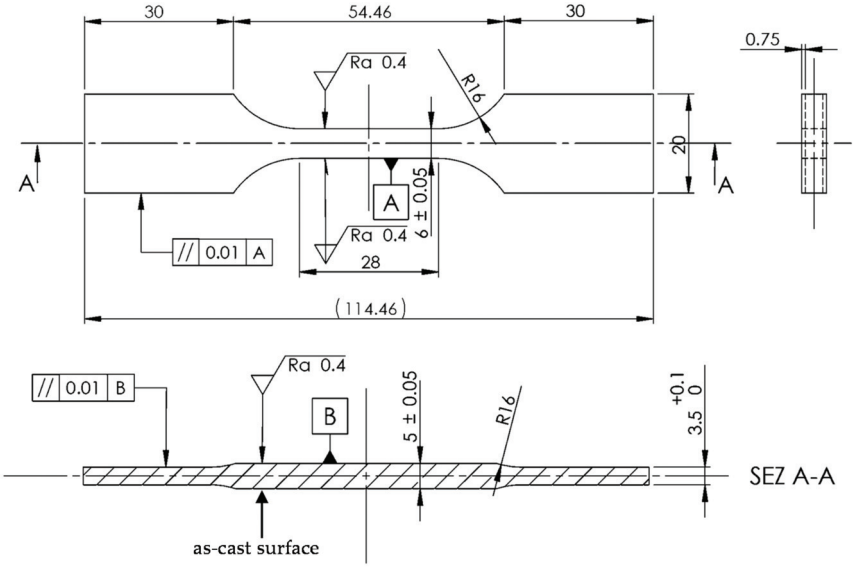

Figure 6. Geometry of plain flat specimens tested under strain-controlled fatigue loading (dimensions are in mm). Specimens have been taken from the axle (see Figure 1 and region 3 of Figure 2), and after that, three surfaces have been machined (Ra = 0.4 μm), while one has been kept as-cast.

It is worth noting that specimens have been taken only from regions 2 (Figures 4 and 5) and 3 (Figure 6) of the off-highway axle shown in Figure 2, while no specimens were taken from region 1, due to the incompatibility of the size of the specimens with the available material in region 1 of the axle.

In all previous cases, given the load applied to the specimen and acquired by the MTS controller, the nominal stress σ has been calculated from the following expression:

$$\sigma = \frac{F}{A_{net}} = \begin{cases} \frac{F}{\frac{\pi}{4} \cdot d_{net}^2} \text{ for cylindrical specimens} \\ \frac{F}{W \cdot t} \text{ for flat specimens} \end{cases} \quad (1)$$

where d_{net} = 5 mm (Figure 4) or 5.5 mm (Figure 5), while W = 6 mm and t = 5 mm (Figure 6).

Finally, Table 3 summarizes the surface conditions and geometries of the tested specimens and the parameters of the static and strain-controlled fatigue tests.

Table 3. Summary of static and fatigue tests performed on specimens made of nodular cast irons.

Material	Raw Component	Specimen Surface	Test	Specimen Geometry	R_ε	N° Tests	f [Hz]	Rate [mm/min]	Failure Criterion
EN-GJS-450-10	Off-highway axle	machined	Static	Figure 4	n.a.	7	n.a.	0.5	separation
					−1	10	0.2–18	n.a.	separation
			Fatigue *	Figure 5	0.1	6	0.2–15	n.a.	separation
					0.5	6	0.2–15	n.a.	separation
		as-cast	Fatigue *	Figure 6	−1	15	0.2–18	n.a.	separation

* strain-controlled fatigue test. n.a. = not applicable.

The fracture surfaces generated after static and fatigue tests have been analyzed by using a Leica Cambridge 440 Scanning Electron Microscope (SEM) (Leica, Wetzlar, Germany) equipped with EDS EDAX microbeam. Occasionally, fatigue fracture surfaces have also been analyzed by a Dino-Lite optical microscope (model AM4115ZT).

3. Results

3.1. Metallographic Analyses and Hardness Measurements on the Tested Samples

Metallographic analyses and Brinell hardness measurements according to [32,33] have been performed on six specimens taken from the real off-highway axle. Figure 7a,b reports the typical microstructures observed before and after Nital 4% etching, which allow to define the composition of the matrix, according to [32]. Table 4 summarizes the obtained results and shows that the pearlite content is in the range between 20% and 50%, the average value being around 40%, as documented in Figure 7, while the Brinell hardness is in the range between 170 and 206. Such results are in fairly good agreement with those collected in Figure 3 and Tables 1 and 2 when analyzing some regions of the real off-highway axle. It is worth noting that the slight difference between the results reported here and in Section 2.2 can be explained due to the different analyzed region (i.e., the axle surface in Section 2.2 and the axle wall thickness in the present section). Moreover, only one metallographic analysis and three hardness measurements have been performed for each axle region in Section 2.2, while in the present section, six metallographic analyses and hardness measurements have been carried out.

Table 4. Pearlite content and Brinell hardness of tested specimens.

Material	Raw Component	Pearlite Content	HBW
EN-GJS-450-10	off-highway axle	20–50%	170–206

EN-GJS-450-10
Axle
Pearlite Content: 40%
HBW: 181

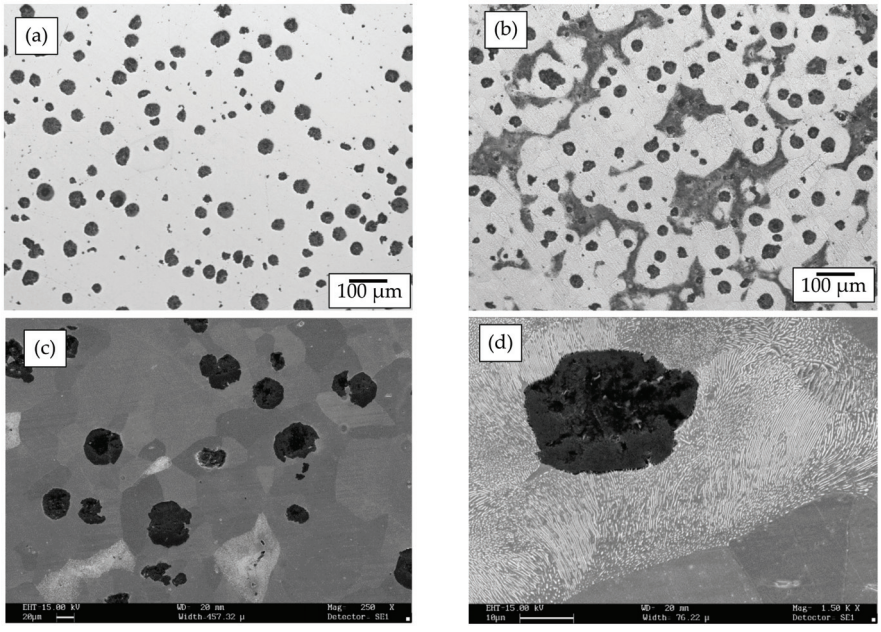

Figure 7. Microstructure of specimens made of EN-GJS-450-10 observed by (**a**,**b**) optical microscope and by (**c**,**d**) SEM. Microstructure (**a**) unetched and (**b**) after Nital 4% etched.

3.2. Static Tensile Test Results

Tensile engineering stress-strain curves obtained from the static tests of seven samples have been reported in Figure 8. It can be observed that all specimens provided a similar stress-strain curve, with only the exception of the sample St_450_04, which will be commented upon later, and it has been excluded from the calculation of the average mechanical properties. Table 5 summarizes the average mechanical properties obtained from the tensile tests. As a result, the static Young's modulus E_s equals 169,174 MPa, the proof stress $\sigma_{p,02}$ results equal to 328 MPa, and the ultimate tensile strength σ_R is 538 MPa, while the elongation after fracture A% and the reduction of area Z% are equal to 12.9% and 10%, respectively. Therefore, all values are in good agreement with those prescribed by [37] for an EN-GJS-450-10 nodular cast iron (i.e., $\sigma_{p,02,min}$ = 310 MPa, $\sigma_{R,min}$ = 450 MPa, and $A\%_{min}$ = 10%). Finally, the true stress-true strain experimental results have been fitted by using a Ramberg–Osgood expression:

$$\varepsilon = \frac{\sigma}{E_s} + \left(\frac{\sigma}{K}\right)^{\frac{1}{n}} \quad (2)$$

The strength coefficient K and the strain hardening exponent n, resulting from the fitting of all curves (apart from that derived from sample St_450_04), are reported in Table 5.

Table 5. Static tensile properties of EN-GJS-450-10. Average values and standard deviations.

Material	Raw Component	Parameter	E_s	$\sigma_{p0.2}$	σ_R	A	Z	K	n
			(MPa)	(MPa)	(MPa)	(%)	(%)	(MPa)	(/)
EN-GJS-450-10	off-highway axle	Average value	169,174	328	563	12.9	10	806	0.1584
		Standard deviation	2383	4	9	1.3	1	26	0.0113

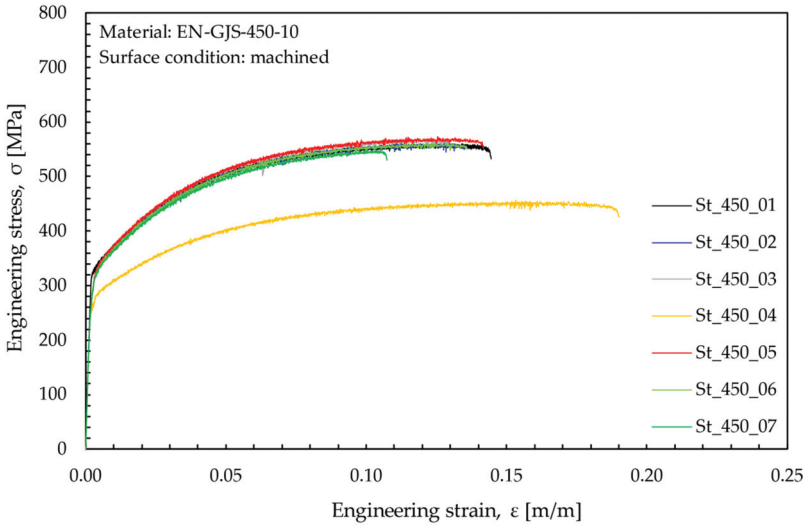

Figure 8. Static engineering stress-strain curves for EN-GJS-450-10.

It has been observed from Figure 8 that the stress-strain curve of sample St_450_04 is different from those generated by all other samples. In more detail, sample St_450_04 exhibited a lower ultimate tensile strength σ_R and a higher elongation after fracture A%, while its elastic modulus resulted in E_s = 166036 MPa, which is only 2% lower than the average value derived by other samples (see Table 5). To learn more about the reasons for such different behaviours, metallographic analyses and Brinell hardness measurements according to [32,33] have been performed on sample St_450_04 and also on sample St_450_05, for comparison purposes. Figure 9 shows the microstructures observed before and after Nital 4% etching and highlights that sample St_450_04 has a pearlite content between 20% and 30% and a Brinell hardness of 127, while sample St_450_05 has a pearlite content between 40% and 50% and a Brinell hardness of 199. In several works in the literature [38–41], it has been shown that as the pearlite content increases in the microstructure, the Brinell hardness, the proof stress $\sigma_{p,02,}$ and the ultimate tensile strength σ_R increases, making the material less ductile. In more detail, in [41], a Follansbee and Estrin-Kocks–Mecking approach accounting for the ferritic grain size and volume fraction of pearlite has been adopted to explicitly correlate the tensile behavior of EN-GJS-400 with its microstructural parameters. The results obtained here are in agreement with those reported in the literature, since sample St_450_04 has a significantly lower pearlite content than other samples, and it therefore also exhibited lower values of the Brinell hardness, the proof stress $\sigma_{p,02}$, and the ultimate tensile strength σ_R.

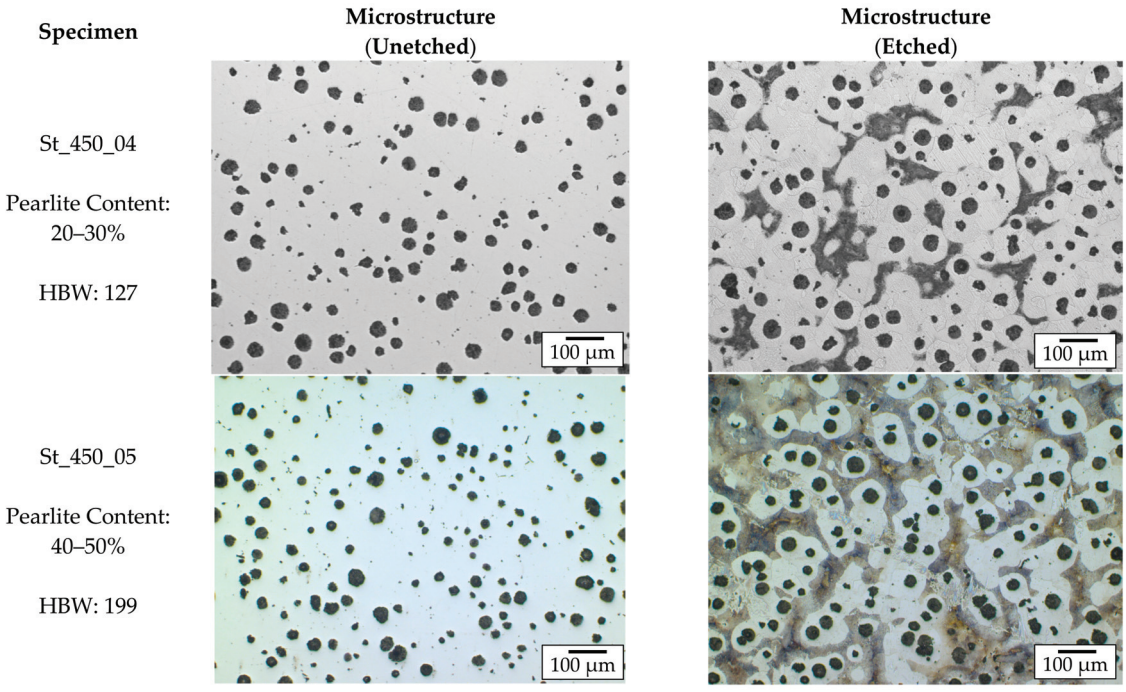

Figure 9. Comparison of the microstructures and Brinell hardnesses of specimens St_450_05 and St_450_04 tested under static tensile loading.

3.3. Strain-Controlled Fatigue Test Results

Each specimen tested under strain-controlled fatigue loading provided the number of reversals to failure $2N_f$ as a function of the applied strain amplitude ε_a and the stress-strain hysteresis loops recorded during the test.

The experimental data $2N_f$ versus ε_a have been collected in Figure 10 for each test series, and they have been fitted using the Basquin [42], Manson [43], and Coffin [44] equations, according to which the total strain amplitude ε_a is divided into its elastic ($\varepsilon_{a,el}$) and plastic ($\varepsilon_{a,pl}$) components [45]:

$$\varepsilon_a = \varepsilon_{a,el} + \varepsilon_{a,pl} = \frac{\sigma'_f}{E}(2N_f)^b + \varepsilon'_f(2N_f)^c \quad (3)$$

The previous expression shows that four unknown material parameters, σ'_f, ε'_f, b and c, in addition to the modulus of elasticity E, must be derived by fitting the experimental fatigue results. The same strain-controlled fatigue data are usually employed to fit the material parameters K′ and n′ of a Ramberg–Osgood-type equation, which describes the stabilized stress-strain relationship due to cycling loadings:

$$\varepsilon = \varepsilon_{el} + \varepsilon_{pl} = \frac{\sigma}{E} + \left(\frac{\sigma}{K'}\right)^{\frac{1}{n'}} \quad (4)$$

By equating the elastic and plastic strain components of Equations (3) and (4), respectively, and removing the dependence on the number of reversals to failure $2N_f$, the following compatibility equations can be derived [26]:

$$\begin{aligned} n' &= \frac{b}{c} \\ K' &= \frac{\sigma'_f}{(\varepsilon'_f)^{\frac{b}{c}}} \end{aligned} \quad (5)$$

Such expressions highlight that only five among the seven material parameters (σ'_f, ε'_f, b, c, E, K′, and n′) appearing in Equations (3) and (4) are independent. In the recent literature [16,46,47], the compatibility between material properties has been further investigated with the aim of providing a unified treatment of the stress-strain-life experimental data.

Before fitting the experimental results to derive the material parameters to be input in Equations (3) and (4), the stress-strain hysteresis loops have been analyzed. The tested EN-GJS-450-10 material does not show a stabilized stress-strain behavior during the applied cyclic deformations; therefore, the hysteresis loops recorded at half the fatigue life, reported in Figure 11, have been evaluated for each tested specimen. First, the elastic strain component has been derived by considering the tangent to the decreasing and increasing linear parts of the analyzed hysteresis loop [35,36], which exhibit almost identical slopes. After that, the plastic strain amplitude was evaluated as half the difference between the total and the elastic strain ranges (i.e., maximum minus minimum values), that is, $\varepsilon_{a,pl} = (\Delta\varepsilon\text{-}\Delta\varepsilon_{el})/2$. The plastic strain component has been evaluated only for specimens exhibiting plastic strains greater than a limit value ε_0 [46,48], which has been set here to 0.01% (100 με, where 1 $\mu\varepsilon = 10^{-6}$ m/m) based on the accuracy of the adopted experimental equipment. Finally, the stress range $\Delta\sigma$ has been derived as the difference between the maximum stress and the minimum stress of the considered hysteresis loop, then the stress amplitude resulted in $\sigma_a = \Delta\sigma/2$. It should be noted that the hysteresis loops recorded at half fatigue life were characterized by a stress ratio R_σ (defined as the ratio between the minimum and the maximum measured stresses), which is different from the nominal strain ratio R_ε. In particular, it ranged between −1.23 and −1.08 in Figure 11a (machined, $R_\varepsilon = -1$), between −1.36 and −0.76 in Figure 11b (as-cast, $R_\varepsilon = -1$), between −1.02 and −0.55 in Figure 11c (machined, $R_\varepsilon = 0.1$), and between −1 and −0.59 in Figure 11d (machined, $R_\varepsilon = 0.5$).

Having in hand the strain components $\varepsilon_{a,el}$ and $\varepsilon_{a,pl}$, the stress amplitude σ_a, and the fatigue life $2N_f$ of each tested specimen, Equations (3) and (4) can be fitted to derive the unknown material parameters. To this aim, two different procedures have been adopted here, (i) a non-compatible one and (ii) a compatible one, depending on whether Equation (5) was strictly satisfied or not.

According to the non-compatible procedure, which is typically employed in practice, the two sets of material parameters appearing in Equations (3) and (4), respectively, are derived by fitting the relevant experimental results independently from the others, even if they have been generated by a unique series of experiments. As a consequence, the compatibility conditions (Equation (5)) are verified only approximately [26]. Moreover, the elastic modulus is assumed equal to that derived in static tensile tests (E_s). Therefore, the equations to be fitted according to the standard procedure [49] are the following:

$$\left.\begin{array}{l}\varepsilon_{a,el} = \frac{\sigma'_f}{E_s}(2N_f)^b \\ \varepsilon_{a,pl} = \varepsilon'_f(2N_f)^c\end{array}\right\} \rightarrow \text{output } \sigma'_f,\ \varepsilon'_f, b, c \quad \varepsilon_{a,pl} = \left(\frac{\sigma_a}{K'}\right)^{\frac{1}{n'}} \Bigg\} \rightarrow \text{output } n',\ K' \qquad (6)$$

On the other hand, the compatible procedure assures that the compatibility conditions (Equation (5)) are strictly verified. First, the elastic strain-life data, converted in a stress-based form according to Basquin [42], and the plastic strain-life data are fitted according to the standard procedure [49] to derive the material constants σ'_f, ε'_f, b, and c. After that, the compatibility equations (Equation (5)) are applied to determine the coefficients of the cyclic stress-strain curve. Finally, the dynamic modulus of elasticity E is derived by fitting the elastic strain-life data.

$$\left.\begin{array}{l}\sigma_a = \sigma'_f(2N_f)^b \\ \varepsilon_{a,pl} = \varepsilon'_f(2N_f)^c\end{array}\right\} \rightarrow \text{output } \sigma'_f,\ \varepsilon'_f, b, c$$
$$\left.\begin{array}{l}n' = \frac{b}{c} \\ K' = \frac{\sigma'_f}{(\varepsilon'_f)^{\frac{b}{c}}}\end{array}\right\} \rightarrow \text{output } n',\ K' \qquad (7)$$
$$\left.\varepsilon_{a,el} = \frac{\sigma'_f}{E}(2N_f)^b\right\} \rightarrow \text{output E}$$

The application of the compatible procedure and the derivation of the coefficients of the cyclic stress-strain curve (Equation (4)) have been performed here only for the cases relevant to a strain ratio $R_\varepsilon = -1$. In such cases, the non-compatible (Equation (6)) and the compatible procedures (Equation (7)) provided similar results, so that the straight lines of Figure 10 derived on the basis of the two methods would be hardly distinguishable one from the other. Therefore, only the strain-life curves evaluated according to the non-compatible procedure have been reported in Figure 10; however, the material parameters obtained following both methods have been included in the same figure, where available.

Figure 11 reports the hysteresis loops recorded at half the fatigue life and the resulting cyclic stress-strain curve according to both the non-compatible (Equation (6)) and the compatible procedures (Equation (7)), where available. Figure 11a,b refers to the case $R_\varepsilon = -1$ and include also the monotonic static curve previously derived in Figure 8; they show that the tested EN-GJS-450-10 material exhibited a hardening behavior. On the other hand, when a strain amplitude lower than 0.2% is applied at $R_\varepsilon = -1$, nearly elastic strains are applied, and the material response is stable during the fatigue test.

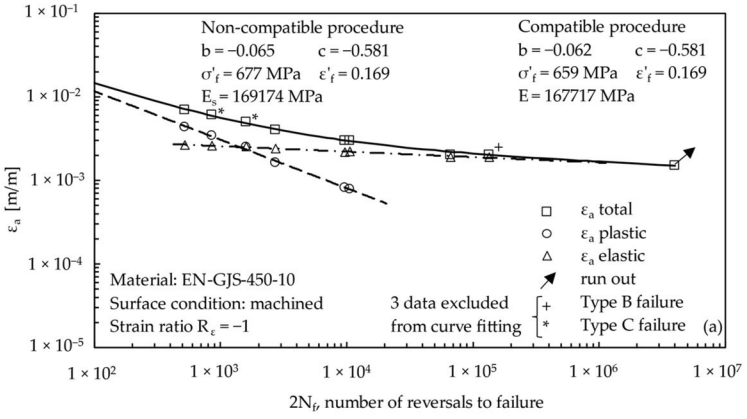

Figure 10. *Cont.*

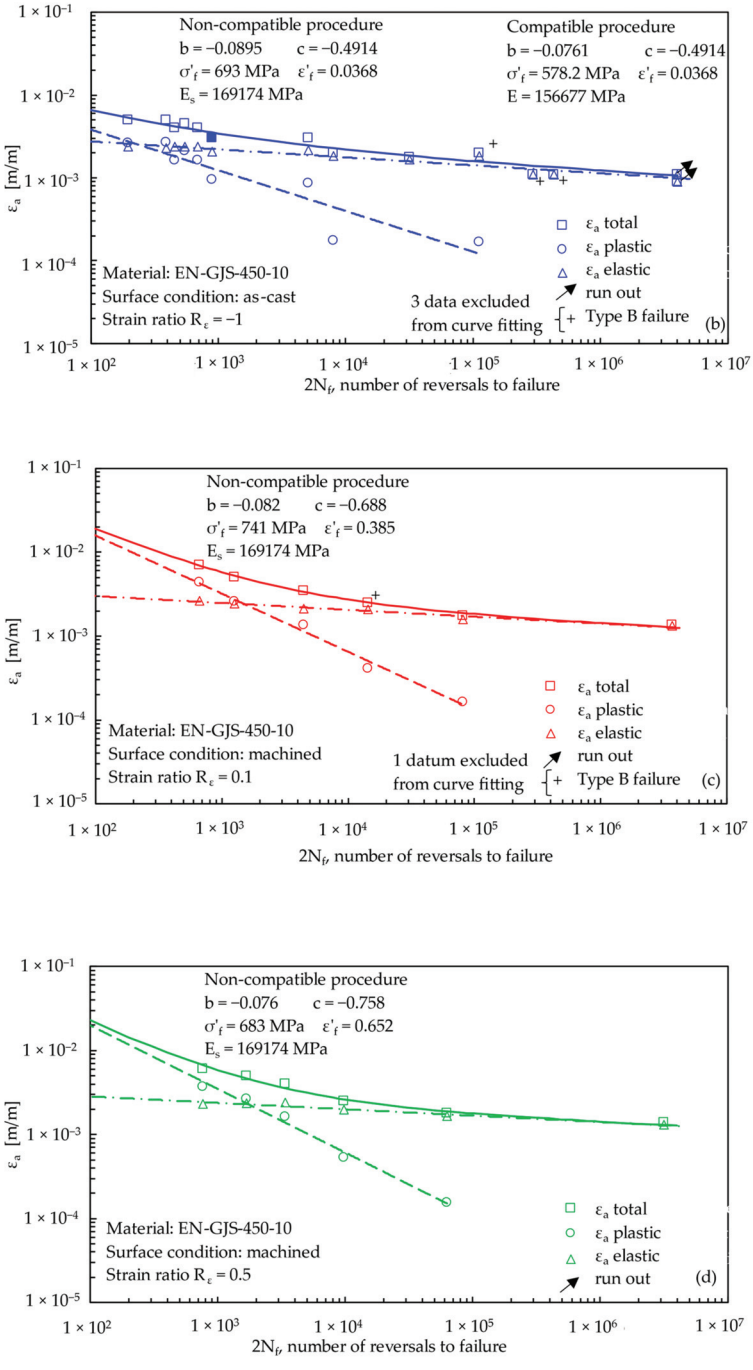

Figure 10. Manson–Coffin curves of EN-GJS-450-10 tested under $R_\varepsilon = -1$ in the (**a**) machined and (**b**) as-cast conditions; (**c**) $R_\varepsilon = 0.1$ and (**d**) $R_\varepsilon = 0.5$ in the machined conditions. The figures include the curves fitted by the non-compatible procedure and the parameters to input in Equation (3) according to both the non-compatible and the compatible procedures.

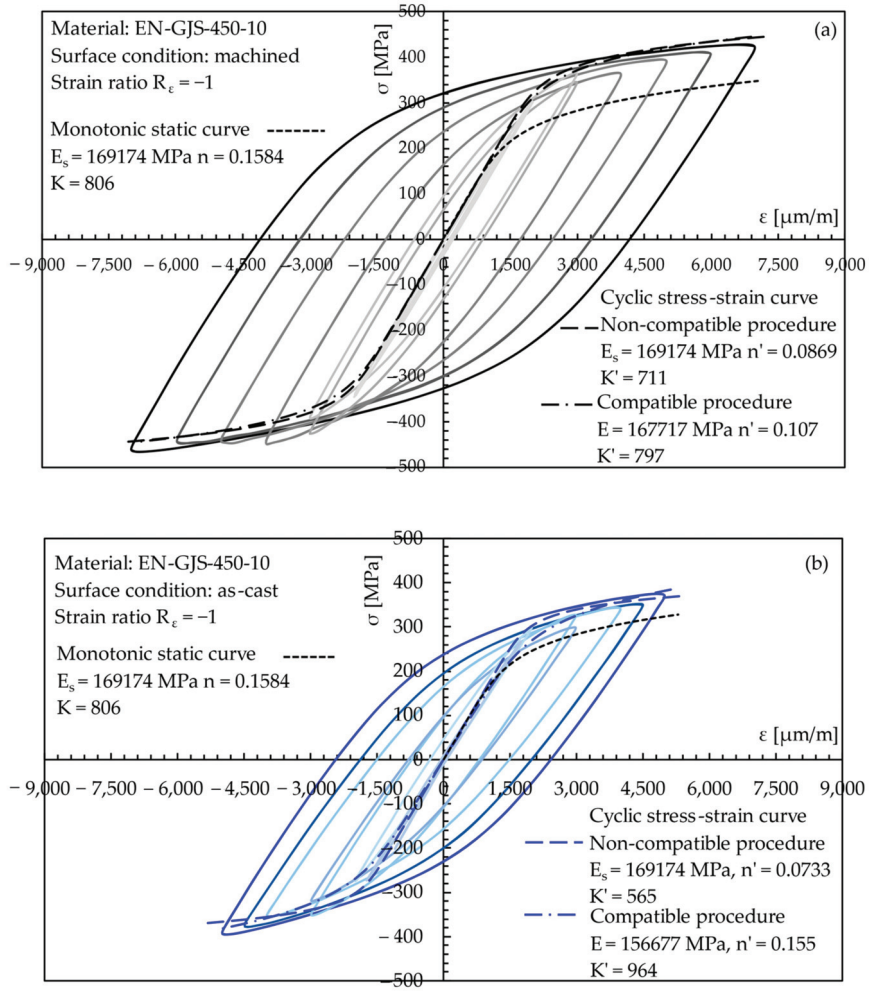

Figure 11. *Cont.*

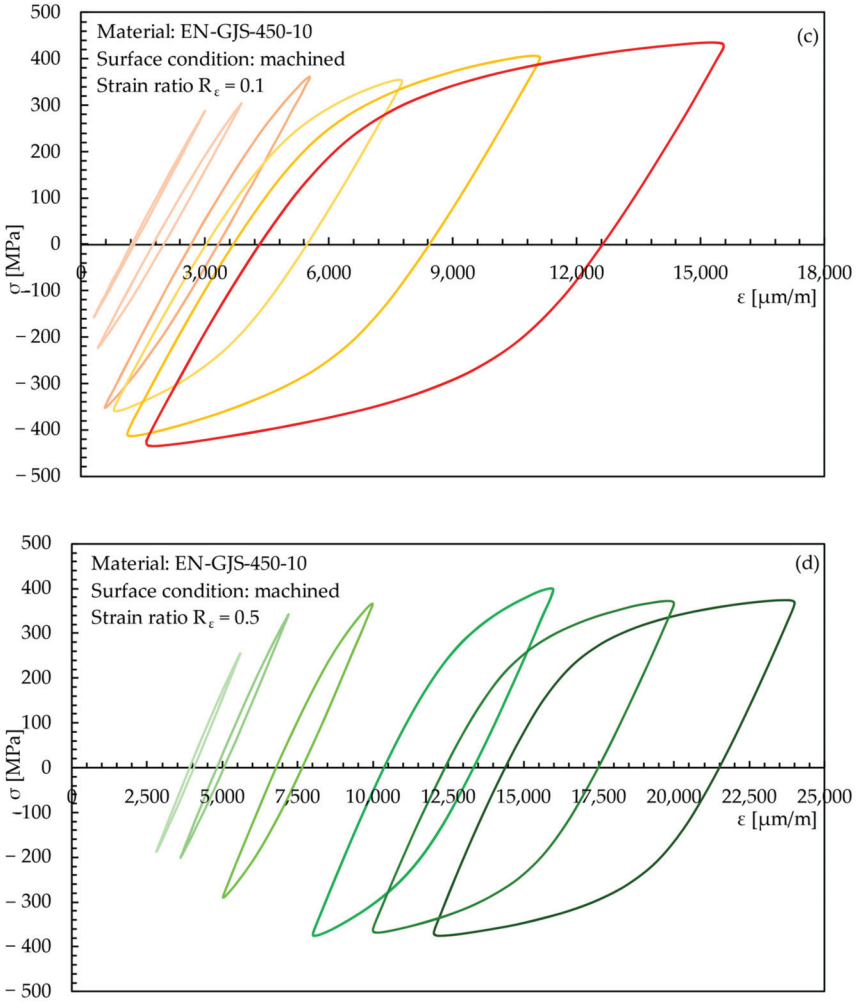

Figure 11. Half-life hysteresis loops of EN-GJS-450-10 tested under R_ε = -1 in the (**a**) machined and (**b**) as-cast conditions; (**c**) R_ε = 0.1 and (**d**) R_ε = 0.5 in the machined conditions. For comparison purposes, the figures relevant to $R_\varepsilon = -1$ include the monotonic static curve, according to Equation (2) and the parameters of Table 5, and the cyclic stress-strain curves, according to Equation (4) and the parameters fitted by both the non-compatible and the compatible procedures.

3.4. Failure Location and Fracture Surface Analyses

The failure criterion adopted in both static and fatigue tests was the complete separation of the specimen. Three different failure locations have been observed: (A) within the gauge length, where the stress state is uniaxial and uniform; (B) at the end of the fillet radius, where a stress concentration factor K_t in the range between 1.07 (Figure 5) and 1.10 (Figure 6) exists; and (C) where the extensometer knife edges were in contact with the specimen surface. Figure 12 shows these failure locations, while Table 6 summarizes the number of failures of each type observed during static and fatigue tests. It is worth noting that only experimental fatigue results generated from specimens exhibiting failure of type (A) (Figure 12 and Table 6) have been adopted to fit the parameters of Equations (3) and (4). Nevertheless, experimental results generated from specimens exhibiting failure of

type (B) and (C) have been included in the plots ε_a versus $2N_f$ of Figure 10, for comparison purposes.

Table 6. Summary of the failure locations observed after the static and fatigue tests (see definitions in Figure 12).

Material	Raw Component	Specimen Surface	Test	Rε	N° Tests	Type A	Type B	Type C	Run Out
EN-GJS-450-10	off-highway axle	machined	Static	n.a.	7	6	0	1	n.a.
			Fatigue *	−1	10	6	1	2	1
				0.1	6	5	1	0	0
				0.5	6	6	0	0	0
		as-cast	Fatigue *	−1	14	9	3	0	2

* Strain-controlled fatigue test. n.a. = not applicable.

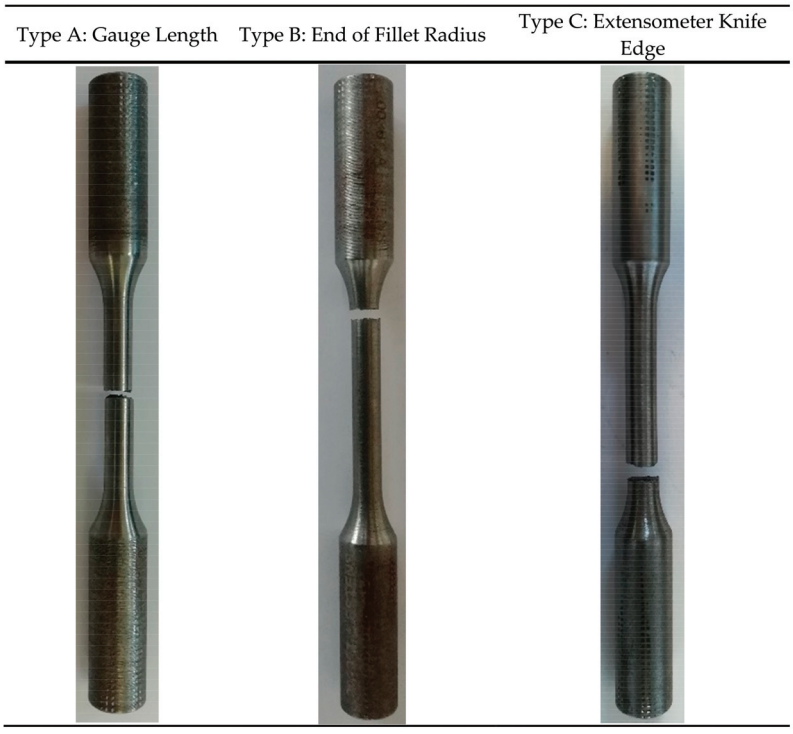

Figure 12. Failure locations observed after the static and the strain-controlled fatigue tests. The figure reports examples relevant to plain cylindrical specimens (Figures 4 and 5); however, the same definitions also apply to plain flat specimens (Figure 6).

Figure 13 reports some examples of fracture surfaces generated by static testing plain cylindrical specimens (Figure 4). It can be observed that EN-GJS-450-10 specimens exhibited an almost flat fracture surface both for specimen St_450_03 and St_450_04, the last one having provided a stress-strain curve different from the others, as already discussed in Section 3.2.

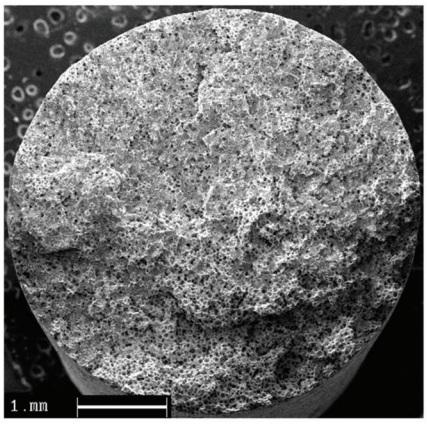

EN-GJS-450-10, machined, St_450_03, $\sigma_{p0.2}$ = 328 MPa, σ_R = 570 MPa, Z = 9.1%

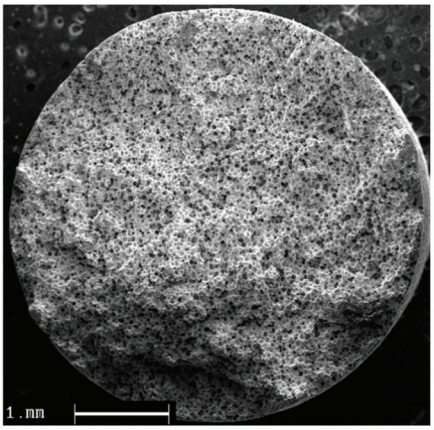

EN-GJS-450-10, machined, St_450_04, $\sigma_{p0.2}$ = 282 MPa, σ_R = 457 MPa, Z = 17.8%

Figure 13. Fracture surfaces of plain cylindrical specimens (Figure 4) after static tensile tests.

Figure 14 reports some typical fracture surfaces of plain cylindrical (Figure 5) and plain flat (Figure 6) specimens made of EN-GJS-450-10 subjected to strain-controlled fatigue tests. In more detail, the figure reports two examples of fracture surfaces for each test series: one referred to a high strain amplitude, and the other to a medium-low strain amplitude.

It can be observed that machined specimens (Figure 14a,b,e–h) exhibited crack initiation from the surface, while no evident defects have been observed.

Dealing with specimens tested with an as-cast surface, crack initiation occurred in most cases from the as-cast surface (Figure 14c), but in a few cases, crack initiation was observed also from one of the machined surfaces (Figure 14d). Moreover, some samples failed prematurely as compared to the average trend; see, for example, the experimental result represented with filled marker in Figure 10b. Its fracture surfaces are reported in Figure 15a,b, which show that a defect was present close to the as-cast surface. To investigate in more detail the type of defect, an SEM analysis of the fracture surface has been performed. Figure 15c–e show that the defect was an inclusion formed by a silicon oxide, as demonstrated by EDS analysis shown in Figure 16a, while Figure 16b reports the EDS analysis of the material region close to the defect and shows that other elements such as oxygen, silicon, magnesium, and iron were detected. Therefore, the defect appears as a slag inclusion resulting from the casting process. Moreover, Figure 15g,h report the microstructures observed by optical microscope at the center of the sample and at the as-cast surface, respectively, and show that degenerate graphite is present in a 0.1 mm layer close to the as-cast surface, due to the rapid cooling process.

Finally, the crack propagation phase is distinguishable only in cases of medium-low strain amplitudes (Figure 14b,d,f,h), while it is almost invisible in the cases of high strain amplitudes (Figure 14a,c,e,g).

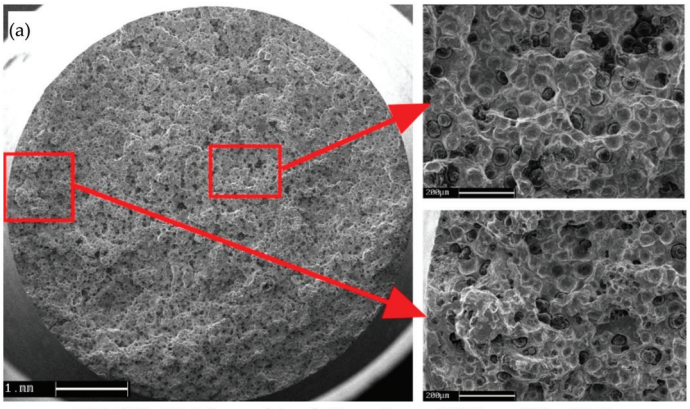

EN-GJS-450-10, machined, $R_\varepsilon = -1$, $\varepsilon_a = 3000$ µε, $2N_f = 9646$

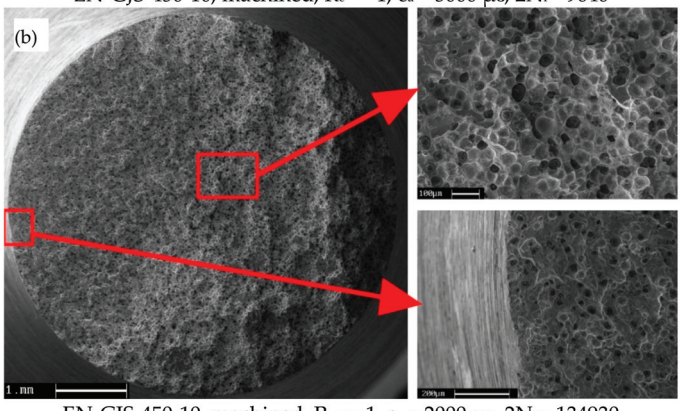

EN-GJS-450-10, machined, $R_\varepsilon = -1$, $\varepsilon_a = 2000$ µε, $2N_f = 134930$

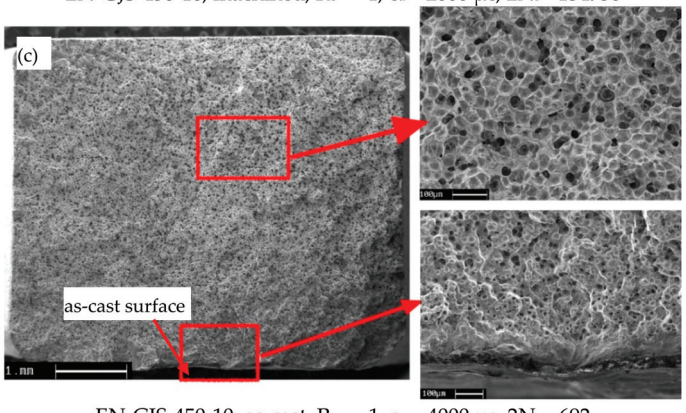

EN-GJS-450-10, as-cast, $R_\varepsilon = -1$, $\varepsilon_a = 4000$ µε, $2N_f = 692$

Figure 14. *Cont.*

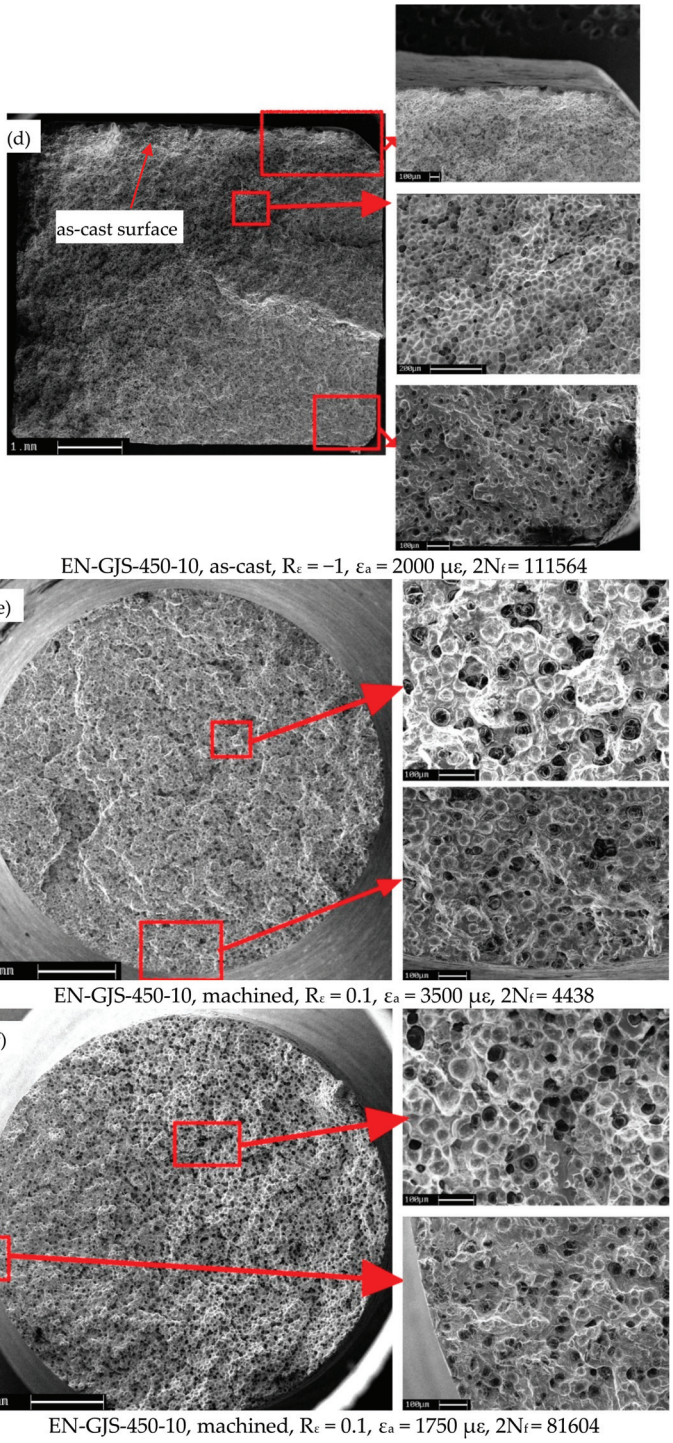

Figure 14. *Cont.*

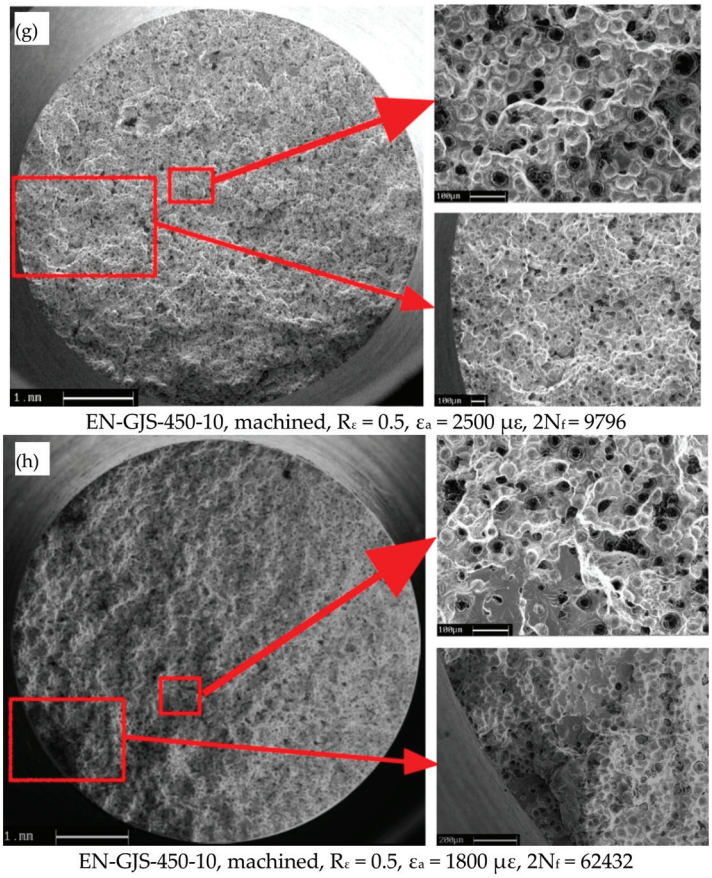

Figure 14. Fracture surfaces after strain-controlled fatigue tests of EN-GJS-450-10 plain specimens (Figures 5 and 6): (**a**,**b**) $R_\varepsilon = -1$, machined conditions, (**c**,**d**) $R_\varepsilon = -1$, as-cast conditions; (**e**,**f**) $R_\varepsilon = 0.1$ and (**g**,**h**) $R_\varepsilon = 0.5$ in the machined conditions.

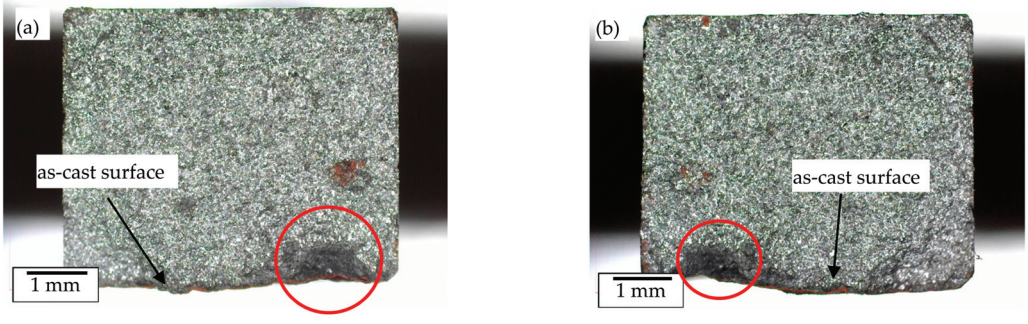

Figure 15. *Cont.*

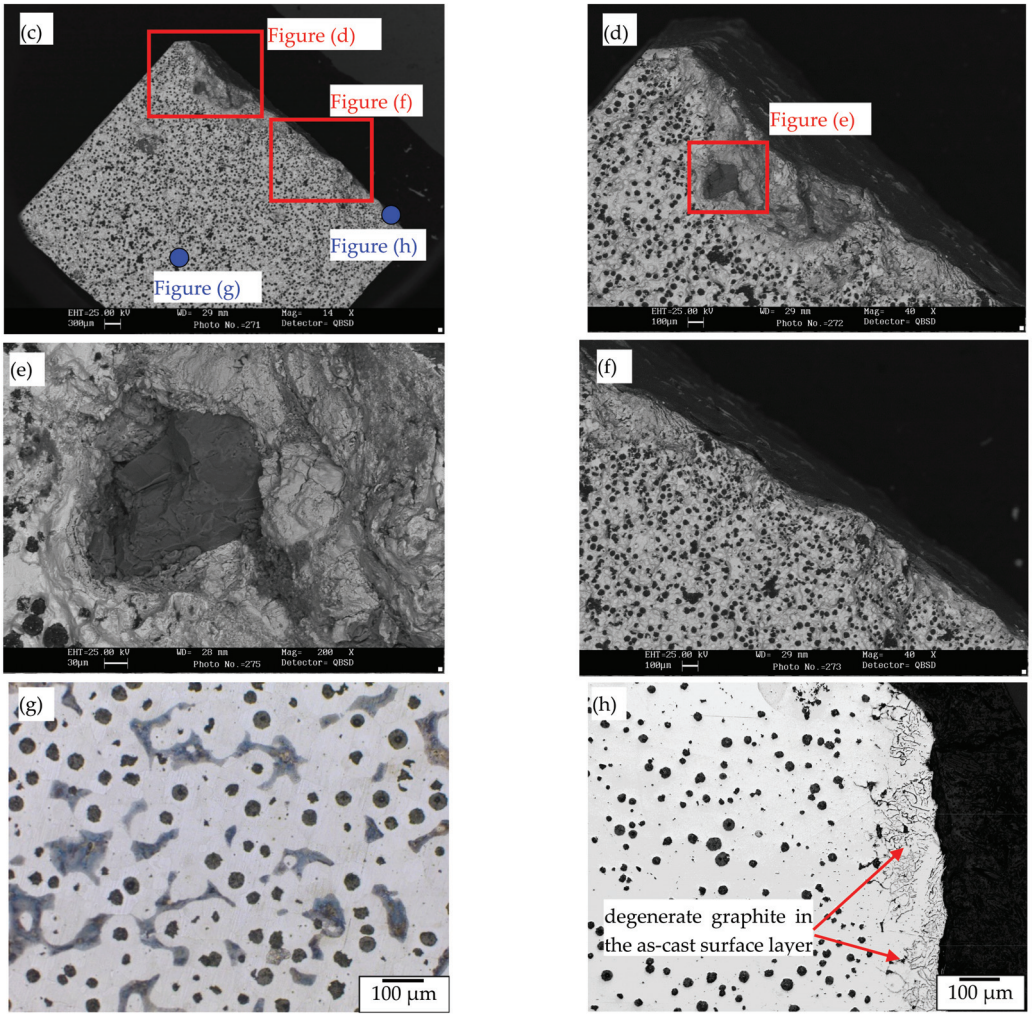

Figure 15. Fracture surfaces of a plain specimen (Figure 6) made of EN-GJS-450-10 and tested at ε_a = 3000 µε under $R_\varepsilon = -1$ in the as-cast conditions. Failure occurred at $2N_f$ = 898. Fracture surfaces observed with (**a**,**b**) a digital microscope and (**c**–**f**) a SEM microscope. Microstructure observed by optical microscope at (**g**) the center of the sample and (**h**) the as-cast surface.

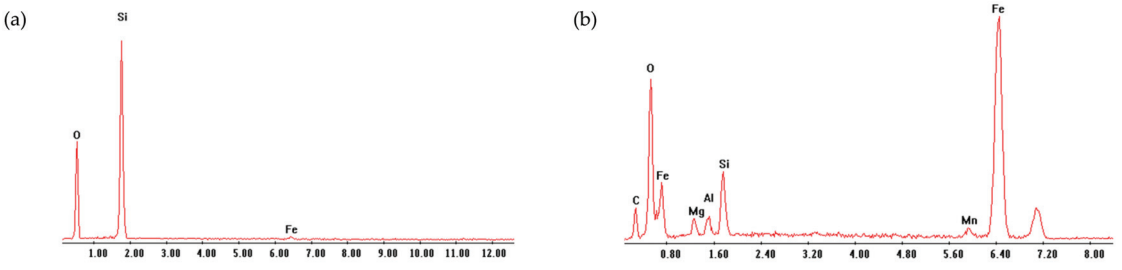

Figure 16. EDS pattern of (**a**) the defect observed in the fracture surface shown in Figure 15; (**b**) the material region closed to the defect.

4. Discussion

It has been observed in Section 3.3 by comparing Figure 10a,b that as-cast specimens have exhibited a lower fatigue life as compared to machined specimens when subjected to strain-controlled fatigue tests under the same strain amplitude at a strain ratio $R_\varepsilon = -1$. This is due to a twofold effect of:

- the higher roughness of as-cast surface as compared to the machined one;
- the presence of defects underneath the as-cast surface.

Therefore, in the present work, the casting skin is defined as the rim zone of the casting, consisting of both surface roughness and a deviating microstructure, which includes both degenerated graphite layer (DGL) with lamellar graphite (Figure 15h) and slag inclusions (see for example Figure 15c–e). The high-cycle downgrading effect of the casting skin at a strain ratio $R_\varepsilon = -1$ can be quantified by introducing a reduction coefficient K_l^*, which has been defined at 2 million cycles (i.e., $2N_f = 4{\cdot}10^6$ reversals) to failure, according to the following expression:

$$K_l^* = \frac{\varepsilon_{a,R_\varepsilon = -1,2N_f = 4\cdot10^6,\text{machined}}}{\varepsilon_{a,R_\varepsilon = -1,2N_f = 4\cdot10^6,\text{as-cast}}} \quad (8)$$

Figure 17 compares the Manson–Coffin curves of specimens made of EN-GJS-450-10 and tested under $R_\varepsilon = -1$ in the machined and as-cast conditions and shows that the coefficient K_l^* is equal to 1.40. In addition, a red circle in Figure 17 highlights that an as-cast sample has almost the same fatigue life of a machined one lying close to the relevant fatigue curve, both samples having been tested at $\varepsilon_a = 2000$ με. However, it should be noted that the as-cast sample failed from one of the machined surfaces, as documented in Figure 14d, which precisely shows the fracture surface of the considered sample. Therefore, the experimental results circled in red are not surprising, the fatigue crack initiating in both cases from a machined surface.

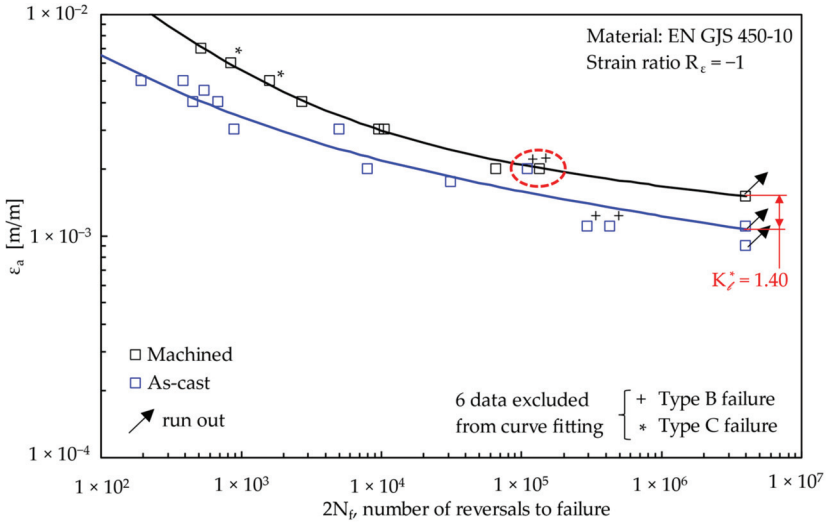

Figure 17. Comparison of the Manson–Coffin curves of EN-GJS-450-10 tested under $R_\varepsilon = -1$ in the machined (Figure 10a) and as-cast (Figure 10b) conditions. Derivation of the parameter K_l^*.

It has been shown in Section 3.3 that machined specimens made of EN-GJS-450-10 have been tested under strain-controlled fatigue loading by adopting different values of the strain ratio R_ε, namely −1, 0.1, and 0.5. By comparing Figure 10a with Figure 10c,d, it can be observed that specimens subjected to a given strain amplitude exhibited a lower fatigue life when increasing the strain ratio R_ε from −1 to 0.5. Such experimental data can

be summarized by using the Smith–Watson–Topper (SWT) expression [50] (Equation (9)), which is able to account for different mean strains.

$$\sigma_{max}\varepsilon_a = \frac{\sigma'^2_f}{E}(2N_f)^{2b} + \sigma'_f\varepsilon'_f(2N_f)^{b+c} \quad (9)$$

In the previous expression, parameters σ'_f, ε'_f, b, and c are those referring to the strain ratio $R_\varepsilon = -1$.

Figure 18 compares the experimental results of machined specimens generated under $R_\varepsilon = -1$, 0.1, and 0.5, which have been expressed in terms of number of reversals to failure $2N_f$ as a function of the parameter $\sigma_{max}\cdot\varepsilon_a$. The figure includes the curve $\sigma_{max}\cdot\varepsilon_a$ versus $2N_f$ (Equation (9)), where the adopted material parameters are those fitted by applying the "non-compatible procedure" only to experimental results relevant to $R_\varepsilon = -1$ (see Figure 10a). It can be observed that this curve is also in fairly good agreement with experimental results relevant to $R_\varepsilon = 0.1$ and 0.5. Accordingly, the SWT expression (Equation (9)) appears to be useful for design engineers to account for the strain ratio effect of EN-GJS-450-10 nodular cast iron under fatigue loading conditions.

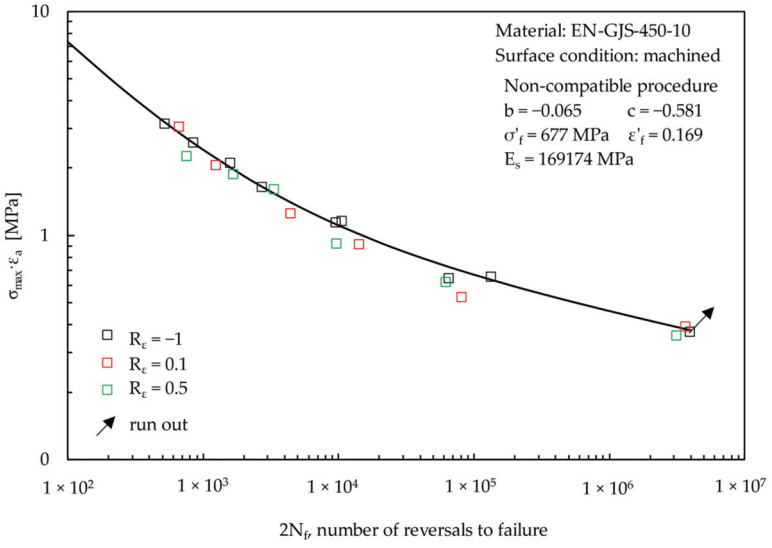

Figure 18. Strain-controlled fatigue test results generated from EN-GJS-450-10 specimens tested under $R_\varepsilon = -1$ (Figure 10a), 0.1 (Figure 10c), and 0.5 (Figure 10d) in the machined conditions and expressed in terms of the parameter $\sigma_{max}\cdot\varepsilon_a$, according to Smith–Watson–Topper [50]. The figure includes the curve $\sigma_{max}\cdot\varepsilon_a$ versus $2N_f$ (Equation (9)), the material parameters being those fitted only on experimental results relevant to $R_\varepsilon = -1$, as reported inside the figure.

Finally, the results reported in the present work appear useful for engineers engaged in the fatigue design of real off-highway axles made of EN-GJS-450-10. In more detail, the cyclic stress-strain curve of the material can be given as input to an FE code in order to properly simulate the elastic-plastic behavior of the material in real off-highway axles under in-service loading conditions. The local strain amplitude ε_a and local strain ratio R_ε can be calculated at the potential crack initiation location from the elastic-plastic FE analysis. After that, the fatigue life $2N_f$ can be estimated by comparing the calculated strain amplitude ε_a with the proper Manson–Coffin curve, by taking into account both the local strain ratio R_ε, through the Smith–Watson–Topper (SWT) expression, and the surface condition, through the reduction coefficient K_1^*.

5. Conclusions

In the present paper, the effects of the casting skin and the strain ratio on the strain-controlled fatigue behaviour of a nodular cast iron EN-GJS-450-10 employed in a real off-highway axle have been investigated. To do this, specimens were taken from a real axle to include the effects of the manufacturing processes. The microstructures of both the axle and the specimens have been identified by metallographic analysis and Brinell hardness measurements. Afterwards, plain specimens made of EN-GJS-450-10 with machined surface have been tested under static and strain-controlled fully reversed ($R_\varepsilon = -1$) fatigue loadings. Fatigue tests have been performed also on specimens with as-cast surface under $R_\varepsilon = -1$, to investigate the detrimental effect of the casting skin, as well as on machined specimens under $R_\varepsilon = 0.1$ and 0.5, to analyze the strain ratio effect. All fracture surfaces have been analyzed by SEM.

The following conclusions can be drawn:

- The analysed EN-GJS-450-10 has graphite nodules with regular spheroidal shape dispersed in a matrix consisting of 50% ferrite and 50% pearlite. Specimens tested under static tensile loading exhibited an almost flat fracture surface and provided a proof stress $\sigma_{P,02}$ equal to 328 MPa, an ultimate tensile strength σ_R equal to 538 MPa, and an elongation after fracture A% and a reduction of area Z% equal to 12.9% and 10%, respectively.
- Concerning the fatigue behaviour, the experimental data were fitted by the Manson–Coffin equation according to the common practice, as well as to a recent procedure, which assures, strictly speaking, the compatibility conditions between stress-strain-life data.
- The analysis of the half fatigue life hysteresis loops shows that the stress ratio R_σ was different from the nominal strain ratio R_ε. In particular, it ranged between -1.36 and -0.76 when $R_\varepsilon = -1$, between -1.02 and -0.55 when $R_\varepsilon = 0.1$, and between -1 and -0.59 when $R_\varepsilon = 0.5$. Moreover, the comparison of the cyclic stress-strain curve with the monotonic static curve highlighted that the tested material exhibited a hardening behavior.
- The analysis of the fracture surfaces shows that machined specimens exhibited crack initiation from the surface, while as-cast specimens failed in most cases from the as-cast surface or from sub-surface defects, such as silicon oxides. A reduction coefficient K_I^* has been defined to account for the high-cycle downgrading effect of the casting skin. At $2N_f = 4 \cdot 10^6$ reversals to failure and with reference to a strain ratio $R_\varepsilon = -1$, K_I^* was equal to 1.40.
- Finally, it has been observed that the higher the strain ratio, the shorter the fatigue life for a given strain amplitude. Experimental fatigue data generated from machined specimens tested under different strain ratios, from -1 to 0.5, have been successfully correlated by using a Smith–Watson–Topper (SWT) expression, previously fitted only on experimental results relevant to $R_\varepsilon = -1$.

Author Contributions: Conceptualization, G.M.; methodology, F.S., A.C., G.M., M.F.; investigation, F.S.; data curation, F.S.; writing—original draft preparation, A.C.; writing—review and editing, A.C., M.F., G.M.; visualization, F.S., A.C., M.F.; validation, A.C., G.M., supervision, G.M. All authors have read and agreed to the published version of the manuscript.

Funding: This research received no external funding.

Institutional Review Board Statement: Not applicable.

Informed Consent Statement: Not applicable.

Data Availability Statement: All data are contained within the present article.

Conflicts of Interest: The authors declare no conflict of interest.

References

1. Borsato, T.; Berto, F.; Ferro, P.; Carollo, C. Effect of in-mould inoculant composition on microstructure and fatigue behaviour of heavy section ductile iron castings. *Procedia Struct. Integr.* **2016**, *2*, 3150–3157. [CrossRef]
2. Konečná, R.; Kokavec, M.; Nicoletto, G. Surface conditions and the fatigue behavior of nodular cast iron. *Procedia Eng.* **2011**, *10*, 2538–2543. [CrossRef]
3. Benam, A.S. Effect of Shot Peening on the High-Cycle Fatigue Behavior of High-Strength Cast Iron with Nodular Graphite. *Met. Sci. Heat Treat.* **2017**, *58*, 568–571. [CrossRef]
4. Meyer, N.; Fatemi, A.; McCutcheon, S.; Havard, B.; Fairchilds, W. Fatigue Behavior of Cast Iron Including Mean Stress Effects. *SAE Int. J. Mater. Manuf.* **2015**, *8*, 425–434. [CrossRef]
5. Shirani, M.; Härkegård, G. Large scale axial fatigue testing of ductile cast iron for heavy section wind turbine components. *Eng. Fail. Anal.* **2011**, *18*, 1496–1510. [CrossRef]
6. Shirani, M.; Härkegård, G. Fatigue life distribution and size effect in ductile cast iron for wind turbine components. *Eng. Fail. Anal.* **2011**, *18*, 12–24. [CrossRef]
7. Clement, P.; Angeli, J.P.; Pineau, A. Short crack behaviour in nodular cast iron. *Fatigue Fract. Eng. Mater. Struct.* **1984**, *7*, 251–265. [CrossRef]
8. Agha, H.Y.; Beranger, A.-S.; Billardon, R.; Hild, F. High-cycle fatigue behaviour of spheroidal graphite cast iron. *Fatigue Fract. Eng. Mater. Struct.* **1998**, *21*, 287–296. [CrossRef]
9. Yamabe, J.; Kobayashi, M. Influence of casting surfaces on fatigue strength of ductile cast iron. *Fatigue Fract. Eng. Mater. Struct.* **2006**, *29*, 403–415. [CrossRef]
10. Zambrano, H.R.; Härkegård, G.; Stärk, K.F. Fracture toughness and growth of short and long fatigue cracks in ductile cast iron EN-GJS-400-18-LT. *Fatigue Fract. Eng. Mater. Struct.* **2011**, *35*, 374–388. [CrossRef]
11. Shirani, M.; Härkegård, G.; Morin, N. Fatigue life prediction of components made of spheroidal graphite cast iron. *Procedia Eng.* **2010**, *2*, 1125–1130. [CrossRef]
12. Nadot, Y. Influence of casting defects on the fatigue limit of nodular cast iron. *Int. J. Fatigue* **2004**, *26*, 311–319. [CrossRef]
13. *SAE J 1099*; Technical Report on Low Cycle Fatigue Properties: Ferrous and Non Ferrous Materials. SAE International: Warrendale, PA, USA, 2002.
14. Petrenec, M.; Tesařová, H.; Beran, P.; Šmíd, M.; Roupcová, P. Comparison of low cycle fatigue of ductile cast irons with different matrix alloyed with nickel. *Procedia Eng.* **2010**, *2*, 2307–2316. [CrossRef]
15. Šamec, B.; Potrč, I.; Šraml, M. Low cycle fatigue of nodular cast iron used for railway brake discs. *Eng. Fail. Anal.* **2011**, *18*, 1424–1434. [CrossRef]
16. Meneghetti, G.; Ricotta, M.; Masaggia, S.; Atzori, B. Comparison of the low-cycle and medium-cycle fatigue behaviour of ferritic, pearlitic, isothermed and austempered ductile irons. *Fatigue Fract. Eng. Mater. Struct.* **2013**, *36*, 913–929. [CrossRef]
17. Boonmee, S.; Stefanescu, D.M. Effect of Casting Skin on Fatigue Properties of CG Iron. *Int. J. Met.* **2013**, *7*, 15–26. [CrossRef]
18. Nasu, S.; Fujita, S.; Furusato, N.; Yamada, S.; Hiratsuka, S. Effect of Casting Skin Condition on Fatigue Strength of Gray Cast Iron. *Int. J. Met.* **2016**, *11*, 155–161. [CrossRef]
19. Rehmer, B.; Skrotzki, B.; Glaubitz, S. Influence of casting skin on the fatigue lifetime of ferritic ductile cast iron. *Mater. Test.* **2016**, *59*, 5–10. [CrossRef]
20. Nain, P.K.S. The Effect of Remaining Casting Skin on Cast Iron Components Fatigue Strength. *Int. J. Eng. Res. Comput. Sci. Eng.* **2017**, *4*, 157–165.
21. Gróza, M.; Váradi, K. Fatigue Design of Ferritic-Pearlitic Nodular Cast Iron Components with Surface Discontinuities. *Stroj. Vestn. J. Mech. Eng.* **2018**, *64*, 373–382. [CrossRef]
22. Lundberg, M.; Peng, R.L.; Ahmad, M.; Bäckström, D.; Vuoristo, T.; Johansson, S. Fatigue Strength of Machined and Shot Peened Grey Cast Iron. *Adv. Mater. Res.* **2014**, *891–892*, 30–35. [CrossRef]
23. Bergner, K.; Bleicher, C.; Wagener, R. Influence of remaining casting skin on the fatigue strength of cast iron components. *Procedia Struct. Integr.* **2019**, *18*, 792–801. [CrossRef]
24. Bergner, K.; Hesseler, J.; Bleicher, C. Fatigue analysis of cast iron components considering the influence of casting skin. *Procedia Struct. Integr.* **2019**, *19*, 140–149. [CrossRef]
25. Anca, D.; Chisamera, M.; Stan, S.; Stan, I.; Riposan, I. Sulfur and Oxygen Effects on High-Si Ductile Iron Casting Skin Formation. *Coatings* **2020**, *10*, 618. [CrossRef]
26. Dowling, N.E. *Mechanical Behavior of Materials—Engineering Methods for Deformation, Fracture and Fatigue*, 4th ed.; Pearson: Harlow, UK, 2013.
27. Sonsino, C.M. Light-weight design chances using high-strength steels. *Mater. Werkst.* **2007**, *38*, 9–22. [CrossRef]
28. Hübner, P.; Pusch, G.; Krodel, L. Fatigue Behaviour of Cast Iron with Globular Graphite. *Adv. Eng. Mater.* **2004**, *6*, 541–544. [CrossRef]
29. Bleicher, C.; Wagener, R.; Kaufmann, H.; Melz, T. Fatigue strength of nodular cast iron with regard to heavy-wall applications. *Mater. Test.* **2015**, *57*, 723–731. [CrossRef]
30. Bleicher, C.; Wagener, R.; Kaufmann, H.; Melz, T. Influence of Different Load Histories on the Cyclic Material Behavior of Nodular Cast Iron for Thick-Walled Application. In Proceedings of the International Offshore and Polar Engineering Conference, San Francisco, CA, USA, 25–30 June 2017.

31. Heinrietz, A.; Hesseler, J. An approach for the fatigue estimation of porous cast iron based on non-destructive testing results. *MATEC Web Conf.* **2014**, *12*, 05001. [CrossRef]
32. *ISO/TR 945-3:2016*; Microstructure of Cast Irons, Part1: Graphite Classification by Visual Analysis. International Organization for Standardization (ISO): Geneva, Switzerland, 2016.
33. *ISO 6506-1:2014*; Metallic Materials—Brinell Hardness Test. International Organization for Standardization (ISO): Geneva, Switzerland, 2014.
34. *ISO 6892-1:2016*; Metallic Materials—Tensile Testing. International Organization for Standardization (ISO): Geneva, Switzerland, 2016.
35. *ISO 12106:2017*; Metallic Materials—Fatigue Testing—Axial-Strain-Controlled Method. International Organization for Standardization (ISO): Geneva, Switzerland, 2017.
36. *ASTM E 606-04*; Standard Practice for Strain-Controlled Fatigue Testing. ASTM International: West Conshohocken, PA, USA, 2004.
37. *EN 1563:2018*; Founding—Spheroidal Graphite Cast Irons. European Standard, 2018. Available online: https://standards.iteh.ai/catalog/standards/cen/e04bc999-3e91-4f24-855b-06dd6cf1d728/en-1563-2018 (accessed on 10 January 2022).
38. Toktaş, G.; Tayanç, M.; Toktaş, A. Effect of matrix structure on the impact properties of an alloyed ductile iron. *Mater. Charact.* **2006**, *57*, 290–299. [CrossRef]
39. Aristizabal, R.; Druschitz, A.; Druschitz, E.; Bragg, R.; Hubbard, C.; Watkins, T.; Ostrander, M. Intercritically Austempered Ductile Iron. In Proceedings of the American Foundry Society Transactions, Schaumburg, IL, USA, 5–8 April 2011; pp. 1–6.
40. Durmuş, A.; Aydın, H.; Tutar, M.; Bayram, A.; Yiğit, K. Effect of the microstructure on the notched tensile strength of as-cast and austempered ductile cast irons. *Proc. Inst. Mech. Eng. Part C J. Mech. Eng. Sci.* **2012**, *226*, 2214–2229. [CrossRef]
41. Angella, G.; Donnini, R.; Ripamonti, D.; Górny, M.; Zanardi, F. The Role of Microstructure on the Tensile Plastic Behaviour of Ductile Iron GJS 400 Produced through Different Cooling Rates—Part II: Tensile Modelling. *Metals* **2019**, *9*, 1019. [CrossRef]
42. Basquin, O.H. The exponential law of endurance tests. *Am. Soc. Test Mater. Proc.* **1910**, *10*, 625–630.
43. Manson, S.S. *Behavior of Materials under Conditions of Thermal Stress. Report No. NACA TN-2933*; Nasa: Washington, DC, USA, 1945.
44. Coffin, L.F. A study of the effect of cyclic thermal stresses on a ductile metal. *Trans. ASME* **1954**, *76*, 931–950.
45. Morrow, J. Cyclic Plastic Strain Energy and Fatigue of Metals. In *Internal Friction, Damping, and Cyclic Plasticity*; ASTM International: West Conshohocken, PA, USA, 1965; pp. 43–45.
46. Niesłony, A.; El Dsoki, C.; Kaufmann, H.; Krug, P. New method for evaluation of the Manson–Coffin–Basquin and Ramberg–Osgood equations with respect to compatibility. *Int. J. Fatigue* **2008**, *30*, 1967–1977. [CrossRef]
47. Atzori, B.; Meneghetti, G.; Ricotta, M. A Three Dimensional Graphical Aid for Fatigue Data Analysis. *Key Eng. Mater.* **2011**, *488–489*, 755–758. [CrossRef]
48. Williams, C.; Lee, Y.-L.; Rilly, J. A practical method for statistical analysis of strain–life fatigue data. *Int. J. Fatigue* **2002**, *25*, 427–436. [CrossRef]
49. *ASTM E739-10 (2010)*; Standard Practice for Statistical Analysis of Linear or Linearized Stress-Life (S-N) and Strain-Life (ε-N) Fatigue Data. ASTM International: West Conshohocken, PA, USA, 2015.
50. Smith, R.; Watson, P.; Topper, T. A stress–strain function for the fatigue of metal. *J. Mater.* **1970**, *5*, 767–778.

metals

MDPI

Article

On Ausferrite Produced in Thin Sections: Stability Assessment through Round and Flat Tensile Specimen Testing

Giuliano Angella [1,*], Riccardo Donnini [1], Dario Ripamonti [1], Franco Bonollo [2], Bogdan Cygan [3] and Marcin Gorny [4]

[1] Research Institute CNR-ICMATE, DSCTM, Via R. Cozzi 53, 20125 Milano, Italy
[2] Department of Management and Engineering, University of Padua, Str. S. Nicola, 3, 36100 Vicenza, Italy
[3] Teksid Iron Poland, Ciężarowa 49, 43-430 Skoczów, Poland
[4] Faculty of Foundry Engineering, AGH University of Science and Technology, Władysława Reymonta 23, 30-059 Kraków, Poland
* Correspondence: giuliano.angella@cnr.it

Abstract: Ductile irons were produced into different casting wall sections, that is, 25 mm, 5 mm and 3 mm. The alloys were then austenitized with the same conditions at 875 °C for 2 h and austempered for three different combinations of temperatures and times: 250 °C for 6 h, 310 °C for 3 h and 380 °C for 1 h. The aim of the investigation was to study the ausferrite stability of austempered ductile irons with three different nominal contents of nickel produced in thin sections through tensile testing. So, strain hardening analysis of tensile flow curves was carried out since it has been found to be a reliable support to ductility analysis in assessing the optimal austempering conditions. Because of different wall sections, round and flat tensile specimens with geometries complying with ASTM E8/E8M-11 were tested. Austempered ductile irons from 5 and 3 mm wall sections were tested through flat geometry specimens only, while 25 mm wall sections were tested through both round and flat geometries. Though the ausferrite was affected by Ni content and the graphite morphology was improved with reduced thin sections, the ausferrite stability and the tensile mechanical behavior were insensitive to Ni content and section thickness below 25 mm. Furthermore, it resulted that the tensile plastic behavior was sensitive to the specimen geometry in a consistent way, increasing the instability of ausferrite and indicating that a proper analysis and comparison of tensile properties of austempered ductile irons must take into account the tensile specimen geometry.

Keywords: austempered ductile iron; ausferrite stability assessment; strain hardening; specimen geometry

Citation: Angella, G.; Donnini, R.; Ripamonti, D.; Bonollo, F.; Cygan, B.; Gorny, M. On Ausferrite Produced in Thin Sections: Stability Assessment through Round and Flat Tensile Specimen Testing. *Metals* **2023**, *13*, 105. https://doi.org/10.3390/met13010105

Academic Editor: Carlos Capdevila-Montes

Received: 16 December 2022
Revised: 26 December 2022
Accepted: 30 December 2022
Published: 4 January 2023

1. Introduction

Austempered ductile irons (ADIs) are advanced spheroidal irons produced through heat-treating conventional ductile irons (DIs), resulting in a dual phase acicular microstructure called ausferrite, consisting of hard bainitic ferrite α and metastable high C content austenite γ_{HC} [1–8]. Ausferrite has an excellent combination of strength, ductility [9–13] and other mechanical properties, such as fatigue and fracture resistance [14–23]. Their properties are similar to cast and wrought steels, with which they can compete as materials for applications in components for heavy transportation, such as trucks, earth-moving machinery and the train industry [24–27], thanks also to their production cost that is about 50% less than the cost of steels and their density that is about 10–12% lower [7,28,29].

The ADI production route consists of two-step heat treatments: a conventional DI is first austenitized at high temperature, typically at about 900 °C, to have homogeneous austenite rich in C; then it is quenched in a salt bath to maximize the heat transfer and is subsequently held at a constant temperature, typically between 250 °C and 380 °C, to trigger the austempering solid-state transformation [1–6]. After a proper austempering

time, the resulting microstructure is the dual phase acicular ausferrite, that is, γ_{HC}+ α, and finally, the system is cooled down slowly to room temperature to avoid any residual stress. However, if the system is held at the austempering temperature for longer times, the reaction $\gamma_{HC} \rightarrow \alpha + \varepsilon$ occurs, where ε is a FeC carbide that dramatically reduces the ausferrite ductility. So, for the production of optimal ausferrite, the proper austempering time window has to be found to maximize the austempering reaction $\gamma \rightarrow \alpha + \gamma_{HC}$ and avoid the detrimental reaction $\gamma_{HC} \rightarrow \alpha + \varepsilon$.

The γ_{HC} and α volume fractions, the acicular microstructure dimension and the α hardness because of upper or lower bainite transformation depend mainly on the austempering temperature [1–6]. Higher austempering temperatures, such as 380 °C, produce coarse acicular or feathery ausferrite with higher volume fractions of γ_{HC} coming into lower yield and tensile strengths, and better ductility. Lower austempering temperatures, such as 250 °C, produce fine ausferrite with lower volume fractions of γ_{HC}, resulting in higher yield and tensile strengths, and reduced ductility. However, it has also been reported that austenitization temperature affects ausferrite since lower austenitization temperatures increase the driving force for austempering reaction, raising the reaction rate and the stability of the resulting ausferrite [6,30–33]. Furthermore, since acicular ferrite formation starts at interfaces of graphite/austenite and inclusions or austenite boundaries, the resulting austempering kinetics are accelerated by fine original microstructure [32,33].

For the quality assessment of ausferrite, the maximum volume fraction of austenite is not the only parameter to be controlled since the higher the C content in austenite, the more stable austenite is. In fact, with austempering, the martensite-start temperature (Ms) should be suppressed at 0 K so that the C-rich austenite is thermally stable at room temperature. Indeed, the C-rich austenite may be neither thermally nor mechanically stable at low temperatures but transforms into martensite as a consequence of cryogenic treatments and external loading [8,24,25,34,35], reporting that stress-induced and deformation-induced austenite-to-martensite ($\gamma \rightarrow$ M) transformation occurs in ADIs, which could contribute to the high ausferrite hardness and tensile strength [24,25]. The evaluation of the tensile mechanical properties of ADIs has to be carried out to assess definitely the stability of ausferrite and, as a consequence, to evaluate the goodness of the austempering production parameters [12,13,36–38]. Tensile ductility is usually analyzed to find the optimal austempering time, but the variability in tensile ductility is indeed the major problem in this approach; on the contrary, the analysis of tensile strain hardening through the dislocation-density-related constitutive equation, such as the Voce equation, has been proved to be very good for optimal austempering time assessment [12,13]. A *Matrix Assessment Diagram* (MAD) is built up by plotting the Voce equation parameters ($1/\varepsilon_c$ vs. Θ_o) found by fitting the tensile strain hardening data of ADI tensile flow curves with the Voce equation. In MADs, data from a single austempered heat that has been heat-treated with a single austempering temperature and different austempering times can be fitted with a best-fitting line, and the Voce data positions in MADs identify the best austempering time [12]. This method can also be used for comparison between ADIs with different chemical compositions that have been heat-treated with the same austempering conditions to identify which chemical composition better matches the imposed austempering setting [13].

Graphite–metallic matrix boundaries affect ferrite nucleation during austempering, so different nodule counts and sizes have effects on the austempering kinetics, which has been modeled in [32] and experimentally measured with dilatometry investigations in [33]. In ADIs, Cu, Ni and Mo are added to improve austemperability [39–42], that is, to avoid stable pearlite formation and to foster homogeneous ausferrite formation. However, increasing alloying results in potentially increasing chemical segregations with heterogeneous final ausferrite, which can be significant in thicker sections, causing the degradation of ADIs' mechanical properties [43–45]. So, thin sections that have a higher nodule count and chemically homogeneous metallic matrix should result in a more homogeneous ausferrite with a little blocky austenite in which martensite might form after loading or cryogenic application. To the authors' knowledge, none of the literature has reported on the effects

of different thin sections on ausferrite stability. In this work, the results of the investigations on the effects of the solidification rates (thickness sections) of the original DIs on the resulting ADIs' microstructure and tensile mechanical properties are reported. Castings with different wall thicknesses, namely 25 mm, 5 mm and 3 mm, with different Ni contents were austenitized at the same temperature and time, and then were austempered at three different temperatures and time conditions. Because of the different ADI sections, tensile specimens with round and flat geometries were tested to assess the tensile mechanical properties and the strain-hardening behavior of the different sections. So, the side investigation was the assessment of specimen geometry on the plastic behavior and stability of ausferrite. The microstructures of the ADI thin sections were analyzed using Scanning Electron Microscopy (SEM) and X-ray Diffraction (XRD).

2. Materials and Experimental

2.1. Original Cast Irons and Austempering Conditions

The original DIs were produced in Teksid Iron Poland, Skoczów, Poland, through different nominal contents of nickel (0.0, 0.7 and 1.5 wt%) into different casting wall sections: 25 mm, 5 mm and 3 mm. Castings with a wall thickness of 25 mm were produced complying with Y-blocks ASTM A536–84(2019)e1 [46], while castings with wall thicknesses of 5 and 3 mm were taken from step test castings. Experimental melts were carried out in medium-frequency induction furnaces with a capacity of 12 tons. The standard procedure for the metal charge was applied: 60% circulating own scrap and 40% steel scrap, with carburizer to correct the content of C. After melting the charge and reaching a temperature of 1420 °C, the slag was removed from the surface of the liquid cast iron, and control samples were taken to assess the chemical composition with emission spectrometry and the metallurgical quality of liquid cast iron. Experimental molds in green sand technology for making castings for testing the microstructure and mechanical properties were made. In mold technology for spheroidization and inoculation, processes were carried out using automatic pouring devices. The tests of C content were made with the LECO apparatus from Mg content using the Atomic Absorption Spectrometry (AAS) method. In Table 1, the chemical compositions of the three different heats are reported.

Table 1. Chemical compositions of the three ADI heats in wt%.

Code	C	Si	Mn	S	P	Mg	Cu	Ni
0.0 wt% Ni	3.500	2.554	0.326	0.015	0.046	0.035	0.762	0.012
0.7 wt% Ni	3.520	2.624	0.305	0.013	0.036	0.050	0.736	0.736
1.5 wt% Ni	3.520	2.540	0.357	0.012	0.042	0.037	0.700	1.533

The alloys were then austenitized at 875 °C for 2 h, and austempered for three different combinations of temperatures and times: 250 °C for 6 h; 310 °C for 3 h; 380 °C for 1 h. Tensile testing was performed with round tensile specimens with geometries complying with ASTM E8/E8M-11 [47], with a strain rate of 10^{-4} 1/s and strain control up to rupture. In Figure 1, the Ultimate Tensile Strengths (UTS) in MPa and Elongations to Rupture (e_R) in % resulted from the average of four tensile tests on ADIs produced with different Ni contents, and 25 mm Y-blocks are reported together with the minimum properties required according to ISO17804:2005 [48]. Indications of the austempering temperatures are reported on the plot for clarity's sake. The produced ADIs were all complying with [48], with UTS and elongations to rupture higher by far than those required. Indeed, only the 1.5 wt% Ni ADI austempered at 380 °C for 1 h matched the minimum properties 900-8; however, elongations to rupture were shown to be lower by far than those of the ADIs with 0.0 and 0.75 wt% Ni austempered at the same austempering temperature.

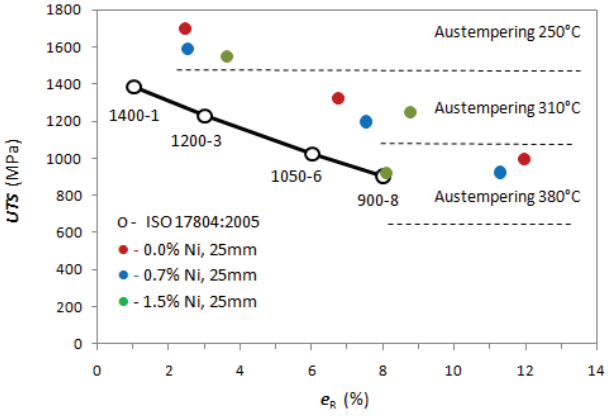

Figure 1. UTS (MPa) vs. e_R (%) for the ADIs produced with different Ni contents and with three different austempering temperatures (austenitization similar for all compositions at 875 °C for 2 h) with round tensile specimens from 25 mm Y-blocks. Minimum tensile properties complying with ISO17804:2005 [48] are reported for comparison purposes. Indications of the austempering temperatures are reported on the plot for clarity's sake.

2.2. Microstructure Analysis

The microstructure was observed in Scanning Electron Microscopy (SEM) with the microscope SU70 by Hitachi, after conventional grinding and polishing, and Backscattered Electron Imaging (BEI) for graphite morphology observations with polishing and then chemical etching with 2% Nital and Secondary Electron Imaging (SEI) for ausferrite observations. Nodularity and nodule count were calculated through digital image analysis complying with ASTM E2567-16a [49], working on BEI micrographs because the reduced gray scale typical of BEI made easier the binarization for image processing.

In order to quantify the volume fractions of retained austenite (V_γ) and to relate them to the observed tensile properties, X-ray Diffraction (XRD) analysis was performed for each sample on properly ground and polished surfaces by conventional metallographic methods. An X-ray diffractometer Siemens D500 with Bragg-Brentano geometry and Cu Kα radiation (λ = 0.1542 nm) was used, and XRD patterns were collected in the 2θ range 20–110° with a step size of 0.02° and 5 s of dwell time. Volume fractions of austenite and ferrite were calculated complying with the ASTM E975-13 [50]; corresponding intensities and peak 2θ positions were obtained for the identified $(111)_\gamma$, $(110)_\alpha$, $(200)_\gamma$, $(200)_\alpha$, $(211)_\alpha$, $(311)_\gamma$ and $(220)_\alpha$ lattice planes by peak approximation with Pearson type VII distribution [51]. For the graphite volume fraction (V_γ), the calculated value of 8% by the aforesaid image analysis was considered. The C content in γ austenite was evaluated according to the empirical equation [52]

$$C^{\gamma}_{s\ \{111\}} = \left(a^{\gamma}_{x} - 0.3573\right)/0.0033 \quad (1)$$

where $a_x{}^\gamma$ is the lattice parameter of γ austenite cell defined as

$$a^{\gamma}_{x} = \left(\frac{\lambda}{sin2\theta}\right)^2 \frac{1}{4}\left(h^2 + k^2 + l^2\right) \quad (2)$$

and h, k and l are the Miller indices of the crystallographic planes.

2.3. Tensile Testing and Flow Curves Analysis

Because of the different casting sections, round and flat tensile specimens with geometries complying with [47] were tested in strain control with strain rate 10^{-4} 1/s. ADIs from 5 and 3 mm wall sections were tested through flat geometry specimens only, while 25 mm wall sections were tested through both geometries. In Figure 2, the picture of flat and round

specimens tested are reported. The gauge ridges were used to connect extensometers and control gauge elongation up to rupture. In the engineering tensile data, stress $S = F/A_o$ and strain $e = (l - l_o)/l_o$, where F is the applied load, A_o and l_o are the initial cross-section and length of the tensile gauge, while l is the instantaneous length of the tensile gauge, were converted into true stress σ vs. true strain ε data according to the relationships $\sigma = S \cdot (1 - e)$ and $\varepsilon = \ln(1 + e)$. The plastic component (ε_P) only of strain was used, that is, $\varepsilon_P = \varepsilon - \sigma/E$, where E is the experimental Young modulus.

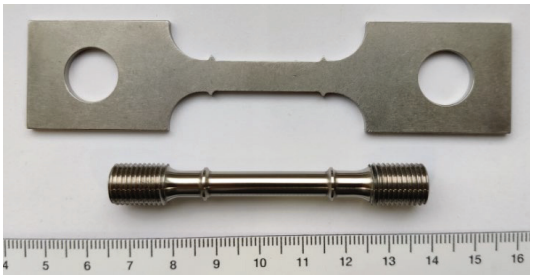

Figure 2. Flat and round geometries of the tensile specimens (marker unit in cm).

As reported in [53–57], the procedure to find out the Voce equation parameters is based on the analysis of the differential data $d\sigma/d\varepsilon_P$ vs. σ, where $d\sigma/d\varepsilon_P$ is the strain hardening rate. According to the Kocks–Mecking model of strain hardening [57–59], strain hardening rate and stress are linearly related:

$$\frac{d\sigma}{d\varepsilon_P} = \Theta_o - \frac{\sigma}{\varepsilon_c} \tag{3}$$

where Θ_o and $1/\varepsilon_c$ are constants with physical meaning that describe the micro-mechanics of plastic deformation and are related to the matrix microstructure [57]. An example of strain hardening analysis based on the Voce equation is reported in Figure 3 for 1.5 wt% Ni ADI from 25 mm Y-block austempered at 380 °C for 1 h.

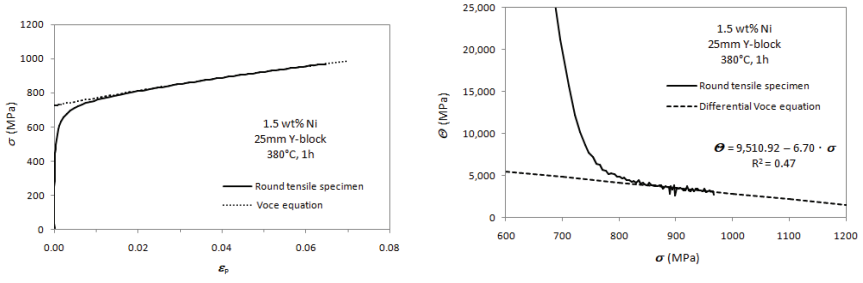

(**a**) (**b**)

Figure 3. Tensile plastic behavior fitting with Voce equation: (**a**) tensile flow curve with round tensile specimen of 1.5 wt% Ni ADI from 25 mm Y-block austempered at 380 °C for 1 h; (**b**) differential data from the flow curve in a) and strain hardening analysis based on Voce equation with best linear fit: intercept Θ_o = 9510.92 MPa; slope $1/\varepsilon_c$ = 6.70.

It has been reported [12,13,53–57] that through plotting $1/\varepsilon_c$ vs. Θ_o of a statistically meaningful set of flow curves, the *Matrix Assessment Diagram* (MAD) is built up with which the cast iron can be classified, and its quality can be assessed. When Voce tensile data from an ADI produced through different austempering times are plotted in MAD, an evaluation of the optimal time for austempering reaction can be made [12,13].

For each 25 mm Y-block, four tensile round specimens were tested for the assessment of the minimum tensile properties reported in Figure 1. The flow curves from round specimens were also used to build up the MAD for all different chemical compositions and austempering conditions. From the thin sections (5 and 3 mm), only flat tensile specimens could be machined off and tested. So, in order to compare properly the different sections, also from 25 mm Y-blocks, flat tensile specimens were tested to evaluate any possible specimen geometry effect, if existing.

3. Results

3.1. Microstructure Characterization

The 25 mm Y-block cast iron microstructure produced with the slowest solidification rate presented the smallest nodule count and the biggest average nodule size while, with decreasing thickness, the section nodule count increased and the average nodule size decreased. This graphite trend was the same for all heats. Nodularity and nodule count vs. thickness with different chemical compositions are reported for comparison in Figure 4. The solidification rate had a significant effect on the nodule count in Figure 4a since the nodule count was around 300 mm^2 in 25 mm castings, between around 500 and 700 mm^2 in 5 mm castings and around 900 mm^2 in 3 mm castings. On the contrary, the nodularity was excellent for all sections, as it was always around and higher than 90%, so well above the threshold reported in ASTM A247-19 [60] for good nodularity, i.e., 80%. Finally Ni content did not seem to affect the nodule count and nodularity in the 25 mm, 5 mm and 3 mm castings.

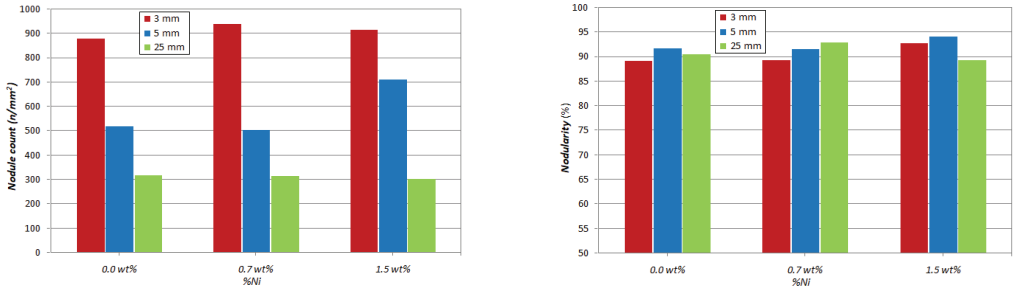

(**a**) (**b**)

Figure 4. Graphite microstructure parameters vs. thickness and Ni content: (**a**) nodule count (number of nodules/mm^2); (**b**) nodularity (%).

3.2. Ausferrite Characterization

Ausferrite was observed through SEM, and it was thinner after the lowest austempering temperatures of 250 °C, increasing in size with increasing austempering temperatures at 310 °C and 380 °C. Selected SEM images of ausferrite in ADI with 1.5 wt% of Ni after austempering at 380 °C for 1 h from 25 mm, 5 mm and 3 mm wall thickness castings are reported in Figure 5, for instance. Though ausferrite appeared to be organized in smaller packets in the 3 mm casting (Figure 5c) and increased in packets in 5 mm and 25 mm casting ausferrite in Figure 5b and Figure 5a, respectively, ausferrite appeared to be similar, equally coarse and feathery. The packet size seemed to reflect the original grain size that was smaller in the 3 mm casting, but no influence of the nodule count on the ausferrite morphology and size seemed to be evident. Similar findings were gathered for the other Ni contents' ausferrite. The ausferrite morphology was not significantly affected by Ni alloying, resulting in similar at the same austempering conditions with different Ni contents. In Figure 6, selected micrographs of ausferrite with different Ni content produced at the same austempering conditions (310 °C for 3 h) and thickness (25 mm Y-blocks) are reported, for instance.

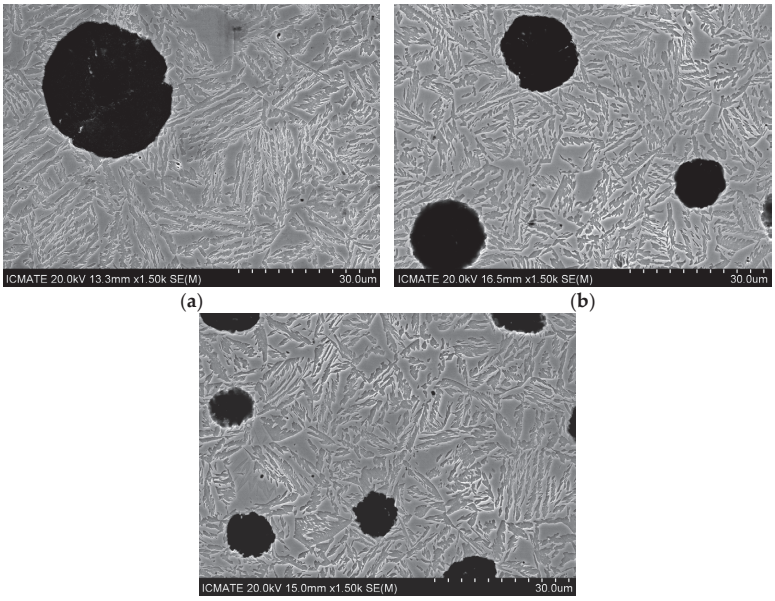

(**a**) (**b**) (**c**)

Figure 5. Selected SEM micrographs through Secondary Electron Imaging (SEI) of ADIs castings with 1.5 wt% of Ni after austempering at 380 °C for 1 h: (**a**) 25 mm wall thickness; (**b**) 5 mm wall thickness and (**c**) 3 mm wall thickness casting.

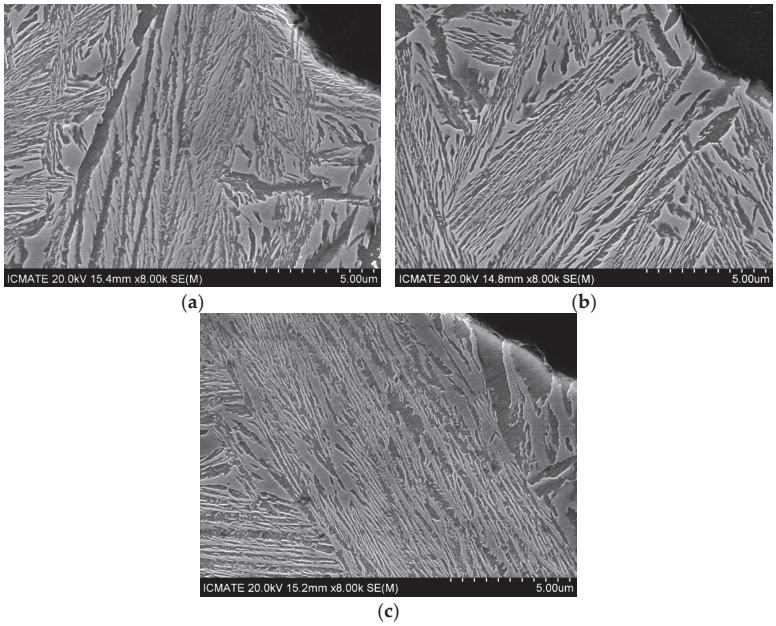

(**a**) (**b**) (**c**)

Figure 6. Selected SEM micrographs through SEI of ADIs castings with different Ni contents after austempering at 310 °C for 3 h: (**a**) 0.0 wt% 25 mm Y-blocks; (**b**) 0.7 wt% 25 mm Y-blocks and (**c**) 1.5 wt% 25 mm Y-blocks.

Fracture surfaces from tensile specimens were observed through SEM. In Figure 7, micrographs of selected fracture surfaces from round and flat tensile specimens of ADI with 0.0 wt% of Ni produced in 25 mm Y-blocks after austempering at 310 °C for 3 h are reported, for instance. The fracture surfaces presented generally ductile features and few brittle cleavage planes, and no differences in the fracture aspects between round and flat tensile specimens of the same ausferrite were found.

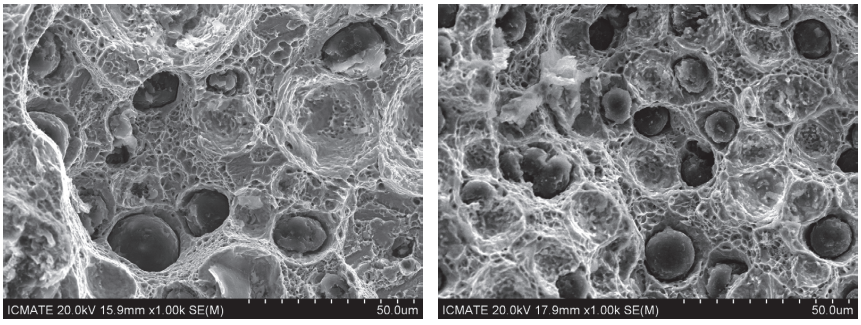

(**a**) (**b**)

Figure 7. Selected SEM micrographs through SEI of tensile specimen fracture surfaces of ADI with 0.0 wt% of Ni produced in 25 mm Y-blocks after austempering at 310 °C for 3 h: (**a**) fracture surface from round tensile specimen; (**b**) fracture surface from flat tensile specimen.

Examples of representative XRD diffraction patterns of ausferrite (normalized to the ferrite peak $\alpha(110)$) after different austempering conditions and corresponding lattice plane identification are reported in Figure 8 for 1.5 wt% of Ni ADI produced in 25 mm Y-blocks. With increasing austempering temperature, the relative intensity of austenite peaks (indicated as $\gamma(hkl)$) increased significantly, indicating that the austenite volume fractions increased with higher austempering temperatures. Austenite volume fractions vs. austempering temperature are reported in Figure 9 for all chemical compositions and austempering conditions.

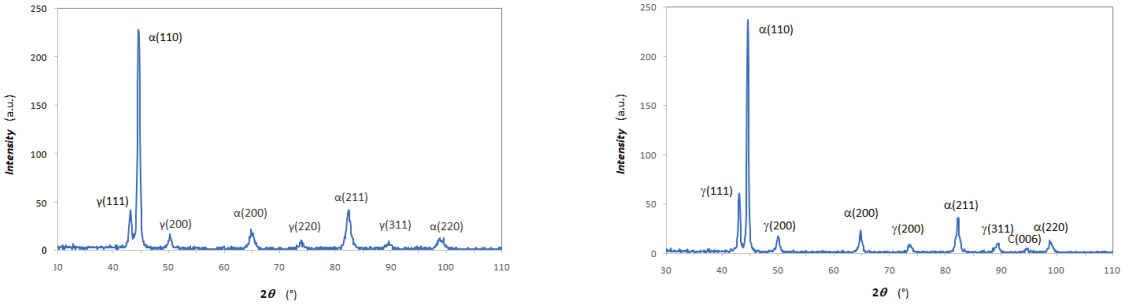

(**a**) (**b**)

Figure 8. *Cont.*

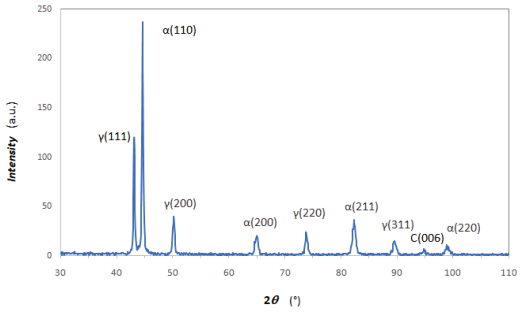

(**c**)

Figure 8. Typical XRD patterns of ausferrite (1.5 wt% of Ni, 25 mm Y-blocks) after different austempering conditions: (**a**) 250 °C with 6 h; (**b**) 310 °C for 3 h and (**c**) 380 °C for 1 h.

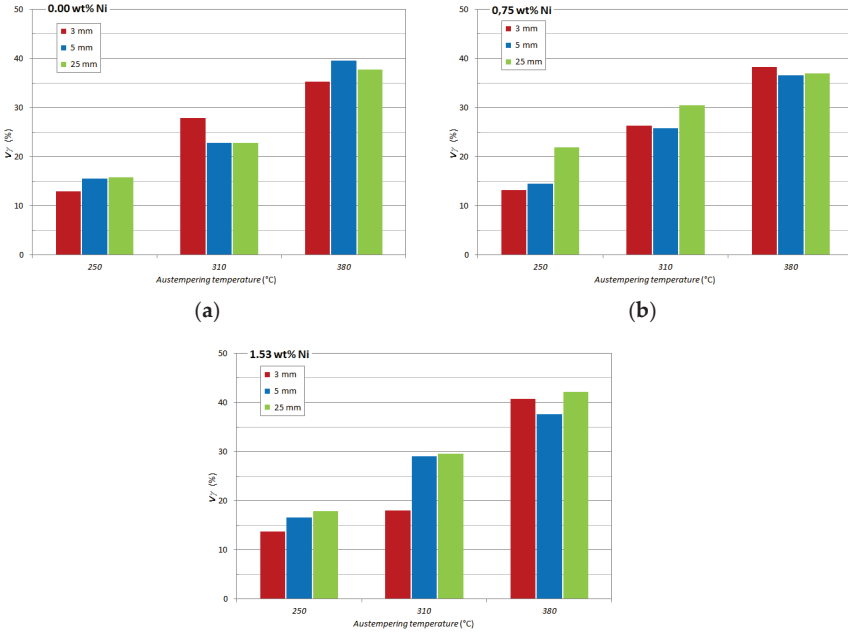

(**a**) (**b**)

(**c**)

Figure 9. Austenite volume fraction $V\gamma$ vs. austempering temperature (250 °C for 6 h, 310 °C for 3 h and 380 °C for 1 h); (**a**) 0.00 wt% of Ni; (**b**) 0.75 wt% of Ni; (**c**) 1.53 wt% of Ni.

For all compositions, there was an increase of austenite volume fraction $V\gamma$ with increasing austempering temperature, according to [1–6]. Though no clear effect of wall thickness was evident, with increasing Ni content, the austenite V_γ seemed indeed to increase. In Figure 10, the average V_γ of different wall thicknesses with constant Ni content is reported at different austempering temperatures. The Ni-bearing ADIs generally presented an austenite volume fraction higher than the Ni-free ADIs, indicating that Ni fostered the austenite retention, which has been already reported [39,41,42].

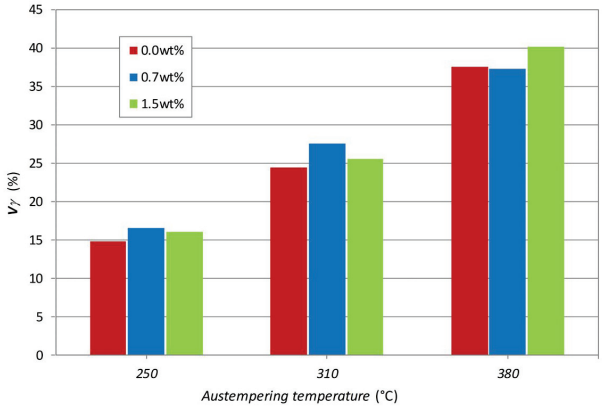

Figure 10. Average austenite volume fraction $V\gamma$ vs. austempering temperature (250 °C for 6 h, 310 °C for 3 h and 380 °C for 1 h).

In Figure 11, the $C^{\gamma}{}_S$ values averaged on the different wall thicknesses with constant Ni content are reported at different austempering temperatures. $C^{\gamma}{}_S$ did not seem to be affected by the Ni content and wall thicknesses, while $C^{\gamma}{}_S$ was affected by austempering; the ADIs austempered at 250 °C for 6 h presented the lowest C contents in austenite compared to the values found after austempering at 310 and 380 °C.

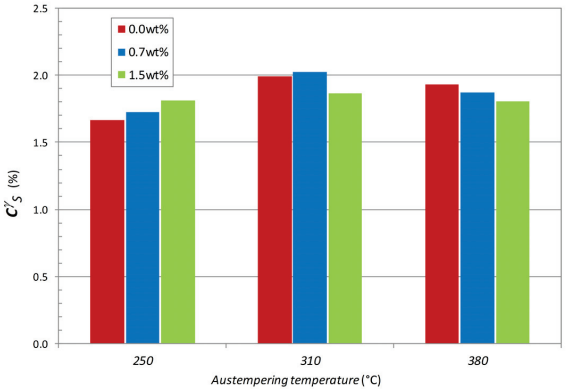

Figure 11. Average C content in γ ($C^{\gamma}{}_S$) vs. austempering temperature (250 °C for 6 h, 310 °C for 3 h and 380 °C for 1 h).

3.3. Tensile Strain Hardening Results on 25 mm Y-blocks: MAD Analysis

Differential data from tensile flow curves of ADIs from 25 mm Y-blocks were analyzed according to the procedure reported in Section 2.3, and the Voce parameters $1/\varepsilon_c$ and Θ_o were plotted according to the MAD reported in Figure 12. MADs for the three austempering conditions (250 °C for 6 h; 310 for 3 h; 380 °C for 1 h) are reported for the three nominal Ni contents (0.0, 0.7 and 1.5 wt%). In each MAD, the data from each chemical composition comes from four tensile tests carried out on round tensile specimens: the scattering of the data points are indications of ausferrite stability [12,13]. The lower the positions of the data points, the more stable the ausferrite is. So, in Figure 12a, reporting data for ADIs austempered at 380 °C for 1 h, the 0.0 wt% Ni ausferrite was more stable than ADIs with Ni alloying, ranging $1/\varepsilon_c$ from 1.99 to 2.90 (or Θ_o from 4722.3 to 5697.5 MPa). Because increasing alloying elements content makes the austempering transformation more sluggish, the MAD results suggested that 1 h time was not enough for stable ausferrite

formation with Ni alloying [13], and longer austempering times should have been imposed. In Figure 12b, reporting data for ADIs austempered at 310 °C for 3 h, the 1.5 wt% Ni ausferrite was more stable than ADIs with other compositions, ranging $1/\varepsilon_c$ from 5.82 to 8.30 (or Θ_o from 10,199.2 to 13,354.9 MPa). In this case, the MAD suggested that 3 h time was too long for stable ausferrite formation with 0.0 and 0.7 wt% of Ni [13], and shorter austempering times should have been imposed, particularly for the 0.0 wt% Ni ausferrite. Finally, in Figure 12c, data from austempering at 250 °C for 6 h are reported; again, the 1.5 wt% Ni ausferrite was more stable than ADIs with other compositions, ranging $1/\varepsilon_c$ from 58.86 to 96.40 (or Θ_o from 98,585.8 to 157,124.5 MPa). Indeed, the ADI with a nickel content of 0.0 wt% seemed to have a similar behavior to 0.7 wt% Ni content with high Voce values, suggesting that both compositions were far from stable. However, generally, the Voce parameters for all compositions were very high after any austempering conditions, indicating that ausferrite instability was high after austempering at 250 °C.

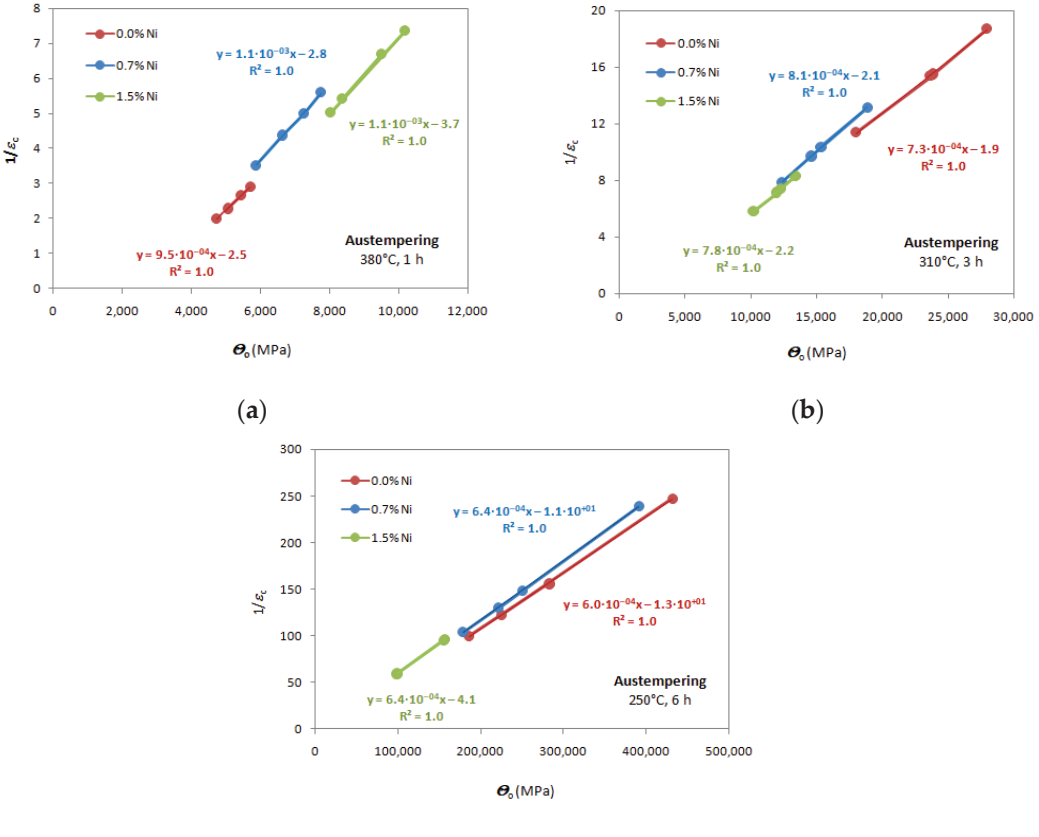

Figure 12. *Matrix Assessment Diagrams* (MAD) for round tensile specimens from 25 mm Y-block ADIs of three nominal Ni contents (0.0, 0.7 and 1.5 wt%) and different austempering conditions: (**a**) 380 °C for 1 h; (**b**) 310 °C for 3 h; (**c**) 250 °C for 6 h.

3.4. Tensile Behavior Comparison between ADIs Produced through 25, 5 and 3 mm Thickness Sections

Because of the lack of material, only flat tensile specimens could be machined off from the 5 and 3 mm castings. So, for proper comparison flat tensile specimens were also machined off from the ADI 25 mm Y-blocks and then tensile tested. The Voce parameters

were found according to the usual procedure in Section 2.3, and the results are in the MADs reported in Figures 13–15. Additionally, the Voce parameters obtained from the round specimens machined off from the 25 mm Y-blocks (see Figure 12) are reported for comparison purposes, as well as the best linear fits of the round tensile specimens data.

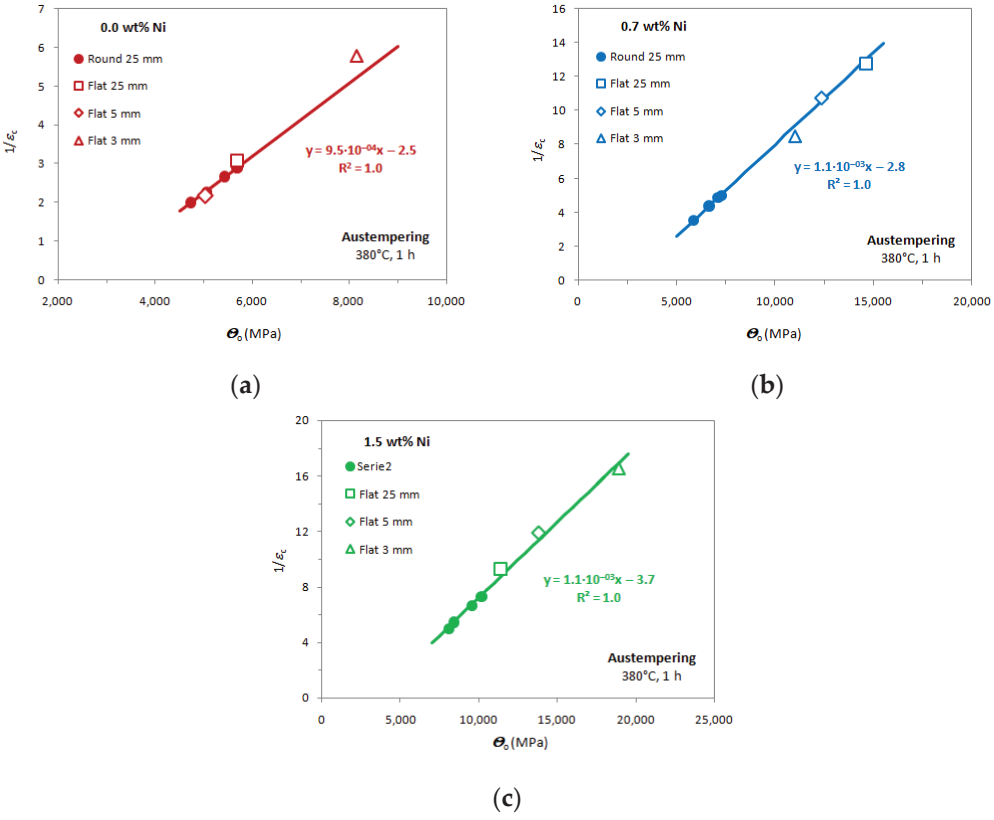

Figure 13. MADs for 25mm Y-block ADIs (round and flat tensile specimens), 5 mm and 3 mm thin castings with austempering conditions 380 °C and 1 h with different Ni content: (**a**) nominal 0.0 wt% Ni; (**b**) nominal 0.7 wt% Ni; (**c**) nominal 1.5 wt% Ni.

In Figure 13, the data from austempering at 380 °C for 1 h are reported for the ADIs with the three different Ni contents. It is noteworthy that, in every composition, the data from the 3 and 5 mm flat tensile specimens lie on the best linear fits obtained by the round specimens data of the ADI 25 mm Y-blocks. So, since the Voce parameters from round and flat tensile specimens had the same best linear fits, this finding indicated that the ausferrite from different sections had similar microstructure with possible different stability. So, chemical composition was the relevant parameter for ausferrite formation, regardless of section thickness. However, the Voce data positions of the flat tensile specimens along the best-fitting lines were higher than the round tensile specimens data with apparently worse ausferrite stability. Furthermore, the Voce data position from flat specimens from different thicknesses was also random, which resulted in none of the three wall thicknesses (3, 5 and 25 mm) seeming to have better ausferrite stability. Another interesting result is that the range width of the flat tensile specimens Voce data was by far wider than the Voce data range from round tensile specimens, which would have suggested that ausferrite stability was lower in 5 and 3 mm thin sections. Indeed, the data values from flat specimens of

the 25 mm Y-blocks were also always bigger than the round specimen data from 25 mm Y-blocks, which could indicate that the tensile specimen geometry might have played some role in the tensile flow behavior of ADIs.

In Figure 14, the data from austempering at 310 °C for 3 h are reported for the three different Ni contents. In Figure 14a, the flat tensile specimen data point from 0.0 wt% Ni ausferrite is missing because of the premature rupture, so the short plastic deformation range could not allow for strain hardening analysis. Again, the data from the 3 and 5 mm sections' flat specimens lie on the best linear fits obtained by the round tensile specimens data of the 25 mm Y-blocks. Additionally, for these austempering conditions, the flat tensile specimens data positions along the best-fitting lines were generally higher and random, indicating that no ausferrite of the three sections (3, 5 and 25 mm) had better stability. It is noteworthy that, though the range width of the flat tensile specimens Voce data appeared to be wider by far than the Voce data from round specimens, the data values from flat specimens of the 25 mm Y-blocks were indeed always bigger than the round specimens data from 25 mm sections.

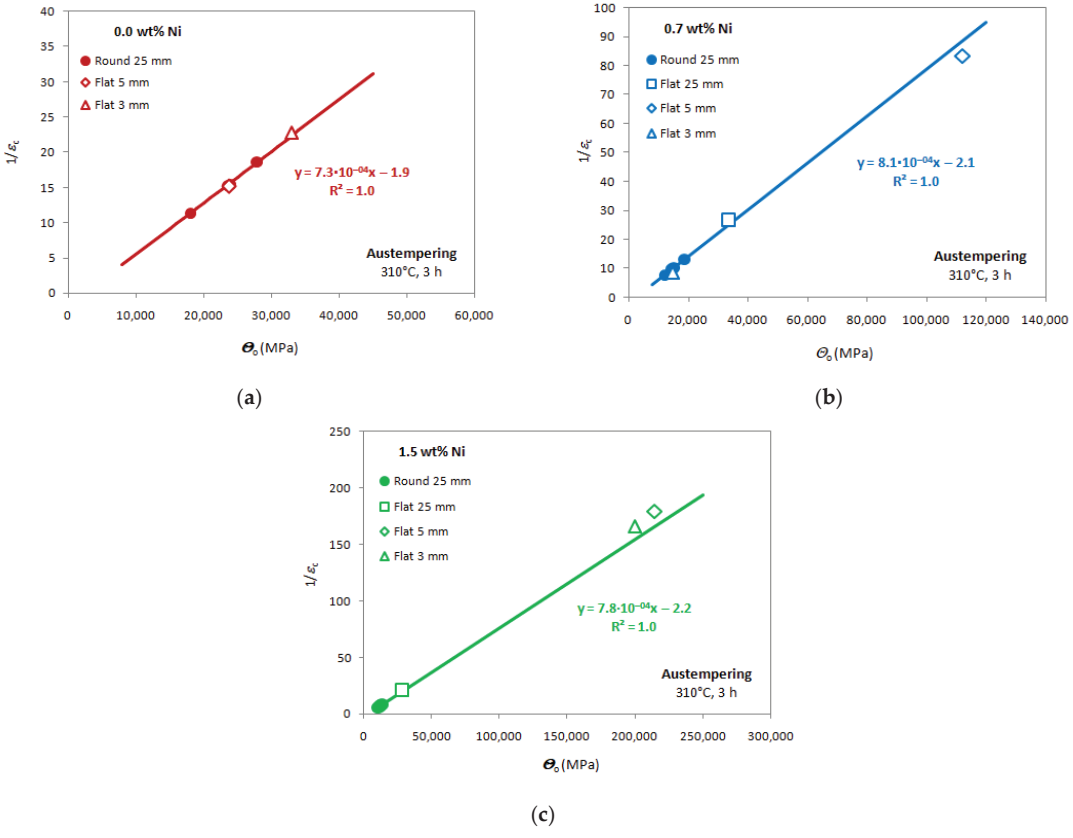

Figure 14. MADs for 25 mm Y-block ADIs (round and tensile specimens), 5mm and 3mm thin castings with austempering conditions 310 °C and 3 h with different Ni content: (**a**) nominal 0.0 wt% Ni; (**b**) nominal 0.7 wt% Ni; (**c**) nominal 1.5 wt% Ni.

In Figure 15, the data from austempering at 250 °C for 6 h are reported for the three different Ni contents. The instability of ausferrite after these austempering conditions was generally quite high, causing premature ruptures and short ductility. Even if the 3 mm casting data points were always the lowest regardless of the Ni contents, it was difficult

to state any trend. In fact, the variability of Voce parameters was so high that premature ruptures occurred just after the proof stress, and strain hardening analysis was difficult. That was the reason why some data points are missing in the MADs of austempering at 250 °C in Figure 15.

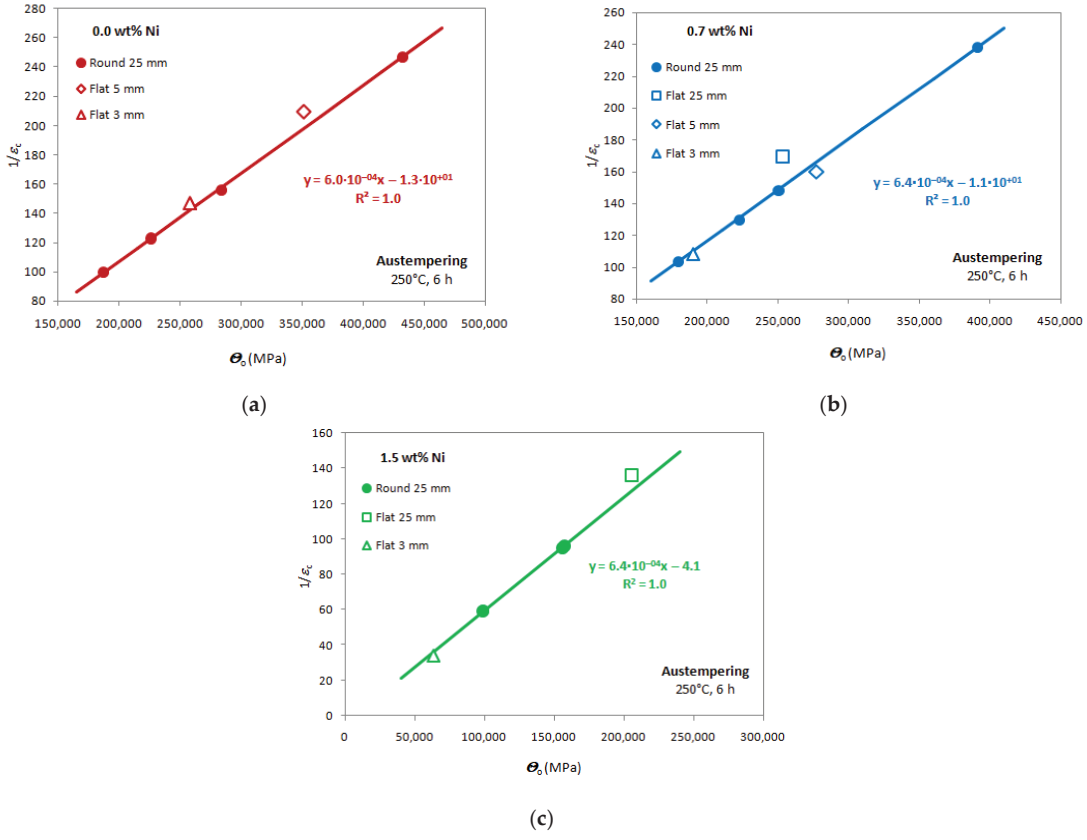

Figure 15. MADs for 25 mm Y-block ADIs (round tensile specimens and flat specimens), 5 mm and 3 mm thin castings with austempering conditions 250 °C and 6 h with different Ni content: (**a**) nominal 0.0 wt% Ni; (**b**) nominal 0.7 wt% Ni; (**c**) nominal 1.5 wt% Ni.

4. Discussion

4.1. Microstructure

The graphite morphology of ADIs was analyzed through digital image analysis complying with the international standard [49]. The nodularity was excellent in all compositions and sections, showing values always above 88% in Figure 4b, so well over the threshold of 80% reported in ASTM 427-19 [60] for high-quality nodular cast irons. The nodule count was instead significantly affected by the section thickness, since nodule count was an average value of about 900 mm^{-2} with the fastest cooling rates in the 3 mm castings regardless of the Ni content, decreasing to an average of about 300 mm^{-2} in the 25 mm Y-blocks. At the intermediate thickness of 5 mm, some variability was found, with a nodule count ranging from about 500 to about 700 mm^{-2} in the 1.5 wt% Ni ausferrite. However, besides these findings, no evidence of Ni influence on the nodule count could be claimed. So, the graphite morphology appeared excellent for any Ni content and consistent with the different cooling rates that seemed to be the only relevant parameter affecting the graphite morphology.

The ausferrite morphology did not seem to be affected by nodule count (section thickness) or Ni content. As reported in Figure 5, the ausferrite seemed to be organized in packets reflecting the original austenite grain size of the material after austenitization. Indeed, mean grain size (D) is proportional to half the inter-nodule distance (λ) through the Fullman's relationship [61]:

$$\lambda = (1 - V_\gamma)/(d \cdot N_G) \quad (4)$$

where d is the mean nodule size (mm) and N_G is the nodule count (number of nodules/mm^2). Through applying equation 4 for 1.5 wt% ausferrite obtained after austempering at 380 °C for 1 h (see Figure 5), $\lambda/2$ resulted in 53.4 µm for 3 mm casting, 60.7 µm for 5 mm casting and 93.5 µm for 25 mm Y-block, which is consistent with the ausferrite packets reported in Figure 5.

The austenite volume fractions V_γ vs. austempering temperatures for any Ni content and cooling rate have been reported in Figure 9a–c. With increasing austempering temperature, V_γ increased as expected [1–6], passing from an average of about 15% at 250 °C of austempering to about 25% at 310 °C and about 37% at 380 °C. However, with increasing Ni content, the austenite V_γ slightly increased, since in Figure 10, where the average V_γ of different wall thicknesses with constant Ni content is reported at different austempering temperatures, the Ni-bearing ausferrite generally presented an austenite volume fraction higher than the Ni-free ADIs, indicating that Ni promoted the austenite preservation, as already reported [39,41,42].

Another important parameter to be measured in ausferrite is the C content in metastable austenite: the higher the C content, the more stable the austenite is. In the literature, the value of 1.8 wt% of C is identified as the target to be achieved for good austenite stability [52]. In Figure 11, the carbon content in austenite values ($C^\gamma{}_S$) averaged for the different wall thicknesses with constant Ni content are reported at different austempering temperatures. $C^\gamma{}_S$ did not seem to be affected by the Ni content and wall thicknesses, so there was no correlation between metastable austenite volume fractions V_γ (that seemed to be affected by Ni content) and C content in austenite. Indeed, $C^\gamma{}_S$ was affected by austempering: the ADIs austempered at 250 °C for 6 h presented the lowest C contents in austenite below 1.8%, while the values found after austempering at 310 °C and 380 °C were always over 1.8%.

4.2. Tensile Behavior of 25 mm Y-Blocks with Round Tensile Specimens: Ausferrite Stability through Analysis of MAD and Tensile Mechanical Properties

The tensile behavior of the ADIs produced in different walls with variable Ni content was investigated according to conventional engineering properties, i.e., UTS and elongations in Figure 1 and according to the *Matrix Assessment Diagram* (MAD) in Figure 10. In the plot UTS vs. elongations to rupture reported in Figure 1, the ADI data points are well above the minimum tensile properties complying with ISO 17804:2005 [48], proving that the austempering conditions selected in this work with differential dilatometry technique were correct and the produced ADIs were excellent. Indeed, the only composition of 1.5 wt% Ni after austempering at 380 °C for 1 h appeared to match the minimum tensile properties [48], but well below the properties measured in the other investigated ADIs.

To give an insight into this finding, the MAD approach based on the Voce analysis of strain hardening was used. In Figure 10, the Voce parameters worked out from the strain hardening analysis of the 25 mm Y-blocks tensile flow curves were reported for any Ni content and austempering condition. So, since different chemical compositions affected the kinetics of the austempering solid reaction, in each MAD the data positions and data point spans were different, indicating that the stability of ausferrite was different after the imposed austempering conditions. In Figure 10a, the austempering conditions of 380 °C for 1 h produced optimal ausferrite for the Ni-free ADI, while alloying with Ni, 380 °C for 1 h was not enough for making the most stable C-rich austenite. For austempering at 310 °C for 3 h in Figure 10b, 1.5 wt% of Ni had the most stable ausferrite, while for lower Ni alloying

ausferrite was over-austempered, having higher Voce parameters. For austempering at 250 °C for 6 h in Figure 10c, 1.5 wt% of Ni again had Voce parameters lower than the other compositions, attesting that 1.5 wt% of Ni ausferrite had the best stability. These conclusions were consistent with the conventional ductility analysis that can be used to support the optimal austempering time investigation in ADI production. In Figure 16, the mean elongations to rupture (e_R) for the different Ni contents and different austempering conditions are reported. For austempering at 380 °C for 1 h in Figure 16a, 0.0 wt% of Ni had the highest mean value e_R, while lower e_R values are reported for ausferrite with higher Ni content. For 1.5 wt% Ni ADI, the austempering conditions were particularly under-austempered, causing an increase in Voce parameters and a dramatic reduction of ductility below 8%, as reported in Figure 16a, which explained why in Figure 1 the 1.5 wt% Ni ADI matched the minimum tensile properties complying with ISO 17804:2005 [48], while for the other compositions and austempering conditions ADIs had better tensile properties by far. So, an austempering time longer than 1 h could have improved the stability of ausferrite in 1.5 wt% Ni ADI, which is consistent with the fact that alloying makes the solid-state transformation more sluggish. For austempering at 310 °C for 3 h in Figure 16b, 1.5 wt% of Ni had the largest mean e_R, while at 250 °C for 6 h in Figure 16c, 1.5 wt% of Ni again had the best ductility, which was consistent with the MAD analysis.

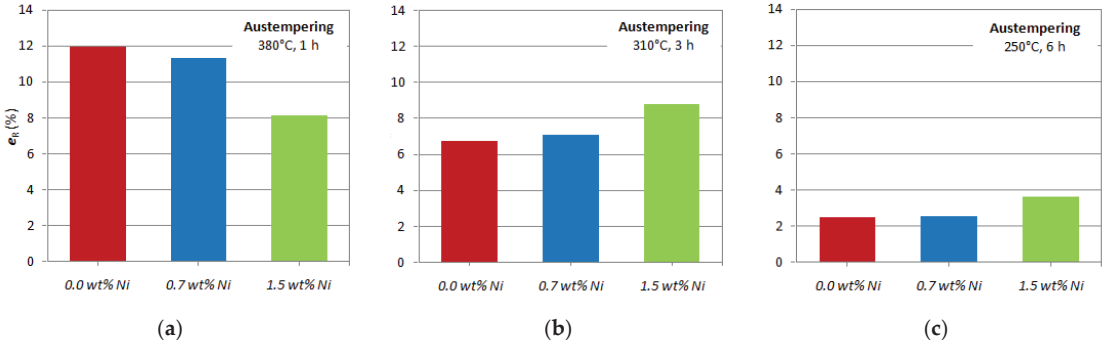

Figure 16. Mean elongations to rupture (e_R) from 25 mm Y-block ADIs for different Ni contents and different austempering conditions: (**a**) 380 °C for 1 h; (**b**) 310 °C for 3 h; (**c**) 250 °C for 6 h.

So, with increasing Voce parameter values that indicate an increase of ausferrite instability, there is a constant and consistent decrease of ductility, as summarized in Figure 17, where the correlation between ductility and Voce analysis strongly supports the new assessment approach of ausferrite stability based on MAD. However, the ductility itself can be misleading if carried out alone because of the wide variability typical of elongations to rupture, while the strain hardening behavior with the MAD approach is less sensitive to rupture and so can be used to validate and strengthen the conclusions about the goodness of the austempering conditions based on ductility. So, Voce analysis is a valid tool to support the ductility analysis for optimal determination of austempering conditions.

It is noteworthy that with increasing the Voce parameter values, their range width in MAD increased significantly, indicating that ausferrite stability and variability of tensile plastic behavior (Voce parameters variability) are correlated. So, in Figure 10, for instance, if the Voce parameter $1/\varepsilon_c$ is considered (the same results would be achieved considering Θ_o, as they are linearly related) the best ausferrite stability was found for Ni 0.0 wt% austempered at 380 °C for 1 h with a mean value of $1/\varepsilon_c$ equal to 2.46: the biggest $1/\varepsilon_c$ value was 2.90, while the smallest $1/\varepsilon_c$ was 1.99. Conversely, the worst ausferrite stability was found for Ni 0.0 wt% austempered at 250 °C for 6 h with a mean value of $1/\varepsilon_c$ equal to 155.49: the biggest $1/\varepsilon_c$ value was 247.24, while the smallest $1/\varepsilon_c$ was 99.98. In Figure 18, the span width of the Voce parameter $1/\varepsilon_c$, that is, $\Delta 1/\varepsilon_c = (1/\varepsilon_c)_{max} - (1/\varepsilon_c)_{min}$, is reported vs. the mean value of $1/\varepsilon_c$ for any Ni content and austempering condition for the round

specimens from the 25 mm Y-block ADIs, showing that when increasing the ausferrite instability there is an increase of $\Delta 1/\varepsilon_c$, that is, an increase of plastic behavior variability.

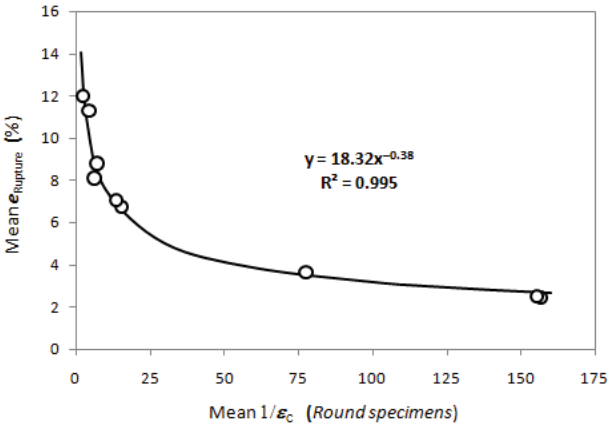

Figure 17. Mean $1/\varepsilon_c$ vs. mean elongation to rupture e_{Rupture} (%) for any Ni content (0.0, 0.7 and 1.5 wt%) and austempering conditions (380 °C for 1 h; 310 for 3 h; 250 °C for 6 h) for the round specimens from the 25 mm Y-block ADIs.

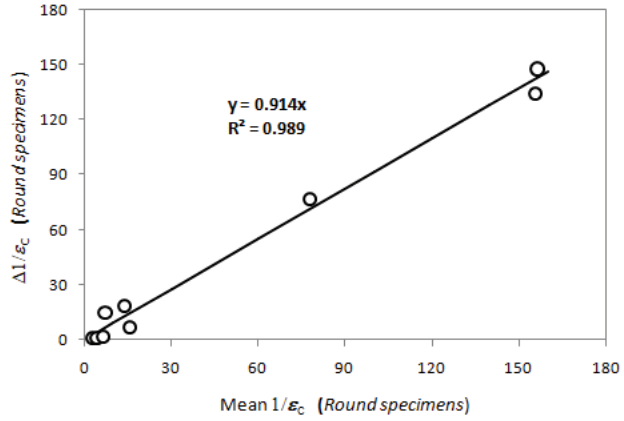

Figure 18. Span width $\Delta 1/\varepsilon_c = (1/\varepsilon_c)_{\max} - (1/\varepsilon_c)_{\min}$ vs. the mean value of $1/\varepsilon_c$ for any Ni content (0.0, 0.7 and 1.5 wt%) and austempering conditions (380 °C for 1 h; 310 °C for 3 h; 250 °C for 6 h) for the round specimens of the 25 mm Y-block ADIs.

In Figure 19, the volume fractions of metastable austenite are reported for different Ni contents and austempering conditions for the 25 mm Y-blocks. The ADIs with Ni alloying often presented the highest volume fractions of austenite at any austempering conditions, indicating that Ni fostered austenite retention, which is well known [39,41,42]. At 380 °C, the best ausferrite stability was for 0.0 wt% Ni content, even if the austenite volume fraction was not the highest if compared to 0.7 and 1.5 wt% of Ni ADIs, while the best ausferrite stability after austempering at 310 °C and 250 °C was for 1.5 wt% of Ni ausferrite, even if corresponding austenite volume fractions were not the highest. So, the volume fractions of austenite seemed to be not tightly related to the stability evaluation of ausferrite through MAD in Figure 12 or ductility in Figure 16.

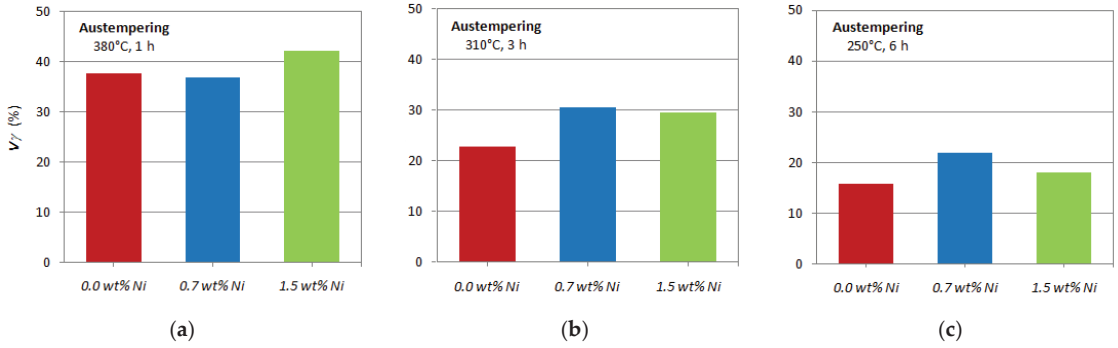

Figure 19. Volume fractions of austenite V_{γ} in 25 mm Y-block ADIs for different Ni contents and different austempering conditions: (**a**) 380 °C for 1 h; (**b**) 310 for 3 h; (**c**) 250 °C for 6 h.

Indeed, what is relevant for ausferrite stability is to have the highest C content in austenite [1–6], which makes it stable at room temperature. In Figure 20, the C content values in austenite are reported for different Ni contents and austempering conditions from the 25 mm Y-blocks. In Figure 20, it is evident that the C content is more related to the austenite stability assessment through MAD in Figure 12 and to the ductility results in Figure 16. For instance, in Figure 20a, after austempering at 380 °C, the C content in austenite was the lowest in 1.5 wt% Ni ADI, consistent with the worst stability in MAD in Figure 12a, and the lowest ductility in Figure 16a (and the worst tensile properties in Figure 1). Again, in Figure 20b, after austempering at 310 °C, the C content in austenite was the lowest in 0.0 wt% Ni ADI for which the stability assessment in Figure 12b was the worst, and the ductility was the lowest in Figure 16b. The same results are for the austempering conditions 250 °C for 6 h in Figure 12c. Furthermore, in Figure 20c, the C content in austenite after austempering at 250 °C for 6 h is the lowest compared to the C content after austempering at 380 °C and 310 °C; this is consistent with the general trend found in Figure 12c, where the high values of Voce parameters indicated that the austenite stability was poor after austempering at 250 °C for any chemical composition, which was also consistent to the low ductility reported in Figure 16c. In conclusion, the C content in austenite was tightly consistent with the stability analysis through MADs in Figure 12 and the ductility results in Figure 16, while the austenite volume fraction was not.

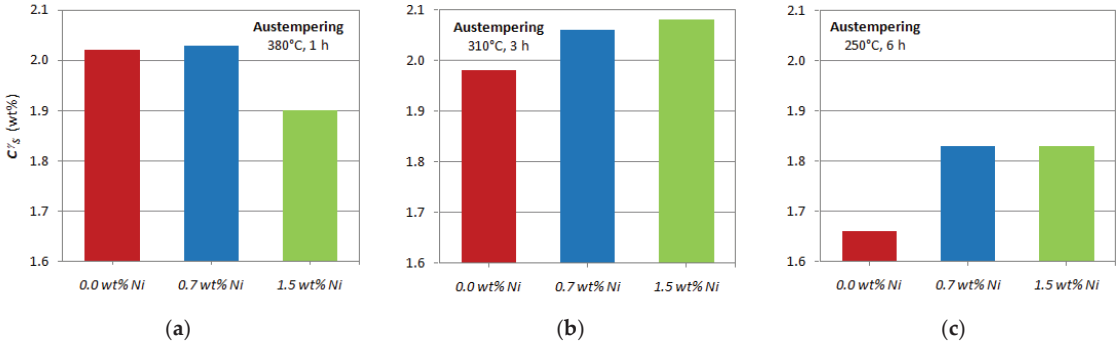

Figure 20. C content in austenite ($C^{\gamma}{}_{S}$) in 25 mm Y-block ADIs for different Ni contents and different austempering conditions: (**a**) 380 °C for 1 h; (**b**) 310 for 3 h; (**c**) 250 °C for 6 h.

4.3. Tensile Behavior and Austenite Stability in ADIs Produced in Different Sections: 25 mm, 5 and 3 mm

The MADs of the Voce data of the flat tensile specimens from 25 mm, 5 mm and 3 mm castings are reported in Figures 13–15 for different Ni contents and austempering conditions. In Figure 13, for the austempering at 380 °C for 1 h, the flat tensile specimen Voce data lie along the best fitting lines obtained by the round specimens data from 25 mm Y-blocks regardless of the Ni content, which indicated that ausferrite plastic behavior for different sections was the same for similar chemical compositions. However, the flat specimens data positions were higher than the round specimens data in MADs and random with no particular trend, suggesting that no ausferrite of the three sections (3 mm, 5 mm and 25 mm castings) had better ausferrite stability, while ausferrite instability increased. In fact, consistent with the findings on the correlation between Voce parameter variability and ausferrite instability in Figures 17 and 18, the ranges of Voce parameters of the flat tensile specimens were often wider than the ones from round tensile specimen data. Similar findings are reported in Figure 14 for austempering at 310 °C for 3 h: the flat tensile specimens data had random positions alongside the best linear fits of the round tensile specimens data regardless of the Ni content, and the ranges of Voce parameter values were wider than the data range from round specimens. In Figure 15, the instability of ausferrite after austempering at 250 °C for 6 h was quite high regardless of Ni content, section thickness and tensile specimen geometry, causing premature ruptures and low ductility; some data points are missing because the tensile flow curves did not have the sufficient plastic range for strain hardening analysis. This instability was consistent with the lower C content that was measured for all ADIs with different Ni contents after austempering at 250 °C for 6 h, reported in Figure 20c. Indeed, the data from 3 mm casting were the lowest for the three different Ni contents, which might suggest that the 3 mm casting ausferrite was more stable. However, the comparison of C contents in austenite in the 3, 5 and 25 mm castings in Figure 11 shows neither higher C content in austenite of the 3 mm castings nor higher volume fractions of austenite, and so no sure trend could be stated.

In Figures 13–15, the widths of the flat specimens Voce data ranges appeared to be wider than the Voce data ranges from round specimens for any Ni content and austempering conditions, which might have suggested that ausferrite stability could be lower in 5 mm and 3 mm castings rather than in 25 mm Y-blocks ADIs. However, the Voce parameters from flat tensile specimens of the 25 mm Y-block sections were also bigger, and the data ranges wider than the Voce data from the round tensile specimens from the same 25 mm Y-blocks, which indeed indicated that the tensile specimen geometry might have played some role in the instability of ausferrite. An example of flat and round tensile specimens' strain hardening behavior is reported in Figure 21 for 1.5 wt% Ni ADI from 25 mm Y-block austempered at 380 °C for 1 h.

The strain to rupture ε_R from flat tensile specimens vs. the average strain to rupture from round tensile specimens from the same Ni contents and austempering conditions are reported in Figure 22a (flat tensile specimen data points of 0.0 wt% Ni ausferrite austempered at 310 °C for 3 h and at 250 °C for 6 h are missing, because the short plastic deformation ranges could not allow strain hardening analysis). In Figure 22a, data points are always below the dichotomy line where strains to rupture from flat and round tensile specimens should match if ductility were the same, regardless of Ni content and austempering conditions. This finding proved that ductility was always lower in flat tensile specimens than in round ones with the same ausferrite, resulting in an average ductility reduction of −21.6% with flat tensile specimens with respect to round tensile specimens. The fracture surfaces analysis did not reveal any difference between the fracture behaviors of round and flat tensile specimens (see Figure 7) that could help to rationalize the different ductility. When comparing the Voce analysis results on flat and round tensile specimens in Figure 22b, the parameters $1/\varepsilon_c$ from flat tensile specimens were always higher than the ones from round tensile specimens, with an average increase of 100.8%, indicating that the

ausferrite instability in flat tensile specimens was more significant, albeit the material was the same.

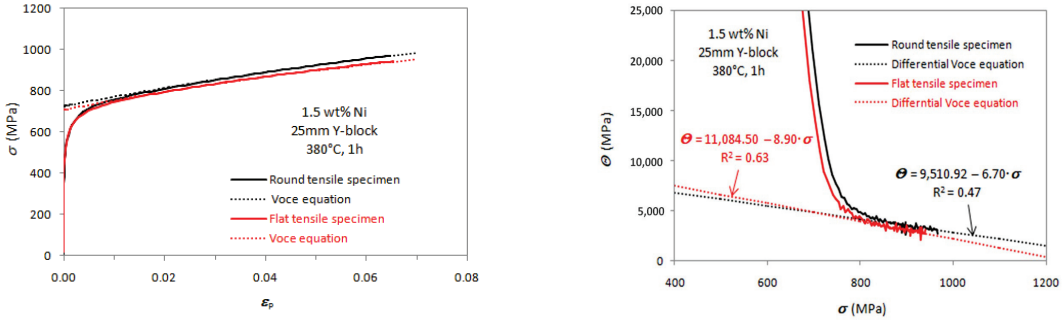

(**a**) (**b**)

Figure 21. Comparison between tensile plastic behavior from round and flat tensile specimens: (**a**) tensile flow curves with round and flat tensile specimen of 1.5wt% Ni ADI from 25 mm Y-block austempered at 380 °C for 1 h; (**b**) differential data from the flow curves in (**a**) and strain hardening analysis based on differential Voce equation.

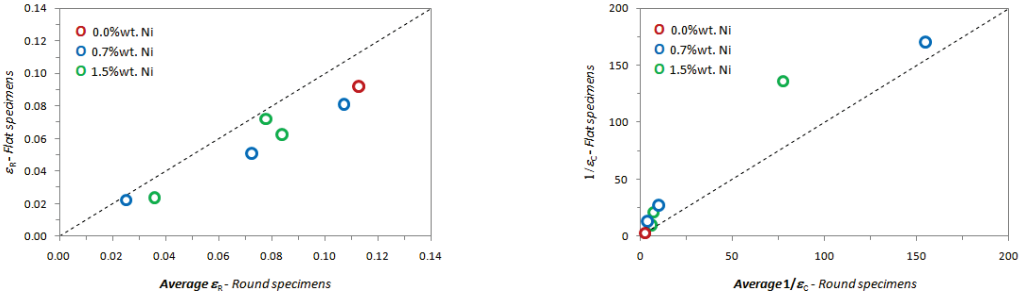

(**a**) (**b**)

Figure 22. (**a**) Strains to rupture (ε_R) comparison from round and flat tensile specimens from 25 mm Y-block ADIs for different Ni contents and austempering conditions: ε_R—flat tensile specimens vs. average ε_R—round tensile specimens; (**b**) $1/\varepsilon_c$—flat tensile specimens vs. average $1/\varepsilon_c$—round tensile specimens (0.0 wt% Ni ausferrite austempered at 310 °C for 3 h and 250 °C for 6 h are missing).

Commercial purity polycrystalline Ni was tensile-tested with round and flat tensile specimens to assess whether the tensile specimen geometry could affect the tensile flow curves. Nickel engineering flow curves from round and flat tensile specimens are reported in Figure 23a for comparison. The flow curves matched up to the uniform elongation, that is, when the UTS was reached, and when localized deformation beyond uniform deformation occurred, there were significant deviations with major elongation reduction in the flat specimen flow curve. Different works [62,63] on the effects of flat tensile specimen geometry on mechanical properties have reported that the tensile flow curves were comparable to UTS as long as tensile specimen geometry complied with international standards. In [64], flow curves from round and flat specimens of a ferritic–pearlitic steel have reported the same results found in nickel in Figure 22, with good matching of the tensile flow curves up to UTS and significant deviation after localized deformation. With Weibull stress numerical calculation [64], the deviation between round and flat tensile specimens beyond uniformed elongations was rationalized to be caused by the different stress distributions at the localized-strain volumes beyond UTS.

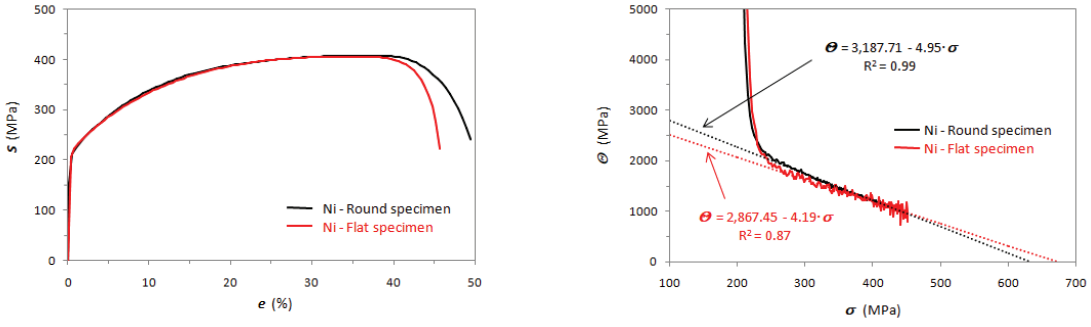

(**a**) (**b**)

Figure 23. Ni polycrystalline tensile plastic behavior comparison between round and flat tensile specimens data: (**a**) engineering stress–strain flow curves; (**b**) differential data (true strain hardening rate Θ vs. true stress σ) from the tensile flow curves in (**a**) and differential Voce equation fittings.

Because of the limited range of the extensometers, the flow curves in Figure 23a had to be stopped at the strain of about 17% and then set to zero for reloading again the specimens with strain control up to the final rupture. This procedure was not necessary with ADIs in the present investigation, as the ADIs' elongations to rupture were always below 14% (see Figure 1). In Figure 23b, differential data of the flow curves up to 0.017 in Figure 23a are reported. Indeed, the round and flat tensile specimen flow curves matched very well and the differential data almost superimposed up to about 17%, well over the typical elongations to rupture of the investigated ADIs, finding that $1/\varepsilon_c$ was 4.19 for flat tensile specimen data and 4.95 for round tensile specimen data. This indicated that the tensile specimen geometry did not affect the flow curves per se, and the effects found in ausferrite and reported in Figures 20 and 21 could be thus ascribed to ausferrite instability. Indeed, reduced ductility, increased Voce parameter values and Voce parameter variability (see Section 3.2) in the flow curves from flat tensile specimens showed that the specimen geometry played a role in the ADI tensile behavior, indicating that the flat geometry enhanced the ausferrite instability. To the authors' knowledge, this effect of tensile specimen geometry on ADIs has never been reported before.

In situ investigations on ADI plastic and fracture behavior have been reported [65–67], even if the main focus of these investigations was on the effects of graphite nodule cracking and graphite–matrix debonding on fracture evolution, rather than on ausferrite plastic behavior. Furthermore, these in situ investigations were only on flat small-sized tensile specimens not complying with international standards. In [67], it was reported that austenite caused some delays in the graphite–matrix debonding, while with bainitic ferrite, the debonding was easier and cracks propagated alongside the ferrite–austenite boundaries [65]. It could be speculated that these observations concerned the external surfaces of flat tensile specimens, causing ductility reduction, while in round tensile specimens, these mechanisms might be less active because of the reduction of the surface/volume ratio of the strain gauge. However, to the authors' knowledge, no insitu observations of ADI round tensile specimens have ever been reported, and further investigations will have to be carried out on this issue.

5. Conclusions

Ductile irons (DIs) with different nominal Ni contents were produced into 25 mm, 5 mm and 3 mm wall castings. The alloys were austenitized at the same conditions of 875 °C for 2 h and then austempered for three different combinations of temperatures and times: 250 °C for 6 h, 310 °C for 3 h and 380 °C for 1 h. So, the combined effects of section thickness, chemical composition and austempering conditions on the tensile mechanical properties of ausferrite were investigated and related to the ausferrite stability.

Strain hardening analysis of tensile flow curves was carried out to analyze the ADIs' tensile plastic behavior according to an innovative material quality assessment procedure based on strain hardening analysis and the Voce equation. Because of the different wall sections, round and flat tensile specimens with geometries complying with ASTM E8/E8M-11 [47] were tested. The following conclusions on the quality assessment procedure based on the Matrix Quality Assessment (MAD) could be drawn:

- MADs are tools for easy determination of the best austempering conditions: the Voce parameter positions in the diagrams indicate how stable the ausferrite is;
- MAD results are consistent with ductility analysis that is conventionally used to find the optimal austempering conditions; lower Voce parameters positions in MADs are consistent with higher ductility and better ausferrite stability, and vice versa: so, MAD and ductility analysis are suggested to be carried out in conjunction;
- In MADs, the widths of the Voce parameter range are also indications of ausferrite stability; high variability of Voce parameters means high instability of ausferrite.

About the effects of section thickness and Ni content on ausferrite in thin sections, the following conclusions could be drawn:

- Ni content promoted higher volume fractions of austenite in ADIs with similar austempering conditions;
- However, higher volume fractions of austenite did not necessarily mean a higher stability of ausferrite;
- Rather, a higher stability of ausferrite was related to higher content of C in metastable austenite, which was independent of Ni content;
- Though thinner sections produced better and finer graphite structure, ADIs from 25 mm, 5 mm and 3 mm castings with the same Ni content had ausferrite with similar tensile mechanical behavior, regardless of the thickness;
- Tensile specimen geometry affected the ausferrite stability, as flat tensile specimens enhanced the ausferrite instability compared to round tensile specimens;
- So, for proper analysis and comparison of the tensile properties of ADIs, the tensile specimen geometry has to be taken carefully into account.

Author Contributions: Conceptualization, G.A., M.G.; methodology, G.A.; investigation, G.A., R.D., D.R.; resources, G.A., B.C., M.G.; data analysis, G.A., M.G.; writing—original draft preparation, G.A.; writing—review and editing, R.D., D.R., F.B., B.C., M.G.; supervision, G.A. All authors have read and agreed to the published version of the manuscript.

Funding: This research received no external funding.

Acknowledgments: Davide Della Torre and Tullio Ranucci are warmly thanked for the technical work carried out in this investigation.

Conflicts of Interest: The authors declare that they have no conflict of interest.

References

1. Janowak, J.F.; Gundlach, R.B.; Eldis, G.T.; Rohrting, K. Technical advances in cast iron metallurgy. *Int. Cast Met. J.* **1982**, *6*, 28–42.
2. Rouns, T.N.; Rundman, K.B.; Moore, D.M. The Relationship Between Microstructure and Tensile Properties in ADI. *AFS Trans.* **1984**, *121*, 815–840.
3. Dubensky, W.; Rundman, K.B. An Electron Microscope Study of Carbide Formation in Austempered ductile Iron. *AFS Trans.* **1985**, *93*, 389–394.
4. Janowak, J.F.; Norton, P.A. A guide to mechanical properties possible by austempering, 1 percent Ni, 0.3 percent Mo Iron. *AFS Trans.* **1985**, *88*, 123–135.
5. Gundlach, R.B.; Janowak, J.F. Austempered ductile irons combine strength with toughness and ductility. *Met. Prog.* **1985**, *12*, 231–236.
6. Moore, D.J.; Noun, T.B.; Rundman, K.B. The relationship between microstructure and tensile properties in austempered ductile cast iron. *AFS Trans.* **1987**, *87*, 165–174.
7. Górny, M.; Stefanescu, D.M. *ASM Handbook. Vol. 1A, Cast Iron Science and Technology*; ASM International: Almere, The Netherlands, 2017; pp. 626–628.

8. Górny, M.; Gondek, L.; Tyrała, E.; Angella, G.; Kawalec, M. Structure homogeneity and thermal stability of austempered ductile iron. *Metall. Mater. Trans.* **2021**, *52*, 2228–2237. [CrossRef]
9. Dodd, J. High strength, high ductility ductile irons. *Mod. Cast.* **1978**, *68*, 60–66.
10. Gundlach, R.B.; Janowak, J.F. Development of a ductile iron for commercial austempering. *AFS Trans.* **1983**, *94*, 377–388.
11. Angella, G.; Zanardi, F.; Donnini, R. On the significance to use dislocation-density-related constitutive equations to correlate strain hardening with microstructure of metallic alloys: The case of conventional and austempered ductile irons. *J. Alloys. Comp.* **2016**, *669*, 262–271. [CrossRef]
12. Donnini, R.; Fabrizi, A.; Bonollo, F.; Zanardi, F.; Angella, G. Assessment of the microstructure evolution of an austempered ductile iron during austempering process through strain hardening analysis. *Metall. Mater. Int.* **2020**, *23*, 855–864. [CrossRef]
13. Angella, G.; Ripamonti, D.; Górny, M. Comparison between ductility examination and a new approach based on strain hardening analysis to support the determination of proper austempering times. *Int. J. Cast Met. Res.* **2020**, *33*, 50–60. [CrossRef]
14. Putatunda, S.K.; Bartosiewicz, L.; Krause, A.R.; Alberts, F.A.; Singh, I. Influence of microstructure on high cycle fatigue behavior of austempered ductile cast iron. *Mater. Char.* **1993**, *30*, 221–234.
15. Shanmugam, P.; Rao, P.P.; Udupa, K.R.; Venkataraman, N. Effect of microstructure on the fatigue strength of an austempered ductile iron. *J. Mater. Sci.* **1994**, *29*, 4933–4940. [CrossRef]
16. Colin, G.E.; Cruz, R.A.; Reyes, C.G.; Romero, S.J.A.; Sanchez, A.R.G.; Hernández, C.M. Influence of nickel addition and casting modulus on the properties of hypo-eutectic ductile cast iron. *J. Min. Metall. Sect. B Metall.* **2019**, *55*, 115–124.
17. Bakhshinezhad, H.; Honarbakhshraouf, A.; Abdollah, P.H. A study of effect of vanadium on microstructure and mechanical properties of as-cast and austempered ductile iron. *Phys. Met. Metallogr.* **2019**, *120*, 441–446. [CrossRef]
18. Haydarzadeh, S.M.; Nili, A.A.; Bahrami, V.A. The role of austempering parameters on the structure and mechanical properties of heavy section ADI. *J. Mater. Process. Technol.* **2004**, *153*, 203–208.
19. Zhang, H.; Wu, Y.; Li, Q.; Hong, X. Mechanical properties and rolling-sliding wear performance of dual phase austempered ductile iron as potential metro wheel material. *Wear* **2018**, *406*, 156–165. [CrossRef]
20. Kim, Y.J.; Shin, H.; Park, H.; Lim, J.D. Investigation into mechanical properties of austempered ductile cast iron (ADI) in accordance with austempering temperature. *Mat. Lett.* **2008**, *62*, 357–360. [CrossRef]
21. Hegde, A.; Sharma, S.; Vikas Sadanand, R. Mechanical characterization and optimization of heat treatment parameters of manganese alloyed austempered ductile iron. *J. Mech. Eng. Sci.* **2019**, *13*, 4356–4367. [CrossRef]
22. Cakir, M.C.; Isik, Y. Investigating the machinability of austempered ductile irons having different austempering temperatures and times. *Mater. Des.* **2008**, *29*, 937–942. [CrossRef]
23. Hegde, A.; Sharma, S.; Shankar, M.C. Machinability and related properties of austempered ductile iron: A review. *J. Mech. Eng. Sci.* **2018**, *12*, 4180–4190. [CrossRef]
24. Putatunda, S.K.; Singh, I. Fracture toughness of unalloyed austempered ductile cast iron. *J. Test. Eval.* **1995**, *23*, 325–332.
25. Panneerselvam, S.; Martis, C.J.; Putatunda, S.K.; Boileau, J.M. An investigation on the stability of austenite in Austempered Ductile Cast Iron (ADI). *Mat. Sci. Eng.* **2015**, *626*, 237–246. [CrossRef]
26. Chernyshev, A.N.; Kaplina, I.N.; Serapin, M.I. Surface hardening with remelting of functional surfaces of cast iron camshafts. *Met. Sci. Heat Treat.* **1996**, *38*, 440–442. [CrossRef]
27. Myszka, D.; Cybula, L.; Wieczorek, A. Influence of Heat Treatment Conditions on Microstructure and Mechanical Properties of Austempered Ductile Iron After Dynamic Deformation Test. *Arch. Metall. Mater.* **2014**, *59*, 1181–1189. [CrossRef]
28. Tanaka, Y.; Kage, H. Development and application of austempered spheroidal graphite cast iron. *Mater. Trans. JIM* **1992**, *33*, 543–557. [CrossRef]
29. Keough, J.R. Austempered ductile iron (ADI)–a green alternative. *Trans. Am. F.* **2011**, *119*, 591–599.
30. Darwish, N.; Elliott, R. Austempering of low manganese ductile irons. *Mater. Sci. Technol.* **1993**, *9*, 572–585. [CrossRef]
31. Darwish, N.; Elliott, R. Austempering of low manganese ductile irons Part 3 Variation of mechanical properties with heat treatment conditions. *Mater. Sci. Technol.* **1993**, *9*, 882–889. [CrossRef]
32. Boccardo, A.D.; Dardati, P.M.; Godoy, L.A.; Celentano, D.J. Sensitivity of Austempering Heat Treatment of Ductile Irons to Changes in Process Parameters. *Metall. Mater. Trans. B* **2018**, *49*, 1522–1536. [CrossRef]
33. Górny, M.; Angella, G.; Tyrała, E.; Kawalec, M.; Paź, S.; Kmita, A. Role of Austenitization Temperature on Structure Homogeneity and Transformation Kinetics in Austempered Ductile Iron. *Met. Mater. Int.* **2019**, *25*, 956–965. [CrossRef]
34. Vuorinen, J.J. Strain-hardening mechanism and characteristics of austempered ductile iron. *AFS Trans.* **1983**, *86*, 577–588.
35. Hayrynen, K.L.; Moore, D.J.; Rundman, K.B. Tensile properties and microstructure of a clean austempered ductile iron. *AFS Trans.* **1990**, *98*, 471–480.
36. Jianghuai, Y.; Putatunda, S.K. Influence of a novel two-step austempering process on the strain-hardening behavior of austempered ductile cast iron (ADI). *Mater. Sci. Eng. A* **2004**, *382*, 265–279.
37. Olofsson, J.; Larsson, D.; Svensson, I.L. Effect of Austempering on Plastic Behavior of Some Austempered Ductile Iron Alloys. *Metall. Mater. Trans. A* **2011**, *42*, 3999–4007. [CrossRef]
38. Angella, G.; Zanardi, F. Comparison among Different Constitutive Equations on Investigating Tensile Plastic Behavior and Microstructure in Austempered Ductile Iron. *J. Cast. Mater. Eng.* **2018**, *2*, 14–23. [CrossRef]
39. Lin, B.Y.; Chen, E.T.; Lei, T.S. The Effect of Alloy Elements on the Microstructure and Properties of Austempered Ductile Irons. *Scr. Metall. Mater.* **1995**, *32*, 1363–1367. [CrossRef]

40. Mi, Y. Effect of Cu, Mo, Si on the Content of Retained Austenite of Austempered Ductile Iron. *Scr. Metall. Mater.* **1995**, *32*, 1313–1317. [CrossRef]
41. Batra, U.; Ray, S.; Prabhakar, S.R. The Influence of Nickel and Copper on the Austempering of Ductile Iron. *J. Mater. Eng. Perform.* **2004**, *13*, 64–68. [CrossRef]
42. Eric, O.; Jovanovic, M.; Sidanin, L.; Rajnovic, D.; Zec, S. The austempering study of alloyed ductile iron. *Mater. Des.* **2006**, *27*, 617–622. [CrossRef]
43. Ratto, P.J.J.; Ansaldi, A.F.; Fierro, V.E.; Agüera, F.R.; Villar, H.N.A.; Sikora, J.A. Low temperature impact tests in austempered ductile iron and other spheroidal graphite cast iron structures. *ISIJ Int.* **2001**, *41*, 372–380. [CrossRef]
44. Sidjanin, L.; Rajnovic, D.; Eric, O.; Smallman, R.E. Austempering study of unalloyed and alloyed ductile irons. *Mater. Sci. Tech.* **2010**, *26*, 567–571. [CrossRef]
45. Čatipović, N.; Živković, D.; Dadić, Z. The effects of molybdenum and manganese on the mechanical properties of austempered ductile Iron. *Tehn. Open Access* **2018**, *25*, 635–642.
46. *ASTM A536–84(2019)e*; Standard Specification for Ductile Iron Castings. ASTM International: West Conshohocken, PA, USA, 2019.
47. *ASTM E8/E8M-11*; Standard Test Methods for Tension Testing of Metallic Materials. ASTM International: West Conshohocken, PA, USA, 2011.
48. *ISO17804:2005*; Ausferritic Spheroidal Graphite Cast Irons—Classification. 2005–2011. ISO International Organization for Standardization: Geneva, Switzerland, 2005.
49. *ASTM E2567-16a*; Standard Test Method for Determining Nodularity and Nodule Count in Ductile Iron Using Image Analysis. ASTM International: West Conshohocken, PA, USA, 2016.
50. *ASTM E975-13*; Standard Practice for X-Ray Determination of Retained Austenite in Steel with Near Random Crystallographic Orientation. ASTM International: West Conshohocken, PA, USA, 2013.
51. Gupta, S.K. Peak decomposition using Pearson type VII function. *J. Appl. Crystall.* **1998**, *31*, 474–476. [CrossRef]
52. Dong, B.; Hou, T.; Zhou, W.; Zhang, G.; Wu, K. The Role of Retained Austenite and Its Carbon Concentration on Elongation of Low Temperature Bainitic Steels at Different Austenitising Temperature. *Metals* **2018**, *8*, 931. [CrossRef]
53. Donnini, R.; Zanardi, F.; Vettore, F.; Angella, G. Evaluation of microstructure quality in ductile irons based on tensile behaviour analysis. *Mater. Sci. Forum.* **2018**, *925*, 342–349.
54. Angella, G.; Zanardi, F. Validation of a new quality assessment procedure for ductile irons production based on strain hardening analysis. *Metals* **2019**, *9*, 837. [CrossRef]
55. Angella, G.; Cova, M.; Bertuzzi, G.; Zanardi, F. Soundness Discrimination in Ferrite Ductile Irons Through Tensile Data Analysis. *Int. J. Met.* **2020**, *14*, 816–826. [CrossRef]
56. Angella, G.; Donnini, R.; Zanardi, F. Assessment of microstructure effects on tensile behaviour in silicon strengthened ductile irons produced through different cooling rates. *Int. J. Cast Metals Res.* **2020**, *33*, 89–102. [CrossRef]
57. Kocks, U.F.; Mecking, H. Physics and phenomenology of strain hardening: The FCC case. *Prog. Mater. Sci.* **2003**, *48*, 171–273. [CrossRef]
58. Angella, G.; Wynne, B.P.; Rainforth, W.M.; Beynon, J.H. Strength of AISI 316L in torsion at high temperature. *Mater. Sci. Eng. A* **2008**, *475*, 257–267. [CrossRef]
59. Angella, G. Strain hardening analysis of an austenitic stainless steel at high temperatures based on the one-parameter model. *Mater. Sci. Eng. A* **2012**, *532*, 381–391. [CrossRef]
60. *ASTM A247-19*; Standard Test Method for Evaluating the Microstructure of Graphite in Iron Castings. ASTM International: West Conshohocken, PA, USA, 2019.
61. Fullman, R.L. Measurements of particles size in opaque bodies. *Trans. AIME* **1953**, *5*, 447–452. [CrossRef]
62. Han, L.; Reynolds, N.; Dargue, I.; Williams, G. The effect of specimen dimensions on obtained tensile properties of sheet metals. *Key Eng. Mater.* **2009**, *410*, 481–491.
63. Masete, M.S.; Muchavi, N.S.; Chikosha, S. The effect of specimen geometry on tensile properties of titanium alloy metal sheet. *IOP Conf. Ser. Mater. Sci. Eng.* **2018**, *430*, 012015. [CrossRef]
64. Strnadel, B.; Brumek, J. Effect of tensile test specimen size on ductility of R7T steel. In Proceedings of the Metals 2013, 22nd International Conference on Metallurgy and Materials, Brno, Czech Republic, 15–17 May 2013; pp. 560–565.
65. Dai, P.Q.; He, Z.R.; Zheng, C.M.; Mao, Z.Y. In-situ SEM observation on the fracture of austempered ductile iron. *Mater. Sci. Eng. A* **2001**, *319*, 531–534. [CrossRef]
66. Petrenec, P.; Tesařová, H.; Krahula, K.; Polák, J. Elastic-plastic behaviour of advanced ADI studied by in-situ SEM tensile test. In Proceedings of the Metals 2013, 22nd International Conference on Metallurgy and Materials, Brno, Czech Republic, 15–17 May 2013; pp. 676–681.
67. Warmuzek, M.; Polkowska, A. Micromechanism of Damage of the Graphite Spheroid in the Nodular Cast Iron During Static Tensile Test. *J. Manuf. Mater. Process.* **2020**, *4*, 22. [CrossRef]

metals

MDPI

Article

Performance Evaluation of Austempered Ductile Iron Camshaft Low Alloyed with Vanadium on an Electric Spin Rig Test

Alejandro Cruz Ramírez [1,*], Eduardo Colin García [1,*], Jaime Téllez Ramírez [2] and Antonio Magaña Hernández [2]

[1] Instituto Politécnico Nacional–ESIQIE, UPALM, Ciudad de México 07738, Mexico
[2] R&D ARBOMEX S.A de C.V., Calle Norte 7 No. 102, Cd. Industrial, Celaya 38010, Guanajuato, Mexico
* Correspondence: alcruzr@ipn.mx (A.C.R.); ecoling1400@alumno.ipn.mx (E.C.G.); Tel.: +52-55-5729-6000 (ext. 54202) (A.C.R.); +52-55-3162-8863 (E.C.G.)

Abstract: Arbomex S.A. de C. V. is one of the largest worldwide manufacturers of ductile cast iron camshafts, produced by means of the phenolic urethane no-bake sand mold casting method and cold box by stack molding technology. As a result of the development of high-strength ADIs, low alloyed with vanadium, for camshaft manufacturing, previous results were published on the as-cast process and the austempering heat treatments applied to the camshafts. In the present work, camshafts of ADIs, low alloyed with 0.2 and 0.3 wt.% V, were produced at austempering temperatures of 265 and 305 °C. The performance of the new camshafts was evaluated by wear testing to ensure the function and durability of the camshafts by means of the block-on-ring wear test and a valve train system to evaluate the volume loss of material removed and the geometrical changes of the camshaft, respectively. The ADIs heat treated to 265 °C showed a microstructure constituted of fine ausferrite that aided in obtaining the highest wear resistance in the block-on ring wear test. No wear or pitting evidence was detected on the camshaft lobes and roller surfaces after the OEM test protocol during the electric spin ring test at low and high conditions for the ADI alloyed with 0.2 wt.% V heat treated at 265 °C.

Keywords: camshaft; ADI; wear; valve train system; microstructure; vanadium

Citation: Cruz Ramírez, A.; Colin García, E.; Téllez Ramírez, J.; Magaña Hernández, A. Performance Evaluation of Austempered Ductile Iron Camshaft Low Alloyed with Vanadium on an Electric Spin Rig Test. *Metals* **2023**, *13*, 198. https://doi.org/10.3390/met13020198

Academic Editors: Annalisa Fortini and Chiara Soffritti

Received: 19 December 2022
Revised: 9 January 2023
Accepted: 13 January 2023
Published: 18 January 2023

1. Introduction

The trend toward reduced size and increased power output in current engine designs has placed demands on component materials. Achieving fuel economy in the automotive industry and reducing vehicle weight have been major research interests over the last few decades. Cast iron and aluminum alloys are the most commonly cast metal parts used in the automotive industry, due to their low cost, ease of machining, ease of casting into complex shapes and desired physical properties [1]. When mechanical properties, density, and cost are included in the material evaluation, ductile iron may offer more advantages than aluminum, especially for thin wall ductile iron parts [2]. If the yield stress/cost ratio of the various materials is compared, austempered ductile iron (ADI) is, most of the time, the preferred choice. ADI material can be used to achieve design flexibility, having minimum energy requirements and maximum material utilization, and, hence, providing a better cost-to-benefit ratio with low-cost production. These properties are beneficial to a wide spectrum of user industries that include the automotive sector, mining sector, railways, etc. [2,3]. ADI is a family of ductile iron (DI) that has been treated by austempering (isothermal heat treatment) [4] resulting in nodules immersed in an ausferritic matrix composed of acicular ferrite (α_{Ac}) and high carbon austenite (γ_{HC}) [5]. The austempering heat treatment to obtain ADI is carried out in a two stage reaction.

$$\text{Stage I reaction}: \ \gamma \rightarrow \alpha_{Ac} + \gamma_{HC} \ (\text{ausferrite})$$

$$\text{Stage II reaction}: \ \gamma_{HC} \rightarrow \ \alpha + \ \text{carbide} \ (Fe_3C \text{ or } \varepsilon)$$

The maximum ausferrite amount is obtained between the two stages of austempering, which is at the end of the first stage and at the onset of the second stage. This period is called the process window (PW). The amount and morphology of the high-carbon austenite and acicular ferrite depend on the austempering parameters, temperature, and holding time [6]. The camshaft, crankshaft, gearbox, engine block, automobile suspension, cylinder head, and steering systems are some of the casting products from foundries used in automotive industries [1]. In the automotive industry, ADI has an important task as a structural material that should have good wear resistance and tensile strength in such applications as camshafts [7,8]. Some forged steel components have been replaced by austempered ductile iron (ADI), mainly in automotive applications, such as camshafts. A camshaft is a critical component required to enable a combustion engine to work. It is constituted of a shaft with shaped lobes (cam lobes) positioned along it. When the shaft is rotated, the profile of the lobe allows it to act upon a valve or switch to a degree matching the speed of rotation controlling the rate of action. The camshafts are connected via a timing belt or chain to the turning of the crankshaft, which directly moves the pistons inside the cylinder [9]. During functioning, camshafts are subject to bending and torsional stresses, and lobe surfaces are highly loaded, so high toughness and wear resistance are essential for this component [10]. Engine camshafts are unique in that the manufacturing requirements are very different from the operating needs of the product. Thus, there must be a balance that achieves the needs of a hard, strong, and wear-resistant material with ease of manufacturing, and, most notably, offering the ability of machining the product. The ever-shorter development times of car manufacturers require ever faster and more effective product development. An elementary component of product development is the validation of new products by testing to ensure the function and durability of such products. Different testing methods are employed to evaluate the performance of camshafts, like cam phaser systems or valve train systems [11,12].

Alloying elements are used to improve the mechanical properties or modify the austemperability of ADI [13]. Since vanadium is a carbide stabilizer, its addition promotes the formation of eutectic carbide that appears as small white inclusions in the microstructure. The addition of vanadium to the ductile cast iron increases its strength and hardness by an increase of the pearlite amount [14].

Arbomex [15]., a Mexican company located at Celaya and Apaseo Guanajuato, as well as El Salto Jalisco, Mexico, specializes in camshaft manufacturing, developing ductile irons, low alloyed with vanadium (0.2 and 0.3 wt.%), for camshaft application [16]. Homogeneous distribution of spheroidal graphite, with high nodularity for casting, was obtained from the regions of the lobes analyzed. A high nodule count of smaller size was found in the lobe surfaces instead of in the middle region where big nodules with low nodule count were found. The tensile properties were increased when the vanadium content increased; however, the toughness and ductility of the as-cast alloys decreased as a result of an increase in the volume fraction of carbide particles [16]. Afterwards, the DI, low alloyed with vanadium, was austempered to 265 and 305 °C for 30, 60, 90, and 120 min to obtain high-strength ADIs. The highest amount of ausferrite was determined at 90 min for both austempering temperatures by X-ray diffraction measurements and was in good agreement with the evolution of microstructures and hardness as the austempering time increased. The mechanical properties of tensile strength, hardness, and toughness were evaluated, obtaining results in the range expected for an ADI grade 3 [17]. Camshafts are an important part of a valve train system. The camshafts are driven by a crankshaft and they run at about half of the angular speed of the crankshaft. In high-speed engines, the rotational speed of the camshaft can be very high, leading to high torsional vibrations, which then leads to high stresses in the valve train system. Cams are commonly used in the opening and closing of valves in internal combustion engines. The inlet and outlet valves are regulated using a cam and follower and the mechanical contact between both components are partially responsible for wear damage. There are different types of wear mechanisms involved; however, adhesive wear is, by far, the most dominant form of material loss among

sliding components in machinery [12,18]. This work aimed to evaluate the performance of camshafts of high-strength ADIs, low alloyed with vanadium, on sliding wear, by means of the block-on-ring wear test, and on an electric spin rig test to check and ensure the durability of the camshaft under engineering specification parameters.

2. Materials and Methods

Arbomex [15] is a North American-based company with more than 45 years of providing Aluminum and Zamak by High-Pressure Die Casting (HPDC), steel and aluminum metal sheet stamping, and cast iron with the lost foam process for applications, such as brackets and housings, for the heavy-duty automotive industry and, on the other hand, camshafts manufactured by molding processes, like the phenolic urethane no-bake sand process, and cold box by stack molding technology.

2.1. Ductile Iron Castings

Two ductile irons, low alloyed with vanadium, and identified as DI-0.2V and DI-0.3V, for camshafts were produced in a dual-track coreless induction furnace by the phenolic urethane no-bake sand mold casting method.

The base iron was produced by using 30 wt.% low carbon steel, 30 wt.% iron burrs from the machining area, and cast-iron scrap as balance at 1400–1440 °C. The base iron was poured into a preheated ladle where the chemical composition was adjusted by adding the ferroalloys: FeSi (70%), high-purity carbon, and FeV (61.5%). The ductile iron alloy was poured into a tundish ladle where 1.05 wt.% of MgFeSi (45% Si, 7.5% Mg, 0.8% Al, 2.6% Ca, 2.48% Rare earth) was added as a nodulizing agent. Later, the melt was poured into a ladle and inoculated with the inoculant FeSi (70% Si + 0.8% Ca, 3.9% Al) by the ladle inoculation method. Each of the two cast alloys was then poured at 1385–1420 °C into phenolic urethane no-bake sand molds, previously obtained by tooling with four cavities of camshafts (intake and exhaust lobes) for the casting method. The nominal chemical composition in the camshafts was analyzed by an OBLF GS 1000 II emission optic spectrograph (OBLF Gesellschaft für Elektronik und Feinwerktechnik mbH, Witten, Germany). Carbon and sulfur content was determined by combustion analysis using a Leco C/S 744 analyzer (LECO Corporation, St. Joseph, MI, USA). The reported values were the average of three measurements on each cast alloy.

2.2. Austempering Heat Treatment

Four camshafts were randomly selected from each alloy and the lobes were sectioned on the cross-section with a metallographic fine cutter disc and liquid cooling for the austempering heat treatment. Figure 1 shows a lobe sample taken from the camshaft and the regions analyzed from the top area (nose of the lobe), middle, and bottom (base circle) for the microstructural characterization.

Two austempering heat treatments were carried out based on the austempering heat treatment cycles of Figure 2. The samples were coated with carbon paint (to avoid decarburization) during austenitizing held at 900 ± 5 °C with a residence time of 180 min. Then, the samples were quickly transferred to a second furnace containing a salt bath melt (50% KNO_3 and 50% $NaNO_3$) at 265 or 305 ± 5 °C. The soaking time was set at 30, 60, 90, and 120 min, and then the samples were water-cooled at room temperature.

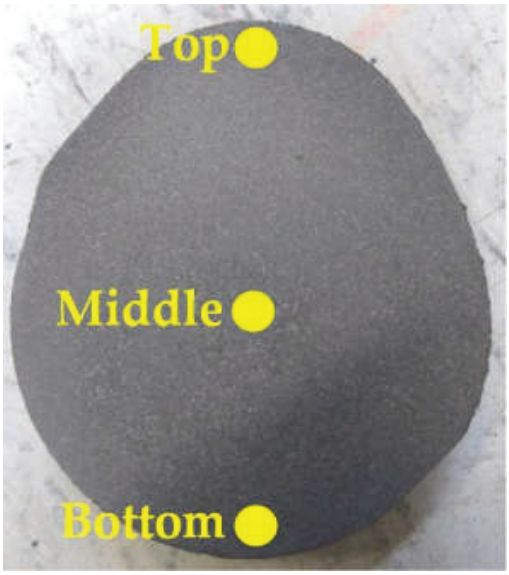

Figure 1. Lobe taken from camshaft showing the three regions analyzed.

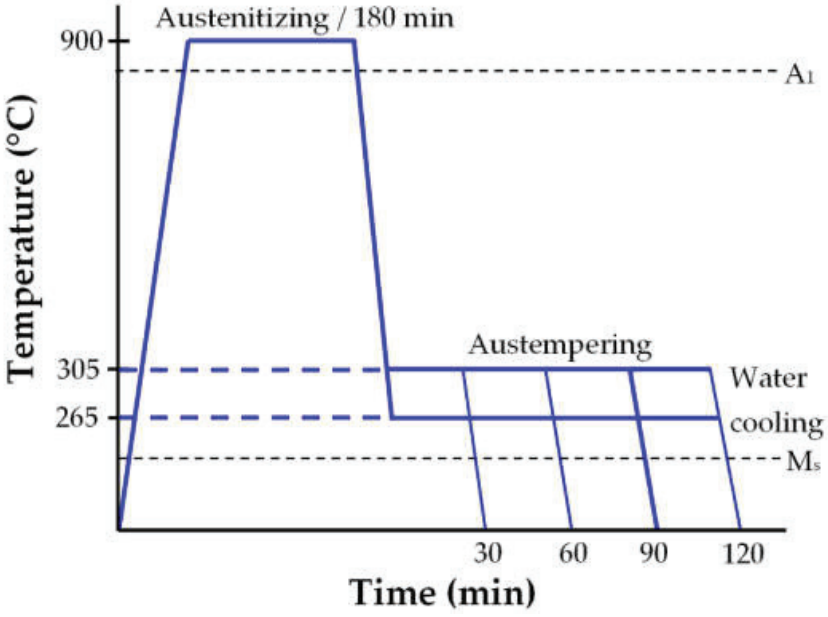

Figure 2. Austempering heat treatment cycles for temperatures of 265 and 305 °C.

2.3. Microstructural Characterization

Microstructural examinations of the DI and ADI samples were carried out by using an optical microscope Olympus PMG-3 model (Olympus Corporation, Center Valley, PA, USA), according to the standard ASTM A247, and Image J software (NIH, Bethesda, MD, USA) to evaluate the nodule count, average nodule size, and nodularity, while the volume fraction of phases and microconstituents were obtained on samples etched with nital 3%.

The optical microscopy results were the average of three different regions on each sample. Carbides were revealed by etching for 3 min with a water solution of ammonium persulfate (10% vol) [19]. The volume fraction of high-carbon austenite (% $V\gamma_{HC}$) was obtained from the heat-treated samples by X-ray diffraction measurements using an X-Ray Bruker D8 Focus diffractometer (Bruker, Billerica, MA, USA) with monochromatic Cu $K\alpha_1$ radiation working in $\theta/2\theta$ configuration, using the method reported by Miller [20].

2.4. Mechanical Properties

Samples were obtained from the camshafts of both alloys for the tensile strength, hardness, wear, and impact properties by the Charpy test. Keel-block castings, based on the standard specification ASTM A 536, were also used to obtain samples for tensile strength to ensure process quality. The samples were austempered according to the procedure reported in Figure 2, and the soaking time was chosen according to the highest high-carbon austenite value obtained by XRD measurements. Figure 3 shows the samples obtained from camshafts and Keel-block casting to evaluate the mechanical properties at room temperature.

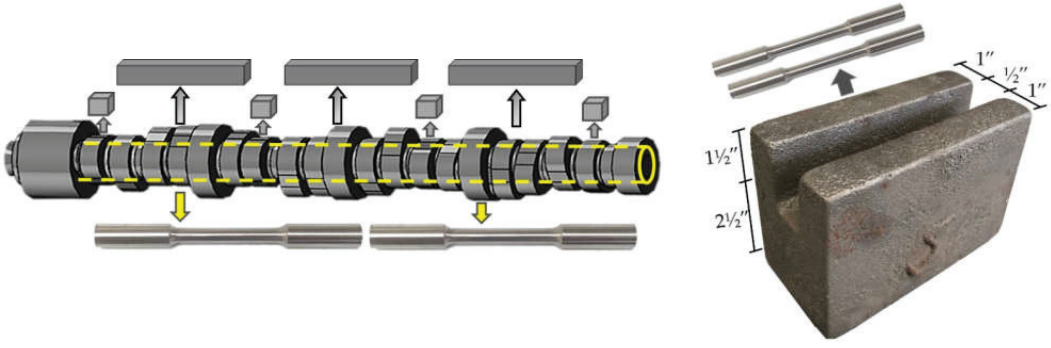

Figure 3. Samples for mechanical properties were obtained from (**a**) Camshafts and (**b**) Keel-block casting.

Rockwell C hardness measurements were made on the polished surfaces of the cross-section of the camshaft lobes with a Wilson 3T TBRB hardness tester (Buehler, Lake Bluff, IL, USA). The hardness test was carried out under the standard specification ASTM E 18-02 and an applied load of 150 kg. Tensile testing was carried out using a universal testing machine, Shimadzu (Shimadzu Corporation, Kyoto, Japan) of 100 kN, with 10 mm/min cross-head speed. The size and geometry of the specimens followed the specifications of ASTM E 8. Charpy unnotched bars impact tests were machined, based on the specifications of ASTM A 327. Four specimens from each cast alloy were taken from the camshaft and were tested for impact in a Tinius Olsen Charpy impact testing machine (Tinius Olsen TMC, Hursham, PA, USA).

The mechanical properties of DIs and ADIs alloyed with 0.2 and 0.3 wt.% vanadium for camshaft production were previously reported [16,17]. High strength, hardness, and toughness were obtained for the evaluated austempering heat treatments; however, the performance of the camshafts had to be evaluated under wearing conditions to ensure the good behavior of the component during functioning. Thus, this work aimed to determine the wear resistance of the camshaft under engineering specification parameters by an electric spin rig test and the block-on-ring wear test.

Wear Test

The standard abrasion testing used was ASTM G77 which determines the resistance of materials to sliding wear using the block-on-ring wear test. This test method covers laboratory procedures for determining the resistance of materials to sliding wear. The

test utilizes block-on-ring friction and a wear testing machine to rank pairs of materials according to their sliding wear characteristics under various conditions. The wear resistance was evaluated in a TE 53SLIM multi-purpose friction machine (Phoenix Tribology, Berkshire, UK) on cube samples of 12.5 mm obtained from the camshaft lobes closer to the lobe nose, as can be observed in Figure 3a, with hardened machined flat surfaces without lubricant. A metal ring, with a hardness of 63 HRC, rotated on the surface of the sample to 300 rpm, applying a load of 45 N for a distance of 100 m. The wear results were obtained with Equation (1):

$$Scar\ volume = \frac{D^2 t}{8}\left[2sin^{-1}\frac{b}{D} - sin\left(2sin^{-1}\frac{b}{D}\right)\right] \quad (1)$$

where D is the diameter of the ring (mm), t is the block width (mm) and b is the width average of the *scar* (mm). The block-on-ring test was used, because it maintained a constant contact area between the sample and the ring during wear.

2.5. Camshaft Bench Testing

During functioning, camshafts are subject to bending fatigue strength and torsional stresses and the lobe surfaces present high Hertzian contact stresses. Thus, high toughness, yield strength, and wear resistance are essential for this component. A spin rig test was used to evaluate the camshaft performance. The electric spin rig machine of Figure 4 is a modification of the original combustion engine OEM V8 5.7L, developed in the Arbomex camshaft testing laboratories. This is an Overhead valve engine (OHV) (OEM Engine, Ramos Arizpe, Coahuila, México), where the camshaft is placed inside the block and the valves are operated through lifters, pushrods, and rocker´s arms. This mechanism is called a valvetrain.

Figure 4. Electric Spin Rig machine—V8 engine 5.7L.

The OHV design is more suitable for larger V6 and V8 engines. The advantages of an OHV engine include lower cost, higher low-end torque, and more compact size; in addition to durability. Figure 5 shows the automotive engine camshafts V8 5.7L made of ADI, low alloyed with vanadium, used for the trials. Prior to the test, the engine and cavities were cleaned, and the engine head gaskets and camshaft support fasteners were changed.

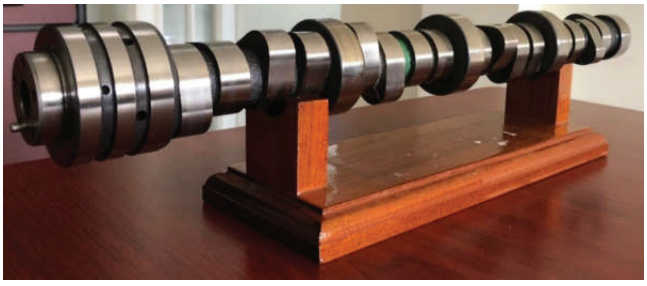

Figure 5. ADI low alloyed with vanadium camshaft 5.7L with 16 intake and exhaust lobes.

The test parameters of Table 1 were used to evaluate the performance of the high-strength camshafts low alloyed with vanadium.

Table 1. Camshaft bench testing parameters.

Speed	Low Condition (500 rpm-Camshaft) (1000 rpm-Engine)	High Condition (2500 rpm-Camshaft) (5000 rpm-Engine)
Test duration	1000 h	300 h
Number of cycles	~24 million cycles	~36 million cycles
Change oil and oil filters	Every 300 h	Only to start the test
Lubrication	5W-30	
Load @Nose Initial Spring length 53.50 mm	1696 N @ to 29.62 mm compress	
Hydraulic roller lifters material	Steel–Superficial 61.5 HRC	

It must be noticed that the bench testing parameters fulfilled the requirements of the OEM test protocol. As can be observed, the requirements were very rigorous and the total number of test cycles exceeded 60 million. The lobes were visually checked every 300 h during testred the temperature of oil and anti-freeze.

3. Results

3.1. Ductile Irons

The chemical composition of the ductile irons alloyed with 0.2 and 0.3 wt.% V is shown in Table 2. The chemical compositions were in the range expected for hyper-eutectic ductile iron and fulfilled the standard specifications of Arbomex for camshaft production. The chemical compositions of the cast alloys produced were similar and the only difference was the amount of vanadium added to the castings. The residual magnesium content of 0.04% indicated an adequate nodule formation, as well as the typical residual sulfur after treatment, recommended in [21]. High manganese and copper amounts were required to form a high amount of pearlite in the camshafts produced. Furthermore, both elements delayed the first stage of the austempering heat treatment. It was reported in [22] that manganese is a carbide-forming element that segregates in eutectic cell boundaries during solidification, while vanadium is a strong carbide-forming element used to increase the strength and hardness of ductile irons, which does not influence the kinetics of the austempering process [23].

Table 2. Chemical composition of camshafts low alloyed with vanadium (wt.%).

Sample	C	Si	Mn	P	S	Mg	V	Ni	Al	Cu	Cr	Mo	Ti	Sn	Pb	CE
DI-0.2V	3.61	2.49	0.96	0.016	0.013	0.045	0.2	0.117	0.016	0.943	0.20	0.098	0.006	0.003	0.001	4.44
DI-0.3V	3.58	2.48	0.94	0.016	0.012	0.041	0.3	0.115	0.016	0.968	0.13	0.092	0.006	0.004	0.001	4.41

Balance Fe. CE: Carbon Equivalent = %C + 1/3%Si + 1/3%P.

A detailed analysis of the graphite features, namely nodule count, nodularity, nodule size, non-metallic inclusions, and porosities, as well as the main phases formed, like graphite, ferrite, pearlite, and carbides, on the ductile iron camshaft lobes low alloyed with vanadium was previously reported in [16]. Only a summary of the main results is given here.

A homogeneous distribution of spheroidal graphite with high nodularity for both ductile irons low alloyed with vanadium was obtained, as can be observed in Figure 6. The etched samples showed a microstructure constituted of graphite nodules in a fully pearlitic matrix with small amounts of white zones attributed mainly to ferrite and carbides. The chemical composition, reported in Table 2, showed high manganese and copper amounts were used to obtain a high amount of pearlite in the camshafts produced, while vanadium was a strong carbide-forming element that was added to increase the strength and hardness of ductile irons [23].

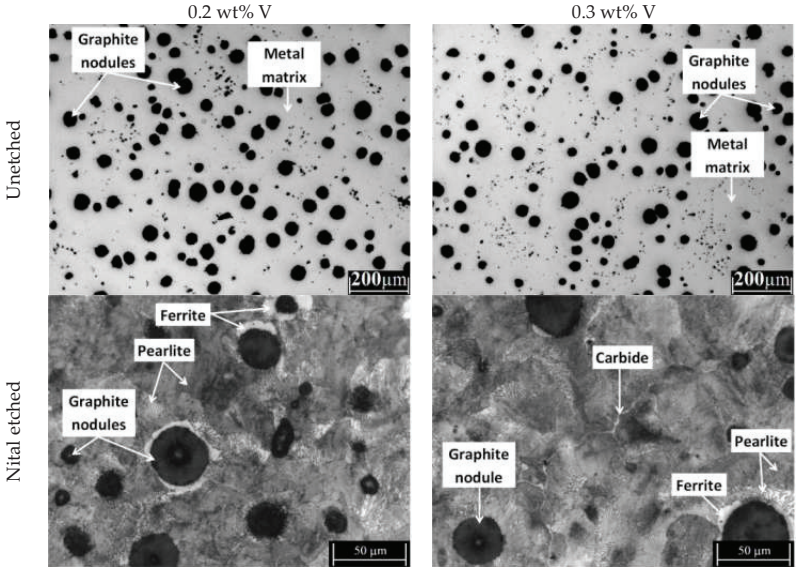

Figure 6. Microstructure at high magnifications for the DI low alloyed with V in unetched condition and etched with nital 3%.

Table 3 summarizes the graphite features and the phases obtained in the ductile irons low alloyed with vanadium, respectively.

Table 3. Graphite features and volume fraction of phases formed for camshaft alloyed with 0.2 and 0.3 wt.% V.

Characteristics	DI-0.2V	DI-0.3V
Nodularity (%)	85.26 ± 3.45	85.32 ± 5.36
Nodule count (particles/mm^2)	223 ± 31.25	216 ± 41.67
Nodule size (μm)	25.91 ± 0.98	31.01 ± 2.03
Porosity, inclusions, and micro-shrinkages (%)	0.69 ± 0.09	0.91 ± 0.16
Graphite (%)	10.11 ± 1.79	11.21 ± 1.73
Ferrite (%)	2.83 ± 0.43	1.21 ± 0.41
Pearlite (%)	85.96 ± 3.98	85.74 ± 4.11
Carbides (%)	0.41 ± 0.10	0.93 ± 0.12

It can be observed from Table 3 that when the vanadium content increased from 0.2 to 0.3 wt.%, the nodule count decreased, while the nodule size and the volume fraction of graphite increased. The low addition of vanadium did not affect the nodule shape, as can be observed in the nodularity results. Being strong in carbide forming, the increase of vanadium allowed for an increase in the volume fraction of carbides. The pearlite content remained almost constant, while the ferrite slightly decreased when the vanadium content increased.

3.2. Austempered Ductile Irons

The DIs low alloyed with vanadium were austempered to 265 and 305 °C for 30, 60, 90, and 120 min to obtain high-strength ADIs. A detailed analysis of the microstructural and hardness evolution as the austempering time increased was previously reported in [17]. The highest amount of high-carbon austenite was obtained for a soaking time of 90 min for both austempering temperatures by means of X-ray diffraction measurements. Table 4 shows the phases formed for an austempering time of 90 min, considering ausferrite as the main phase formed during the heat treatment. The ADIs obtained were designated, in terms of the vanadium content and the austempered temperature, as ADI-0.2V-265, ADI-0.3V-265, ADI-0.2V-305, and ADI-0.3V-305.

Table 4. The volume fraction of phases for the ADIs produced.

Phases	ADI-0.2V-265	ADI-0.2V-305	ADI-0.3V-265	ADI-0.3V-305
High-carbon Austenite (%)	9.53	10.93	8.83	12.93
Carbides (%)	0.18	0.12	0.27	0.21
Graphite (%)	10.11	10.11	11.21	11.21
Acicular ferrite (%)	80.17	78.73	79.77	75.64

Figure 7 shows the microstructure by light microscopy of the ADIs containing 0.2 and 0.3 wt.% V for the austempering temperatures of 265 and 305 °C and 90 min of soaking time. It was observed that the ADIs showed a fine ausferrite matrix, composed mainly of tiny fine acicular ferrite (needle-like) and a few blocks of high-carbon austenite. This microstructure was related to the low austempering temperature. It was reported in [24] that a fine ausferrite morphology was obtained for austempering heat treatments carried out at temperatures lower than 325 °C, while feathery ausferrite was obtained at austempering temperatures higher than 350 °C. The results showed that the ADIs obtained at 265 °C presented a finer ausferrite microstructure, with a high-volume fraction of acicular ferrite and a low-volume fraction of high-carbon austenite. An opposite behavior was observed when the austempering temperature was increased to 305 °C, as is reported in Table 3. During the austempering heat treatment, the ferrite formed from unstable austenite by a nucleation and growth process in the solid state, for a low austempering temperature, such as 265 °C, the supercooling rate was higher, which increased the ferrite nucleation, obtaining larger regions of acicular ferrite [25]. On the other hand, the small blocks of high-

carbon austenite were attributed to a low diffusion of carbon atoms when austempering reactions occurred at low temperatures. The unstable austenite ejected the carbon atoms forming ferrite. Due to the low diffusion of carbon atoms, only a small block of austenite was stable [26].

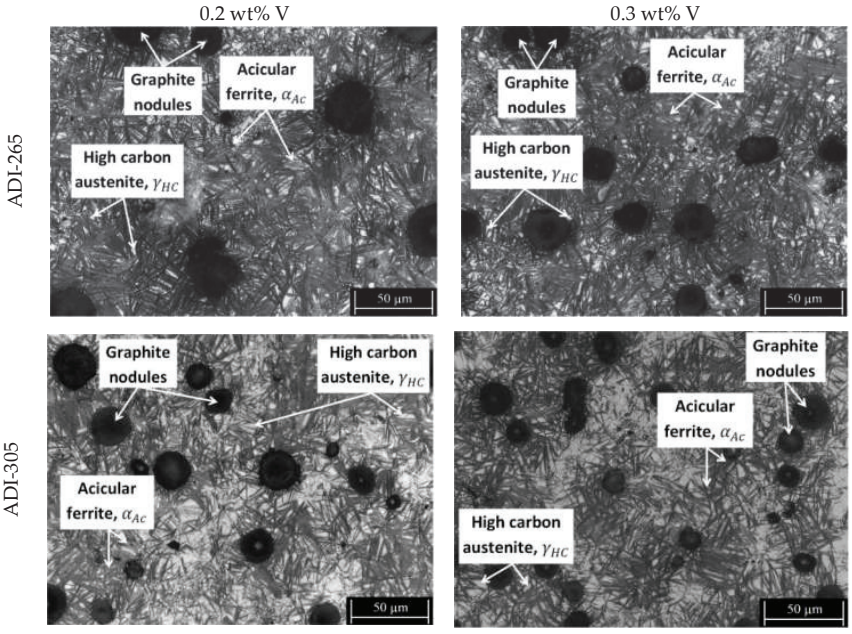

Figure 7. Microstructure of ADI alloyed with 0.2 wt.% V heat-treated to 265 °C and 305 °C for 90 min.

When the austempering temperature was increased to 305 °C, the ausferrite was coarser and the high-carbon austenite increased slightly over those obtained at 265 °C. In this case, the cooling was slower; thus, less acicular ferrite was nucleated and the volume fraction of high-carbon austenite increased [25,27]. The effect of the austempering temperature and its influence on the fine or coarse ausferrite formation was previously reported by Bendikiene [28] in ADIs obtained at austempering temperatures in the range from 270 to 330 °C.

Table 5 summarizes the results of the mechanical tests performed on DIs and ADIs low alloyed with vanadium at room temperature. The ADI mechanical properties were evaluated for the austempering of both DIs to 265 and 305 °C for a soaking time of 90 min, where the highest high-carbon austenite value was obtained. The mechanical results were previously reported and analyzed in [16,17].

Table 5. Mechanical properties of the ADI camshafts low alloyed with 0.2 and 0.3 wt.% V.

Mechanical Properties	DI-0.2V	DI-0.3V	ADI-0.2V-265	ADI-0.2V-305	ADI-0.3V-265	ADI-0.3V-305
Hardness (HRC)	37.05 ± 2	36.54 ± 2	44 ± 0.7	43 ± 0.5	47 ± 0.8	44 ± 1.2
Yield strength (MPa)	559 ± 21	588 ± 25	1032 ± 32	781 ± 28	1051 ± 22	999 ± 29
Tensile strength (MPa)	775 ± 28	782 ± 26	1107 ± 25	989 ± 21	1200 ± 24	1176 ± 30
Elongation (%)	4.5 ± 0.6	3.6 ± 0.4	3.04 ± 0.3	3.5 ± 0.3	3.58 ± 0.4	3.32 ± 0.4
Impact energy (J)	14.8 ± 1.2	11.0 ± 1.4	29.08 ± 3	30.58 ± 3.4	25.88 ± 3.1	40.45 ± 3.3

The mechanical properties of hardness, tensile strength, and impact energy were increased by the austempering heat treatment because the mechanical behavior depended directly on phases and microconstituents. The microstructure obtained in the as-cast

condition contained pearlite, ferrite, and carbides formed during the camshaft solidification process, while the austempering heat treatment applied to the ductile iron promoted phase transformations forming harder phases as ausferrite and martensite with a low volume fraction of vanadium carbides homogeneously distributed in the camshaft microstructure. In general, hardness and tensile strength were higher in ADIs obtained at an austempering temperature of 265 °C, due to the microstructure being constituted by fine ausferrite with bigger volume fractions of acicular ferrite. However, the elongation and impact energy were higher for ADIs heat treated to 305 °C, due to the formation of coarser ausferrite with an increase of the volume fraction of high-carbon austenite, based on the results of Table 3. Similar mechanical results were obtained for ADIs alloyed with manganese in the range from 0.2 to 1 wt.% heat treated to the austempering temperatures in the range of 320 to 420 °C [29].

3.3. Wear Resistance

The block-on-ring wear test was carried out on DI and ADI samples; the scar width was measured and, by using Equation (1), the volume loss of material removed by the abrasion of the sample with the metal ring was determined. The wear scars of the DIs and ADIs are shown in Figure 8, while the volume loss of each material is observed in Figure 9. As expected, the as-cast condition microstructure was mainly constituted of pearlite, which was a softer phase when compared with the ausferrite and martensite microstructures obtained for ADIs, as can be observed in Figures 6 and 9. The volume loss of material was higher for the as-cast condition than the ADIs, because of the hardness difference in both materials; therefore, exhibiting lower wear resistance [30].

It was observed that the austempering temperature affected the wear resistance of the ADIs evaluated. The higher wear resistance values were obtained for the ADIs heat-treated at 265 °C because of the higher volume fraction of ferrite acicular and lower volume fraction of high carbon austenite presented in the fine ausferritic matrix. This condition was beneficial to improve wear resistance due to hardness [31]. On the contrary, higher austempering temperatures increased the volume fraction of high-carbon austenite, and the ausferrite was coarser; hence, the wear resistance decreased [32].

The addition of vanadium promoted the formation of eutectic carbide that appeared as small white inclusions in the microstructure. The presence of carbides reinforced the metallic matrix, due to its high hardness, increasing the wear resistance of the material [33]. Figure 10 shows the DI and ADIs microstructures etched with ammonium persulfate to identify only the carbides. A small number of carbides, identified as white regions with elongated shapes, was observed for the DIs, while the ADIs showed a lower carbide amount as dotted particles homogeneously distributed.

Despite the high thermodynamic stability of alloyed carbides, due to the vanadium addition in the ductile irons [34], there was a reduction in the carbide formation after application of the heat treatment, as can be observed in the as-cast results compared with the ADIs obtained, reported in Tables 2 and 3, respectively. It was reported in [17] that a microsegregation effect in the middle region of the camshaft occurred because this region is the last to freeze. Therefore, the presence of carbides was expected to promote an increase in the abrasion wear resistance; however, toughness was expected to decrease for ADIs containing higher carbide contents. The ADIs heat treated to 265 °C, with different vanadium contents, had a fine ausferrite microstructure, improving the wear resistance, due to the hardness of the acicular ferrite and the low amount of high-carbon austenite [35]. Although both ADIs presented fine ausferrite, it was observed that ADI-0.3V-265 showed a lower volume loss than ADI-0.2V-265. This behavior was because the ADI-0.3V-265 contained the highest volume fraction of carbides in the matrix. The wear resistance in ADIs improved when the microstructure was constituted of fine ausferrite with fine carbides dispersed in the matrix without martensite [36]. Similar wear results on DIs and ADIs were obtained by Balos [37], who evaluated the wear resistance of DIs and ADIs with different microstructures with the pin-on-disc wear test. The results showed, in all cases,

that ADIs had a lower volume loss than the DIs matrix and the wear resistance improved for ADIs heat treated to low austempering temperatures.

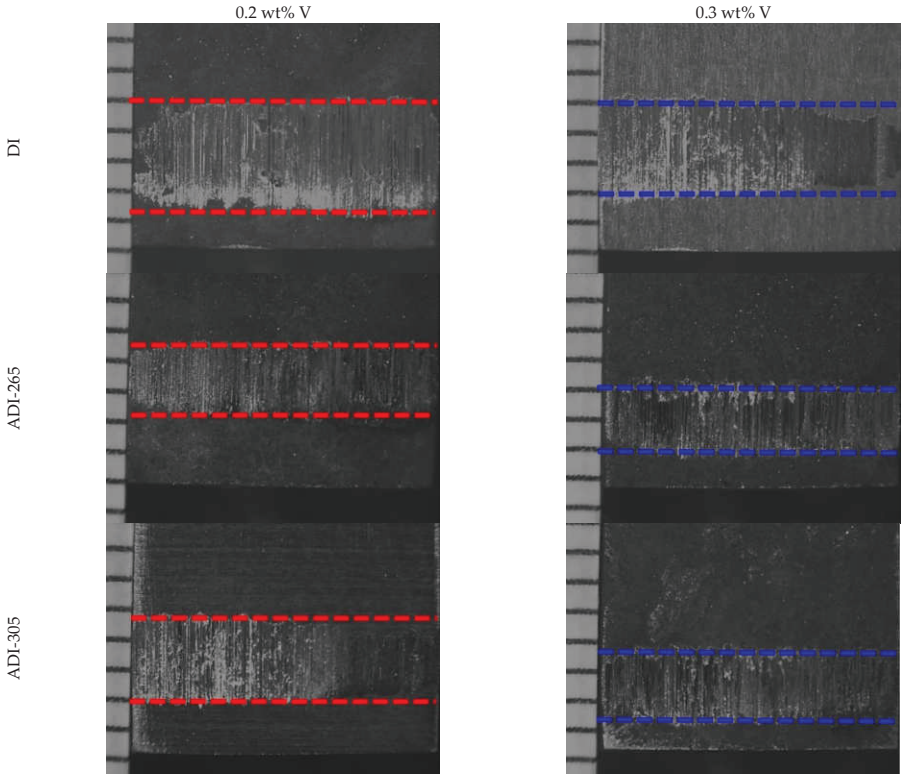

Figure 8. Wear scars samples for DI and ADI alloyed with 0.2 and 0.3 wt.% V, austempered at 265 and 305 for 90 min.

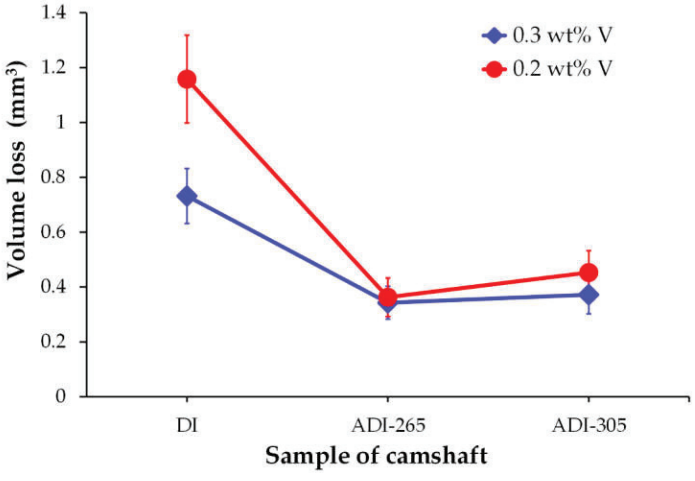

Figure 9. Effect of the austempering temperature and vanadium content on the wear resistance for the evaluated ADIs.

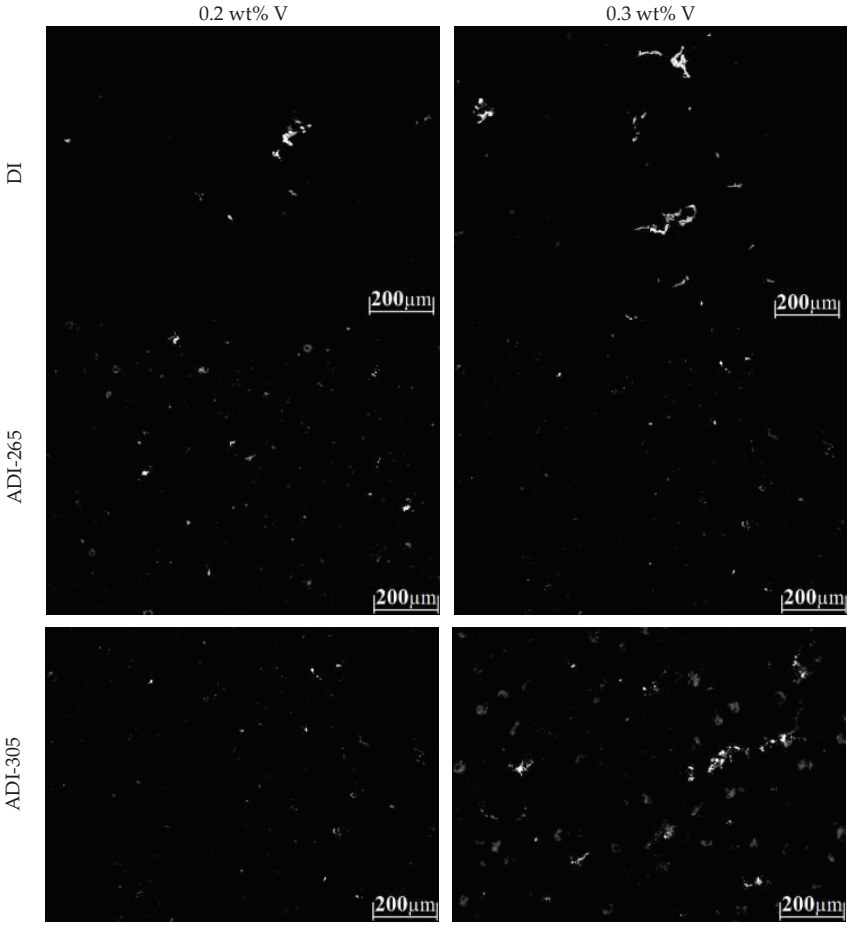

Figure 10. Etched microstructure with ammonium persulfate revealed the carbide phases (white regions) of the DIs and ADIs low alloyed with vanadium.

3.4. Bench Testing

The research and development department of Arbomex focuses on the development of new products, such as high-strength camshafts using a wide variety of testing methods during different stages of the product development process. Camshaft functionality testing, through the electric spin rig machine, was carried out for the camshaft ADI-0.2V-265. This sample was chosen, based on the results of Table 5 and Figure 9, because adequate hardness and wear resistance were obtained for the lowest vanadium content and austempering temperature. For the bench testing, a component-compatible test oil was used, and its properties simulated those of engine oil. The oil temperature was monitored for low and high conditions, according to the specifications reported in Table 1, and the results are shown in Figure 11.

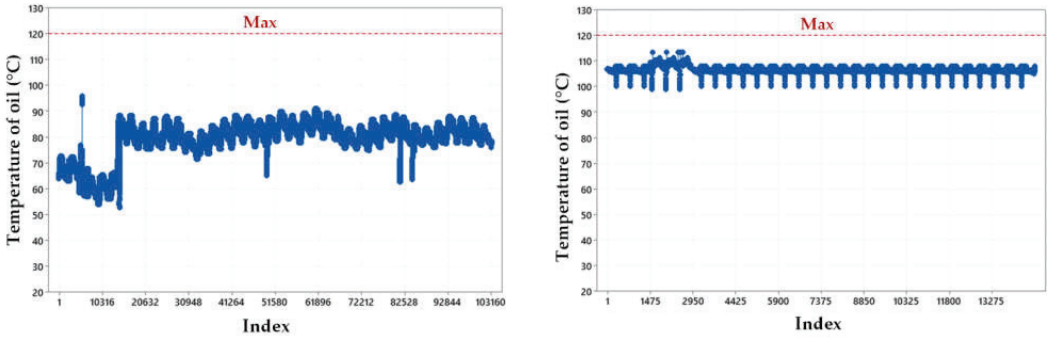

(**a**) (**b**)

Figure 11. Oil temperature monitoring for (**a**) low condition (500 rpm camshaft), and (**b**) high condition (2500 rpm camshaft).

The results of Figure 11 show that the oil temperature remained lower than the maximum temperature allowed for the test protocol for both conditions. The index represents the number of temperature inspections that were carried out during each condition of the tests through an automatic system that recorded the data in real time for a database. As can be seen, at the beginning of the test for the low condition, the oil temperature was close to 55–66 °C and, as the engine progressed through its work cycles, this temperature increased slightly and stabilized throughout the test. For the high condition, the oil temperature did not present any considerable variation for the whole test. It is essential to control the oil temperature, considering the environment in which the engine is exposed during functioning, because oil temperature is directly related to its fluidity. Prior to the spin rig test, the camshaft was dimensionally evaluated according to OEM test protocol. The camshaft machining line considers a dimensional inspection of profiles and roundness as one of the last manufacturing operations to assure the quality of the parts. The camshaft parameters inspected were angularity, camshaft lobe lift error, center deviation, chatter, concentricity, profiles, and runout. Figure 12 shows the camshaft extraction from the bench testing for visual and dimensional inspection of profiles and roundness to evaluate wear presence, damage or superficial defects originating from the test.

Figure 12. Removing the camshaft after complying with the test protocol.

Figure 13 shows the results of the radius base circle and the error angle of the sixteen lobes of the camshaft for the initial and final dimensions after the test. It can be observed in Figure 13a that, during the test, the surface lobes showed a micro-expansion regarding reference (zero). The increase in volume modified the lobes reference, as observed in the error angle measurement (Figure 13b) because the offset was even along the entire camshaft. This micro-expansion was considered insignificant and did not affect the camshaft performance in any way. Automotive engine camshafts need to be able to resist high rolling contact loads and the adhesive wear (pitting) conditions that result from the functioning of the camshaft. The austenite contained in the ausferrite is thermodynamically, but not mechanically, stable. When a high normal force is applied to an austempered component, a strain-induced transformation of austenite to martensite occurs. This results in the formation of a layer of hard, wear-resistant martensite that is backed by tough ausferrite. This ability to form martensite is the primary reason for the excellent wear properties of austempered ductile irons [38].

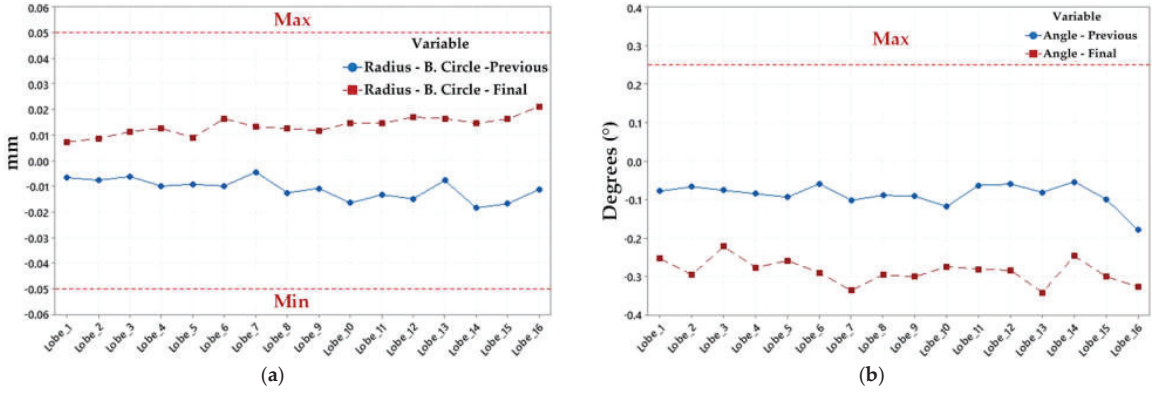

(**a**) (**b**)

Figure 13. Dimensional measurements of the camshaft lobes before and after the spin rig test for (**a**) radius base circle, and (**b**) error angle.

Despite the behavior shown in Figure 13, the chatter measurements on the flank closing, flank opening, and base circle kept the same tendency in closer values to the previous and final conditions in the surfaces for every lobe (Figure 14). Therefore, there was no sign of material loss, wear, or scuff marks on the lobe surface that was in contact with the steel roller during the entire spin rig test (Figure 15).

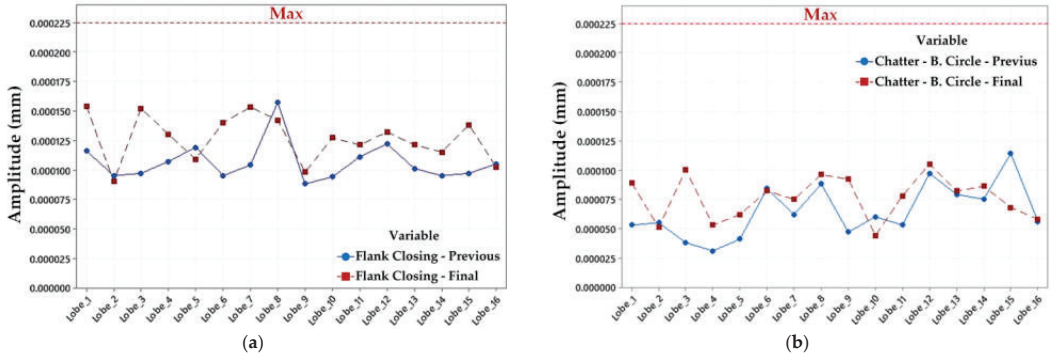

(**a**) (**b**)

Figure 14. *Cont.*

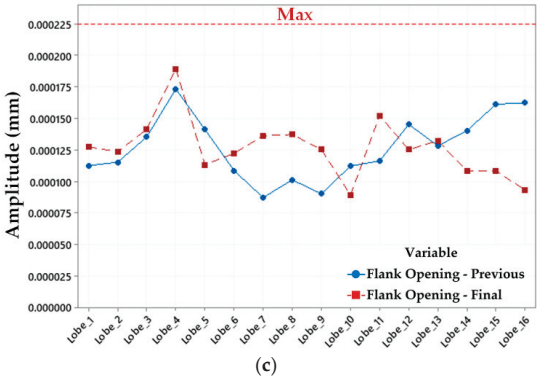

(**c**)

Figure 14. Dimensional measurements of the camshaft lobes before and after the spin rig test for (**a**) flank closing, (**b**) base circle, and (**c**) flank opening.

(**a**) (**b**)

Figure 15. Condition of parts after spin rig test (**a**) lobe surfaces and journals, and (**b**) roller surfaces.

It is possible to increase the hardness and wear resistance of the camshafts by increasing the amount of vanadium; however, the strong carbide-forming tendency of the vanadium could affect further mechanical operations in camshaft production. An adequate balance between hardness and wear resistance was obtained for the ADI-0.2V-265 sample, where there was no evidence of wear damage or any defect based on the geometrical measurements of the camshaft carried out in the spin rig electric testing machine.

The camshaft is subject to different mechanisms of degradation, such as multiaxial stresses, corrosion, abrasion, creep, and wear, as a result of contact stresses and temperature operations that can induce cracking or failure. Wear is developed at the top of the cams causing a change in the design contour. Based on the requirements of the component, the samples of ADIs heat treated to 265 °C showed the highest wear resistance, compared to the ADIs obtained at 305 °C (Figure 9). However, the sample ADI-0.3V-265 had the highest carbide amount (Table 4) and the lowest toughness (Table 5). The reduction in toughness and an increase in the volume fraction of carbides could affect the continuity of the matrix acting as crack initiation sites causing a possible fracture mechanism. For these reasons, the sample ADI-0.2V-265 was the best choice to ensure optimal performance of the component, as was proven by the spin rig electric test.

4. Conclusions

In this work, two austempered ductile irons were produced from ductile irons low alloyed with 0.2 and 0.3 wt.% V, which were heat-treated to 265 and 305 °C for camshaft

production. A sliding wear evaluation of the high-strength ADIs was carried out using a block-on-ring wear test and a spin rig electric machine, according to OEM protocol for the V8 engine, to evaluate the volume loss of material removed and the geometrical changes of the camshaft, respectively. The results obtained can be summarized as follows:

1. The vanadium addition to the DI allowed the obtaining of carbides that were partially dissolved by the applied austempering heat treatment to obtain a low volume fraction of fine carbides homogeneously distributed in the cams.
2. The high-volume fraction of acicular ferrite and the low high-carbon austenite microstructure, together with the fine carbide particles, increased the wear resistance in the ADIs heat treated to 265 °C, showing the lowest volume loss of material removed by the block-on-ring wear test.
3. After the OEM test protocol at low and high conditions (~60 million total cycles); no signs of wear or pitting were detected in any lobe along the camshaft; only "dark" mirror marks were observed on the lobe's surfaces because of the oil color, the same phenomenon was presented in the roller surfaces.
4. Lobe's surfaces presented a micro expansion according to the dimensional inspection of profiles and roundness carried out previous to, and after, the spin rig test. This behavior was potentially due to contact stresses between the lobe and roller surfaces. The high load produced a strain-induced transformation of austenite to martensite. This micro-expansion was considered insignificant according to the flank closing, base circle, and flank opening results after the test and did not affect the camshaft performance in any way.
5. The sample ADI-0.2V-265 fulfilled the mechanical requirements of hardness, wear resistance, and toughness in the camshaft to ensure optimal performance of the component, as was evidenced by the spin rig electric test.

Author Contributions: Data curation, A.C.R., E.C.G. and A.M.H.; Formal analysis, A.C.R. and E.C.G.; Investigation, E.C.G., A.C.R. and A.M.H.; Methodology, E.C.G., A.C.R., J.T.R. and A.M.H.; Project administration, J.T.R.; Supervision, J.T.R.; Validation, A.C.R. and J.T.R.; Visualization, A.C.R. and A.M.H.; Writing—original draft, A.C.R. and E.C.G.; Writing—review and editing, A.C.R. and E.C.G. All authors have read and agreed to the published version of the manuscript.

Funding: This research received no external funding.

Institutional Review Board Statement: Not applicable.

Informed Consent Statement: Not applicable.

Data Availability Statement: No additional data.

Acknowledgments: The authors wish to thank the enterprise Arbomex for the facilities given for the trial's development. A. Cruz and E. Colin wish to thank the Institutions CONACyT, SNI, COFAA, and SIP-Instituto Politécnico Nacional for their permanent assistance to the Process Metallurgy Group at ESIQIE-Metallurgy and Materials Department.

Conflicts of Interest: The authors declare no conflict of interest.

References

1. Foundry Products: Competitive Conditions in the U.S. Market. Available online: https://www.usitc.gov/publications/332/pub3771.pdf (accessed on 12 November 2020).
2. Stefanescu, D.M.; Ruxanda, R. Lightweight iron castings-can they replace aluminum castings. In Proceedings of the 65th World Foundry Congress, Gyeongju, Republic of Korea, 20–24 October 2002.
3. Samaddar, S.; Das, T.; Chowdhury, A.K.; Singh, M. Manufacturing of engineering components with austempered ductile iron—A review. *Mater. Today Proc.* **2018**, *5*, 25615–25624. [CrossRef]
4. Blackmore, P.A.; Harding, R.A. The effects of metallurgical process variables on the properties of austempered ductile irons. *J. Heat Treat.* **1984**, *3*, 310–325. [CrossRef]
5. Cekic, O.E.; Sidjanin, L.; Rajnovic, D.; Rajnovic, D.; Balos, S. Austempering kinetics of Cu-Ni alloyed austempered Ductile Iron. *Met. Mater. Int.* **2014**, *20*, 1131–1138. [CrossRef]

6. Erfanian-Naziftoosi, H.R.; Haghdadi, N.; Kiani-Rashid, A.R. The effect of isothermal heat treatment time on the microstructure and properties of 2.11% Al austempered ductile iron. *J. Mater. Eng. Perform.* **2012**, *21*, 1785–1792. [CrossRef]
7. Meena, A.; Mansori, M.E. Study of dry and minimum quantity lubrication drilling of novel austempered ductile iron (ADI) for automotive applications. *Wear* **2011**, *271*, 2412–2416. [CrossRef]
8. Cetin, B.; Meco, H.; Davut, K.; Arslan, E.; Can, M. Microstructural analysis of austempered ductile iron castings. *Hitt. J. Sci. Eng.* **2016**, *3*, 29–34. [CrossRef]
9. Pulkrabeth, W.W. Introduction Engine components. In *Engineering Fundamentals of the Internal Combustion Engine*; Prentice-Hall: Upper Saddle River, NJ, USA, 2004; pp. 18–19.
10. Bereteu, L.; Crâştiu, I.; Nyaguly, E.; Simoiu, D. Investigation of a camshaft repaired by welding using the vibration signal analysis. *Adv. Mat. Res.* **2015**, *1111*, 199–204. [CrossRef]
11. INA-Schaeffer KG, Testing Cam Phaser Systems; Herzogenaurach, Germany. Communication, 2004.
12. Hatwalane, S.; Kothavale, B. Camshaft torque analysis of diesel engine. *Int. J. Curr. Eng. Tech.* **2017**, *7*, 1–5.
13. Padan, D.S. Microalloying in austempered ductile iron (ADI). *AFS Proc.* **2012**, *12–19*, 1–12.
14. Sadighzadeh, B.A. Effect of alloying elements on austempered ductile iron (ADI) properties and its process: Review. *China Foundry* **2015**, *12*, 54–70.
15. Arbomex Web Page. Available online: https://www.arbomex.com (accessed on 28 November 2022).
16. Colin, G.E.; Cruz, R.A.; Reyes, C.G.; Téllez, R.J.; Magaña, H.A. Microstructural and mechanical assessment of camshafts produced by ductile cast iron low alloyed with vanadium. *Metals* **2021**, *11*, 146. [CrossRef]
17. Colin, G.E.; Cruz, R.A.; Reyes, C.G.; Chávez, A.J.F.; Téllez, R.J.; Magaña, H.A. Heat treatment evaluation for the camshafts production of ADI low alloyed with vanadium. *Metals* **2021**, *11*, 1036. [CrossRef]
18. Patel, G.; Minstry, K.; Patel, M. Experimental analysis of cam and follower of valve train system for prediction of wear rate. *IJARIIE* **2017**, *3*, 1–11.
19. Pedro, D.I.; Dommarco, R.C. Rolling contact fatigue resistance of Carbidic Austempered Ductile Iron (CADI). *Wear* **2019**, *418–419*, 94–101. [CrossRef]
20. Aranzabal, J.; Gutierrez, I.; Rodriguez-Ibabe, J.M.; Urcola, J.J. Influence of Heat treatments on microstructure and toughness of austempered ductile iron. *Mater. Sci. Technol.* **1992**, *8*, 263–273. [CrossRef]
21. Cueva, G.; Sinatora, A.; Guesser, W.L.; Tschiptschin, A.P. Wear resistance of cast irons used in brake disc rotors. *Wear* **2003**, *255*, 1256–1260. [CrossRef]
22. Hamid, A.A.S.; Elliot, R. Influence of austenitising temperature on austempering of an Mn-Mo-Cu alloyed ductile iron Part 1 Austempering kinetics and the processing window. *Mater. Sci. Tech.* **1996**, *12*, 1021–1031. [CrossRef]
23. Rezvani, M.; Harding, R.A.; Campbell, J. The effect of vanadium in as-cast ductile iron. *Int. J. Cast Metal Res.* **1997**, *10*, 1–15. [CrossRef]
24. Han, J.M.; Zou, Q.; Barber, G.C.; Nasir, T.; Northwood, D.O.; Sun, X.C.; Seaton, P. Study of the effects of austempering temperature and time on scuffing behavior of austempered Ni-Mo-Cu ductile iron. *Wear* **2012**, *290–291*, 99–105. [CrossRef]
25. Putatunda, S.K.; Gadicherla, P.K. Effect of austempering time on mechanical properties of a low manganese austempered ductile iron. *J. Mater. Eng. Perform.* **2000**, *9*, 193–203. [CrossRef]
26. Parhad, P.; Umale, S.; Likhite, A.; Bhatt, J. Characterization of inoculated low carbon equivalent iron at lower austempering temperature. *Trans. Indian Inst. Met.* **2012**, *65*, 449–458. [CrossRef]
27. Wang, B.; Barber, G.C.; Qiu, F.; Zou, Q.; Yang, H. A review: Phase transformation and wear mechanisms of single-step and dual-step austempered ductile irons. *J. Mater. Res. Technol.* **2019**, *9*, 1054–1069. [CrossRef]
28. Bendikiene, R.; Ciuplys, A.; Cesnavicius, R.; Jutas, A.; Bahdanovich, A.; Marmysh, D.; Nasan, A.; Shemet, L.; Sherbakov, S. Influence of austempering temperatures of the microstructure and mechanical properties of austempered ductile cast iron. *Metals* **2021**, *11*, 967. [CrossRef]
29. Hegde, A.; B M, G.; Hindi, J.; Sharma, S.; M C, G. Effect of austempering temperature and manganese content on the impact energy of austempered ductile iron. *Cogent Eng.* **2021**, *8*, 1939928. [CrossRef]
30. Minkoff, I. *The Physical Metallurgy of Cast Iron*; John Wiley and Sons: Salisbury, UK, 1983; p. 183.
31. Zhou, W.S.; Zhou, Q.D. Lubricated sliding and rolling wear of austempered ductile iron. *Wear* **1993**, *162–164*, 696–702. [CrossRef]
32. Sellamuthu, P.; Harris Samuel, D.G.; Dinakaran, D.; Premkumar, V.P.; Li, Z.; Seetharaman, S. Austempered ductile iron (ADI): Influence of austempering temperature on microstructure, mechanical and wear properties and energy consumption. *Metals* **2018**, *8*, 53. [CrossRef]
33. Laino, S.; Sikora, J.A.; Dommarco, R.C. Development of wear resistant carbidic austempered ductile iron. *Wear* **2008**, *265*, 1–7. [CrossRef]
34. Caldera, M.; Rivera, G.; Boeri, R.; Sikora, J. Precipitation and dissolution of carbides in low alloy ductile iron plates of varied thickness. *Mater Sci. Technol.* **2005**, *21*, 1187–1191. [CrossRef]
35. BabaZadeh, M.; PourAsiabi, H.; PourAsiabi, H. Wear Characteristics of ADIs; a compressive review on mechanisms and effective parameters. *J. Basic Appl. Sci. Res.* **2013**, *3*, 646–656.
36. Pérez, M.J.; Cisneros, M.M.; López, H.F. Wear resistance of Cu-Ni-Mo austempered ductile iron. *Wear* **2006**, *260*, 879–885. [CrossRef]

37. Balos, S.; Rajnovic, D.; Dramicanin, M.; Labus, D.; Eric-Cekic, O.; Grbovicn-Novakovic, J.; Sidjanin, L. Abrasive wear behavior of ADI material with various retained austenite content. *Int. J. Cast Met. Res.* **2016**, *29*, 187–193. [CrossRef]
38. Keough, J.R.; Hayrynen, K.L. Wear properties of Austempered Ductile Irons. *Appl. Process Inc. Technol. Div. USA SAE Int.* **2005**, *1690*, 1–9.

metals

MDPI

Article

Wear Behavior of Nb Alloyed Gray Cast Iron for Automotive Brake Disc Application

Pietro Tonolini [1,*], Lorenzo Montesano [1], Annalisa Pola [1], Gianpietro Bontempi [2] and Marcello Gelfi [1]

[1] Department of Mechanical and Industrial Engineering, University of Brescia, Via Branze 38, 25123 Brescia, BS, Italy
[2] Fonderia di Torbole S.r.l., Via Travagliato, 18, 25030 Torbole Casaglia, BS, Italy
* Correspondence: p.tonolini002@unibs.it

Abstract: Gray cast iron (GCI) with a pearlitic matrix and type-A graphite remains the most widely used material in the manufacturing of brake discs. To reduce the environmental impact of disc wear during braking, alternative materials and/or compositions to the standard ones are being studied. In this study, the effect of variation in niobium content (0–0.7 wt%) on microstructure and wear behavior of samples machined from brake discs made of hypoeutectic gray cast iron was investigated. The wear behavior of GCI was examined through pin-on-disc (PoD) wear tests using low-metallic-friction material discs as the counterparts. Microstructural analyses and hardness measurements were also conducted to evaluate the effect of Nb addition on the morphology of graphite, eutectic cells, and distribution of carbides. In addition, the wear mechanisms of different samples were evaluated using scanning electron microscope analysis. The results revealed that adding 0.3% of Nb promotes the highest wear resistance of the alloys.

Keywords: brake discs; cast iron; niobium; wear

Citation: Tonolini, P.; Montesano, L.; Pola, A.; Bontempi, G.; Gelfi, M. Wear Behavior of Nb Alloyed Gray Cast Iron for Automotive Brake Disc Application. *Metals* **2023**, *13*, 365. https://doi.org/10.3390/met13020365

Academic Editor: Amilcar Ramalho

Received: 20 January 2023
Revised: 7 February 2023
Accepted: 9 February 2023
Published: 11 February 2023

1. Introduction

In a braking event, the pistons inside the caliper squeeze two pads against the side of the disc rim or braking band, converting the kinetic energy of a moving vehicle into thermal energy generated by friction between the mating surfaces [1]. Therefore, similar to any tribosystem, the tribological behavior of the braking system depends on the properties of both the disc and pad materials used, and is influenced by speed, braking pressure, temperature, and humidity [2].

Gray cast iron (GCI) with a pearlitic matrix and type-A graphite remains the most widely used alloy in the production of brake discs for passenger vehicles. The presence of type-A graphite flakes promotes high thermal conductivity and diffusivity of the alloy, whereas the pearlite matrix guarantees appropriate mechanical properties [3,4]. Furthermore, the excellent vibration damping, together with good castability, workability, and low cost [5,6], make GCI alloys difficult to replace for disc brake applications, especially for entry-level cars, despite their high density and low corrosion resistance [7].

However, it has been proven for years that the sliding wear process of a braking system contributes to the emission of non-exhaust traffic-related PM10 (particles with an average aerodynamic diameter D: 2.5 μm < D < 10 μm) and PM2.5 (particles with D: 0.1 μm < D < 2.5 μm) derived from the wear of both discs and pads [8], affecting human health, especially in urban areas [9]. Therefore, it is necessary to limit the pollution of the braking systems. To promote this, the proposal of the new Euro 7 regulation 2022/0365(COD) [10] sets for the first time a limit on the brake particle emissions of 7 mg/km of PM10 for vehicles until 2034, which will thereafter become stricter. The fact that the limit has been imposed only on PM10 emissions could be counterproductive, as it could lead to an increase in the emission of even finer particles, and therefore result in greater harm to human health [11]; however, this is beyond the scope of this work.

Despite this, recent studies have already demonstrated a reduction of 50% in brake system emissions by improving the wear resistance of the disc by employing heat treatment [12] or by the application of wear-resistant coatings [13–17], thus contributing to both reducing pollution and increasing the life of brake discs. In fact, for this purpose, it is nowadays possible to find commercial solutions for premium cars that involve the use of wear-resistant coatings [18,19]. Unfortunately, these solutions are too expensive for lower car segments. Therefore, it is necessary to develop cheaper alternative solutions. Among others, one almost inexpensive method to control the properties of gray cast iron consists of tailoring the microstructure through the addition of alloying elements.

Niobium is a refractory metal (Tm = 2468 ± 10 °C) that has been widely used for decades as a micro-alloyed element (<0.1%) in steels owing to the refined grain size effect during thermomechanical processing by the strain-induced precipitation of nanosized NbC or NbCN [20,21], resulting in an increase in strength [22].

However, unlike steel, cast iron does not employ Nb as frequently, and the majority of research on the addition of this element to cast iron focuses on white cast iron for applications requiring wear resistance [23–25].

Regarding gray cast iron alloys, as demonstrated in previous studies, the addition of Nb promotes the refinement of the eutectic cells (ECs) and graphite structure, as well as a reduction in the interlamellar pearlite spacing, favoring an increase in hardness and tensile strength [23,26–30]. Furthermore, the addition of Nb up to 0.2% in cast iron used for cylinder heads also improves the fatigue and thermal fatigue properties of the alloy [30–32]. However, the proposed refining mechanism, level of refinement, and corresponding increase in mechanical properties are not always comparable among different studies. Nb also affects the wear behavior of gray cast iron via the precipitation of Nb carbide into the matrix. In this regard, the use of Nb in brake discs is not new [33], even though it seems to have found renewed interest [34–36]. However, the data obtained from the literature reveal a significant scatter in the wear rate trend as a function of the Nb concentration in the alloy, and a detailed study on the involvement of NbC precipitates in the wear mechanism has never been conducted.

In this study, the wear resistance of gray cast iron samples, taken from brake discs industrially produced with different percentages of Nb, was evaluated. The tribological behavior was investigated through pin-on-disc-type laboratory tests using pad material discs as the counterparts. The wear behavior was then correlated with the microstructural features of the alloys under examination. The results of this work will be used to identify a more wear-resistant Nb composition that will then be tested on a brake inertia dynamometer equipped with a particle emission collector to evaluate PM10 emissions from a complete brake system.

2. Materials and Methods

Four brake disc batches with a fixed bell were industrially produced, as the simplest geometry achievable, following the standard foundry procedures: cupola-furnace melting, stream inoculation with ferrosilicon 75, and casting into sand molds using an in-line plant. Each batch presented different niobium contents (0%, 0.3%, 0.51%, and 0.72%), as shown in Table 1, where the mean chemical composition of the discs is shown.

Table 1. Mean chemical composition of the investigated discs (wt%).

Samples	C	Si	Mn	P	S	Cr	Mo	Sn	Ti	Nb	CE *
D-0	3.20	1.91	0.63	0.04	0.14	0.1	0.01	0.08	0.02	0.00	3.8
D-0.3	3.38	1.58	0.63	0.04	0.13	0.1	0.01	0.07	0.01	0.30	3.9
D-0.5	3.26	1.62	0.55	0.04	0.10	0.2	0.01	0.05	0.01	0.51	3.8
D-0.7	3.24	1.59	0.52	0.04	0.09	0.2	0.01	0.05	0.01	0.72	3.8

* CE (carbon equivalent) = %C + (%Si + %P)/3.

To investigate the homogeneity of the distribution of the precipitated carbides inside the braking band of discs D-0.3, D-0.5, and D-0.7, metallographic characterization was performed on two cross sections, prepared following the standard metallographic procedures. In detail, the samples were taken from each disc in two positions of the rim, that is, a position close to the gate and a position named opposite to the gate (90° to the gates) (Figure 1a). Nb carbide analysis was carried out using an optical microscope Leica DMI 5000M (Leica Microsystem, Wetzlar, Germany) equipped with image analyzer LAS 4.12 software (4.12, Leica Microsystem, Wetzlar, Germany) on 10 micrographs collected at a magnification of 500× from each position in the cross-section, that is, bottom, mold parting line, and upper position (Figure 1b), for a total of 60 micrographs for each disc. The output of the image software analysis was the average total area of the carbides (μm^2) and the area of the largest carbide (μm^2) detected in each position (Figure 1b) for each cross-section. The maximum area of carbide for each disc was then calculated as the average of the three largest carbides detected in each position.

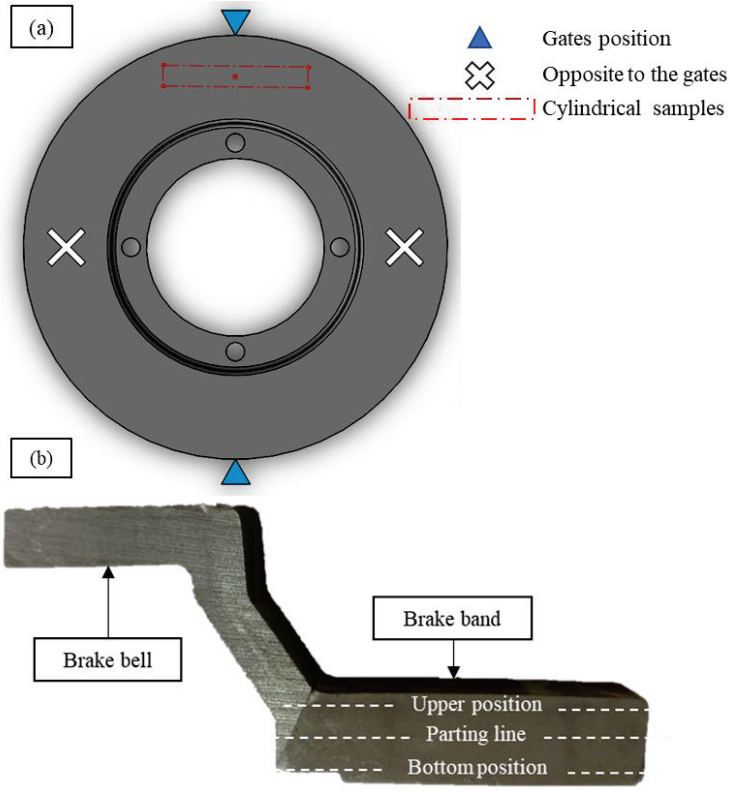

Figure 1. (**a**) Schematic drawing of the top view of a brake disc indicating the gates and the position named opposite to the gates and (**b**) Cross-section view of the considered brake discs.

Subsequently, samples for microstructural characterization were machined from the centerline of each braking band of the four brake discs and shaped into cylinders with a diameter of 10 mm and a length of 100 mm (dashed rectangle of Figure 1a). The cross-sections of the cylinders were polished to a 1 µm finishing and then analyzed.

Ten images with a magnification of 100× were collected from each sample to classify the graphite morphology according to UNI EN ISO 945-1 by using an optical microscope (Leica DMI 5000M, Leica Microsystem, Wetzlar, Germany).

The effect of Nb addition on the microstructure of the samples was investigated, after chemical etching with 2% Nital, through the same optical microscope and a scanning electron microscope (LEO EVO 40, Carl Zeiss AG, Milan, Italy) integrated with an energy-dispersive spectroscopy microprobe (EDS, Oxford Instruments, Wiesbaden, Germany). The eutectic cell densities of the different samples were evaluated using a digital microscope (Leica DMS300, Leica Microsystem, Wetzlar, Germany) after chemical etching with the Stead reagent.

The effect of Nb addition on the hardness of GCI samples was investigated through the average of five Brinell measurements (187.5 Kg and 2.5 mm carbide ball). HB 10/3000 measurements were also performed at the foundry's laboratory on the surfaces of the braking band, confirming the trend found on the machined samples' increasing Nb content. Furthermore, the possible influence of Nb addition on the mechanical properties of the pearlitic matrix was evaluated by the average value of 10 micro-Vickers indentations (300 g, Mitutoyo Hm200, Mitutoyo Italiana srl, Lainate, Italy).

To simulate the tribological behavior of brake discs [37], pin-on-disk (PoD) dry wear tests were performed at room temperature using a THT tribometer (CSM Instruments, Peseux, Switzerland). For this purpose, cylindrical pins were machined from the cylindrical samples taken from the discs, as mentioned above, with a size of Ø 4 mm × 10 mm, and then finished to obtain the roughness (Ra) of the two parallel circular surfaces of approximately 0.4 µm. The counterparts for the wear test were manufactured starting from standard commercial low-metallic copper-free [38] brake pad friction material in the form of a hot-pressed disc with a diameter of 50 mm. The average composition of the friction material is listed in Table 2.

Table 2. EDS qualitative chemical composition of the friction material, acquired on an area of about 20 mm^2.

Elements	C	O	Mg	Al	Si	S	Ca	Ti	Cr	Fe	Zn	Sn
Contents (wt%)	51.12	28.16	5.22	2.06	1.17	0.93	0.64	1.38	0.59	6.54	0.54	1.65

The test parameters were chosen to identify possible differences between the wear resistances of the samples under investigation within a reasonably limited time. In particular, a sliding speed of 1 m/s and a load of 9 N (0.71 MPa, approximately the mean nominal pressure of city traffic [16]) were applied for a total sliding distance of 15 km, with a wear track radius of 16 mm. During the tests, the friction force was monitored and the coefficient of friction (CoF) was obtained as the ratio between the friction force and the applied load, then plotted as a function of the sliding distance.

Preliminary wear tests conducted on the same pins highlighted the great variability both in the wear rates and friction coefficients as a function of the friction material disc used, underlining the strong non-homogeneity of the pad material and therefore its importance in the tribological system. For this reason, after a test evaluated as a run-in step for the friction material, the pins were tested using the same friction disc. The results presented are the average of three test repetitions for each pin. The pins were therefore tested in a random sequence, again to avoid a possible influence of the heterogeneity of the friction material also along the thickness of the disc on the results (i.e., wear rate and coefficient of friction).

The mass of the pins was measured before and after each test using an analytical balance with a precision of 10^{-4} g to estimate the mass loss during the test (Δm). The specific wear rate, K_a, was calculated for each pin as: $K_a = \frac{\Delta m}{\rho d F}$ (m^2/N), where ρ is the density of the pins (7.2 g/cm^3), d is the sliding distance, and F is the applied load.

To investigate the wear mechanisms and possible differences related to the different amounts of alloyed Nb, the surfaces of the worn pins were observed at the end of the test using a scanning electron microscope and an energy-dispersive spectroscopy micro-

probe. Finally, the pin cross-sections were analyzed by SEM to further investigate the wear mechanism.

3. Results and Discussion

3.1. Microstructure

As expected, the microstructural analysis showed the presence of Nb-rich particles in all samples alloyed with the relevant amounts of Nb. As an example, Figure 2 displays the SEM backscattered images of sample D-0.3. In Figure 2a, several white particles are detectable with different shapes: elongated, rod-shaped, Y- and V-shaped, or cuboid and triangular. EDS analysis revealed that these phases were effectively niobium carbide particles (Figure 2b and Table 3), and the shape of these particles was common for all the Nb-alloyed samples. Considering the simulation calculation of NbC precipitation and the microstructural observation conducted by Zhou et al. [39], the elongated NbC particles precipitated during the solidification process, while the cuboid particles precipitated in the liquid phase as primary carbides.

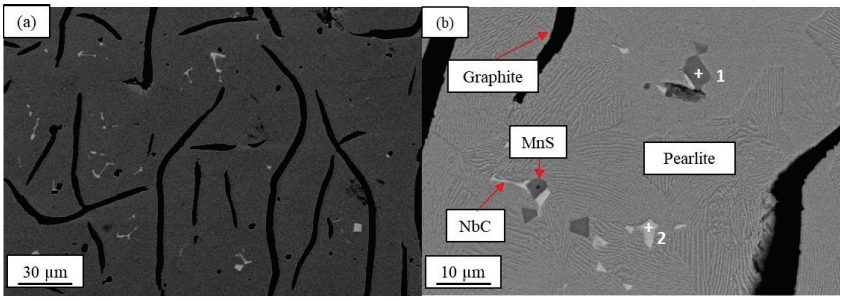

Figure 2. SEM images of D-0.3 sample. (**a**) low magnification, (**b**) high magnification, where +1 and +2 identify the location of the EDS analyses reported in Table 3.

Table 3. EDS analysis (wt%) of Figure 2b.

Spectrum	C	S	Mn	Ti	Fe	Nb
1	-	37.93	54.59	-	7.48	-
2	26.15	-	-	1.72	2.29	69.85

The EDS analysis shown in Table 3 reveals the presence of Ti within the Nb-rich particles. As reported in Table 1, all the investigated cast irons contained at least 0.01% Ti. The presence of Ti inside the Nb-rich particles was also found in other gray cast irons with different Nb levels [32,36,39–41]. By analogy with ductile cast irons, Ti could remain as an accompanying element in NbC [42] or could be related to the fact that oxide precursors (Ti-, Si-, Mg- oxides) present in the liquid phase can act as inoculants for NbC precipitates [43].

Furthermore, it is interesting to note the presence of MnS particles (Figure 2b) in proximity to or on top of NbC particles. It is likely that these particles can act as heterogeneous nuclei for some primary MnS particles.

The homogeneous distribution of these carbides within the braking band of the brake discs was confirmed. In fact, from the histogram in Figure 3, it can be observed that both the total area of carbides and the maximum area of the largest carbides are comparable in the two investigated positions (i.e., at the gate and opposite to the gate) for each disc. Hence, the samples machined from the center of the braking band can be considered representative of the entire brake disc. Furthermore, it is evident from Figure 3 that by increasing the Nb content, the total area of the carbides as well as the area of the largest carbides increases, as also reported by other authors [26,30,39].

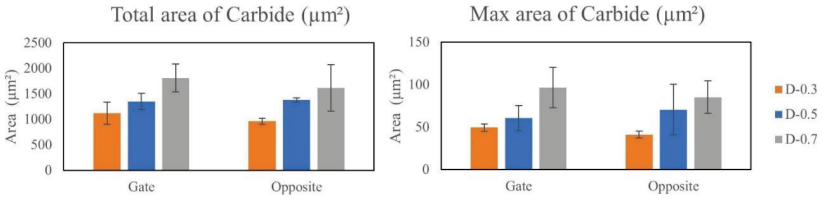

Figure 3. Carbide distribution by image analysis.

The morphology of graphite is shown in Figure 4. All samples were characterized by graphite flakes of form I, type-A, and size 4, according to the ISO945-1 standard, indicating that Nb addition does not affect the graphite morphology. Furthermore, the area fraction of graphite (%) measured in the samples accounted for 13.3%, 14.5%, 12.3%, and 10.7% for samples D-0, D-0.3, D-0.5, and D-0.7, respectively. The graphite content was related to the CE of the alloy. As can be noted from Table 1, the CE of the considered alloy slightly differs from one sample to the other because of the difficulty in obtaining a fixed chemical composition in an industrial process. Moreover, under the hypothesis that all Nb binds with C to form NbC, the resulting CE would be 3.85%, 3.88%, 3.75%, and 3.69% for samples D-0, D-0.3, D-0.5, and D-0.7, respectively. This new trend explains the trend in the graphite content.

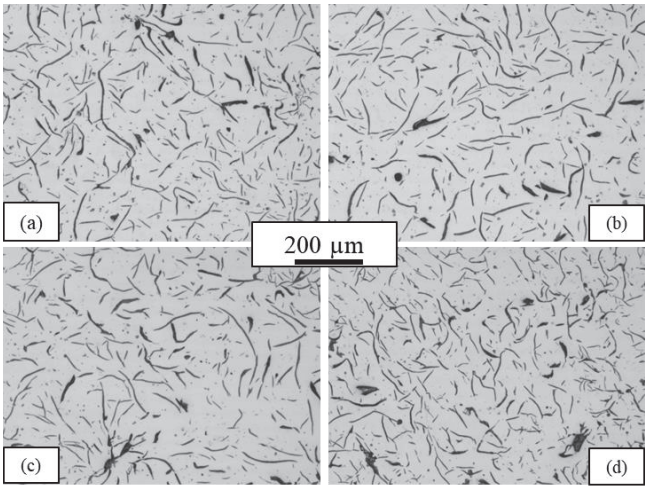

Figure 4. Graphite morphologies of the samples (**a**) D-0; (**b**) D-0.3; (**c**) D-0.5 and (**d**) D-0.7.

In Figure 5, the results of the graphite quantification by image analysis of 10 micrographs are presented. Figure 5a shows the average length of the 10 longest graphite flakes of type-A. The addition of Nb seems to promote refinement of the graphite, whose average length is shorter than that of the D-0 sample by 11%, 12%, and 18% for samples D-0.3, D-0.5, and D-0.7, respectively. Therefore, refinement appeared to be effective for the lowest concentrations of Nb. Similar results were also found in other studies [32,44], with a reduction in the graphite length of 11% for the addition of Nb up to 0.2 (wt%), while other authors reported a graphite length reduction of 56% for 0.27% Nb [39]. Furthermore, considering the graph in Figure 5b, the number of graphite flakes that account for size classes 3 and 4 according to ISO945-1 appears to decrease as the Nb content increases.

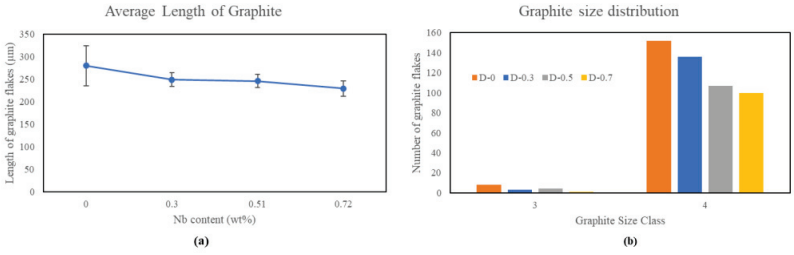

Figure 5. (**a**) Average length of graphite and (**b**) graphite size distribution.

As shown in Figure 6 and Table 4, small MnS and NbC particles are detected within the graphite flakes. It is well accepted that complex (Mn, X)S particles (usually <5 µm) act as heterogeneous nucleation sites for graphite during eutectic reaction [45]. Similarly, graphite refinement encountered for samples D-0.3, D-0.5, and D-0.7 could be caused by the graphite nucleating effect of small primary NbC particles precipitated before the eutectic temperature [32,36]. The higher the number of nucleation sites, the higher the nucleation rate; thus, the refinement of the graphite flakes is promoted. Furthermore, Nb prevents carbon from moving during solidification, which limits its ability to grow and causes it to become thin and short [26,28].

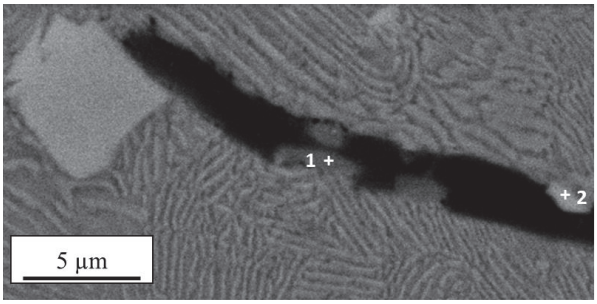

Figure 6. BS SEM image of the sample D-0.3 where +1 and +2 identify the location of the EDS analyses reported in Table 4.

Table 4. EDS analyses (wt%) of Figure 6.

Spectrum	C	O	Mg	Si	S	Ti	V	Mn	Fe	Nb
1	N/A	-	-	-	30.99	-	-	45.23	23.78	-
2	N/A	12.46	1.04	1.08	-	1.02	1.09	-	14.47	68.83

According to the optical microscope images in Figure 7, the microstructure of each sample after Nital 2% etching is characterized by a fully pearlitic matrix. Some NbC particles with different shapes and sizes were also visible within the microstructure of the Nb alloyed samples (Figure 7b–d).

Although the pearlite lamellar spacing and pearlite grain size were not statistically evaluated in this work, according to the literature, the addition of Nb up to 0.8% promotes pearlite refinement. In fact, according to some authors [28,39,41], Nb in solid solution in austenite decreases the eutectoid temperature and increases the nucleation rate and, on the other hand, Nb precipitates prevent carbon migration favoring a further pearlite refinement. A reduction in the pearlite interlamellar spacing should promote an increase in pearlite strength, which corresponds to an increase in hardness [46]. However, only a few authors [30,41,44] have conducted micro-HV measurements on pearlite colonies, and they concluded that Nb addition to GCI does not affect the pearlite hardness values. Similar

results were also presented in this study. This means that Nb is not a strong perlitizer element, especially if other strong perlitizers such as Sn are present in the alloy.

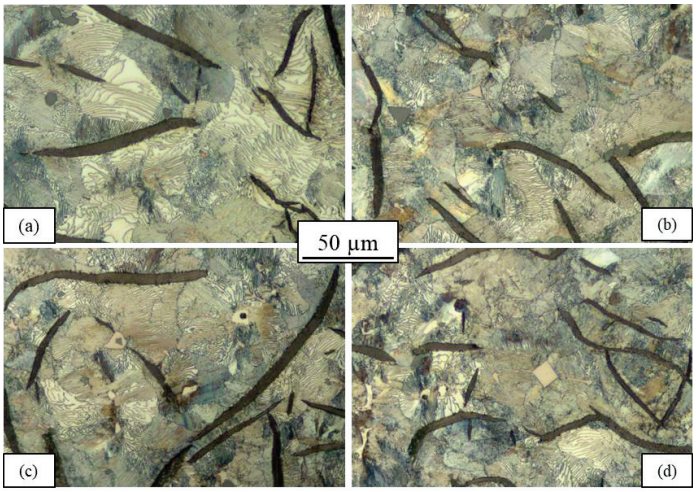

Figure 7. Microstructure of samples (**a**) D-0; (**b**) D-0.3; (**c**) D-0.5, and (**d**) D-0.7.

The microstructure presented in Figure 8 highlights the contours of the eutectic cells for different samples etched using Stead's reagent. It should be noted that the addition of Nb promotes refinement of the ECs; even if the addition is higher than 0.3%, the effect is attenuated. In fact, the measured EC densities were 26%, 22%, and 28% higher for samples D-0.3, D-0.5, and D-0.7 compared with D-0.

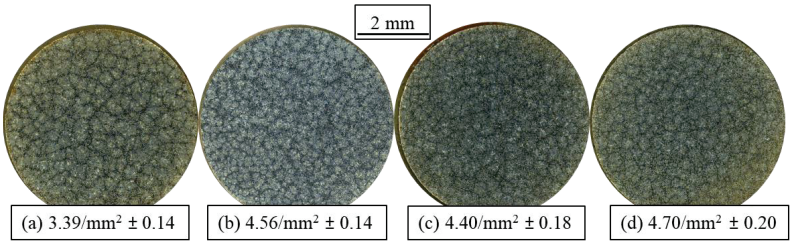

Figure 8. Eutectic cell density of samples (**a**) D-0; (**b**) D-0.3; (**c**) D-0.5, and (**d**) D-0.7.

In the hypoeutectic GCI and Nb quantities considered in this work, NbC particles are already available in the liquid when primary austenite begins to form [36,39]. According to the literature works [45–47], particles of Nb(C, N) observed inside austenite dendrites would promote the nucleation of these, refining them, and therefore indirectly would also increase the number of eutectic cells. However, owing to the quasi-eutectic composition of the alloy under investigation, only a few austenite dendrites formed at the eutectic temperature. ECs represent eutectic solidification units that are formed as a result of the cooperative growth of graphite and austenite during the eutectic reaction. Graphite is the leading phase during the eutectic reaction; thus, some graphite nuclei will form inside the eutectic liquid, and their growth will produce as many eutectic cells as the graphite nuclei [47]. In this scenario, the refinement of the eutectic cell size seems to be a direct consequence of the increased graphite nucleation rate following the addition of Nb, which results in a higher number of graphite cores that are shorter and thinner, from which a higher number of eutectic cells are generated, as also supported by other authors [27,28,33].

Furthermore, as for the refinement of graphite length, also the increased ECs density is related to an enhancement in the mechanical properties of the alloy [48,49].

3.2. Hardness Measurements

As shown in Figure 9a, the average Brinell hardness values increased slightly with increasing Nb content. This increase is probably due to the refinement of ECs together with the homogeneous dispersion of hard NbC primary precipitates, with a fraction area that increases with Nb content, as shown in Figure 3. Similar results were also found in other studies [28,34], where the hardness increment was related to perlite refinement, together with the presence of NbC particles. However, in the present case, the micro-Vickers hardness measurements performed on the pearlitic matrix of the samples, as shown in Figure 9b, do not suggest a clear pearlite refinement effect following the addition of Nb. This is probably due to the presence of strong perlitizer elements (i.e., Sn) already in the base alloy.

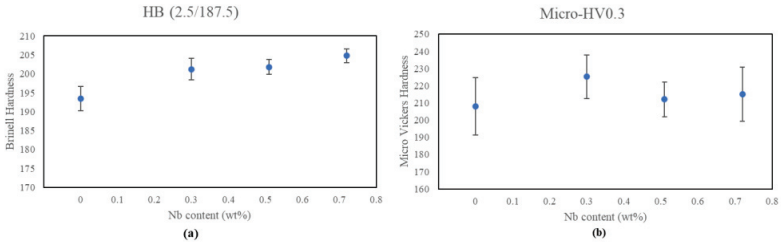

Figure 9. Effect of Nb addition on the hardness (**a**) Brinell and (**b**) micro-Vickers.

3.3. Tribological Behavior

Figure 10a shows a representative trend of the coefficient of friction (CoF) for each sample with the sliding distance recorded during the PoD test. In all the cases, the CoF reached a steady-state condition after approximately 1500 m of sliding. The steady-state CoF differs slightly between the samples, as shown in Figure 10b. However, it must be noted that the measured CoF values are in the range of typical values reported in the literature for the combination of cast iron discs and low-metallic Cu-free pads [50].

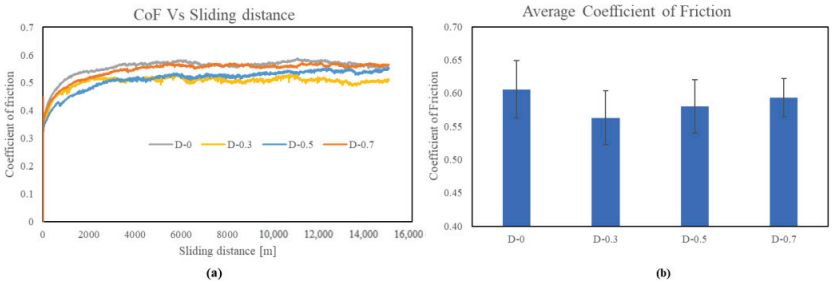

Figure 10. Coefficient of friction: (**a**) representative trend Vs sliding distance; (**b**) samples average values.

Regarding the specific wear rate, Figure 11 shows that the most wear-resistant composition is the one with the lowest Nb alloying content among those tested (i.e., D-0.3), whose wear rate is 27.8% lower than that registered for the D-0 sample. With a further increase in the Nb content, the wear resistance of the alloys decreased slightly, as the wear rates of the D-0.5 and D-0.7 samples were 23.1% and 21.7% lower than that of the D-0 sample, respectively.

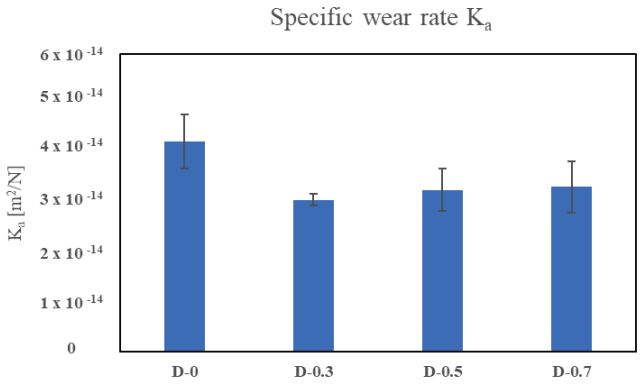

Figure 11. Specific wear rate Ka.

In general, the wear resistance enhancement of samples D-0.3, D-0.5, and D-0.7 concerning sample D-0 could be ascribed to the increase in hardness following alloying with Nb (Figure 9a). It is well known that the increase in hardness is related to an increase in the plastic deformation resistance, promoting a higher wear resistance of the alloy [2]. However, in this case, the slight increase in the wear rate with increasing Nb addition was neither reflected in the hardness measurements shown in Figure 8a, nor in the micro-HV trend of Figure 8b. Furthermore, the hard NbC particles can act as initial friction surfaces, thus behaving as load-bearing phases [28], and promoting a general wear resistance enhancement of alloys D-0.3, D-0.5, and D-0.7 compared with D-0.

To further analyze the tribological behavior, the morphologies of the worn surfaces of all tested pins are presented in the SEM images in Figure 12, whereas the cross-sections of the worn pins are shown in Figure 13. The abrasive wear mechanism seems to be predominant under all investigated conditions, as indicated by the presence of abrasive grooves (Figure 12). These plow grooves can be generated by the sliding of the hard particles embedded in the friction material disc (two-body abrasive wear), as well as by the presence of oxidized debris between the mating surfaces (three-body abrasive wear). In fact, the presence of friction material debris on the surfaces of the pins is demonstrated, as highlighted by the white arrows in Figures 12 and 13, and by the EDS analyses of Table 5, where Mg and Sn elements from the pad were detected, suggesting that adhesive wear also occurs to some extent. However, some of these wear fragments seemed to be placed inside the craters on the surfaces of the pins, probably because some coarse graphite flakes peeled off during sliding [34].

Furthermore, some NbC particles were identified on the worn surfaces, as can be observed from the backscatter images in Figure 12b,c. The magnification of the detail presented in Figure 12b suggests that some NbC particles are effective in stopping some groove advancement, whereas other particles can be passed by the scratches without severe deformation, as shown in Figure 12c.

However, the coarser particles of NbC, especially if oriented unfavorably in the sliding direction, that is, with the edges protruding from the surface, as shown in Figure 13d, can experience brittle fracture owing to their poor toughness, generating hard debris that can promote an increase in three-body abrasive wear [23]. Considering that the size of these particles increased as the Nb content increased, this phenomenon could contribute to the slight increase in the wear rate of samples D-0.5 and D-0.7 with respect to sample D-0.3, notwithstanding the increase in the overall hardness of the samples.

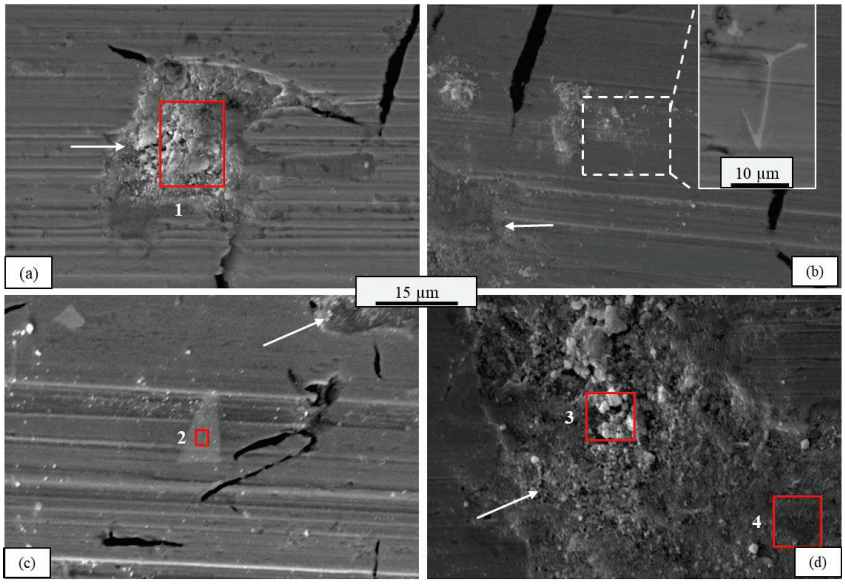

Figure 12. Worn surfaces of the pins (**a**) D-0; (**b**) D-0.3; (**c**) D-0.5; and (**d**) D-0.7. White arrows highlight pad material debris. The red rectangles (1, 2, 3 and 4) identify the location of the EDS analyses reported in Table 5. The white dashed square in Figure 12b identify the area where it was detected the NbC particle shown at higher magnification in the white rectangle.

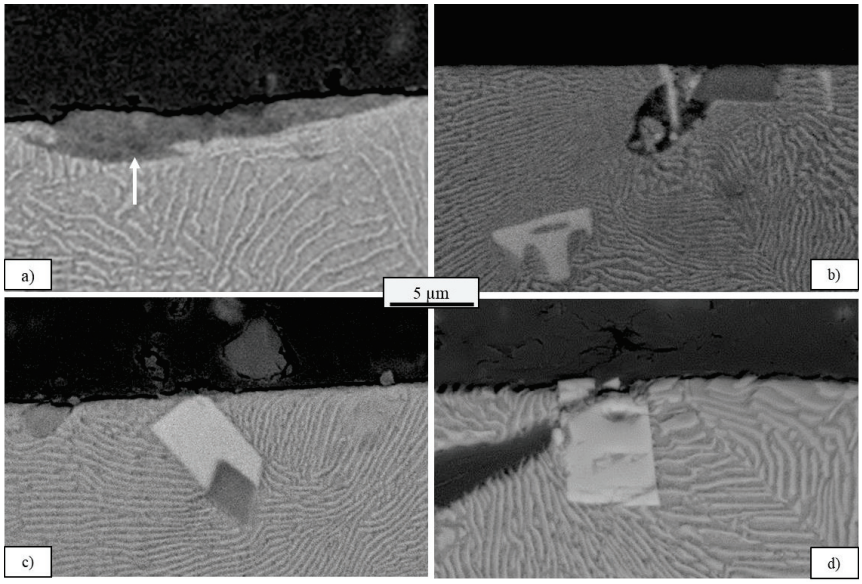

Figure 13. Cross-sectional view of the worn pins (**a**) D-0; (**b**) D-0.3; (**c**) D-0.5; and (**d**) D-0.7. White arrow in (**a**) highlight pad material debris.

Table 5. EDS analysis (wt%) of Figure 12.

Spectrum	C	O	Mg	Al	Si	S	Mn	Ti	Fe	Sn	Nb
1	N/A	33.02	1.60	-	1.65	0.71	0.77	-	62.25	-	-
2	N/A	-	-	-	-	-	-	1.85	2.96	-	95.19
3	N/A	44.26	1.93	0.84	1.16	0.73	-	-	49.26	1.82	-
4	N/A	46.16	1.41	0.93	1.21	-	-	-	48.34	1.96	-

4. Conclusions

In this study, the effect of different niobium additions (0%, 0.30%, 0.51%, 0.72%) on the microstructure and wear behavior of samples machined from brake-disc hypoeutectic gray cast iron was investigated. The wear behavior of GCI was examined by PoD wear tests performed with low-metallic friction material discs as counterparts. The presence of NbC particles in the microstructure of all samples alloyed with Nb was verified by using an optical microscope. NbC particles, having both cuboid and elongated shapes, appeared evenly distributed within the braking band of the cast iron samples, and their quantity and size increased with the addition of Nb.

Microstructural analysis revealed a pearlitic matrix for all the considered samples, indicating that, in the presence of other strong perlitizer elements, the addition of Nb did not affect the microstructure, as also confirmed by the micro-HV measurements performed in the matrix. Additionally, the graphite shape was unaffected by Nb, while the graphite flake length was slightly reduced, probably because the formation of small NbC particles in the liquid acted as heterogeneous nuclei for the graphite, enhancing their nucleation rate. This graphite refinement was also associated with a reduction in eutectic cell size. The reduced graphite flake length and the refinement of eutectic cells, together with the presence of well-distributed carbide particles, were responsible for the increase in hardness measured on the Nb-added samples as compared to the base alloy.

Abrasive wear was detected as the main wear mechanism in the PoD tests, even if some adhesive wear also occurred. Compared with the base alloy, the addition of Nb improved the wear strength, favored by the increase in hardness and the presence of hard NbC particles that could act as a load-bearing phase. However, the highest wear resistance was recorded for relatively low Nb addition (i.e., 0.3% Nb). Further addition of Nb did not appreciably modify the cast iron properties and negatively induced the coarsening of NbC particles. During sliding, coarse particles with poor toughness can easier experience brittle fracture, generating hard debris that promotes an increase in the three-body abrasive wear. Hence, it is advisable to not exceed 0.3% Nb in the composition of cast iron to improve their wear resistance and maintain low alloying costs.

Author Contributions: Conceptualization, G.B., A.P. and P.T.; methodology, P.T. and L.M.; investigation, P.T., L.M. and M.G.; writing—original draft preparation, P.T.; writing—review and editing, A.P. and M.G.; supervision, A.P. and M.G.; project administration, G.B.; funding acquisition, G.B. All authors have read and agreed to the published version of the manuscript.

Funding: This research was funded by the Ministry of Economic Development, EcoBrakeSystem (EBS) project, call FRI n° F/150040/01/X40, CUP B38I20000280005.

Data Availability Statement: Not applicable.

Acknowledgments: Authors would like to acknowledge Elkem ASA Foundry Products, Norway, for the support in the preparation of the samples.

Conflicts of Interest: The authors declare no conflict of interest.

References

1. Andrews, D. Braking of Road Vehicles. In *Braking of Road Vehicles*, 1st ed.; Butterworth-Heinemann: Oxford, UK, 2014.
2. Straffelini, G. *Friction and Wear (Springer Tracts in Mechanical Engineering)*; Springer: Cham, Switzerland, 2015.

3. Jimbo, Y.; Mibe, T.; Akiyama, K.; Matsui, H.; Yoshida, M.; Ozawa, A. Development of high thermal conductivity cast iron for brake disk rotors. In *SAE Transactions*; SAE International: Warrendale, PA, USA, 1990. [CrossRef]
4. Xu, W.; Ferry, M.; Wang, Y. Influence of alloying elements on as-cast microstructure and strength of gray iron. *Mater. Sci. Eng. A* **2005**, *33*, 326–333. [CrossRef]
5. Maluf, O.; Angeloni, M.; Milan, M.; Spinelli, D.; Wladimir, W.; Filho, B. Development of materials for automotive disc brakes. *Pesqui. Technol. Minerva* **2004**, *2*, 149–158.
6. Grabiec, T. Wear and Friction Behavior of Friction Pairs Tested with Different Types of Grey Cast Iron and Low Met Friction Material. *SAE Int. J. Passeng. Cars—Mech. Syst.* **2014**, *7*, 1361–1368. [CrossRef]
7. Djafri, M.; Bouchetara, M.; Busch, C.; Weber, S. Effects of humidity and corrosion on the tribological behaviour of the brake disc materials. *Wear* **2014**, *321*, 8–15. [CrossRef]
8. Grigoratos, T.; Martini, G. Non-exhaust traffic related emission. Brake and tyre wear PM. In *European Commission Joint Research Centre- Institute of Energy and Transport 2014*; Publications Office of the European Union: Luxembourg, 2014; Available online: https://ec.europa.eu/jrc/en/publication/eur-scientific-and-technical-research-reports/non-exhaust-traffic-related-emissions-brake-and-tyre-wear-pm (accessed on 20 July 2020).
9. Gonet, T.; Maher, B.A. Airborne, Vehicle-Derived Fe-Bearing Nanoparticles in the Urban Environment: A Review. *Environ. Sci. Technol.* **2019**, *17*, 9970–9991. [CrossRef] [PubMed]
10. *2022/0365(COD)*; Type-Approval of Motor Vehicles and Engines and of Systems, Components and Separate Technical Units Intended for such Vehicles, with Respect to Their Emissions and Battery Durability (Euro 7). European Parliament Legislative Observatory: Strasbourg, France, 2022.
11. Puisney, C.; Oikonomou, E.K.; Nowak, S.; Chevillot, A.; Casale, S.; Baeza-Squiban, A.; Berret, J.-F. Brake wear (nano)particle characterization and toxicity on airway epithelial cells: In vitro. *Environ. Sci. Nano* **2018**, *5*, 1036–1044. [CrossRef]
12. Perricone, G.; Matějka, V.; Alemani, M.; Valota, G.; Bonfanti, A.; Ciotti, A.; Olofsson, U.; Söderberg, A.; Wahlström, J.; Nosko, O.; et al. A concept for reducing PM10 emissions for car brakes by 50%. *Wear* **2018**, *396–397*, 135–145. [CrossRef]
13. Aranke, O.; Algenaid, W.; Awe, S.; Joshi, S. Coatings for Automotive Gray Cast Iron Brake Discs: A Review. *Coatings* **2019**, *9*, 552. [CrossRef]
14. Federici, M.; Menapace, C.; Moscatelli, A.; Gialanella, S.; Straffelini, G. Pin-on-disc study of a friction material dry sliding against HVOF coated discs at room temperature and 300 degrees C. *Tribol. Int.* **2017**, *115*, 89–99. [CrossRef]
15. Menapace, C.; Mancini, A.; Federici, M.; Straffelini, G.; Gialanella, S. Characterization of airborne wear debris produced by brake pads pressed against HVOF-coated discs. *Friction* **2019**, *8*, 421–432. [CrossRef]
16. Wahlström, J.; Lyu, Y.; Matjeka, V.; Söderberg, A. A pin–on–disc tribometer study of disc brake contact pairs with respect to wear and airborne particle emissions. *Wear* **2017**, *384–385*, 124–130. [CrossRef]
17. Tonolini, P.; Montesano, L.; Pola, A.; Landriani, E.; Gelfi, M. The effect of laser-cladding on the wear behavior of gray cast iron brake disc. *Procedia Struct. Integr.* **2021**, *33*, 1152–1161. [CrossRef]
18. Elbrigmann, T. Hard like Diamond. *Porsche Cust. Mag. Christophorus* **2017**, *4*, 384.
19. Bosch. iDisc. Available online: https://www.bosch-mobility-solutions.com/en/solutions/driving-safety/idisc/ (accessed on 1 March 2020).
20. Dutta, B.; Palmiere, E.; Sellars, C. Modelling the kinetics of strain induced precipitation in Nb microalloyed steels. *Acta Mater.* **2001**, *49*, 785–794. [CrossRef]
21. DeArdo, A.J. Niobium in modern steels. *Int. Mater. Rev.* **2003**, *48*, 371–402. [CrossRef]
22. Sun, L.-Y.; Liu, X.; Xu, X.; Lei, S.-W.; Li, H.-G.; Zhai, Q.-J. Review on niobium application in microalloyed steel. *J. Iron Steel Res. Int.* **2022**, *29*, 1513–1525. [CrossRef]
23. Bedolla-Jacuinde, A. Niobium in Cast Irons. In *Progress in Metallic Alloys*; Vadim, G., Ed.; IntechOpen: Rijeka, Croatia, 2016. [CrossRef]
24. Pourasiabi, H.; Gates, J. Effects of niobium macro-additions to high chromium white cast iron on microstructure, hardness and abrasive wear behaviour. *Mater. Des.* **2021**, *212*, 110261. [CrossRef]
25. Filipovic, M.; Kamberovic, Z.; Korac, M.; Gavrilovski, M. Microstructure and mechanical properties of Fe–Cr–C–Nb white cast irons. *Mater. Des.* **2013**, *47*, 41–48. [CrossRef]
26. Zhou, W.; Zhu, H.; Zheng, D.; Hua, Q.; Zhai, Q. Effect of niobium on solidification structure of gray cast iron. *TMS Annu. Meet.* **2010**, *3*, 817–828.
27. Wenbin, Z.; Hongbo, Z.; Dengke, Z.; Hongxing, Z.; Qin, H.; Qijie, Z. Niobium alloying effect in high carbon equivalent grey cast iron. *China Foundry* **2011**, *8*, 36–40.
28. Mohrbacher, H.; Zhai, Q. Niobium alloying in grey cast iron for vehicle brake discs. In Proceedings of the Materials Science and Technology Conference and Exhibition 2011, MS&T'11, Columbus, OH, USA, 16–20 October 2011; Taylor & Francis: Oxford, UK; Volume 1, pp. 434–445.
29. Hanna, I. Mechanical Properties of Niobium Alloyed Gray Iron. Master Thesis, Royal Institute of Technology, Stockholm Sweden, 2011.
30. Yao, Y. The Influence of Niobium Content and Cooling Rate on Mechanical Properties of Grey Cast Iron. Master Thesis, KTH Royal Institute of Technology, Stockholm, Sweden, 2019. Available online: http://urn.kb.se/resolve?urn=urn:nbn:se:kth:diva-244999 (accessed on 15 December 2022).

31. James, J.; Ronald, C.; Leonard, M.; Michael, M.; John, E. High Strength Gray Cast Iron Containing Niobium. Patent Appl. WO 2008/105987 A1, 4 September 2008.
32. Pan, S.; Zeng, F.; Su, N.; Xian, Z. The effect of niobium addition on the microstructure and properties of cast iron used in cylinder head. *J. Mater. Res. Technol.* **2019**, *9*, 1509–1518. [CrossRef]
33. Joachim, P.; Lotz, W. Optimized Gray Cast Iron Plate Alloy for Utility Vehicle Brake Disks. Patent Number US005894010A, 13 April 1999.
34. Li, Q.; Zhang, Y.; Zhang, Y.; Liu, H.; Ren, H.; Zhong, Y.; Huang, X.; Huang, W. Influence of Sn and Nb additions on the microstructure and wear characteristics of a gray cast iron. *Appl. Phys. A* **2020**, *126*, 282. [CrossRef]
35. Leal, G.; Enloe, C.M.; Meira, M.; Franca, E.; Nascimento, F.; Halonen, A. Wear evaluation of niobium-added cast iron for brake disc and drum applications. *SAE Int. J. Adv. Curr. Prac. Mobil.* **2020**, *3*, 980–987. [CrossRef]
36. Weitao, S.; Bin, W.; Xiaoliang, L.; Yuqian, W.; Jian, Z. Controlling the tribology performance of gray cast iron by tailoring the microstructure. *Tribol. Int.* **2022**, *167*, 107343. [CrossRef]
37. Metinoz, I.; Matejka, V.; Alemani, M.; Wahlström, J.; Perricone, G. Could pin-on-disc tribometers be used to study the friction/wear performance of disc brake materials? In Proceedings of the Eurobrake, Milano, Italy, 13–15 June 2016.
38. Chan, D.; Stachowiak, G.W. Review of automotive brake friction materials. *Proc. Inst. Mech. Eng. Part D: J. Automob. Eng.* **2004**, *218*, 953–966. [CrossRef]
39. Zhou, Z.-H.; Song, S.-Q.; Cromarty, R.; Chen, Y.-L.; Xue, Z.-L. The Precipitation of Niobium Carbide and Its Influence on the Structure of HT250 for Automobile Wheel Hubs. *Materials* **2021**, *14*, 6109. [CrossRef]
40. Devecili, A.O.; Yakut, R. The Effect of Nb Supplement on Material Characteristics of Iron with Lamellar Graphite. *Adv. Mater. Sci. Eng.* **2014**, *2014*, 465947. [CrossRef]
41. Reis, B.C.M.; dos Santos, A.J.; Pereira, N.F.S.; do Carmo, D.J.; de Faria, G.L.; Câmara, M.A.; de Faria, P.E.; Abrão, A.M. Effect of Nb Addition on the Machinability of a Pearlitic Gray Cast Iron. *J. Mater. Eng. Perform.* **2022**, *31*, 5983–5999. [CrossRef]
42. Ahmed, M.; Soliman, M.; Youssef, M.; Bähr, R.; Nofal, A. Effect of Niobium on the Microstructure and Mechanical Properties of Alloyed Ductile Irons and Austempered Ductile Irons. *Metals* **2021**, *11*, 703. [CrossRef]
43. Chen, X.; Zhao, L.; Zhang, W.; Mohrbacher, H.; Wang, W.; Guo, A.; Zhai, Q. Effects of niobium alloying on microstructure, toughness and wear resistance of austempered ductile iron. *Mater. Sci. Eng. A* **2019**, *760*, 186–194. [CrossRef]
44. Hasbrouck, M. The Effects of Molybdenum, Chromium, and Niobium On Gray Iron For Brake Rotor Applications. Master Thesis, Michigan Technological University, Houghton, MI, USA, 2021.
45. Riposan, I.; Chisamera, M.; Stan, S.; Hartung, C.; White, D. Three-stage model for nucleation of graphite in grey cast iron. *Mater. Sci. Technol.* **2010**, *26*, 1439–1447. [CrossRef]
46. Clayton, P.; Danks, D. Effect of interlamellar spacing on the wear resistance of eutectoid steels under rolling-sliding conditions. *Wear* **1990**, *135*, 369–389. [CrossRef]
47. Pero-Sanz Elorz, J.A.; Fernández González, D.; Verdeja, L.F. (Eds.) Stable Eutectic—Graphite Morphologies. In *Physical Metallurgy of Cast Irons*; Springer International Publishing: Cham, Switzerland, 2018; pp. 19–31.
48. Collini, L.; Nicoletto, G.; Konečná, R. Microstructure and mechanical properties of pearlitic gray cast iron. *Mater. Sci. Eng. A* **2008**, *488*, 529–539. [CrossRef]
49. Willidal, T.; Bauer, W.; Schumacher, P. Stress/strain behaviour and fatigue limit of grey cast iron. *Mater. Sci. Eng. A* **2005**, *413-414*, 578–582. [CrossRef]
50. Lyu, Y.; Leonardi, M.; Wahlström, J.; Gialanella, S.; Olofsson, U. Friction, wear and airborne particle emission from Cu-free brake materials. *Tribol. Int.* **2019**, *141*, 105959. [CrossRef]

metals

MDPI

Article

Surface Evolution of Vermicular Cast Iron in High Frequent Cyclic Plasma and Different Facial Cooling Airflows

Lei Liu *, Ke Zhao, Haijun Zhang, Chengwei Tang, Qinxin Han, Jiajia Chen, Dong Tao and Zhong Yang

School of Materials and Chemical Engineering, Xi'an Technological University, Xi'an 710021, China
* Correspondence: liuleinin@126.com; Tel./Fax: +86-029-83208080

Abstract: The surface evolution of vermicular cast iron in a high frequent cyclic plasma and facial cooling airflow was studied to understand the behavior and mechanism in different cooling conditions under a unique thermal shock environment. Results indicated that both the mass and linear loss presented titled inverted V-shaped relationships with the flux of the cooling airflow, while the change in roughness decreased continuously. As the cooling airflow rose, the eroded zone was reduced, the iron oxides lessened, and fluctuation of the surface temperature weakened. In combination with the thermodynamic calculations and thermal analysis, it was confirmed that the oxidation and mechanical erosion had contrary tendencies with the rising flux in the facial cooling airflow. The transformation of the dominant factor from oxidation to peeling off by thermal stress and scouring resulted in the evolution of mass and thickness. The surface oxides dominated the change in the roughness.

Keywords: vermicular cast iron; plasma; facial cooling; cyclic impact; oxidation

Citation: Liu, L.; Zhao, K.; Zhang, H.; Tang, C.; Han, Q.; Chen, J.; Tao, D.; Yang, Z. Surface Evolution of Vermicular Cast Iron in High Frequent Cyclic Plasma and Different Facial Cooling Airflows. *Metals* **2023**, *13*, 577. https://doi.org/10.3390/met13030577

Academic Editor: Francesco Iacoviello

Received: 10 February 2023
Revised: 28 February 2023
Accepted: 8 March 2023
Published: 13 March 2023

1. Introduction

Vermicular cast iron (RuT), also named compacted cast iron, has both the advantages of gray and nodular cast irons. The outstanding casting performance and good combination of mechanical and thermal properties have made RuT a perfect material for the cylinder head and blocks of a high power density (HPD) diesel engine [1–3]. Furthermore, the RuT has also received increasing attention on the application for a heavy truck brake system [4].

In a HPD diesel engine, as a key power of large machinery and transportation tool, the cylinder block or cylinder head material will be damaged by the high frequent impact of high temperature and high pressure generated by the detonation of flame. Due to its unique working environment, it is required that the high temperature components in the diesel engine must be able to withstand severe cyclic mechanical and thermal load throughout its service life. With the continuous development in the performance of a diesel engine, its working conditions become more and more severe, which results in higher and higher requirements on the comprehensive performance of RuT.

To improve the mechanical, anti-wear, and thermal properties of RuT, alloying [5,6], heat treatment [7,8], process, and surface modification [9,10] were all greatly studied. The nanoparticles were also used to adjust the microstructure [4]. Among these works, more and more attention have focused on surface treatment since many failures originated from there. Methods such as atmospheric plasma spraying [10], plasma transfer arc cladding [11], laser cladding [12], laser melt injection [13], diffusion thermo-reactive treatment [14], and some others have all been performed to optimize the surface for an improvement in the properties. Meanwhile, many studies such as thermal exposure [15], oxidation [16,17], creep [18,19], thermal shock [20], thermal fatigue [21,22], and thermal-mechanical fatigue [23–25] have focused on the high temperature performances and failure mechanism of the RuT to understand the practical problems of relative components. Great efforts have been made from the perspective of mechanics. Qiu et al. [15] mainly studied the effect of thermal exposure conditions on the in situ tensile fracture behavior. With the increase in the

thermal exposure time, the strength of the compacted graphite cast iron decreased, but the elongation at break increased. Guo et al. [16,17] analyzed the high temperature oxidation behavior of vermicular cast iron with different vermicular graphite rates and found that the oxidation weight gain decreased rapidly with the decrease in the vermicular graphite rate. Meanwhile, graphite was the core and channel of oxidation. The pearlite in the vermicular cast iron was oxidized and decomposed into ferrite and cementite at high temperature. Wu and Jing et al. [18,19] found that when the ratio of test temperature to melting temperature was greater than 0.5 and the load was higher than 150 MPa, obvious creep deformation would occur. In addition, creep damage was easy to occur in compacted graphite cast iron under wide temperature and stress conditions. Combined with the multi-objective optimization method, the creep constitutive model was constructed. Wang et al. [20] studied the oxidation and thermal cracking behavior under a high temperature and thermal shock environment, and found that graphite on the surface oxide scale was beneficial to the formation of surface thermal cracks. In addition, it can be inferred that the path of hot crack propagation along the thickness direction was the graphite-oxide network. Zhang et al. [22] studied two different types of compacted cast iron, and found that the ferrite grain boundary sliding temperature and pearlite transition temperature had an important influence on the thermal fatigue cracks of the two materials. Hilbery et al. [23] found that with the increase in the average length of graphite inclusions, the thermal mechanical fatigue life decreased, and the graphite content had no effect on it. Furthermore, Norman et al. [25] studied the thermo-mechanical fatigue properties of heterogeneous compacted cast iron at different maximum temperatures and mechanical strain ranges, and found that the micro-cracks independently expanded from fatigue to the rapid connection point of the cracks, resulting in final failure. Some other investigations found that thermal chemical reactions [26] and phase transformations [27] were also important to the failure of the diesel engine cylinder head. Some oxides could promote the crack propagation.

In the working condition of a cylinder head in a HPD diesel engine, the combustion and mixed air–oil have an impact on the RuT at high frequency. Obviously, this is different from the widely studied static oxidation, normal thermal shock, or thermal fatigue in the laboratory. However, few studies can be found on the evolution of RuT in a unique thermal shock environment, which has limited both the optimization of materials and structure. Referring to the large number of studies of flame tests for aerospace applications [28–30], some bench tests have recently been performed to simulate the working condition [31–34]. In our previous work, RuT [35], piston Al alloy [36], and modified C/C composites [37] were studied in the high frequent cyclic impact of combustion and airflow. The RuT and the others presented different erosion behavior from normal oxidation and thermal shock.

With the development of the diesel engine, key components possessing high precision and low roughness are always necessary. Furthermore, keeping the precision and surface state of service stable is also important for the cylinder head since an evident change in the size or roughness is sometimes fatal. When excess oxides are peeled off from the original surface, the combustion chamber like piston will be greatly damaged, which might lead to a failure of the whole machine. Additionally, working in various climatic environments is inevitable. The RuT for the cylinder head will undergo different cooling states, resulting in various intensities of thermal shock and surface damage. Therefore, as a following work in high frequency cyclic plasma, this study mainly dealt with the influence of facial cooling airflow on the surface erosion of RuT.

2. Materials and Methods

2.1. Preparation of the Vermicular Cast Iron

The raw materials used for the preparation of the vermicular cast iron were pig iron and 45 scrap steel. These were melted by a medium-frequency induction furnace. When the temperature reached 1300 °C, the material was completely melted, and the creeping agent and inoculant were added, respectively. The main components of the creeping agent and inoculant were 0.45~0.5 wt% Mg–Re alloy and 0.8 wt% 75Si–Fe. Then, the melt was

cleaned at a temperature of about 1470 °C and poured into the sand mold through the bottom gate system. Before pouring, the quality of the fracture triangular test block should be analyzed. The following cast was carried out only when the quality met the demand. The specimen for the test was cut from the bottom of the castings when cooled to room temperature, then the specimens were machined into a wafer type of $\varphi 30 \times 5$ mm^3. After sanding with different types of sandpaper (#80, #240, #600, #800, #1200, #1500, #2000) in order, the surface was polished by the cross method and dried for later experiments.

2.2. Tests and Characterization

As shown in Figure 1, the tested sample was cyclic impacted by plasma and cooling airflow through reciprocating motion under a 2 s period. The plasma was generated by Multiplaz 3500 using H_2O as the medium. The working voltage was 160 V and the relevant current was 6 A. The cooling airflow was provided by an air compressor under a pressure of 0.4 MPa. All of the tested samples were divided into four groups according to the different facial cooling airflows. The groups in fluxes of 0, 1, 2, 3 m^3/h were marked as RuT-0, RuT-1, RuT-2, and RuT-3, respectively. During the experiment, both the plasma and airflow jets were vertical to the surface of the tested sample and scoured for 0.5 s in each cycle. Both the diameters of the nozzles were 2 mm and their tips were 10 mm far from the sample surface. Moreover, the plasma was about 2300 °C at this distance, which was confirmed by a porous zirconia and an Endurance E1RH infrared thermometer (1000~3200 °C with a precision of ±0.5%). During the test, the surface temperature was real-time monitored by an Endurance E3ML infrared thermometer with a response time of 20 ms (50~1000 °C with a precision of ±0.3%). The infrared thermometer was located at about 1 m in front of the measured sample surface, forming a certain angle with the sample surface.

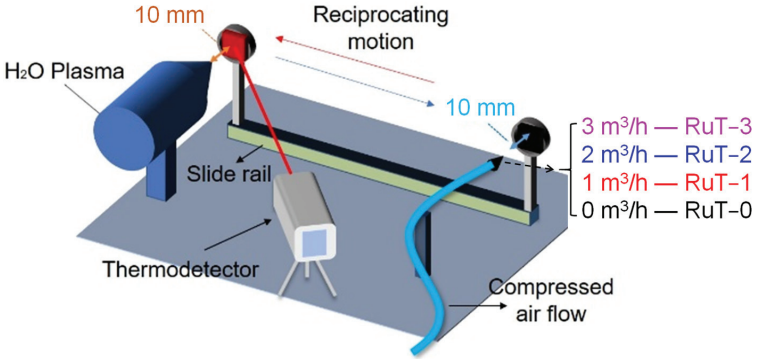

Figure 1. Schematic test of the vermicular cast iron in high frequency cyclic plasma and facial cooling airflow.

The mass and linear losses were calculated according to the weight changes and thickness variation of the sample center. The specific formulas are as follows:

$$M = (m_0 - m_1) \quad (1)$$

$$L = (l_0 - l_1) \quad (2)$$

where M is the mass loss and L is the linear loss; m_0 and m_1 are the mass of the sample before and after the test, and l_0 and l_1 are the thickness of the sample center before and after test. Furthermore, the change of roughness was also calculated through the roughness before the test minus that after the test. The roughness was measured by a detecting instrument (TR200) with a resolution of 0.01 μm/±20 μm. The surface roughness measurement of each specimen was carried out five times and the average value was taken.

Differential scanning calorimetry (DSC) and thermogravimetric (TGA) analysis of the vermicular cast iron was performed in air from room temperature to 1100 °C at a heating rate of 10 °C/min on a METTLER TOLEDO (Columbus, OH, USA) TGA/DSC 1 Thermal Analysis System. An optical microscope (NIKON EPIHOT3000, Tokyo, Japan) and scanning electron microscope (SEM, JSM6460) with energy dispersive spectroscopy (EDS) were used to observe the microstructure and morphology and analyze the chemical composition of the vermicular cast iron before and after the test. The phase analysis was carried out by a Shimadzu (Kyoto, Japan) X-ray diffractometer with the LabXXRD–6000 model.

3. Results and Discussion

3.1. Microstructure of the Vermicular Cast Iron

Figure 2 shows the microstructure, EDS analysis, and XRD pattern of the prepared RuT. Figure 2a,b shows the morphology of the unetched and etched specimen under the optical microscope. In Figure 2a, it was obvious that two different phases existed in the vermicular cast iron. The uniformly distributed black phase should be graphite and most of the phase was worm-like. Thus, there was no doubt that the black phase was vermicular graphite. In the OM morphology after corrosion by 4 wt% nitric acid alcohol, it was found that the gray phase in Figure 2a was composed of white ferrite (F) and dark gray pearlite (P). The blunt ferrite enwrapped the vermicular graphite. Depending on the calculation by ImageJ software through three representative microscopic photographs, it was confirmed that the vermicular rate was 80~85%. Combined with the EDS results in Figure 2c and the XRD pattern in Figure 2d, the elemental composition of the vermicular cast iron was ascertained to be Fe, with a small amount of C, Si, and Mn, and some other trace elements.

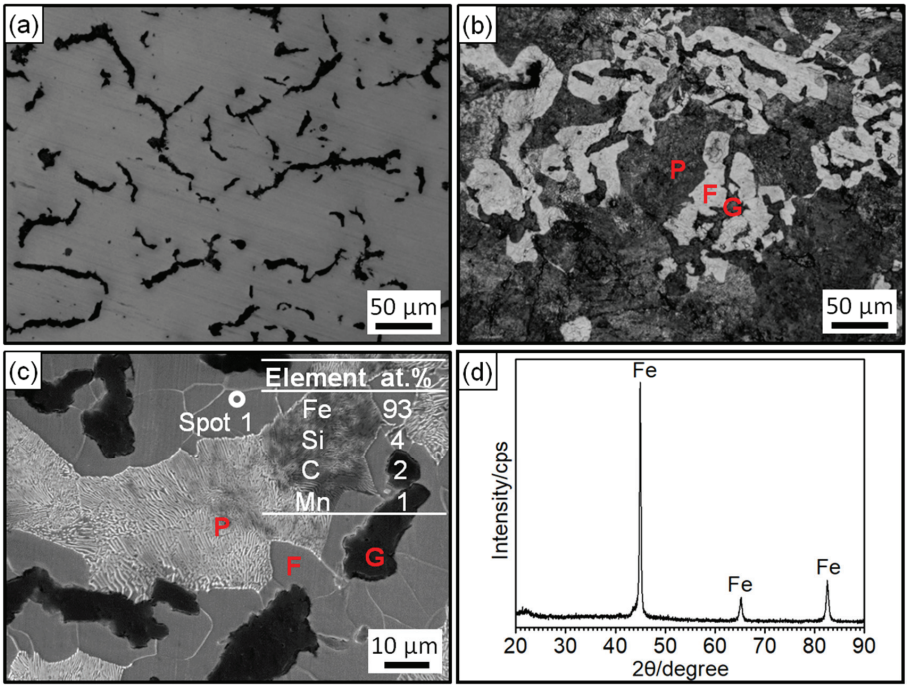

Figure 2. Microstructure, EDS analysis, and XRD pattern of the RuT: (**a**) OM morphology without corrosion; (**b**) OM morphology after corrosion; (**c**) second-electron morphology and EDS analysis; (**d**) XRD pattern.

3.2. Impact in High Frequency Cyclic Plasma and Facial Cooling Airflow

All of the changes in the mass, thickness, and roughness of the RuT after the test in different facial cooling airflows are displayed in Figure 3. As the flux of the cooling airflow elevated, the mass and linear loss showed similar changing rules, which increased first and then decreased, and presented titled inverted V-shaped curves. Furthermore, the values of thickness and mass losses were negative when the cooling airflow was below 1 m^3/h, and became positive under a higher flux of airflow. As the airflow increased to 3 m^3/h, the loss of thickness and mass were still positive but showed certain decreases. Obviously, the vermicular cast iron had a weight and thickness gain first, and then went into reverse with the rising flux in the facial cooling airflow. In contrast, the change in roughness exhibited a continuously declining trend, which should be closely related to the surface oxides.

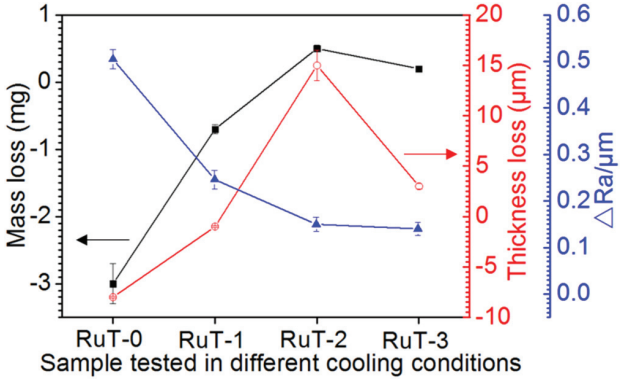

Figure 3. Evolution of the thickness, mass, and roughness of the RuT after the test in high frequency cyclic plasma and different facial cooling airflows.

Figure 4a shows the macroscopic photos of the RuT after the test in different facial cooling airflows. Due to the scouring of the circulating plasma and cooling airflow, different degrees of changes in the macroscopic shape of the sample came into being. It was clear that the surface center (marked by dotted circle) was heavily oxidized and had a distinct color in comparison with the surrounding region. With the increase in the flux of the cooling airflow, the region became smaller and smaller, which indicated that the heat affected zone decreased continuously. Due to the high temperature of the plasma, several oxides would be generated in the center zone since the oxidation of iron will form a variety of oxides. As presented in the XRD patterns (Figure 4b), the main composition of the tested surface comprised Fe, Fe_2O_3, and Fe_3O_4; no FeO was detected. It could be inferred that the oxides on the surface were a mixture of Fe_2O_3 and Fe_3O_4 while the Fe_2O_3 was greater. Furthermore, it could be seen that the intensities of both the Fe_2O_3 and Fe_3O_4 diffraction peaks declined with the strengthening of the facial cooling airflow. When the airflow rate was 3 m^3/h, the Fe_3O_4 could not be detected and the diffraction peak of Fe_2O_3 was the weakest. Reconsidering the result in Figure 3, it was deduced that the oxides was the key factor of roughness, and the greater the oxides, the rougher the tested surface. When the cooling airflow worked on the surface, thermal shock was enhanced and the oxides were peeled off under scouring. As more oxides would be blown off the surface by the rising facial cooling airflow, the increases in the mass and linear losses displayed in Figure 3 were reasonable.

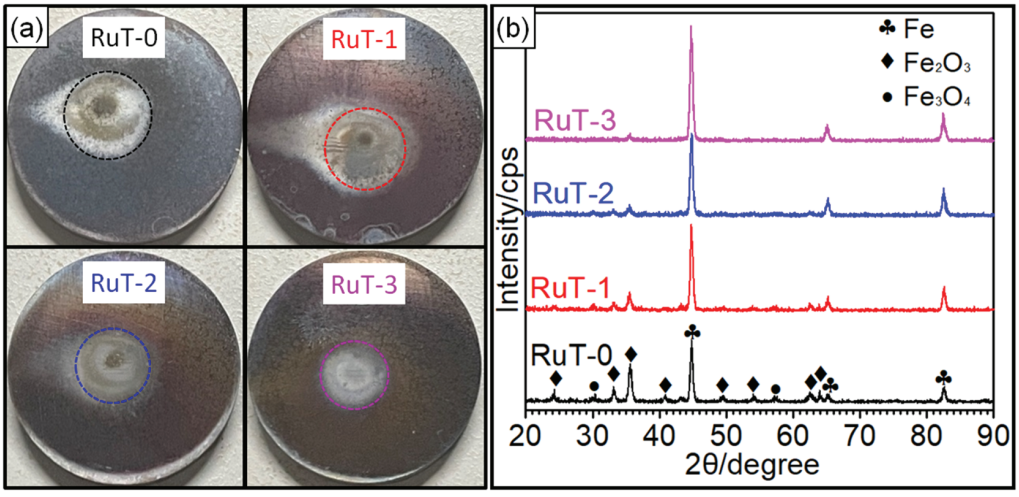

Figure 4. Macro-photos and XRD patterns of the RuT after testing in high frequency cyclic plasma and different facial cooling airflows: (**a**) macro-photos; (**b**) XRD patterns.

Figures 5 and 6 exhibit the surface and cross-section morphologies of the RuT after test in the cyclic plasma and different facial cooling airflows, respectively. When the airflow was zero, the outer oxide layer could be clearly observed and the surface of the sample was uneven, as presented in Figures 5a and 6a. The oxide layer gradually decreased as the airflow strengthened (Figures 5b,c and 6b,c). When the flux of the airflow reached 3 m^3/h (Figures 5d and 6d), there was no obvious oxide layer on the surface, the oxide and matrix alloys tended to be integrated, and only some oxide particles (marked by dotted ellipse) were distributed on the tested surface. According to the EDS analysis, the outside of the oxide layer was composed of Fe_2O_3, which was consistent with the normal oxidation in static air. Compared with the original morphology, it was obvious that several pores were formed on the tested surface by the oxidation of graphite. These pores tended to be closed (in Figure 5a) due to the continuous expansion of these iron oxides. When the facial cooling airflow came into being, the oxidation of Fe was inhibited and the pores from the oxidized graphite became clear.

Figure 7 shows the surface temperature of the tested samples during thermal shock. All curves of the four groups first rose and then tended to stabilize. Under the condition of the gas flow rate of 0 m^3/h, the temperature peak gradually increased to more than 700 °C with the rising time, and when the gas flow rate was elevated to 3 m^3/h, the peak decreased to about 450 °C. In other words, the peak value of the temperature decreased continuously with the heightening of the airflow, which should result from the more consumption of heat during cooling. Furthermore, some abnormal fluctuations of the surface temperatures (indicated by green dotted circle) occurred and reduced with the rising airflow. Considering that the temperature was obtained from the radiant intensity of the surface phases, it could be deduced that some surface oxides were peeled off during test since the oxide is a decisive factor of the surface temperature for its different thermal characteristics with substrate iron. Usually, the scouring is enhanced with the increased flux of the facial airflow, and more oxides should be blown away. However, the lessened and weakened abnormal fluctuation indicated that the stripped oxides were reduced. This might be related to the decline in surface temperature and the inhibited oxidation of Fe. The change in the surface states might be the main reason for the inflection of the mass and linear losses in Figure 3.

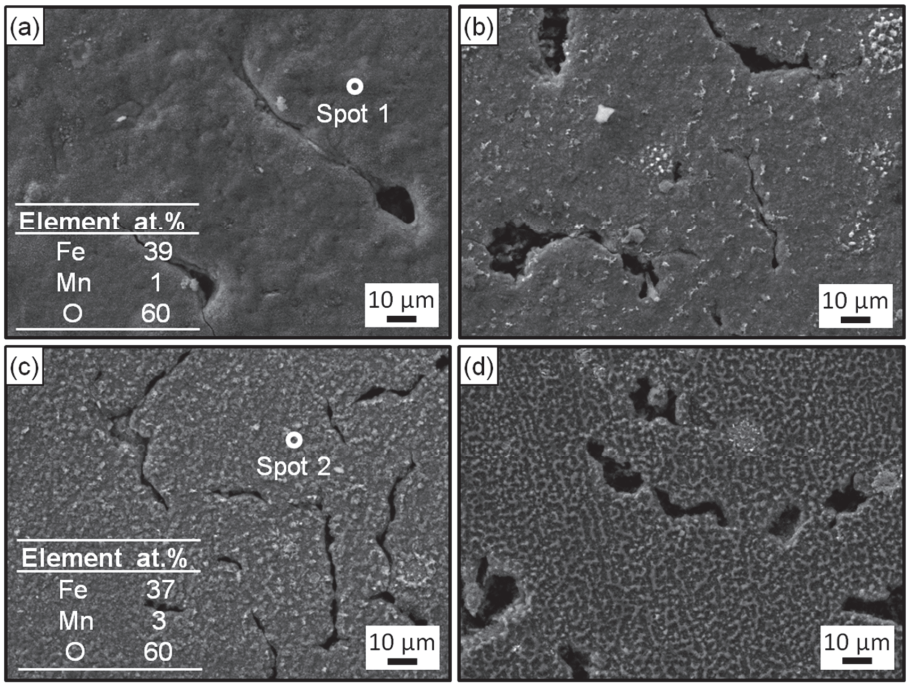

Figure 5. Surface morphologies and EDS analysis of the RuT after testing in high frequency cyclic plasma and different facial cooling airflows: (**a**) RuT-0; (**b**) RuT-1; (**c**) RuT-2; (**d**) RuT-3.

In conclusion, after the high frequency impact of plasma and different facial cooling airflows on the vermicular cast iron, new oxides of Fe_2O_3 and Fe_3O_4 were generated on the surface compared with the original sample. With the increase in cooling airflow, the thermal eroded area reduced at a macroscopic scale. Microscopically, the amount of oxide generated on the surface of the sample decreased until no obvious oxide layer was observed. In other words, the oxide layer and the matrix alloy gradually tended to integrated under the increasing airflow, and only some oxide particles were situated at the tested surface under 3 m^3/h. Meanwhile, the surface became flat. Furthermore, when the facial cooling air flow increased from 0 to 3 m^3/h, the pores formed by graphite oxidation changed from closed to gradually open, the peak surface temperature of the tested surface gradually decreased, and the oxidation of iron was obviously suppressed.

3.3. Erosion Mechanism in the Thermal Shock

During thermal shock, phase transformation, thermal chemical reactions, and thermal stress always induce surface damage. In plasma, scouring by the fluid was also a key destructive factor; this scouring will have a large impact on the surface condition of the material. To understand the erosion mechanism of the vermicular cast iron in the high frequency cyclic plasma and different facial cooling airflows, how phase transformation, thermal chemical reactions, and the others work should be clarified.

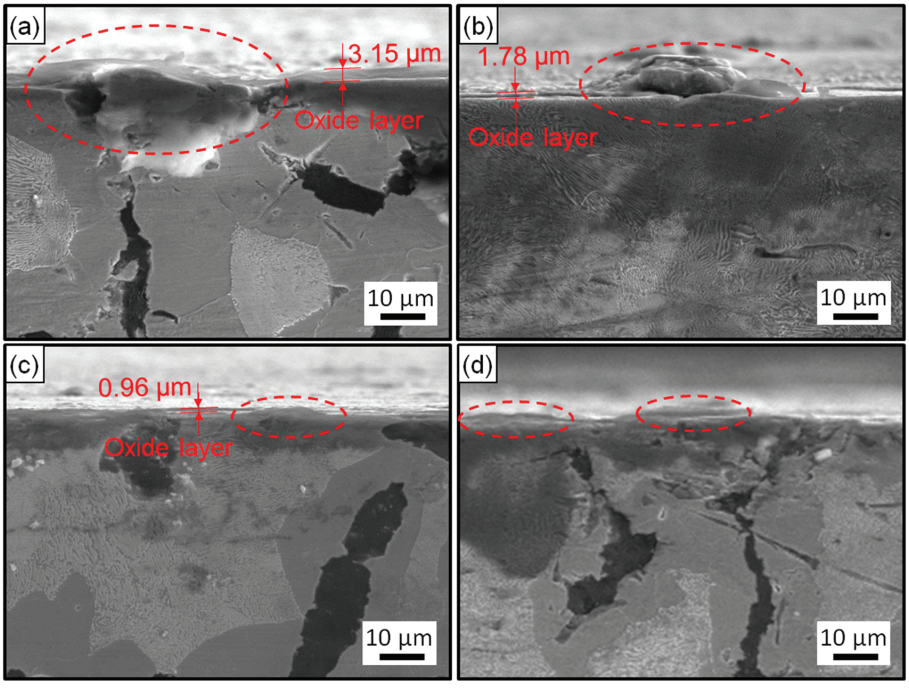

Figure 6. Cross-section morphologies of the RuT after test in high frequent cyclic plasma and different facial cooling airflows: (**a**) RuT-0; (**b**) RuT-1; (**c**) RuT-2; (**d**) RuT-3.

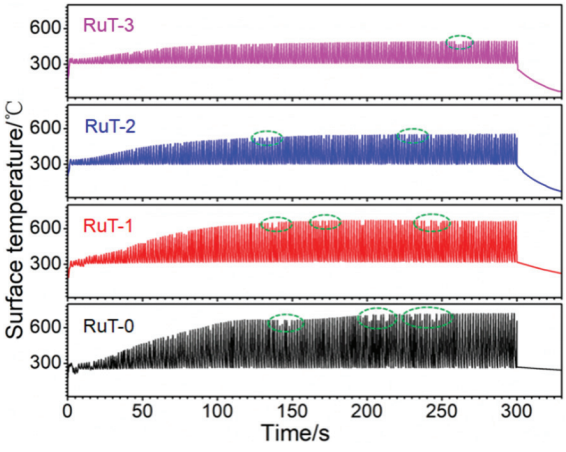

Figure 7. Surface temperatures of the RuT during testing in high frequency cyclic plasma and different facial cooling airflows.

Figure 8 presents the DSC/TGA thermal analysis of the RuT in air. As can be seen from the graph, the material gained weight throughout the process, which could explain that the mass and linear losses were negative when the airflow rate was low. Moreover, it can be clearly seen that an obvious weight gain occurred above 900 °C, which suggests that the oxidation below 900 °C was mild. Furthermore, there was a sudden fluctuation decrease in the curve of the heat flow at 750~800 °C, which corresponded to the phase transformation from pearlite to austenite. From Figure 7, it can be seen that all of the surface

temperatures of the four tested groups were lower than 750 °C. Thus, phase transformation played a limited role in the erosion of the vermicular cast iron, and the oxides were mainly from the mild oxidation reaction.

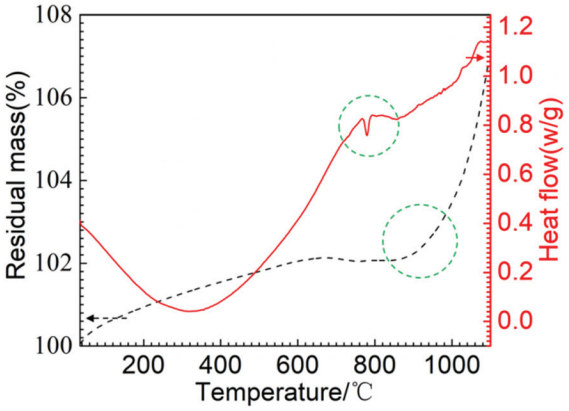

Figure 8. TGA/DSC thermal analysis of the RuT.

Figure 9 shows the Gibbs free energy change curves of the possible reactions during the thermal shock process. In the case of sufficient oxygen in air, oxygen reacts with metal and graphite, corresponding to reaction Equations (3)–(6), and in the case of the scarcity of oxygen in air, the reactions of reaction Equations (7)–(10) occur.

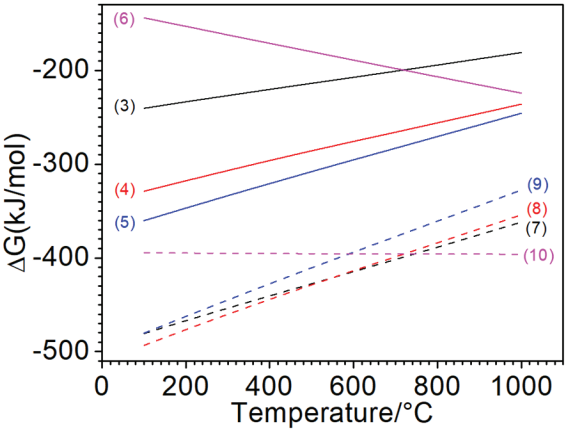

Figure 9. Changes in the standard Gibbs free energies of the relative reactions.

The reaction chemical formulas are as follows:

$$Fe + 1/2O_2 \rightarrow FeO \quad (3)$$

$$Fe + 2/3O_2 \rightarrow 1/3Fe_3O_4 \quad (4)$$

$$Fe + 3/4O_2 \rightarrow 1/2Fe_2O_3 \quad (5)$$

$$C + 1/2O_2 \rightarrow CO \quad (6)$$

$$2Fe + O_2 \rightarrow 2FeO \quad (7)$$

$$3/2Fe + O_2 \rightarrow 1/2Fe_3O_4 \quad (8)$$

$$4/3Fe + O_2 \rightarrow 2/3Fe_2O_3 \quad (9)$$

$$C + O_2 \rightarrow CO_2 \quad (10)$$

As well-known, chemical reactions can proceed spontaneously at negative Gibbs free energy change, where the smaller the Gibbs free energy value, the greater the tendency for the reaction to occur relatively. Therefore, from the Gibbs free energy change curve, it can be concluded that the dominant reaction is mainly controlled by the mass transfer of the oxidizing atmosphere on the surface. In the case of sufficient oxygen, Reaction (5) has a stronger tendency to proceed, followed by Reaction (4), so the outer surface is apt to form Fe_2O_3, while the sub-layer tends to generate Fe_3O_4. Combined with the XRD pattern, it can be determined that the oxides on the tested surface were mainly Fe_2O_3, which mixed with the underlying Fe_3O_4. Normally, the oxidation products of Fe are mainly controlled by the relative content of oxygen and the reaction temperature. At high temperature, the phases from inside to outside of the oxidized cast iron should be Fe–FeO–Fe_3O_4–Fe_2O_3. No FeO detected in this work should come from its low content or decomposition during cooling.

Figure 10 shows the schematic mechanism of the RuT surface evolution in the high frequency cyclic plasma and facial cooling airflow. Based on the above analysis, it can be inferred that the thermal chemical reactions, thermal stress, and scouring by the plasma were the main destructive factors. With an increase in the flux of the facial cooling airflow, the oxidation was reduced for the decreased heat affected zone and surface temperature. All of the morphologies in Figures 4a, 5, and 6 prove this. Therefore, it seems that a lower mass and linear gain are reasonable. However, the mass and linear losses showed positive values and an inflection appeared at 1 m^3/h. This is because during the test, the surface damage was first caused by oxidation, and then the increase in the facial cooling airflow promoted oxide stripping under thermal stress and scouring. Therefore, when the oxidation dominated the erosion, the mass and linear losses were negative, which would become positive under stronger mechanical erosion by thermal stress and scouring. When the cooling airflow was further strengthened, even though the thermal stress and scouring ability to strip the oxide increased, less oxide was formed due to the decrease in surface temperature, which led to the peeling off being limited As a result, the mass and linear losses fell after a rise. Meanwhile, the different densities and thermal expansion behaviors between the oxides and Fe substrate resulted in a large change in roughness under thermal shock. As fewer oxides formed and were peeled off by thermal stress and scouring, it decreased and approached a stable value.

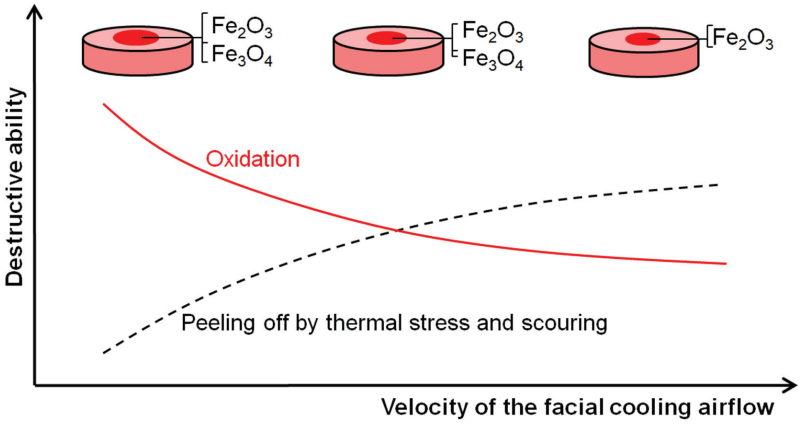

Figure 10. Schematic surface evolution of the RuT in high frequency cyclic plasma and facial cooling airflow.

4. Conclusions

The microstructural evolution, oxidative erosion behavior, and mechanism analyses of vermicular cast iron after being subjected to high frequent cyclic plasma and different facial cooling airflows were investigated. Based on the experimental results and discussion, the following conclusions can be drawn:

(1) In high frequency cyclic plasma and airflow, both the mass and linear losses of the vermicular cast iron displayed titled inverted V-shaped relationships with the strengthening of facial airflow cooling, and had negative values when the flux was zero. Meanwhile, the roughness change, area of the eroded zone, and the fluctuated surface temperature decreased continuously.

(2) The oxidation was weakened while the peeling off by thermal stress and cooling airflow was enhanced with the rise in the flux of the facial cooling airflow. Weight gain from oxidation dominated the erosion first, and was then replaced by the peeling off, which determined the inflexion of the mass and linear losses, and the surface oxides dominated the change in the roughness.

Author Contributions: L.L.: Conceptualization, Formal analysis, Methodology, Validation, Writing-original draft; K.Z.: Data curation, Formal analysis, Writing-original draft; H.Z.: Formal analysis, Investigation, Writing-original draft; C.T. and Q.H.: Formal analysis, Writing-original draft; J.C.: Writing-review & editing; D.T.: Resources; Z.Y.: Supervision. All authors have read and agreed to the published version of the manuscript.

Funding: This research was funded by the Youth Innovation Team of Shaanxi Universities (No. 22JP031), the Natural Science Foundation of Shaanxi Province (No. 2022JQ-480), and the Innovation and Entrepreneurship Training Program for College Students (No. X202210702166).

Data Availability Statement: All data included in this study are available upon request by contacting the corresponding author.

Conflicts of Interest: The authors declare that they have no competing financial interest or personal relationship that could have appeared to influence the work reported in this paper.

References

1. Pierce, D.; Haynes, A.; Hughes, J.; Graves, R.; Maziasz, P.; Muralidharan, G.; Shyam, A.; Wang, B.; England, R.; Daniel, C. High temperature materials for heavy duty diesel engines: Historical and future trends. *Prog. Mater. Sci.* **2019**, *103*, 109–179. [CrossRef]
2. Liu, Y.; Li, Y.; Xing, J.; Wang, S.; Zheng, B.; Tao, D.; Li, W. Effect of graphite morphology on the tensile strength and thermal conductivity of cast iron. *Mater. Charact.* **2018**, *144*, 155–165. [CrossRef]
3. Prasad, N.S.; Ganesh, N.; Kumarasamy, A. Technologies for high power density diesel engines. *Def. Sci. J.* **2017**, *67*, 370–374. [CrossRef]
4. Wang, B.; Qiu, F.; Zhang, Y.; Yang, J.; Cui, W.; Jin, Y.; Cai, G.; Yuan, Y.; Guo, S.; Li, H.; et al. Influences of dual-phased nanoparticles on microstructure, mechanical properties and wear resistance of vermicular graphite cast iron. *Mater. Lett.* **2022**, *308*, 131296. [CrossRef]
5. Song, L.; Guo, E.J.; Wang, L.P.; Liu, D.R. Effects of silicon on mechanical properties and fracture toughness of heavy-section ductile cast iron. *Metals* **2015**, *5*, 150–161. [CrossRef]
6. Riposan, L.; Stefan, E.; Stan, S.; Pana, N.R.; Chisamera, M. Effects of inoculation on structure characteristics of high silicon ductile cast irons in thin wall castings. *Metals* **2020**, *10*, 1091. [CrossRef]
7. Chen, Y.; Pang, J.C.; Li, S.X.; Zou, C.L.; Zhang, Z.F. Damage mechanism and fatigue strength prediction of compacted graphite iron with different microstructures. *Int. J. Fatigue* **2022**, *164*, 107126. [CrossRef]
8. Dawson, S. Compacted graphite iron: Mechanical and physical properties for engine design. *Vdi Ber.* **1999**, *1472*, 85–106.
9. Essam, M.A.; Shash, A.Y.; Megahed, H.; El-Kashif, E. Effect of section thickness on microstructure and mechanical properties of compacted graphite iron for diesel engine applications. *Heliyon* **2021**, *7*, e5930. [CrossRef]
10. Gao, P.H.; Chen, B.Y.; Zeng, S.C.; Yang, Z.; Guo, Y.C.; Liang, M.X.; Xu, T.; Li, J.P. Effect of vacuum annealing on the nickel-based coatings deposited on a CGI cast iron through atmospheric plasma spraying. *Metals* **2020**, *10*, 963. [CrossRef]
11. Sun, F.Z.; Cai, K.Q.; Li, X.X.; Pang, M. Research on laser cladding Co-based alloy on the surface of vermicular graphite cast iron. *Coatings* **2021**, *11*, 1241. [CrossRef]
12. Mariani, F.E.; Takeya, G.S.; Lombardi, A.N.; Picone, C.A.; Casteletti, L.C. Wear and corrosion resistance of Nb-V carbide layers produced in vermicular cast iron using TRD treatments. *Surf. Coat. Technol.* **2020**, *397*, 126050. [CrossRef]

13. Verezub, O.; Kálazi, Z.; Buza, G.; Verezub, N.V.; Kaptay, G. In-situ synthesis of a carbide reinforced steel matrix surface nanocomposite by laser melt injection technology and subsequent heat treatment. *Surf. Coat. Technol.* **2009**, *203*, 3049–3057. [CrossRef]
14. Chen, B.; Gao, P.; Zhang, B.; Zhao, D.; Wang, W.; Jin, C.; Yang, Z.; Guo, Y.; Liang, M.; Li, J.; et al. Wear properties of iron-based alloy coatings prepared by plasma transfer arc cladding. *Coatings* **2022**, *12*, 243. [CrossRef]
15. Qiu, Y.; Pang, J.C.; Li, S.X.; Yang, E.N.; Fu, W.Q.; Liang, M.X.; Zhang, Z.F. Influence of thermal exposure on microstructure evolution and tensile fracture behaviors of compacted graphite iron. *Mat. Sci. Eng. A-Struct.* **2016**, *664*, 75–85. [CrossRef]
16. Guo, Q.Q.; Yang, Z.; Tao, D.; Gao, P.H.; Guo, Y.C.; Li, J.P. Effects of vermicular graphite rate on the oxidation resistance and mechanical properties of vermicular graphite iron. *J. Alloy. Compd.* **2018**, *765*, 213–220. [CrossRef]
17. Guo, Q.Q.; Yang, Z.; Guo, D.; Tao, D.; Guo, Y.C.; Li, J.P.; Bai, Y.P. Research on the oxidation mechanism of vermicular graphite cast iron. *Materials* **2019**, *12*, 3130. [CrossRef]
18. Wu, Y.; Li, J.P.; Yang, Z.; Guo, Y.C.; Ma, Z.J.; Liang, M.X.; Yang, T.; Tao, D. Creep behavior accompanying oxidation of compacted graphite cast iron. *Mat. Sci. Eng. A-Struct.* **2018**, *723*, 174–181. [CrossRef]
19. Jing, G.X.; Li, S.B.; Chen, G.; Wei, J.C.; Sun, S.; Zhang, J.H. Research on creep test of compacted graphite cast iron and parameter identification of constitutive model under wide range of temperature and stress. *Appl. Sci.* **2022**, *12*, 5032. [CrossRef]
20. Wang, X.S.; Zhang, W.Z. Oxidation and thermal cracking behavior of compacted graphite iron under high temperature and thermal shock. *Oxid. Met.* **2017**, *87*, 179–188. [CrossRef]
21. Tong, X.; Zhou, H.; Ren, L.Q.; Zhang, Z.H.; Zhang, W.; Cui, R.D. Effects of graphite shape on thermal fatigue resistance of cast iron with biomimetic non-smooth surface. *Int. J. Fatigue* **2009**, *31*, 668–677. [CrossRef]
22. Zhang, M.X.; Pang, J.C.; Meng, L.J.; Li, S.X.; Liu, Q.Y.; Jiang, A.L.; Zhang, Z.F. Study on thermal fatigue behaviors of two kinds of vermicular graphite cast irons. *Mat. Sci. Eng. A-Struct.* **2021**, *814*, 141212. [CrossRef]
23. Kihlberg, E.; Norman, V.; Skoglund, P.; Schmidt, P.; Moverare, J. On the correlation between microstructural parameters and the thermo-mechanical fatigue performance of cast iron. *Int. J. Fatigue* **2021**, *145*, 106112. [CrossRef]
24. Lopez, C.E.; Ghodrat, S.; Kestens, L.A. Semi in-situ observation of crack initiation in compacted graphite iron during thermos mechanical fatigue. *Int. J. Fatigue* **2020**, *137*, 105648. [CrossRef]
25. Norman, V.; Skoglund, P.; Moverare, J. Damage evolution in compacted graphite iron during thermo-mechanical fatigue testing. *Int. J. Cast. Met. Res.* **2015**, *29*, 26–33. [CrossRef]
26. Jing, G.X.; Zhang, M.X.; Qu, S.; Pang, J.C.; Fu, C.M.; Dong, C.; Li, S.X.; Xu, C.G.; Zhang, Z.F. Investigation into diesel engine cylinder head failure. *Eng. Fail. Anal.* **2018**, *90*, 36–46. [CrossRef]
27. Palkanoglou, E.N.; Baxevanakis, K.P.; Silberschmidt, V.V. Thermal debonding of inclusions in compacted graphite iron: Effect of matrix phases. *Eng. Fail. Anal.* **2022**, *139*, 106476. [CrossRef]
28. Ragav, P.; Panakaraju, P.; Farhan, M.; Joseph, E.R. Solid particle erosion behavior of melt-infiltrated SiC/SiC ceramic matrix composites (CMCs) in a simulated turbine engine environment. *Compos. Part B-Eng.* **2021**, *216*, 108860.
29. Guo, J.; Fu, S.; Deng, Y.P.; Xu, X.; Laima, S.; Liu, D.Z.; Zhang, P.Y. Hypocrystalline ceramic aerogels for thermal insulation at extreme conditions. *Nature* **2022**, *606*, 909–916. [CrossRef]
30. Yan, M.; Hu, C.; Li, J.; Zhao, R.D.; Pang, S.Y.; Liang, B.; Tang, S.F.; Liu, G.; Cheng, H.M. An unusual carbon–ceramic composite with gradients in composition and porosity delivering outstanding thermal protection performance up to 1900 °C. *Adv. Funct. Mater.* **2022**, *32*, 2204133. [CrossRef]
31. Yan, J.H. Study on structure and ablation resistance of ceramic coating on the top of engine piston. *Intern. Combust. Eng. Parts* **2016**, *6*, 8–11.
32. Qin, Z.J.; Jia, C.F.; Zhang, W.Z.; Wang, L.J. Investigations on ablation for highly-intensified diesel engine piston material. Case Stud. *Therm. Eng.* **2019**, *13*, 100371.
33. Reghu, V.; Lobo, R.; Basha, K.A.; Tilleti, P.; Shankar, V.; Ramaswamy, P. Protection offered by thermal barrier coatings to Al-Si alloys at high temperatures—A microstructural investigation. *Mater. Today Proc.* **2019**, *19*, 676–681. [CrossRef]
34. De Goes, W.U.; Markocsan, N.; Gupta, M.; Vaßen, R.; Matsushita, T.; Illkova, K. Thermal barrier coatings with novel architectures for diesel engine applications. *Surf. Coat. Technol.* **2020**, *396*, 125950. [CrossRef]
35. Tang, C.W.; Liu, L.; Yang, Z.; Tao, D.; Li, J.P.; Guo, Q.Q.; Zhen, J.R.; He, Y.L.; He, H.X. Surface evolution of vermicular cast iron in ultra-high temperature combustion with different single-pulsing duration. *Eng. Fail. Anal.* **2022**, *141*, 106679. [CrossRef]
36. Liu, L.; Tang, C.W.; Li, B.Y.; Li, J.P.; Bao, T.; Yang, Z.; Guo, Y.C.; Feng, W.; Lei, Z.; Li, H.Y. Surface evolution of Al-Si-Cu alloy in a high frequent pulsing oxyacetylene combustion. *Case Stud. Therm. Eng.* **2022**, *31*, 101854. [CrossRef]
37. Liu, L.; Li, B.Y.; Feng, W.; Tang, C.W.; Zhang, J.P.; Yao, X.Y.; Yang, Z.; Guo, Y.C.; Wang, P.; Zhang, Y. Effect of loading spectrum with different single pulsing time on the cyclic ablation of C/C-SiC-ZrB_2-ZrC composites in plasma. *Corros. Sci.* **2021**, *192*, 109817. [CrossRef]

MDPI
St. Alban-Anlage 66
4052 Basel
Switzerland
www.mdpi.com

Metals Editorial Office
E-mail: metals@mdpi.com
www.mdpi.com/journal/metals

Academic Open
Access Publishing

mdpi.com

ISBN 978-3-0365-8717-2